

# **Real-time Electrohydraulic Motion Tracking by Order-Separated Novel Feedforward Controller with PID Feedback in Single-Cylinder to Multi-Cylinder Serial-Parallel Manipulator**

Thesis submitted by  
**Aniruddha Sarkar**

For the degree of  
**Doctor of Philosophy (Engineering)**

**Department of Mechanical Engineering  
Faculty Council of Engineering & Technology  
Jadavpur University  
Kolkata, India**

**2023**



**JADAVPUR UNIVERSITY**  
**KOLKATA-700032, INDIA**

INDEX NO. 148/17/E

**1. Title of the Thesis: Real-time electrohydraulic motion tracking by order-separated novel feedforward controller with PID feedback in single-cylinder to multi-cylinder serial-parallel manipulator**

**2. Name, Designation and Institution of the Supervisor/s:**

(a) **Prof. Saikat Mookherjee**

Professor, Department of Mechanical Engineering  
Jadavpur University, Kolkata - 700032

(b) **Prof. Dipankar Sanyal**

Professor, Department of Mechanical Engineering  
Jadavpur University, Kolkata - 700032

**3. List of Publications:**

(a) **Journals**

- i. Sarkar, A., Saha, R., Mookherjee, S., & Sanyal, D. (2023) **Validation and Real-time Application of a Novel Order-Separated Feedforward Controller with PI Feedback for Electrohydraulic Actuation of Linear Motion.** *Journal of the Brazilian Society of Mechanical Sciences and Engineering.* vol. 45, Article 361, <https://doi.org/10.1007/s40430-023-04232-8>
- ii. Sarkar, A., Maji, K., Chaudhuri, S., Saha, R., Mookherjee, S., & Sanyal, D. (2023). **Actuation of an electrohydraulic manipulator with a novel feedforward compensation scheme and PID feedback in servo-proportional valves.** *Control Engineering Practice*, vol. 135, Article 105490, <https://doi.org/10.1016/j.conengprac.2023.105490>

(b) **Book Chapter:** Nil

(c) **International Conferences:**

- i. Sarkar, A., Naskar, N., Ghosh, A., Paul, N., & Pal, N. **Heave tracking by an electrohydraulic serial-parallel manipulator.** *67th Congress of the Indian Society of Theoretical and Applied Mechanics (ISTAM) (An International Conference)*, December 14-16, 2022, Paper ID: ISTAM/2022/PA0229

- ii. Sarkar, A., Saha, R., Mookherjee, S., Acharyya, S., & Sanyal, D. **Analysis of a flow efficient gait transition from static walk to trot for an electrohydraulic quadruped.** *INCOM18: Proceedings of the 1<sup>st</sup> International Conference*, Mechanical Engineering, Jadavpur University Kolkata India January 4 – 6, 2018 Paper No. INCOM18-214.

**4. List of Patents:** None

**5. List of Presentations in National/International Conferences and Workshops:**

- i. Sarkar, A., Saha, R., Mookherjee, S., Acharyya, S., & Sanyal, D. **Analysis of a flow efficient gait transition from static walk to trot for an electrohydraulic quadruped.** *INCOM18: Proceedings of the 1<sup>st</sup> International Conference*, Mechanical Engineering, Jadavpur University Kolkata India January 4 – 6, 2018 Paper No. INCOM18-214.



**JADAVPUR UNIVERSITY  
FACULTY OF ENGINEERING AND TECHNOLOGY**

**STATEMENT OF ORIGINALITY**

I, Shri Aniruddha Sarkar registered on 27<sup>th</sup> April 2017, do hereby declare that this thesis entitled "**Real-time electrohydraulic motion tracking by order-separated novel feedforward controller with PID feedback in single-cylinder to multi-cylinder serial-parallel manipulator**" contains literature survey and original research work done by the undersigned candidate as part of Doctoral studies.

All information in this thesis have been obtained and presented in accordance with existing academic rules and ethical conduct. I declare that, as required by these rules and conduct, I have fully cited and referred all materials and results that are not original to this work.

I also declare that I have checked this thesis as per the "Policy on Anti Plagiarism, Jadavpur University, 2019", and the level of similarity as checked by iThenticate software is 0 %.

Signature of Candidate: *Aniruddha Sarkar*

Date : *19/6/2023*

Certified by Supervisor(s):

(Signature with date, seal)

1. *Saikat Mookherjee* 19/6/23  
(Prof. Saikat Mookherjee)

PROFESSOR  
Mechanical Engineering Deptt  
Jadavpur University  
Kolkata - 700 032

2. *Dipankar Sanyal* 19/6/23  
(Prof. Dipankar Sanyal)

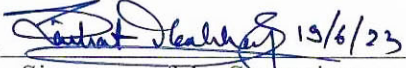
PROFESSOR  
Mechanical Engineering Deptt  
Jadavpur University  
Kolkata - 700 032



**JADAVPUR UNIVERSITY**  
**FACULTY OF ENGINEERING AND TECHNOLOGY**

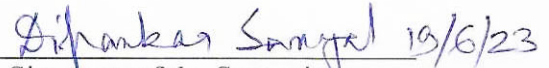
**CERTIFICATE FROM THE SUPERVISOR/S**

This is to certify that the thesis entitled '**Real-time electrohydraulic motion tracking by order-separated novel feedforward controller with PID feedback in single-cylinder to multi-cylinder serial-parallel manipulator**' submitted by Mr. Aniruddha Sarkar, who got his name registered on 27<sup>th</sup> April, 2017 with a Registration Index number **148/17/E** for the award of Ph. D. (Engineering) degree of Jadavpur University is absolutely based upon his own work under the supervision of **Prof. Saikat Mookherjee** and **Prof. Dipankar Sanyal** and that neither his thesis nor any part of the thesis has been submitted for any degree/diploma or any other academic award anywhere before.

1.  19/6/23

Signature of the Supervisor  
with date and Office Seal

**PROFESSOR**  
**Mechanical Engineering Deptt**  
**Jadavpur University**  
**Kolkata - 700 032**

2.  19/6/23

Signature of the Supervisor  
with date and Office Seal

**PROFESSOR**  
**Mechanical Engineering Deptt**  
**Jadavpur University**  
**Kolkata - 700 032**



*Dedicated to my Revered Guide*

*Prof. Dipankar Sanyal*

*Prof. Saikat Mookherjee*

*Prof. Rana Saha*



# Acknowledgements

*I would like to take this opportunity to express my heartfelt gratitude to my supervisors, **Prof. Saikat Mookherjee** and **Prof. Dipankar Sanyal**, Department of Mechanical Engineering, Jadavpur University, Kolkata, for their invaluable assistance, advice, and encouragement throughout the duration of this thesis work. Since my master's curriculum, it has been an unequivocal pleasure to have mentorship from them in the form of knowledge sharing, conversations, criticism, and countless opportunities to work under their patronage. This opportunity has allowed me to grow not just in my understanding of robotics and control but also in my ability to visualize problems, apply effective solutions, master the art of debugging, and develop a positive work ethic. In this regard, I will always be grateful to **Prof. Rana Saha** for the crucial advice and support he gave me over the course of my research.*

*My profound appreciation also extends to the other members of the Project Neptune team, including Professors Kamalesh Majumdar, Shankar Dhar, Sanjib Kr. Acharyya, Kumardeb Banerjee, Swarnendu Sen, Achintya Mukhopadhyay, Kaushik Ghosh, Nirmal Manna, and the research scholars, for sharing their invaluable experiences, providing encouragement, and providing tremendous cooperation throughout the thesis work.*

*I am thankful to **Prof. Amit Karmakar**, Head of the Department of Mechanical Engineering at Jadavpur University, for his assistance in a variety of academic and non-academic matters. In addition, I would also like to thank the **Centre for Artificial Intelligence and Robotics, Bengaluru (DRDO India)**, for their complete funding support and suggestions for conducting the research.*

*I would like to thank **Dr. Shauvik Chaudhuri**, **Dr. Aritra Mukherjee**, and **Mr. Krishnendu Maji**, my fellow researchers on the **Quadruped Project**, for all the innovative concepts we came up with together. **Dr. Shauvik Chaudhuri**, who has generously shared his expertise on both the hardware and software levels, should be singled out for special attention. I would also like to express my appreciation to **Mr. Niladri Naskar** and **Mr. Ritam Pal**, two of my current and previous junior lab members. whose unwavering assistance and input over the course of my PhD studies have been invaluable. I wish them success on their own journey. My special thanks are also extended to **Drs. Pranibesh Mondal**, **Shauvik Chaudhuri**, **Nitesh Mondal**, and **Saurav Sarkar**, with whom I have discussed a broad range of mechanical engineering topics.*

*Anindita Chakrabarty is a person who holds a special place in my heart, and I would like to take this opportunity to convey my heartfelt love, admiration, and gratitude for her. She will remain in my mind forever, as long as I continue to live.*

*This acknowledgement would be incomplete without mentioning my mother's arduous efforts and dedication to providing me with appropriate care. I would like to honour my mother, **Mrs. Uma Sarkar**, an ex-employee of the Mechanical Engineering Department at Jadavpur University, for her countless struggles, sacrifices, and love for me. My deepest gratitude also extends to my late father, **Dr. Satyabrata Sarkar**, an ex-employee and alumnus of Jadavpur University, for the many blessings he bestowed upon me throughout every moment of my life. I would also like to appreciate my older sister, **Mrs. Anuradha Sarkar**, for having faith in my abilities and providing moral support and affection. In addition, I appreciate everyone in my family for supporting me. I would like to single out my uncle, **Mr. Subrata Sarkar**, for being an inspiration to me ever since I was a kid. There are no words to describe how much he helped me after the loss of my father.*

*Finally, I would like to express my gratitude to my alma mater for giving me the best opportunities to grow intellectually, learn to think critically, and enrich my mind. The person I have become today is a testament to the exceptional education and experiences I received at this esteemed institution.*

*The person you created up to this point is now standing before you to offer his sincere regards and affection.*

**Aniruddha Sarkar**

*PhD Fellow, Jadavpur University*







# ***Abstract***

*Electrohydraulic actuation systems, or **EHAS**, are widely employed in a variety of modern industries, from those demanding ruggedness to those requiring great precision and sophistication. Despite many benefits and widespread industrial applications of **EHAS**, its real-time control is extremely challenging in terms of precision and faster tracking. The inherent nonlinearities of **EHAS** with parametric uncertainties and external disturbances pose serious challenges to the controller design. These effects are even substantial for sophisticated servosystems meant for high-precision robotic manipulators. Rugged systems are cheaper, but additionally associated with hard nonlinearities like static friction in the actuators and large deadband in the proportional valves – especially for manipulator systems. Both model-free and model-based controllers have been developed and investigated for effective control of electrohydraulic systems. But in absence of a suitable physical model, either optimal performance or stability remains questionable. In this regard, model-based controllers are considered to be superior. Feedforward controllers use differentially flat system models to account for known disturbances and nonlinear effects. Existing feedforward models for double-acting single-rod cylinders necessitate a close match between the flow-area ratio across the piston and the peripheral lengths of the corresponding metering valve ports cut along its sleeve. The variation of pump pressure resulting in energy savings has not yet been addressed within the existing feedforward frameworks, and in the case of single-rod cylinders, the effect of oil compressibility has also been disregarded. In addition, either of flow leakage in valves or cylinder friction were neglected from the model. A novel order-separated feedforward, or **OSFF** model has been proposed in the present work to incorporate all of these issues under a generally acceptable assumption for the piston-induced flow to predominate over compressibility-induced flows or leakage flows. In addition, a conventional feedforward, or **CFF**, model has been developed for which the matching constraint of the flow-area ratio with port lengths cannot be relaxed. The parameters of both feedforward models have been estimated using offline **GA**-based minimization of the difference between an experimental result and its corresponding simulations. By coupling a PI feedback in real-time to construct **OSFFPI** and **CFFPI** controllers, the effects of assumptions and approximations of the feedforward*

parts have been compensated. The PI gains have been determined using a proposed extension of Routh stability criteria for the linearized time-variant error dynamics.

While the comparison with the **CFFPI** scheme established the **OSFFPI** controller's acceptability, its higher performance over existing **PI** controller and other nonlinear controllers, like **ARHNSMC-AB**, **ASMIC** is also noteworthy. The response of the **OSFFPI** controller has demonstrated superior tracking up to 4Hz sinusoidal-frequency demand compared to all these controllers, and reduced control effort compared to **CFFPI** and **ASMIC**. The designed controller's energy-saving potential has also been estimated in contrast to previously designed nonlinear controllers applied with fixed pump pressure. Except for very low-velocity motion requirement, the experiments under the two proposed methods demonstrated higher energy efficiency of the **OSFFPI** controller when compared to the fixed-displacement pump mode.

The first section of the present work is devoted to the design and performance analysis of a feedforward control algorithm, as well as its validation by means of rigorous experimental analysis on a double-acting, single-rod cylinder coupled with a proportional valve. Motivated by the successful implementation of the newly designed controller on a single degree-of-freedom (**DOF**) actuation system, additional work has been done to implement the same control algorithm in its suitable form for serial and serial-parallel type manipulator systems, considered here to be the second part of this work. The coupling of nonlinear actuation dynamics and multiple actuations and inherent hydraulic nonlinearities makes it difficult for electrohydraulic manipulators to achieve effective tracking control at frequencies above 0.1Hz. In this regard, the newly designed novel order-separated feedforward model has been implemented in an electrohydraulic manipulator system having four legs fitted with servo-proportional valve cylinder pair with a body to form a quadruped. Initially the designed controller has been implemented on a single leg structure acting as a serial manipulator followed by the four legs of the entire system acting as a serial-parallel manipulator. Studies on different motion demands have been conducted in serial manipulation mode with two valves and in serial-parallel mode with twelve valves. Oil leakage and cylinder friction have been accounted for as lower-order effects for the tight radial clearance and near-zero overlap in the valves coupled with low-friction cylinders. A numerical exercise has validated the assumptions of negligible inertia and suspended weight beneath the pistons. During real-time tracking, a **PID** feedback has been provided by the **OSFFPID** controller. Real-time studies of reciprocating and circular

*motion demand in serial mode, heave tracking of the body in parallel mode, and a representative version of a static walk motion plan in serial-parallel mode have been conducted. More precise and smoother tracking has been achieved up to 1Hz in the serial mode mostly with lower expense of energy than a conventional **PID** controller. Results indicate **FF** guidance mitigates oscillations occasionally apparent in **PID** case due to either hunting among multiple solutions or gain sensitivity of the nonlinear system. For parallel actuation excellent heave tracking has been obtained up to **0.2Hz**. The controller has been shown to be capable of rejecting significant disturbances caused by tension in the connecting oil hoses. A potential application of the **FF** model for diagnosing valve or cylinder faults caused by their ageing has also been described. The real-time results, for all the case study make it abundantly evident that the straightforward yet efficient feedforward architecture delivers better performance than a traditional and straightforward **PID** controller and other nonlinear controllers.*

# Contents

<i>Abstract</i> .....	i
<b>Contents</b> .....	<b>iv</b>
List of Figures .....	viii
List of Tables .....	xiv
List of Abbreviations .....	xvi
List of Symbols .....	xvii
1 Introduction.....	1
1.1 Overview of Electrohydraulic Systems .....	1
1.1.1 Electrohydraulic Actuation Systems (EHAS) .....	2
1.1.2 Applications of EHAS for Robotic Manipulators .....	11
1.2 EHAS Control.....	14
1.2.1 Modelling Challenges for Electrohydraulic Systems .....	15
1.2.2 Control of EHAS (Feedforward-Feedback Control Strategies) .....	23
1.3 Classification of Robotic Manipulators .....	26
1.3.1 Applications of Serial, Parallel and Combined Serial-parallel Manipulators ...	29
1.3.2 Modelling Challenges for Different Manipulator Systems .....	34
1.3.3 Mode of Actuators for Different Manipulator Systems.....	36
1.3.4 Motivations for Using Electrohydraulic Systems in Actuators of Manipulators .....	38
1.3.5 Literature Survey on Control Strategies for Electrohydraulic Manipulators ....	39
1.4 Motivation of the Present Work.....	41
1.5 Objectives of the Present Work .....	43
1.6 Contributions of the Present Work .....	44
1.7 Organization of the Thesis .....	46
2 System Description and Modeling.....	49
2.1 Introduction.....	49
2.2 System Description of Single Cylinder Test Bench .....	51
2.2.1 Hydraulic Power Pack .....	51
2.2.2 Actuation System.....	53
2.2.3 Data Acquisition and Control System .....	56
2.3 Serial Manipulator Test Bench .....	56
2.3.1 Hydraulic Power Pack .....	59

2.3.2 Actuation Systems .....	59
2.3.3 Data Acquisition and Control System .....	60
2.4 Serial-Parallel Manipulator Test Bench .....	61
2.5 Actuation System Modeling for Single Cylinder Test Bench .....	63
2.5.1 Piston motion dynamics.....	64
2.5.2 Cylinder Friction.....	64
2.5.3 Valve Leakage .....	65
2.5.4 Metered Valve Flows and Pressure Dynamics in Cylinder Chambers.....	67
2.5.5 Pump Characteristics and its Flow Coupling with Valve and Cylinder .....	69
2.6 Actuation System Modeling for Manipulators .....	71
2.6.1 Dynamic Modeling of Actuators .....	73
2.6.2 Pressure and Flow Modeling .....	73
2.6.3. Kinematic Modeling for Serial Manipulator .....	74
2.7 Kinematic Modeling for Serial-Parallel Manipulator .....	76
2.7.1. Design of Foottip and Body Motion for Serial-Parallel Manipulator .....	76
2.7.2 Proposed Motion Plan Sequence for Serial-Parallel Manipulator.....	84
2.7.3 Kinematic Model .....	86
2.8 Summary .....	87
3 Controller Design and Real Time Analysis for Single Cylinder System.....	90
3.1 Introduction.....	90
3.2 Basic Controller Structure.....	93
3.3 Conventional Feedforward Controller Design.....	96
3.4 Order-Separated Feedforward Controller Design .....	98
3.4.1 Estimation of Motion-Inducing Voltage and Chamber Pressures in the Cylinder .....	100
3.4.2 Estimation of Leakage-Compensating Voltage.....	101
3.4.3 Estimation of Compressibility-Compensating Voltage.....	101
3.5 Parameter Identification Procedure.....	102
3.6 Estimation of Feedforward Parameters.....	104
3.7 Proposed Methodology for Controller Stability Assessment.....	107
3.8 Controller Stability for CFFPI and OSFFPI Controllers .....	111
3.9 Results and Discussions.....	114
3.10 Summary.....	125
4 Controller Design and Real-time Analysis for Serial Manipulator .....	129

4.1 Introduction.....	129
4.2 Inverse Kinematic and Dynamic Modeling .....	130
4.3 Design of Order-Separated Feedforward Controller.....	133
4.4 Forward Kinematic Modeling.....	139
4.5 Numerical Study and Stability Analysis of the Controller .....	140
4.6 Identification of Feedforward Parameters & Condition Monitoring .....	143
4.7 Experimental Results and Discussion .....	144
4.7.1 Experimental Scheme and Performance Estimation Procedure .....	144
4.7.2 Comparison of Performance Indices for OSFFPID and PID Controllers .....	146
4.7.3 Time Domain Performance Comparison between OSFFPID and PID Controllers .....	148
4.7.4 Composition of OSFFPID Excitation Voltages.....	151
4.7.5 Free-point Trajectory and Error Components for Vertical Reciprocation and Circular Motion Demand.....	154
4.7.6 Instability Mitigation Role of the Proposed FFPID Controller .....	157
4.8 Outlining the use of Feedforward Model for Manipulator Design .....	159
4.9 Summary .....	167
5 Controller Design and Real-time Analysis for Serial-Parallel Manipulator.....	170
5.1 Introduction.....	170
5.2 Motion Plan Design for Serial-Parallel Manipulator .....	172
5.3 Feedforward Controller Formulation for Serial-Parallel Manipulator.....	177
5.4 Experimental Results and Discussion .....	179
5.4.1 Comparison of FFPID and PID Controllers for Serial-Parallel Actuation .....	179
5.4.2 Comparison of FFPID and PID Controllers for Parallel Actuation.....	185
5.5 Summary .....	188
6 Conclusions and Future Scope.....	191
6.1 Conclusions of the Present Work.....	191
6.2 Scope for Future Works .....	194
<b>References.....</b>	<b>200</b>
<b>Appendix.....</b>	<b>220</b>





# List of Figures

<b>Figure No.</b>	<b>Description</b>	<b>Page No.</b>
1.1	Circuit Diagram of <b>axial piston pump</b> with <b>pressure-compensation</b> arrangement	04
1.2	Schematic representation of solenoid driven <b>proportional valve</b>	06
1.3	Schematic diagram of different cylinders used in <b>EHAS</b> , (i) single acting with spring return (ii) double acting asymmetrical, (iii) double acting symmetrical	07
1.4	Single channel data acquisition system ( <b>DAQ</b> )	10
1.5	Working of valve amplifier circuit	11
1.6	Input and output representation of saturation nonlinearity in <b>EHAS</b>	17
1.7	Input and output representation of deadband nonlinearity in <b>EHAS</b>	18
1.8	Relation between friction and displacement in dynamic friction	19
1.9	Formation of frictional hysteresis loop	20
1.10	Representation of backlash nonlinearity	21
1.11	Schematic of Serial manipulator ( <b>SCARA Series</b> ) performing drilling operations	30
1.12	Laboratory-scale electrohydraulic parallel manipulator in the Form of a 6-DOF <b>Stewart platform</b>	32
1.13	Laboratory-scale electrohydraulic serial-parallel manipulator in the form of a <b>Quadruped</b>	33
2.1	An experimental setup for electrohydraulically actuated linear-motion study in (a) photographic view and (b) circuit diagram	52
2.2	<b>EHAS</b> with a double-acting single-rod cylinder and electrohydraulic valve	55
2.3	Schematic of experimental setup of a serial manipulator	57
2.4	Schematic of (a) valve details and (b) its role in electrohydraulic circuit for serial manipulator	58

<b>Figure No.</b>	<b>Description</b>	<b>Page No.</b>
2.5	Schematic of experimental setup of serial-parallel manipulator with component list	62
2.6	Cylinder friction (a) with Stribeck variation and (b) in simplified form	65
2.7	Bell-shaped leakage between spool land and bush	66
2.8	Characteristics of a variable-displacement swash-plate axial-piston pump	69
2.9	Kinematic relations of the <b>2-DOF</b> serial manipulator	75
2.10	Schematic of initial leg configuration of <b>6 DOF</b> serial-parallel manipulator	78
2.11	Effect of variation of $a_f$ on foot tip (a) displacement and (b) velocity along $x_f$ direction	80
2.12	(a) Displacement and (b) velocity of foot tip along $z_f$ direction	81
2.13	Foot tip trajectories in $(x_f - z_f)$ plane	83
2.14	(a) Displacement and (b) velocity of <b>COM</b> along positive $X$ direction	84
2.15	Sequence of proposed static walk ( <b>SW</b> ) motion plan for serial-parallel manipulator	85
2.16	Line diagram of initial and displaced leg configuration for serial-parallel manipulator	87
3.1	Schematic illustration of the <b>FFPI</b> control structure.	95
3.2	Schematic illustration of conventional <b>FFPI</b> control structure.	97
3.3	Schematic illustration of order separated <b>FFPI</b> control structure.	99
3.4	Block diagram for <b>RCGA</b> based parameter Identification	103
3.5	Parameter estimation for the proposed feedforward models	106
3.6	Predicted variations of responses with time for different gains and fixed parameter values	106
3.7	Variation of coefficients of characteristic equations over sinusoidal demand cycles of different frequencies for <b>CFFPI</b> in (a) to (d) and <b>OSFFPI</b> in (e) to (h)	113
3.8	Effect of proportional gain variation on $r_{31}$ under (a) <b>CFFPI</b> and (b) <b>OSFFPI</b> controllers	113
3.9	Variation of $r_{41}$ over a cycle for 100V/(m-s) I gain and P gains of (a) 180V/m and (b) 7000V/m under <b>CFFPI</b> controller and (c) 180V/m and (d) 5000V/m under <b>OSFFPI</b> controller	114

<b>Figure No.</b>	<b>Description</b>	<b>Page No.</b>
3.10	Comparison of frequency responses of <b>CFFPI</b> , <b>OSFFPI</b> with existing <b>ASMIC</b> and <b>ARHNNSMC-AB</b> controllers	118
3.11	Comparison of <b>PI</b> , <b>CFFPI</b> , <b>OSFFPI</b> , <b>ASMIC</b> and <b>ARHNNSMC-AB</b> controllers for time variation of excitation voltage for a sinusoidal demand at frequency of (a) 0.1Hz, (b) 0.5Hz, (c) 1Hz, (d) 2Hz and (e) 3Hz	120
3.12	Comparison for <b>PI</b> , <b>CFFPI</b> , <b>OSFFPI</b> , <b>ASMIC</b> and <b>ARHNNSMC-AB</b> controllers at 0.1Hz frequency of a sinusoidal demand for the (a) response and (b) error	121
3.13	Comparison for <b>PI</b> , <b>CFFPI</b> , <b>OSFFPI</b> , <b>ASMIC</b> and <b>ARHNNSMC-AB</b> controllers at 0.5Hz frequency of a sinusoidal demand for the (a) response and (b) error	121
3.14	Comparison for <b>PI</b> , <b>CFFPI</b> , <b>OSFFPI</b> , <b>ASMIC</b> and <b>ARHNNSMC-AB</b> controllers at 1Hz frequency of a sinusoidal demand for the (a) response and (b) error	121
3.15	Comparison for <b>PI</b> , <b>CFFPI</b> , <b>OSFFPI</b> , <b>ASMIC</b> and <b>ARHNNSMC-AB</b> controllers at 2Hz frequency of a sinusoidal demand for the (a) response and (b) error	122
3.16	Comparison for <b>PI</b> , <b>CFFPI</b> , <b>OSFFPI</b> , <b>ASMIC</b> and <b>ARHNNSMC-AB</b> controllers at 3Hz frequency of a sinusoidal demand for the (a) response and (b) error	122
3.17	Comparison of <b>CFFPI</b> and <b>OSFFPI</b> controllers on variable-displacement pump for (a) pressure and discharge variations over a cycle and (b) power saving over fixed displacement working.	124
4.1	(a) Kinematic diagram (b) Schematic line diagram of a single leg structure	131
4.2	Comparison of feedforward estimates of individual forces and computed net piston thrusts incorporating neglected effects in feedforward estimation	141
4.3	Maximum <b>IAE</b> in a generations and predicted variations of response with time during friction parameter estimation	143
4.4	Block diagram representation of experimental scheme for Serial manipulator	145
4.5	Variations of free-point position error under <b>OSFFPID</b> and <b>PID</b> controllers at frequencies of 0.1, 0.2, 0.5 and 1.0Hz reciprocation demand.	148
4.6	Variations of free-point position error under <b>OSFFPID</b> and <b>PID</b> controllers at frequencies of 0.1, 0.2, 0.5 and 1.0Hz circular-motion demand.	148
4.7	Variations of actuation errors in lower and upper pistons under <b>OSFFPID</b> and <b>PID</b> controllers at frequencies of 0.1, 0.2, 0.5 and 1.0Hz reciprocation demand	149

<b>Figure No.</b>	<b>Description</b>	<b>Page No.</b>
4.8	Variations of actuation errors in lower and upper pistons under <b>OSFFPID</b> and <b>PID</b> controllers at frequencies of 0.1, 0.2, 0.5 and 1.0Hz circular-motion demand.	149
4.9	Variations of excitation voltage in lower and upper valves under <b>OSFFPID</b> and <b>PID</b> controllers at frequencies of 0.1, 0.2, 0.5 and 1.0Hz reciprocation demand.	150
4.10	Variations of excitation voltage in lower and upper valves under <b>OSFFPID</b> and <b>PID</b> controllers at frequencies of 0.1, 0.2, 0.5 and 1.0Hz circular-motion demand.	150
4.11	<b>OSFFPID</b> voltage contributions for reciprocation demand at frequencies of 0.1, 0.2, 0.5 and 1.0Hz at (a) lower valve and (b) upper valve.	152
4.12	<b>OSFFPID</b> voltage contributions for circular motion demand at frequencies of 0.1, 0.2, 0.5 and 1.0Hz at (a) lower valve and (b) upper valve.	154
4.13	Tracking of free-point vertical reciprocating motion demand at frequencies of 0.1, 0.2, 0.5 and 1.0Hz under <b>OSFFPID</b> and <b>PID</b> controllers	155
4.14	Variations of vertical and horizontal error components for free-point vertical reciprocation under <b>OSFFPID</b> and <b>PID</b> controllers at frequencies of 0.1, 0.2, 0.5 and 1.0Hz.	155
4.15	Tracking of free-point circular motion demand at frequencies of 0.1, 0.2, 0.5 and 1.0Hz under <b>OSFFPID</b> and <b>PID</b> controllers.	157
4.16	Variations of radius error of free-point for circular-motion demand under <b>OSFFPID</b> and <b>PID</b> controllers at frequencies of 0.1, 0.2, 0.5 and 1.0Hz.	157
4.17	Error and voltage variations at 0.2Hz for <b>OSFFPID</b> and <b>PID</b> controllers for different proportional gains in the upper valve.	158
4.18	Effect of variation of $\overline{hk}$ on actuator stroke and velocities	161
4.19	Effect of variation of $\overline{hk}$ on actuation forces.	161
4.20	Effect of variation of $\overline{hk}$ on actuation discharge and actuation power	162
4.21	Effect of variation of $\overline{kf}$ on actuator stroke	162
4.22	Effect of variation of $\overline{kf}$ on actuation forces	163
4.23	Effect of variation of $\overline{kf}$ on actuation discharge and actuation power	163
4.24	Effect of variation of $\overline{kl}_r$ on actuator stroke and velocities	164
4.25	Effect of variation of $\overline{kl}_r$ on actuation forces	164
4.26	Effect of variation of $\overline{kl}_r$ on actuation discharge and actuation power	165
4.27	Effect of variation of $\overline{hu}_r$ on actuator stroke and velocities	165

<b>Figure No.</b>	<b>Description</b>	<b>Page No.</b>
4.28	Effect of variation of $\overline{hu_r}$ on actuation forces	166
4.29	Effect of variation of $\overline{hu_r}$ on actuation discharge and actuation power	166
5.1	Representative version of Static walk motion plan for the realization of combined Serial-Parallel actuation	174
5.2	Ramp demand during initialization phase before execution of forward motion under <b>OSFFPID</b> and <b>PID</b> controllers	181
5.3	Real time actuator response during initialization phase for the formation of parallelogram orientation of four foot-tips	182
5.4	Tracking of <b>COM</b> and foot-tip along ( <b>XZ</b> ) plane during execution of forward motion under <b>OSFFPID</b> and <b>PID</b> controllers.	183
5.5	<b>COM</b> and foottip error along ( <b>XZ</b> ) plane under <b>OSFFPID</b> and <b>PID</b> controllers.	184
5.6	Variations of actuation errors in lower and upper pistons of each leg under <b>OSFFPID</b> and <b>PID</b> controllers	184
5.7	Variations of voltage contribution in lower and upper pistons of each leg under <b>OSFFPID</b> and <b>PID</b> controllers during execution of model static walk	185
5.8	<b>COM</b> motion and error along ( <b>XZ</b> ) plane under <b>OSFFPID</b> and <b>PID</b> controllers at frequencies of 0.1 and 0.2Hz reciprocation demand.	186
5.9	Variations of actuation errors in lower and upper pistons of each leg under <b>OSFFPID</b> and <b>PID</b> controllers at frequencies of 0.1, 0.2Hz reciprocation demand.	187
5.10	Variations of voltage contribution in lower and upper pistons of each leg under <b>OSFFPID</b> and <b>PID</b> controllers at frequencies of 0.1, 0.2Hz reciprocation demand.	188



# List of Tables

<b>Table No.</b>	<b>Description</b>	<b>Page No.</b>
2.1	Component specifications of Single-Cylinder Test Bench	53
2.2	Lengths in mm, weights in N and angles in ° for Manipulator Components	57
2.3	Component specifications of Manipulators Power Pack	58
3.1	Specified System Parameters $\mathbf{p}_s$	104
3.2	Bounds and converged system parameters for <b>CFF</b> model	105
3.3	Bounds and converged system parameters for <b>OSFF</b> model	106
3.4	Variation of performance indices with frequency for different controllers	117
4.1	Comparison of performance indices for Serial Manipulator	147





# List of Abbreviations

---

<b>Abbreviations</b>	<b>Description</b>
<b>ASMIC</b>	: <b>A</b> daptive <b>S</b> liding <b>M</b> ode <b>I</b> ntegral <b>C</b> ontroller
<b>ARHNSMC-AB</b>	: <b>A</b> daptive <b>R</b> ecurrent <b>N</b> euro <b>S</b> liding- <b>M</b> ode <b>C</b> ontroller with <b>A</b> daptive <b>B</b> ias
<b>DASRC</b>	: <b>D</b> ouble <b>A</b> cting <b>S</b> ingle <b>R</b> od <b>C</b> ylinder
<b>CE</b>	: <b>C</b> ontrol <b>E</b> ffort
<b>CFE</b>	: <b>C</b> onventional <b>F</b> eedforward
<b>COM</b>	: <b>C</b> entre- <b>o</b> f- <b>M</b> ass
<b>CV</b>	: <b>C</b> heck <b>V</b> alve
<b>EHAS</b>	: <b>E</b> lectro <b>h</b> draulic <b>A</b> ctuation <b>S</b> ystem
<b>EP</b>	: <b>E</b> nd <b>P</b> late
<b>FF</b>	: <b>F</b> eedforward
<b>FM</b>	: <b>F</b> low <b>m</b> eter
<b>IAE</b>	: <b>I</b> ntegral <b>A</b> bsolute <b>E</b> rror
<b>IADE</b>	: <b>I</b> ntegral <b>A</b> bsolute <b>D</b> erivative <b>E</b> rror
<b>IADCE</b>	: <b>I</b> ntegral <b>A</b> bsolute <b>D</b> erivative <b>C</b> ontrol <b>E</b> ffort
<b>ICE</b>	: <b>I</b> ntegrated <b>C</b> ontrol <b>E</b> lectronics
<b>IM</b>	: <b>I</b> nterface <b>M</b> odule
<b>ISCE</b>	: <b>I</b> ntegral <b>S</b> quare <b>C</b> ontrol <b>E</b> ffort
<b>LVDT</b>	: <b>L</b> inear <b>V</b> ariable <b>D</b> ifferential <b>T</b> ransformer
<b>OM</b>	: <b>O</b> utput <b>M</b> odule
<b>PID</b>	: <b>P</b> roportional <b>I</b> ntegral <b>D</b> erivative
<b>PT</b>	: <b>P</b> ressure <b>T</b> ransducer
<b>PV</b>	: <b>P</b> roportional <b>V</b> alve
<b>RCGA</b>	: <b>R</b> eal <b>C</b> oded <b>G</b> enetic <b>A</b> lgorithm
<b>RMSE</b>	: <b>R</b> oot- <b>M</b> ean <b>S</b> quare <b>E</b> rror
<b>RTS</b>	: <b>R</b> eal- <b>T</b> ime <b>S</b> ystem
<b>RV</b>	: ( <b>P</b> ressure) <b>R</b> elief <b>V</b> alve
<b>SD</b>	: <b>S</b> tandard <b>D</b> eviation
<b>SP</b>	: <b>S</b> upport <b>P</b> late
<b>SPV</b>	: <b>S</b> ervo <b>P</b> roportional <b>V</b> alve
<b>TV</b>	: <b>T</b> otal <b>V</b> ariation

---

# List of Symbols

## *English Alphabets*

Symbol	Description	Unit
$a$	Amplitude	mm
$a_i$	Linearized error dynamics coefficients	$s^{-4}, s^{-3}, s^{-2}, s^{-1}$ for $i = -1, 0, 1$ and 2
$a_f$	Scaling factor	-
$A_c$	Flow area in cap end chamber	$m^2$
$A_r$	Flow area in rod end chamber	$m^2$
$c_{lA}$	Leakage coefficient of flow in port <b>A</b>	$m^{3.5}kg^{-1/2}$
$c_{lB}$	Leakage coefficient of flow in port <b>B</b>	$m^{3.5}kg^{-1/2}$
$c_{lc}$	Cylinder leakage constant	$m^{3.5}kg^{-1/2}$
$c_{vA}$	Valve coefficient of flow in port <b>A</b>	$m^{3.5}V^{-1}kg^{-1/2}$
$c_{vB}$	Valve coefficient of flow in port <b>B</b>	$m^{3.5}V^{-1}kg^{-1/2}$
$d_c$	Cap end diameter of piston	m
$d_r$	Rod end diameter of piston	m
$e_f$	Error with respect to free-point demand	m
$e_i$	Error with respect to actuation demand	m
$e_{f\rho}$	Error in radius demand of foot tip motion	m
$\dot{e}$	Velocity error	m/s
$\ddot{e}$	Acceleration error	$m/s^2$
$\ddot{\ddot{e}}$	Time derivative of acceleration error	$m/s^3$
$f$	Frequency	Hz
$F_c$	Coulomb friction	N
$F_{cld}$	Lower cylinder end force	N
$F_f$	Friction force	N
$F_{rld}$	Rod end force on lower piston	N
$F_{rud}$	Rod end force on upper piston	N
$F_s$	Static friction	N
$F_{sp}$	Spring load	N
$g$	Acceleration due to gravity	$m/s^2$
$I_\delta$	Integral absolute error for RCGA	m-s

<b>Symbol</b>	<b>Description</b>	<b>Unit</b>
$k$	Stiffness of the spring	N/m
$k_D$	Derivative gain	V-s/m
$k_P$	Proportional gain	V/m
$k_{p0}$	Reference proportional gain	V/m
$k_I$	Integral gain	V/(m-s)
$\overline{l_c l_r}$	End-to-end length of lower piston-cylinder arrangement of serial manipulator	m
$\overline{l_c l_r} _c$	Closed length of lower actuating piston of serial manipulator	m
$\overline{l_c l_r} _d$	Demanded end-to-end length of lower piston-cylinder arrangement of serial manipulator	m
$L_f$	Reciprocating demand of free point of serial manipulator in vertical plane	m
$m$	Moving mass of piston assembly	kg
$n$	Number of cycles	-
$p_c$	Cap end pressure perturbation	Pa
$P_c$	Cap end chamber pressure	Pa
$P_{cf}$	Cap end chamber pressure estimate in feedforward model	Pa
$P_{cf0}$	Initial value of cap end chamber pressure estimate in feedforward model	Pa
$\dot{P}_c$	Cap end pressure derivative	Pa/s
$\dot{P}_{cf}$	Cap end pressure derivative in feedforward model	Pa/s
$P_{ci}$	Pump cut-in pressure	Pa
$p_p$	Pump pressure perturbation	Pa
$P_p$	Pump pressure	Pa
$P_{pf}$	Pump pressure estimate in feedforward model	Pa
$p_r$	Rod end pressure perturbation	Pa
$P_r$	Rod end chamber pressure	Pa
$P_{rf}$	Rod end chamber pressure estimate in feedforward model	Pa
$P_{rf0}$	Initial value of rod end chamber pressure estimate in feedforward model	Pa
$\dot{P}_r$	Rod end pressure derivative	Pa /s
$\dot{P}_{rf}$	Rod end pressure derivative estimate in feedforward model	Pa/s
$P_{RV}$	Relief valve pressure	Pa
$\overline{P}_S$	Average power saved	Watt
$P_T$	Tank Pressure	Pa

<b>Symbol</b>	<b>Description</b>	<b>Unit</b>
$Q_{a\dot{y}_d}$	Motion induced discharge in the feedforward model	$\text{m}^3/\text{s}$
$Q_{a\beta}$	Compressibility related discharge in the feedforward model	$\text{m}^3/\text{s}$
$Q_A$	Discharge through port <b>A</b> of <b>PV</b>	$\text{m}^3/\text{s}$
$Q_{Af}$	Discharge through port <b>A</b> of <b>PV</b> estimate in feedforward model	$\text{m}^3/\text{s}$
$Q_B$	Discharge through port <b>B</b> of <b>PV</b>	$\text{m}^3/\text{s}$
$Q_{Bf}$	Discharge through port <b>B</b> of <b>PV</b> estimate in feedforward model	$\text{m}^3/\text{s}$
$Q_l$	Total leakage	$\text{m}^3/\text{s}$
$Q_{ld}$	Total leakage in feedforward model	$\text{m}^3/\text{s}$
$Q_A^l / Q_{lA}$	Leakage through port <b>A</b> of <b>PV</b>	$\text{m}^3/\text{s}$
$Q_{Ad}^l$	Leakage through port <b>A</b> of <b>PV</b> in feedforward model Leakage through port <b>A</b> of <b>PV</b> in feedforward model	$\text{m}^3/\text{s}$
$Q_B^l / Q_{lB}$	Leakage through port <b>B</b> of <b>PV</b>	$\text{m}^3/\text{s}$
$Q_{Bd}^l$	Leakage through port <b>B</b> of <b>PV</b> in feedforward model	$\text{m}^3/\text{s}$
$Q_{l0}$	Maximum leakage for bell-shaped leakage model	$\text{m}^3/\text{s}$
$Q_{l1}$	Minimum leakage for bell-shaped leakage model	$\text{m}^3/\text{s}$
$Q_c$	Characteristic discharge of pump model	$\text{m}^3/\text{s}$
$q_p$	Pump discharge perturbation	$\text{m}^3/\text{s}$
$Q_p$	Pump discharge	$\text{m}^3/\text{s}$
$Q_{p0}$	Total pump discharge during fixed displacement mode	$\text{m}^3/\text{s}$
$Q_s$	Total actuation discharge	$\text{m}^3/\text{s}$
$r_{k1}$	Leading coefficients of third and fourth rows of Routh array for $k = 3$ and 4 respectively	$\text{s}^{-2}, \text{s}^{-3}$ for $k = 3$ and 4
$s_f$	Horizontal stride of foot-tip	m
$s_v$	Vertical stride of foot-tip	m
$t$	Time	s
$T$	Total time period	s
$T_c$	Time interval during uniform motion of foot-tip in swing phase	s
$T_s$	Time interval during sinusoidal motion of foot-tip in swing phase	s
$\overline{u_c u_r}$	End-to-end lengths of upper piston-cylinder arrangement of serial manipulator	m
$\overline{u_c u_r} _c$	Closed length of upper actuating piston of serial manipulator	m
$\overline{u_c u_r} _d$	Demanded end-to-end length of upper piston-cylinder arrangement	m
$v_s$	Stribeck velocity	m/s
$V$	Total voltage	V

<b>Symbol</b>	<b>Description</b>	<b>Unit</b>
$V_{0c}$	Cap end initial oil volume	$m^3$
$V_{0r}$	Rod end initial oil volume	$m^3$
$V_f$	Feedforward voltage	V
$V_{f0}$	Motion induced feedforward voltage	V
$v$	Velocity of piston	m/s
$v_b$	Feedback voltage	V
$v_f$	Friction compensating feedforward voltage	V
$v_{fl}$	Leakage compensating feedforward voltage	V
$v_{f\beta}$	Compressibility compensating feedforward voltage	V
$W_c$	Weight of the lower cylinder of manipulator system	N
$W_l$	Weight of the lower member of manipulator system	N
$W_p$	Weight of the lower piston for manipulator system	N
$W_u$	Weight of the upper member of manipulator system	N
$x_{c'}(t)$	Horizontal displacement of vertical projection of COM	m
$x_f$	Coordinate of free point of serial manipulator along horizontal direction	m
$x_{fj}(t)$	Displacement of swinging free point/foot-tip of manipulator in the horizontal direction	m
$y$	Displacement of piston	m
$y_{di}$	Demanded displacement of piston for the $i^{\text{th}}$ actuations system of the manipulator for $i = l, u, t$	m
$\dot{y}$	Velocity of piston	m/s
$\dot{y}_d$	Demanded velocity of piston	m/s
$\ddot{y}$	Acceleration of piston	$m/s^2$
$\ddot{y}_d$	Demanded acceleration of piston	$m/s^2$
$\dddot{y}$	Third order derivative of piston displacement	$m/s^3$
$\dddot{y}_d$	Derivative of Demanded acceleration of piston	$m/s^3$
$z_f$	Coordinate of free point of serial manipulator in vertical direction	m
$z_{fj}(t)$	Displacement of $j^{\text{th}}$ foot-tip of manipulator in the vertical direction for $j = 1$ to 4	m

## *Greek Alphabets*

<b>Symbol</b>	<b>Description</b>	<b>Unit</b>
$\alpha_d$	Angle between lower limb of manipulator with vertical axis	degree
$\alpha_l$	Scaling factor used in bell-shaped leakage model	-
$\alpha_v$	Coefficient of viscous friction	N-s/m
$\beta$	Bulk modulus of hydraulic fluid	Pa
$\beta_d$	Angle made between the middle limb of manipulator with vertical axis	degree
$\gamma_{ld}$	Angle between lower limb and lower piston-cylinder axis	degree
$\gamma_{ud}$	Angle between portion of middle limb $\overline{hu_r}$ and upper piston-cylinder axis	degree
$\varepsilon_d$	Angle made by the middle limb of manipulator with vertical axis	degree
$\varepsilon_l$	Limit of convergence	m-s
$\lambda$	Cylinder area ratio	-
$\Pi_s$	Expended actuation power for manipulator system	Watt
$\rho$	Radius of circular motion demand	m
$\Omega$	Ratio of product of valve coefficient and cylinder flow area	-





# CHAPTER 1

## Introduction

### 1.1 Overview of Electrohydraulic Systems

**D**espite the rapid spread of electric power generation, hydraulic fluid power is one of the earliest kinds of power transmission that still has wide application in industries. In large industrial processes, mechanical power is typically required to move an object from one location to another or to provide a force to hold, lift or compress an object. Electrical energy is utilized to produce mechanical power in the form of motion, i.e., rotation, translation, or force, through the use of electrical motors as prime movers. Yet, electrical devices in the form of prime movers are not the only way to generate this type of mechanical energy. Compressed liquids can also be utilized in a specifically constructed enclosed system to produce mechanical energy from fluid energy and transport the same by generating rotary or linear motion and/or greater forces. Hydraulic systems are enclosed fluid-based systems that utilize pressured liquids as transmission media. Electrohydraulic systems or, more specifically, electrohydraulic actuation systems (EHAS), combine the advantages of hydraulic systems with an electrical interface for the precise actuation of diverse systems in order to meet the functional needs of specific applications. In these systems, the input is an electrical signal, and the output is mechanical power through a mechanical actuator, which imparts the required motion and/or force to the application space in which it is employed. This method of power transmission for running a wide variety of equipment has gained widespread acceptance in present day industries because to its inherent benefits over other methods. The most notable benefits of EHAS include the use of smaller and lighter components, higher heat dissipation capacity, and a high power-to-weight ratio (Merritt 1967), multiple actuations with a single power source, and the elimination of backlash in contrast to electro-mechanical systems. The several advantages of EHAS are listed below:

- High power-to-weight ratio;
- Highly back-drivability;

- wide dynamic range of operation;
- Multiple actuations with a single power source;
- Stepless speed control can be obtained from a less complex system;
- fast speed of response of actuation system;
- No backlash error presents in a hydraulic system, unlike mechanical systems;
- Efficient power transmission is possible over a long distance;
- Easy dissipation of heat generated by the hydraulic fluid.
- The working hydraulic fluid acts as lubricant.

Electrohydraulic actuation systems have attracted a great deal of interest in a variety of industries, ranging from applications requiring ruggedness to those requiring high precision and sophistication. EHAS is used in the development of cutterhead driving systems for tunnel boring machines (Liu et al. 2019), in forests for tree planting machines (Chen et al. 2019), for agricultural harvesting (Daher & Ivantysynova, 2014), and the improvement of energy-efficient hydraulic presses (Huang et al. 2018). For more sophisticated applications, EHAS are utilized in high-precision robotics (Briot et al. 2015), aircraft (Kaya and Bilgin, 2019), and automobiles (Briot et al. 2015; Kaya and Bilgin, 2019; Plummer et al. 2007; Daher & Ivantysynova, 2014).

### 1.1.1 Electrohydraulic Actuation Systems (EHAS)

A typical EHAS consists of two well-defined sections, viz., the hydraulic section and the electrical/electronic section, with each of these sections further integrated with some additional elements or units. The different units of the hydraulic section involve a power supply, a control, and actuation, whereas the corresponding units in the electrical and electronic section involve data transmission, data acquisition, a control computer, and a signal amplifier. A brief description of each element has been given below.

**Hydraulic Section:** The different elements of hydraulic section for EHAS are described below.

1. **Power Supply Unit:** In EHAS, the hydraulic power can be supplied with the help of a pump, where the pump delivery pressure either remains fixed, being independent of the external load acting on the actuator or is variable and is a

function of the external loading. Mainly positive displacement type pumps like gear, vane, and piston pumps are normally installed in hydraulic systems. The choice of pump depends on the maximum pressure and flow requirements of the system during operations. In its most basic form, the power supply section employs a fixed displacement type pump **P** normally driven by a motor **M** serving as a prime mover. However, for mobile hydraulic systems, the electrical motor **M** is often replaced by an **internal combustion engine**. The pump sucks the hydraulic oil from a reservoir denoted by tank or **T** and supplies pressurized oil to the system. In order to supply dirt free oil to the system, an oil filter **F** is fitted before the suction of the pump. A pressure relief valve, or **RV**, is used at the outlet of the pump to limit the maximum pressure attained in the system ensuring its overall safety. To make the pump flow unidirectional at the outlet of the pump, a non-return valve, or **NRV**, can be used. For proper heat dissipation, occasionally an air- or water type cooling arrangement is installed in the form of a heat exchanger. The simplest form of power supply stated above does however increase the energy loss of the system, followed by the rise in working fluid temperature. To cater to this situation, an energy-efficient power supply can be designed by employing an additional attachment of an accumulator and an unloading valve (Walter 2012), along with the simple power supply circuit stated above. Sometimes a variable displacement pump with a pressure compensating arrangement can be installed in the system to get the energy-efficient hydraulic power supply. Conventionally, the **EHAS** uses an axial piston-type pump with a variable swashing angle (Mondal et al. 2019; Walter 2012) for this purpose.

Figure 1.1 shows a schematic circuit diagram of an axial piston pump with a pressure compensation arrangement. The corresponding hydraulic symbol is also clearly shown in the figure. The pump **P** is coupled with an internal combustion engine **M** and rotates in a clockwise direction. The oil is supplied from the tank **T** with a filter **F** in the suction line, as shown. The pump supplies flow to the system where the flow variation further depends on the system demand which affects the loading on the pump. The non-return valve **NRV** fitted at the outlet of the pump makes the flow unidirectional in the system. For the pump to be operated in fixed

displacement mode with a fixed swash angle, the pump delivery pressure should be kept below cut-in limit.

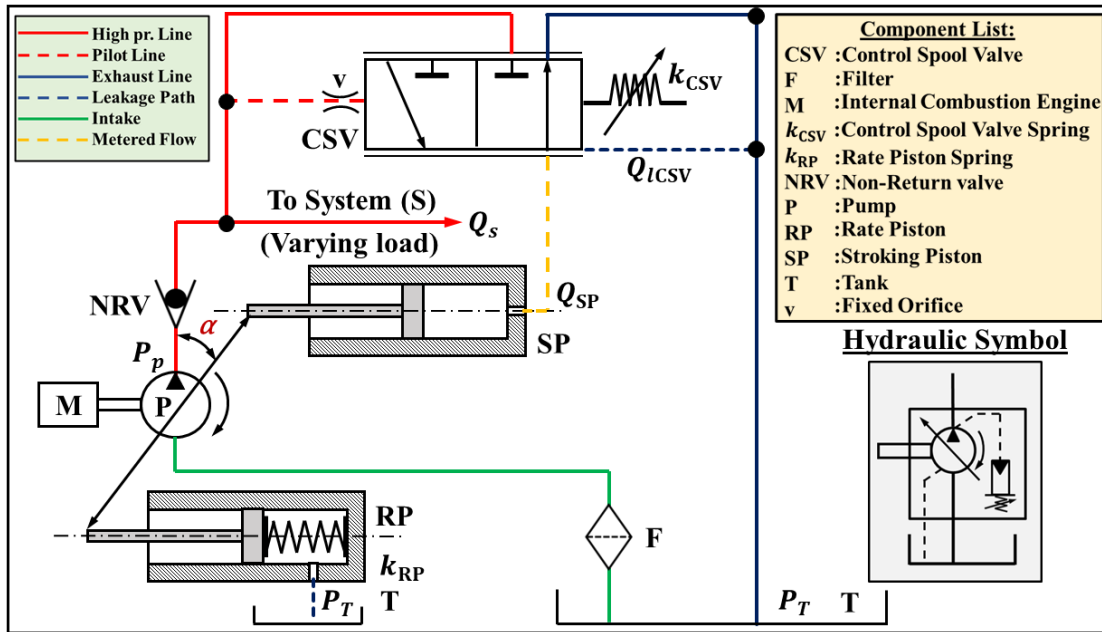


**Figure 1.1: Circuit diagram of axial piston pump with pressure compensation arrangement**

The pressure compensation arrangement of the pump consists of a **2-way, 2-position** control spool valve **CSV**, a stroking piston **SP**, and a rate piston **RP**. The control spool is fitted with a pre-compressed spring  $k_{CSV}$  the stiffness of whose pre-compression can be altered to set the cut-in value of the delivery pressure. There is another pre-compressed spring of stiffness  $k_{RP}$  inside the rate piston. The delivery pressure is communicated to the left end of the **CSV** through the radial clearance between the left land of the spool and the bush. This end-land radial clearance acts as an orifice, shown as  $v$  in the above figure. When the pump delivery pressure is below the cut-in value, the pre-compressed spring inside the **CSV** presses the spool in the extreme left position in such a way that no flow occurs through the metered port of the spool to the stroking cylinder chamber. Based on the system loading when the delivery pressure of the pump exceeds the cut-in limit, the spool moves against the spring and flow is initiated from the valve **CSV** to the stroking cylinder. Hence, pressure will build up inside the stroking cylinder chamber. This pressurized fluid causes the **SP** to move out of the stroking cylinder and rotate the cradle against the force exerted by the spring inside the **RP**. As a result, the swash angle  $\alpha$  will reduce lowering the flow to the system and the corresponding delivery pressure are

altered. There is also a flow from the control valve to the tank across the central land. When the spool is actuated, this flow as a leakage will flow across the radial clearance of the central land. The system shown in Figure 1.1 is thus considered to be an **energy-efficient** hydraulic power supply unit for the **EHAS**.

- 2. Control Unit:** In a simple hydraulic circuit, the position, motion direction, and velocity of the actuation system are typically controlled by a direction control valve **DCV** or a flow control valve **FCV**. This valve can be manually operated or controlled by an electrical signal. Conventionally, valves operate either as a standard on/off switch, i.e., fully open during switch on (current on) and fully closed for switch off (current off), or as a dimmer switch, allowing the valve to operate in any intermediate spool position between the fully open and closed conditions. This type of valve is known as a solenoid-driven proportional valve, or simply a **PV**, when the electrical current flowing through it is regulated rather than simply switched on or off. Figure 1.2 provides a clear depiction of the internal components of a **PV** and its corresponding hydraulic symbol for a better understanding of the working principle. The valve contains a spool with a spool rod **8** and spool lands **9** as a single unit within the valve body **7** to regulate the direction and speed of the connected actuation system by opening and closing the control ports or metering ports **A** and **B**, as depicted in Figure 1.2. The valve also contains two other ports, labelled **P** for pump port and **T** for tank port, for the unmetered supply and return of fluid through the valve. To achieve a continuous sliding of the spool, the **PV** is controlled by a pair of solenoids denoted by **S<sub>1</sub>** and **S<sub>2</sub>** whose activation is determined by the polarity of the input signal. Each solenoid consists of coil **2** and armature **4** assembly housed within the yoke **1** and core tube **3**. The tube **3** directs the axial motion of the armature, as depicted in the figure. Prior to each armature, two pole pieces **6** are installed. Typically, the input to a **PV** system is either current- or voltage. In the present case, the Figure 1.2 depicts a **PV** driven by current. By varying the solenoid current, the spool movement attached to the armature of either solenoid can be altered, allowing for the control of the valve's flow rate.

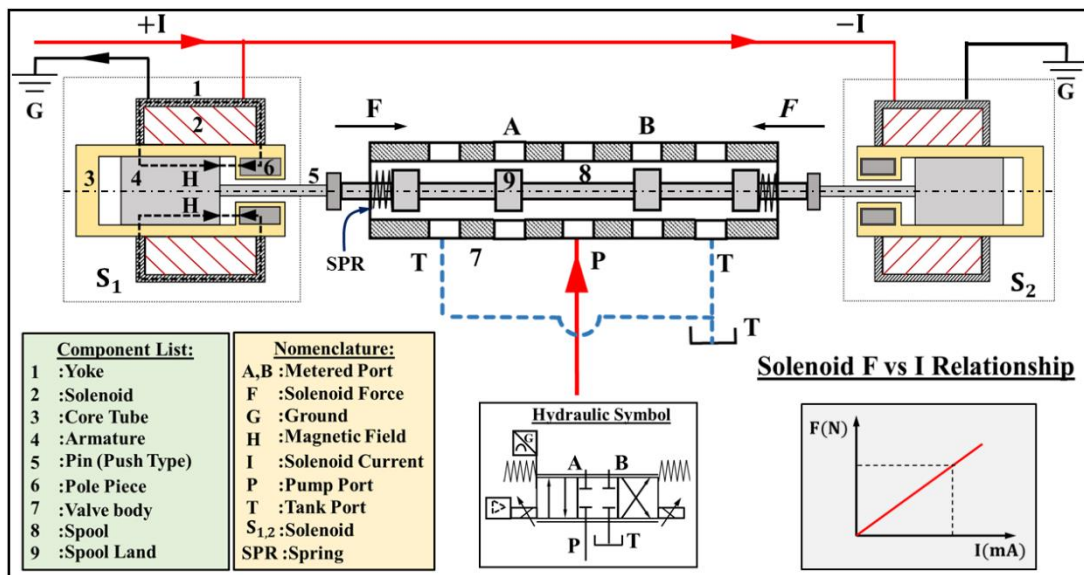


**Figure 1.2: Schematic representation of solenoid driven proportional valve**

The pole pieces **6** and armature **4** are both composed of ferromagnetic materials; when the coil is energized, a strong magnetic field **H** is established, which in turn generates an electromagnetic force between **6** and **4**, across an air gap between the two. As shown in Figure 1.2, this force is proportional to the magnetic field strength and maintains a linear relationship with the current. A push pin **5** is installed between the valve's armature **4** and spool rod **8**. When the coil current increases, so does the force, which is transmitted to the spool **8** via the push pin **5** in order to move the spool against the spring **SPR**. The movement of the spool in turn varies the opening of the metered ports **A** and **B** to adjust the flow to the actuator. **PV** as a single unit controls velocity, flow, pressure, and motion direction across the actuation system. This type of valve is typically employed for precision control.

As a control element, another type of valve known as a servo valve **SV** is sometimes used. The **SV** is extremely precise and quick to respond. Typically, it moves smoothly and has low hysteresis. However, this valve is quite expensive. Because servovalves **SV** and servo actuators have fine radial clearances, sophisticated servo systems require oil filtration of the highest quality. This prohibits their use in long-term, continuous, rugged services, for which **PV** and industrial-grade cylinders are better suited. However, sophisticated servo systems are typically designed for high-precision robotic and aircraft applications (Semini et al. 2015). (Kaya & Bilgin. 2019).

3. **Actuation Unit:** Actuators in EHAS are responsible for converting the hydraulic energy supplied by the pump through the control element into an equivalent amount of mechanical work. This is also known as the "driving unit." Actuators are broadly divided into two types based on their output: linear actuators, or hydraulic cylinders, and rotary actuators, or hydraulic motors. The rotary actuators generate rotary motion at high and low speeds with high and low output torque. They are divided into two categories based on the transfer of speed and torque: high-speed, low-torque, and vice versa. The most frequently employed hydraulic actuators are linear actuators, also known as piston-cylinder arrangements, which typically consist of a piston fitted with a rod as a single arrangement which can slide inside a hollow cylinder. Based on their ability to transmit power, linear actuators can be either single- or double-acting. The single-acting actuators have a single port and drive power in a single direction. The return of the piston can be caused by either external forces viz. dead weight or a spring installed on the opposite side. Both cylinder chambers of double-acting cylinders have a port each for the supply of pressurized fluid. It generates force in both directions. In addition to double-acting symmetrical and single-acting asymmetrical cylinders, linear actuators can also be constructed with double-acting asymmetrical cylinders.

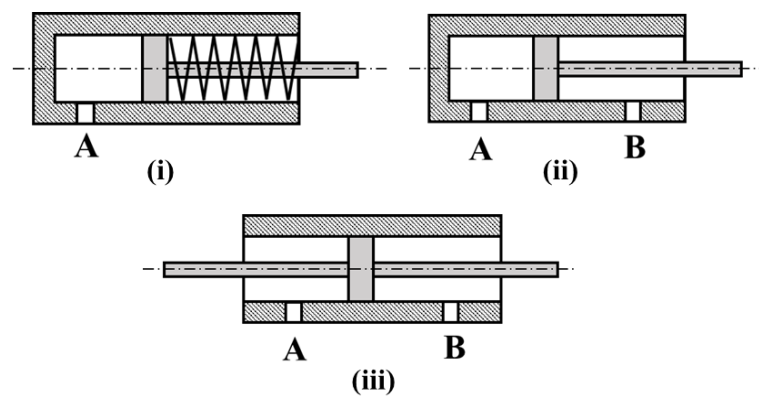


**Figure 1.3: Schematic diagram of Different cylinders used in EHAS, (i) single acting with spring return (ii) double acting asymmetrical, (iii) double acting symmetrical**

Double-rod or symmetrical cylinders are typically expensive and have a large overall size. They are primarily employed in high-performance servo systems (Walter, 2012). Figure 1.3 depicts the various piston-cylinder configurations typically utilized for EHAS. Whereas Figure 1.3 (i) depicts a single-acting asymmetrical cylinder with one port (A) and spring force return, Figures 1.3 (ii) and

1.3 (iii) respectively illustrate asymmetrical (single rod) and symmetrical (double rod) double-acting cylinders with two ports **A** and **B**

A single-rod cylinder requires a shorter length than a double-rod cylinder with the same work output to accommodate the extension or retraction of the piston rod from one end of the cylinder, while the other end remains capped. Resulting compactness makes single-rod systems considerably more prevalent (Mattila et al. 2017; Du et al. 2017; Quan et al. 2014). Comparatively, the cost of the single-rod system is much lower than that of the double-rod system. On the basis of frictional characteristics between the mating cylinder and piston arrangement, linear actuators can also be classified as servo-grade or industrial-grade actuators.

**4. Electrical/Electronic Section:** The different units of this section are elaborated briefly

*a. Sensors and Data Transmission Unit:* This unit consists of transducers or sensors with data transmission cables. Transducers sense the output signal of the actuation unit and convert the signal into an equivalent electrical signal in order to monitor the final output of the actuation unit for an open loop control system and to feedback the same signal for a closed loop control system in order to control the final output of the actuation unit. The output variables to be monitored or controlled for an EHAS are normally force, position, velocity, pressure, flow, etc. Generally, transducers sense the final output of the system in the form of force, velocity, position, etc. and convert the output into a low-powered electrical signal. Different transducers to measure the different output variables stated above are commercially available on the market. To measure the force exerted by the actuators, *load cells* are used, which normally measure the load in one direction. The actuator position at any instant can be measured either by a contact or non-contact method, by using position sensors. Whereas the *potentiometer* is used to measure the position of the actuator by the contact method, the *Linear Variable Differential Transformer (LVDT)* and *Rotary Variable Differential Transformer (RVDT)* are used to measure the linear and rotary position by non-contact method, respectively. Both the LVDT and RVDT are analog devices, however, encoders and proximity sensors are the digital position sensors. Velocity transducer or *Tachometers* are generally used to measure actuator speed, *Pressure Transducers* are used to measure pressure at



a single point or to measure the pressure difference from two different pressure tapings. Different flow meters of *Positive Displacement Type* or *Resistance Type* are used to measure the flows at any point of EHAS.

**b. Data Acquisition Unit:** The term "data acquisition (**DAQ**)" refers to the process of digitization of any real-time signal for the purpose of storage, analysis, and display in the computer. The system through which this process of acquisition can be done is known as the data acquisition system. It is thus a collection of both software and hardware. Already stated above, the transducers capture the desired output signal of the actuators in real time and convert the signal into an equivalent electrical signal. The data acquisition system consists of signal conditioning circuitry, which improves the quality of the sensor signal into a form that can be further converted into digital signals. This conditioned signal is then entered into the analog-to-digital converter (**ADC**) to convert it into an equivalent digital value of 0 or 1. This conversion is required in order to process and store the data inside microprocessor of a computer.

The feedback data from the transducer in its digital form is then processed inside the microprocessor to perform some complex mathematical calculations of closed loop control to find the control command as output in its digital form. The digital control command is then further processed inside the digital-to analog converter (**DAC**) to transform the signal into its equivalent analog form to further transfer the signal as input to the **PV** of the EHAS. The (**DAQ**) hardware can either be operated in standalone mode, where the control command and the data are stored inside the system memory by the microprocessor and further processed in different ways, or it can be operated by interfacing with a PC. The (**DAQ**) hardware is normally obtained in modules, and during the interface of the (**DAQ**) system with a remote PC, it can be connected either externally via Ethernet cables or internally to the slot inside the motherboard of the PC. Some of the popular industry-grade data-acquisition systems involve *Computer Automated Measurement and Control (CAMAC)*, *PowerLab*, *VXI*, *Compact Reconfigurable Input Output (cRIO)* modules, etc. Some of the well-known **DAQ** softwares used to interface (**DAQ**) hardware with PCs are C++, Visual C++, Fortran, LabVIEW, Matlab/SIMULINK etc.

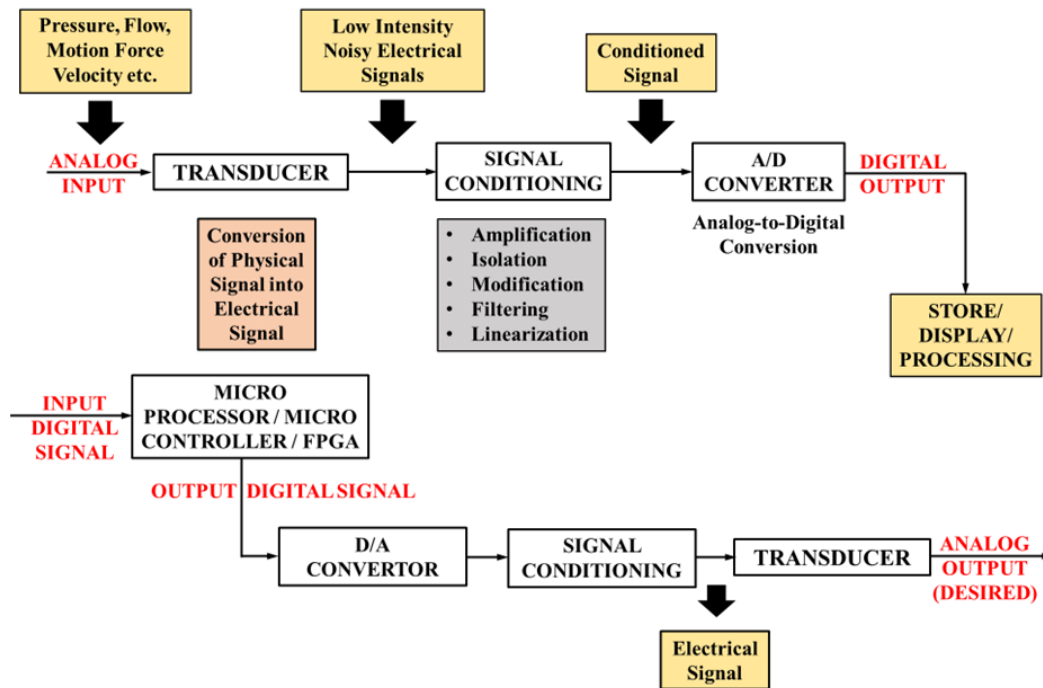


**Figure 1.4: Single channel data acquisition system (DAQ)**

- c. **Control Computer:** The control computer acts as an external device in the electrical and electronic sections. Already stated, the analog-to-digital converter converts the analog signal of the hydraulic actuation unit obtained from the transducer as feedback into its equivalent digital version. This data, with the help of an Ethernet cable, can be sent inside the computer to design and develop a closed loop controller with the help of several software packages mentioned above. The control demand in its digital form is further sent inside the (DAC) of the (DAQ) system. via ethernet cables. Alternatively, the designed controller can be directly written inside the microprocessor of (DAQ) system with the help of software known as the *Integrated Development Environment (IDE)*. Once programmed, the microprocessor can repeatedly perform the same task with precision and accuracy. The control computer unit, which was working as an external device before for running the controller, becomes an integral part of the electrical/electronic section. For mobile hydraulic systems, this type of arrangement is suitable. However, during the research and development stage of controller design, the use of the control computer as an external part is much more suitable.

*d. Valve Amplifier:* The solenoid of the PV normally requires 2A to 3A of current for its operation. However, the strength of the desired output signal obtained from the controller is weak (in the order of mA), and hence an additional circuit is required to boost the strength of the signal obtained from the controller as an output, referred to as a valve amplifier. A power amplifier is used for this purpose. The valve amplifier required a power supply of 12 to 24 VDC and a control signal obtained from the controller as input. The output of the amplifier circuit is regulated by the input signal provided by the controller. Increasing the input signal to the amplifier circuit will further increase the output current required to drive the solenoid. The input control device thus acts as a potentiometer.

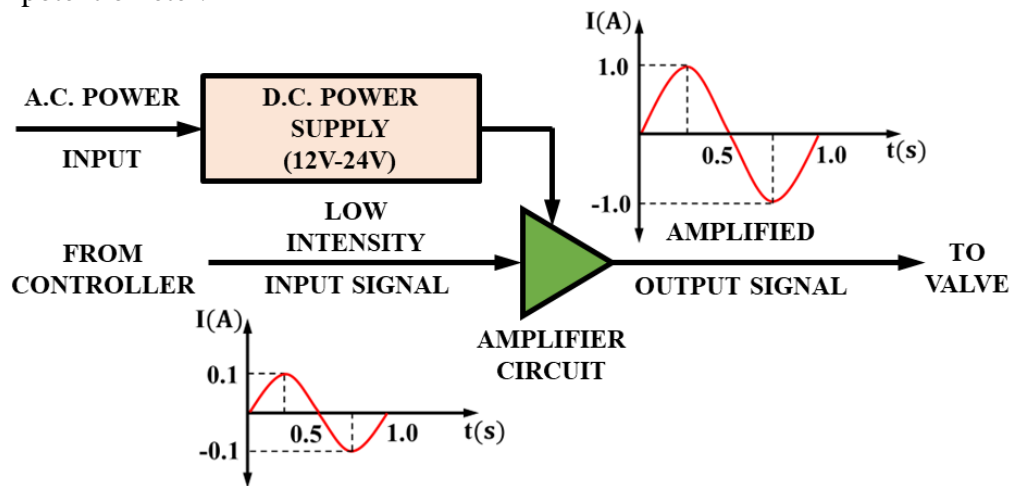


**Figure 1.5: Working of valve amplifier circuit**

Proper handshaking between each element of the hydraulic and electrical/electronic sections explained above finally produces a high-precision motion control system, termed as EHAS, to be used in different applications ranging from aerospace to several other industries like automobiles, automation, robotics, etc. where high power is required within a compact space.

### 1.1.2 Applications of EHAS for Robotic Manipulators

The presence of several inherent advantages, viz., an excellent power-to-weight ratio, a wider dynamic range, the ability to apply a large magnitude of force or torque with rapid response time, etc. (Hollerbach et al. 1992; Baghestan et al. 2015; Yang et al. 2019), within EHAS, endorse its diverse domain application in modern industries. The application of EHAS for driving robotic manipulators is also widely used, starting from manufacturing,

construction, mining, agriculture, and forestry to more advanced systems, viz., mobile robotics for working in hazardous environments, during disaster relief operations, in medical robotics for public health care, etc. A brief idea of some of the important applications is listed below.

- a. *Manufacturing Process:*** Manufacturing industries conventionally use electrical servo motors to drive different manipulators to perform several operations, viz., assembly, material handling, pick and place of objects, testing and inspection, etc. However, servo motors are normally meager to handle large payload. EHAS has proven its potential to drive a SCARA-type manipulator to handle large payloads at high speed (Liyanage et al. 2011). In sheet metal forming operations, EHAS are used to develop multi-stage feeding mechanisms for multi-station presses to perform several operations like rolling, stamping, coining, etc. (Suling et al. 2010). CNC operated hydraulic press brakes also use EHAS for punching operations (Altintas et al. 1997). A parallel kinematic manipulator with a restricted degree of freedom is especially useful in manufacturing industries to perform some specific operations that require limited motions of the manipulator. A 2-DOF parallel kinematic machine (PKM) suitable for drilling, punching, and changing orientation of machine tool tables is normally driven with EHAS (Sarkar 2017). In the modern injection molding process, EHAS's actuation mechanism efficiently conveys molten polymer to the mold to form plastic parts. (Zheng et al. 2003).
- b. *Construction and Mining:*** Tunneling is one of the essential tasks for the infrastructural development of large cities, along with expansion of public transport, transmission of electrical power, development of a communication system, etc. Shield tunneling machines (STM) are the most efficient and promising boring machines used for this purpose. EHAS are normally used to control STM due to their capability of negotiating large forces (Huayong et al. 2009). Another essential heavy equipment, termed excavators, or diggers, used in construction projects for material handling, mining operations, river dredging, and demolition purposes can also be controlled by EHAS (Nguyen et al. 2006; Ranjan et al. 2019).
- c. *Agriculture and Forestry:*** Off-highway vehicles such as tractors, lift trucks, etc. normally move through steep and uneven terrain and are used for agricultural purposes. The control of this type of vehicle is incredibly challenging. However,

the vehicles are equipped with an electrohydraulically actuated steering system to drive the vehicle and the articulated frame within it. (Qiu et al. 2001; Daher & Ivantysynova 2014). EHAS are also used to drive heavy-duty harvester manipulators to efficiently harvest forestry resources (Papadopoulos et al. 2003).

- d. Mobile Robotic Applications:* Starting from early initiatives for the development of mobile robotic platforms that involve wheeled or tracked systems for negotiating flat terrains, legged animals' locomotion inspired several researchers to also pursue the development of legged machines to obtain greater mobility and versatility in negotiating unknown, unstructured terrain (Semini et al. 2011) and also hazardous environments. The use of EHAS in the field of legged robotic applications has already advanced due to extensive research performed by several industries, like Boston Dynamics for developing BigDog, LS3, etc. (Raibert et al. 2008), and academia, like IIT, Genova, Italy, for developing HYQ and HYQ2Max (Semini et al. 2011; Mattila et al. 2017). Autonomous or semi-autonomous walking-legged robots, mostly available in two, four, six, or eight legs, could be highly effective in accomplishing rescue operations, disaster management, and maintenance in situations, where any other means could be difficult to deploy, and human assistance could even be life-threatening.

Commercially available semi-automated machines, viz. **Sandvik AutoMine**, **John Deere Intelligent Boom Control (IBC)**, etc., for working in different hazardous environments like mining, forestry, etc., can be driven efficiently by using EHAS (Mattila et al. 2017). Unmanned underwater vehicles (UUV), commonly used in offshore, marine science, and defense applications for performing different rescue activities like repair inspection, etc. under water, can be effectively manipulated with an electrohydraulic system (Clegg et al. 2001). Electrohydraulic actuators developed by smart materials or piezoelectric materials are used as a new class of actuators to be used in aerial robotics for the actuation of unmanned aerial vehicles (UAV) (Anderson et al. 2003; Sneed et al. 2007).

- e. Medicine and Healthcare Applications:* EHAS revolutionizes the field of surgical robotics by developing a hydraulically actuated robotic manipulator with multiple instruments with dimensions in the millimeter range to perform minimally invasive surgery (MIS), also known as laparoscopic surgery (Pourghodrat et al. 2014). In

healthcare applications, the development of wearable robotic systems refers to the augmentation of human unhealthy limb functionalities, termed as powered orthoses, functional replacement of human limbs referred to as prostheses, and developing powered exoskeletons to work in parallel with human limbs (Herr 2009). This system is also termed "human-robot augmentation." These prosthetics or exoskeleton robots can be effectively driven by EHAS (Kaminaga et al. 2010; Song et al. 2020). Wearable robotic systems are used for both medical and nonmedical applications. Use for medical rehabilitation and assistance refers to power-assist systems, and nonmedical applications refer to powered exoskeletons that are used in defense and industry (Song et al. 2020). EHAS are also used to effectively drive a multi-DOF Patient Transfer Assist Device (**PTAD**) for mobility limited patients (Humphreys et al. 2018).

## **1.2 EHAS Control**

EHAS finds a wide range of applications, from rugged to sophisticated, in the fields of motion and high force or torque control. as these systems are compact, fault-tolerant, back-drivable, and precisely controllable. For rugged and uninterrupted applications, EHAS are provided with proportional valves and industry grade cylinders. These systems are indeed cheaper, but they normally provide low to moderate precision due to the presence of strong nonlinearities in the system. To obtain more sophisticated systems, normally servo-grade valves and actuators are used. Sophisticated servosystems provide higher precision. But since servovalves and servo actuators have fine radial clearances, the system requires high-grade filtration of oil and routine maintenance (Mandal et al. 2016), which further prohibits their use under long-duration uninterrupted rugged services. Also, due to the requirement for high precision machining, the manufacturing and operating costs of servosystems are extremely high. Thus, an emerging trend in the domain of electrohydraulic industrial research involves the design and implementation of finely tuned advanced controllers for low-cost, rugged electrohydraulic systems to yield precise tracking performance comparable with that of more sophisticated systems (Mandal et al. 2016). All EHAS are associated with some inherent nonlinearities coupled with parametric uncertainties and external disturbances in the system (Mattila et al. 2017), which further influence the system performance and thus pose serious challenges and complexities in the real time controller design to drive the EHAS. Hence, in order to design an efficient, high-precision, robust

controller, meticulous understanding is required of several control challenges in the form of nonlinearities, uncertainties, and disturbances present in the EHAS. The next section provides a brief overview of these challenges that are commonly encountered during the design of any controller for EHAS.

### **1.2.1 Modelling Challenges for Electrohydraulic Systems**

The design of a controller to drive an EHAS requires a meaningful and suitable mathematical model of the real time system. As already stated, because the EHAS are inherently associated with different nonlinearities, uncertainties, and disturbances, the system modeling and finally the controller design of the EHAS become quite challenging for the designer. For this reason, extensive knowledge about these challenges is needed to be explored properly.

**Nonlinearities:** The associated nonlinearities present in an EHAS can be broadly classified into two types: **soft nonlinearities (continuous type)** and **hard nonlinearities (discontinuous type)**.

The soft nonlinearities, also termed "continuous type," are the most generic form of nonlinearities present in the system in the form of square-root pressure-discharge relations at the metering valve ports, electromagnetic characteristics of the valve drives, especially for permanent-magnet motors, sliding friction between the actuator and cylinder pair, and compressibility of hydraulic oil (Merritt 1967). These effects are substantial, even for sophisticated servosystems.

The hard nonlinearities, or discontinuous type, on the other hand, are normally present in the system in the form of deadbands due to high static friction in the actuators (Merritt 1967) and from the overlap of valve ports (Hu et al. 2011; Na et al. 2011). Recently, a class of land-based mobile system applications of moderate sophistication is emerging (Mattila et al. 2017), for which zero-lap proportional valves could provide a cost compromise with respect to narrower radial-clearance servovalves. The absence of the deadband in a zero-lap valve causes a drastic reduction of the hard nonlinearity at the cost of higher oil leakage through the radial clearance in the valve bypassing the actuator.

Different nonlinearities stated above, viz. deadband, along with some others like saturation, backlash, and hysteresis, are inherently present in a physical system due to some

manufacturing imperfections or limitations of the physical components present in an electrohydraulic system. A brief idea of these nonlinear features has been explained below.

- a. Saturation:* The most common occurrence of discontinuous nonlinearity in electrohydraulic systems is due to saturation of the control input (Yu et al 2004), where the system output is proportional to the input up to a certain interval and beyond that, the output tends to become constant. This type of nonlinearity can be primarily observed in pairs of both rugged industrial and servo grade systems, where the maximum and minimum magnitude of the input to the valve is in the form of voltage and current, and the output corresponds to the displacement of the actuator and is limited by physical length of the cylinder.

Figure 1.6 shows a typical representation of sinusoidal input and the corresponding output to exhibit the saturation phenomenon of the valve actuator pair for EHAS. Whereas Figures 1.6(a) and 1.6(b) depict the sinusoidal input and output of the system in the time domain, Figure 1.6(c) represents combined input and output characteristics. Considering the maximum and minimum control signal required to drive a voltage-driven proportional or servo valve is limited to within (V), any signal higher than this value will provide saturation (S) to the output of the system, as shown in Figure 1.6(b). The figure clearly depicts the occurrence of saturation of actuator stroke beyond 60mm during both extension and retraction stroke, even after increasing the valve input signal higher than (V). Along with these two plots, the combined input-output plot given in Figure 1.6(c), also provides the complete information regarding the saturation phenomenon of EHAS explained above.



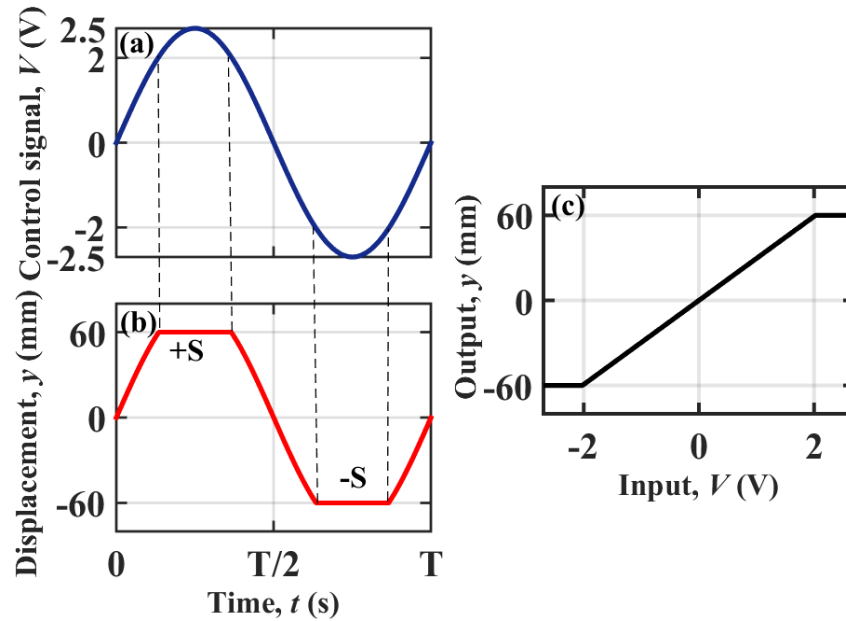


**Figure 1.6: Input and output representation of saturation nonlinearity in EHAS**

*b. Deadband* : This is another type of nonlinearity found in EHAS, where the system does not respond up to a given range of control signal input termed "deadband ( $\mathbf{D}$ )". Normally, this phenomenon can occur due to the presence of Coulomb friction in the system and overlapped valve ports (Merritt 1967; Yu et al. 2004) in an industry-grade rugged valve-actuator pair. When the input signal crosses the limiting value of ( $\mathbf{D}$ ), the system becomes responsive. Considering again the same valve-actuator pair as discussed earlier, the deadband situation in the system can be clearly explained by the input and output waveforms as depicted in Figure 1.7. The figure shows that up to a certain range of voltage, the actuator displacement is zero for both the positive and negative halves of the excitation. The range up to which the displacement remains zero is termed the deadband ( $\mathbf{D}$ ), where the corresponding input voltage is termed the deadband voltage.

The presence of this type of nonlinearity may degrade the system's tracking performance and can destabilize the system. The deadband in EHAS may also increase the limit cycle oscillation and further instability.

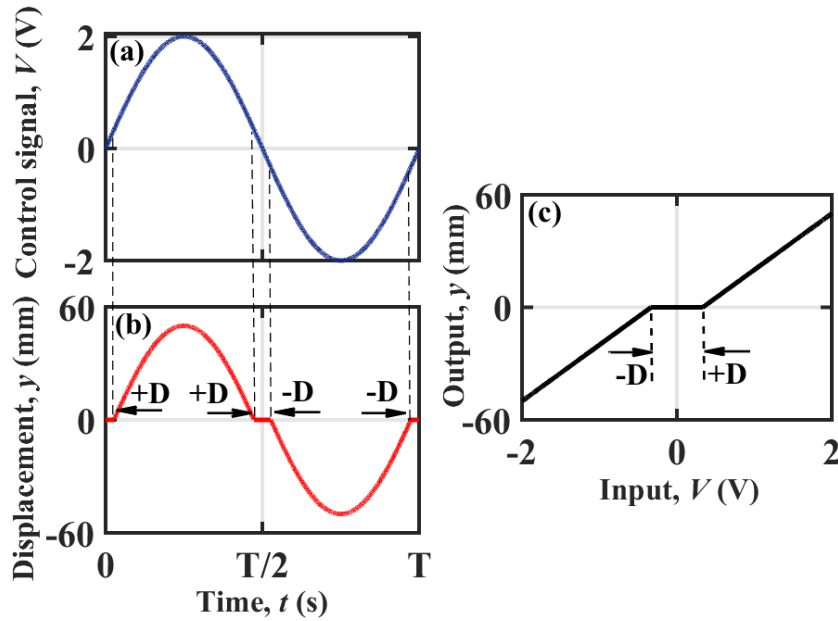


**Figure 1.7: Input and output representation of deadband nonlinearity in EHAS**

*c. Friction:* The most complex time-varying nonlinearity found in EHAS is friction. Friction can be seen in hydraulic actuators between piston rings and the surface of the cylinder, as well as between the piston rod and seal. The viscous effect of the hydraulic oil also generates friction. The presence of friction in the system notably affects the system's performance by increasing tracking error, limit cycles, and stick-slip motion (Rahmat et al. 2011). It also affects the stability of the system. Also, friction alone can consume a large part of actuator torque (Owen et al. 2003; Gao et al. 2022).

One of the major challenges with this nonlinear effect is the proper lack of understanding of this complicated feature leading to the development of several friction models. These friction models over a long period of time, they can be broadly classified into two categories: static and dynamic. The **Coulomb friction**, the **static friction**, and the **Stribeck effects** are the characteristics of the static model. The static model of friction is also known as the "classical" **Friction Model** which include models like the **Karnopp** and **Armstrong** friction models, etc. Normally, in a static model, the friction force is mathematically represented as a function of the relative velocity of the moving object with respect to a stationary surface. The main advantage of the static model is that the mathematical modeling is well defined, and the corresponding parameters that represent the model can be

easily determined. Thus, the static model can meet the control performance requirements to a certain extent. (Gao et al. 2022; Olsson et al. 1998).

However, the static model fails to explain the dynamic characteristics of friction, where the friction becomes a function of both relative velocity and the displacement of the moving object. The dynamic model was first developed by Dahl (1976) and referred to as the Dahl model. Several other models, like the Bristle model (Haessig et al. 1991), a series of dynamic models proposed by Bliman (1992), and the LuGre model (Freidovich et al. 2010), are also very well known. Broadly, the main characteristics of dynamic friction are classified as–

1. **Pre-Sliding Displacement-** A small positional displacement of object can be observed due to deformation of contact surface during static friction stage also known as pre sliding displacement. The removal of frictional force will not bring the object back to its initial position, leaving a residual displacement as shown clearly in figure 1.8.

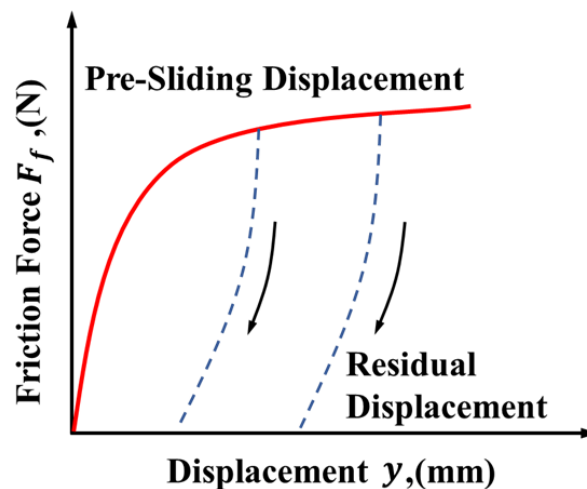


**Figure 1.8: Relation between friction and displacement in dynamic friction**

2. **Friction Hysteresis-** Where the pre-sliding displacement phenomenon clearly depicts the dependence of friction force with the corresponding microscopic displacement near the static zone of friction, the friction hysteresis corresponds to the dependence of frictional force with the variation of velocity. The relationship between the two variables was first observed by Hess and Soom in (Hess & Soom 1990), where hysteresis was observed with the variation of velocity.

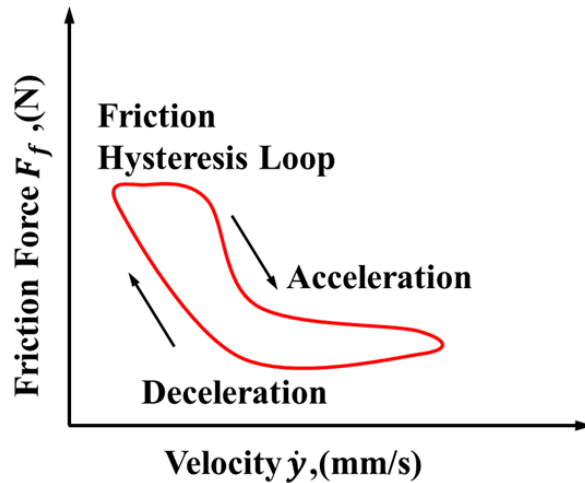


**Figure 1.9: Formation of frictional hysteresis loop**

Figure 1.9 exhibits the hysteresis phenomenon. From the figure, it is seen that the friction force decreases more during deceleration compared to the increase during acceleration. Thus, the friction force curves during acceleration and deceleration do not coincide. Normal load, viscosity, and frequency of velocity variation can all be used to increase the size of the loop (Olsson et al. 1998). The hysteresis due to friction is also termed as frictional memory (Gao et al. 2022).

3. **Crawling Phenomenon-** The phenomenon of alternate stopping and sliding on the surface is termed as "crawling." When the operating speed of the system is less than a critical value, this type of pulsating motion can be seen on the moving parts, which further initiate vibration in the system based on the magnitude of the low-speed jitter. The presence of crawling motion may degrade the control performance, produce limit cycle oscillation, and finally bring instability to the system (Armstrong 1993; Gao et al. 2022).
  
- d. **Backlash:** Backlash is another form of nonlinearity normally present in most mechanical and hydraulic systems and normally increases with the wearing of the system for long duration of operation. In this case of nonlinearity, the input changes by an amount before any initiation of output motion. However, for the initiation of motion in the reverse direction, the input should be kept twice as high as the initial input. The plot between input and corresponding output in Figure 1.10 depicts this situation. Backlash mainly occurs due to loose gear meshing or loose fittings of pins

in the joints of the system, etc. This type of nonlinearity mainly produces sustained oscillations in the system, which can make the system unstable (Merritt 1967).

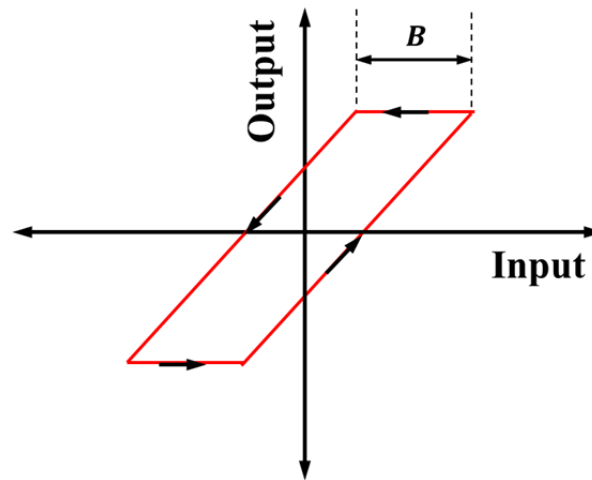


**Figure 1.10: Representation of backlash nonlinearity**

**Uncertainties:** Apart from several nonlinearities, the modeling of an EHAS also encounters another challenge known as uncertainty. Broadly, the uncertainty present in the system can be categorized into two types: parametric uncertainties and modeling uncertainties, or uncertain nonlinearities (Garimella & Yao 1997; Yin et al. 2021). Because hydraulic fluid is the primary medium of energy transmission in an EHAS, the system is prone to having uncertain hydraulic parameters such as density, viscosity, effective bulk modulus, and so on. These parameters are normally a function of pressure and temperature and, up to a certain limit, remain constant. Beyond this limit, the nonlinear variation of the parameters magnitudes with pressure and temperature affects the control performance significantly. The parametric uncertainties can also be present in the physical characteristics of several components of the overall system, viz., hydraulic cylinders, valves, etc. Due to normal wear and tear of the physical system or temperature variation, parametric variations can be seen in both the physical and geometric configuration of the hydraulic actuator, which includes the mass of the piston and piston rod, the mass of the cylinder, the internal volume of the cylinder, and the cap and rod end diameters (Yao, Bu & Chiu 2001). With the aging of valves and cylinders, as the leakage through narrow clearances between the sliding surfaces increases, the valve flow coefficient, or leakage coefficient obtained from the valve literature as a parameter, may differ from time to time, which further affects the system performance and brings challenges during the development of controllers. The

variation of external load to be negotiated by the system, viz. weight, inertial force, spring force, etc., due to change in the parameters like mass, spring stiffness, etc. after long uninterrupted operation also comes under parametric uncertainty, which may affect the overall system dynamics and further the control performance (Mandal et al. 2016).

Another type of uncertainty commonly encountered in EHAS is termed as modeling uncertainties or uncertain nonlinearities. The presence of friction and leakage in the system is regarded as the most complex nonlinear phenomenon, which further cannot be modeled exactly and correspondingly adds to the uncertainties. This type of uncertainty in the modeling level is termed as modeling uncertainty or uncertain nonlinearity. As the nonlinear function of these phenomena is not properly known, the system model becomes erroneous, and the designed controller may give degraded performance due to unmodeled disturbances (Yao, Al-Majed & Tomizuka 1997; Onder, Bayrak & Aksoy 2021).

**External Disturbances:** Normally for the measurement of several physical quantities viz. Pressure, flow, displacement etc. EHAS are integrated with different sensors that produce electrical noise during interference with other nearby electrical devices. During measurement of the physical quantity, the actual reading gets corrupted by this noise, and directly affect the system's performance. There may exist some other source of noise in the external environment as well, which further degrades the system and controller performance by inducing instability. These unknown external disturbances imposed on the system also fall under the category of uncertain nonlinearities (Yao, Al-Majed & Tomizuka 1997).

The different sources of nonlinearities, uncertainties, and external disturbances stated above are the recurrent phenomena to be found in EHAS, which directly influence the real-time performance of the system, and affect its stability. Apart from these challenging factors, the articulated EHAS with a higher DOF, viz., serial, parallel or serial/parallel manipulators that require a higher number of pairs (Cetinkunt et al. 2004; Chaudhuri et al. 2020b), also experiences the distinct challenge of the nonlinearity of the connected multibody dynamics, which along with other nonlinearities, uncertainties, and disturbances stated above complicates the controller design further (Mattila et al. 2017).

### **1.2.2 Control of EHAS (Feedforward-Feedback Control Strategies)**

Low-cost EHAS with a rugged valve paired with industry grade actuator are mostly preferred in electrohydraulic industries for their low cost and uninterrupted use as compared to sophisticated servo systems. These systems mostly offer low to moderate precision since the systems are associated with several nonlinearities and disturbances, as stated above. However, the use of an advanced controller may enhance the performance of the system up to a high precision level with faster response, which is the prime requisite of mobile robots. Thus, the current trend in modern automation industries that uses EHAS as the prime driving unit, especially in the field of mobile robotic research, involves the development of more advanced level controllers to drive low-cost EHAS with high precision tracking performance (Sirouspour & Salcudean 2001; Semini et al. 2011; Mandal et al. 2016; Matilla et al. 2017).

Over several decades, different classes of controllers have been designed in order to drive EHAS which include linear, robust, adaptive, and intelligent, or model-free" controllers. The most commonly-used and popular controller in the electrohydraulic industries for its ease of implementation is the fixed-gain linear PID controller. This controller is also considered as model free as its operation is based on only input and output data. Such linear controllers due to their incompetence to handle associated nonlinearities and uncertainties that are normally common in electrohydraulic system, only provide limited control performance near some operating point. However, the performance of the controller is also dependent on its parameter values. Several studies have been conducted to determine these parameters, ranging from traditional methods to various single- and multi-objective optimization techniques (Li, Zhang, and Sun 2014). In several research studies, PID is combined with feedforward controllers in order to compensate the higher order nonlinearities (Sarkar et al. 2013). The implementation of a feedforward loop in the system may further call for a rigorous mathematical model and tedious characterization experiments (Papadopoulos, Bin and Frenette 2003; Sarkar et al. 2013; Mandal et al. 2016).

The challenges in modeling several nonlinearities with uncertain parametric variations for EHAS can also be well handled by implementing adaptive and robust control and model-free controllers, which include sliding mode control SMC (Utkin 1992), fuzzy logic control, neural networks based control etc. One of the most popular adaptive control methods among several is SMC control, which provides a robust solution and becomes insensitive to modeling uncertainties and disturbances (Cerman & Hušek 2012; Feng, Yu & Han

2013). However, SMC, due to the discontinuous nature of the control structure, suffers from high-frequency oscillation near the sliding surface leading to undesirable chattering problem, which may further produce fatigue in mechanical systems (Bartolini et al. 2003). SMC can be combined with a nonlinear integral (I) controller, which is applied in the near-zero error region, to ensure robustness and eliminate chattering due to control (Dasmahapatra et al. 2018). Model-free fuzzy logic control or neural networks are beneficial to EHAS because of their universal approximation capability to handle unknown system nonlinearity (Cerman & Hušek 2012), which ultimately leads to the emergence of adaptive fuzzy sliding mode control or (AFSMC) (Chan, Rad & Wang 2001; Chen et al. 2009). The fuzzy logic can also be utilized for the adaptation of the SMC parameters to achieve better performance and to attenuate chattering of control input (Hung et al. 2007). This adaptive fuzzy SMC or AFSMC method stated has been successfully applied in several domains, like the automotive industry (Huang & Chen 2006), missile launching (Bao et al. 2006), mobile robotics systems (Lian 2012), etc. Normally, model free controllers are easy to implement in real-time systems and often preferred to avoid the difficulties in modeling the nonlinearities of EHAS, but at the cost of non-optimal use of the control and rigorous qualification tests to achieve high-quality performance (Mandal et al. 2016).

Unlike model-free controllers, model-based controllers (Du, Plummer and Johnston, 2017; Kaya & Bilgin, 2019; Daher & Ivantysynova 2014) require rigorous mathematical models, which are further difficult to develop and implement. However, model-based controller design (Tripathi & Sun 2016) is at times essential to account for the pressure-flow dynamics inside hydraulic cylinders in case of high speed servo-valves (Merritt 1967), and to obtain precise tracking performance, Model-based design, like a feedforward controller when implemented with the aid of sound physical principles, can result in optimal use of the available command-signal without the need for early or transient saturation, which is frequently encountered for simple PID and for even more advanced model-free controllers.

Conventionally a two-degree-of-freedom (DOF) controller, consisting of a feedforward and feedback unit, can be a good option for achieving precise tracking performance in the presence of a suitable plant or system model (Tripathi & Sun 2016). Customarily, to determine the control signal needed to produce the desired trajectory, the feedforward control algorithm approximates the inverse of the system model as described by (Tripathi and Sun 2016). Feedforward controller design (Fliess et al. 1995; Du et al. 2017; Sahoo et



al. 2018; Faessler et al. 2018; Sira-Ramirez et al. 2017) is popular for its ability to tackle known disturbances and nonlinearities by exploiting the system model at the appropriate level to estimate the variations of the command signal to fulfill the given demands. For instance, compressible and incompressible-flow models are suitable for high-and low-pressure hydraulic systems, respectively. Simple substitutions following certain approximations in the state-space model of the system lead to the estimation of the feedforward command in terms of the output and its derivatives in a conventional design of feedforward controller. Such an estimation is known as inversion of a system model with the differential flatness property. (Fliess et al. 1995; Sira-Ramirez et al. 2017; Kock et al. 2012). Most of the existing EHAS have single cylinders, each capped at one end with a single rod extending or retracting from the other end. Such a cylinder (Du et al. 2017; Mattila et al. 2017) indeed consumes less space than a double-acting, double-rod cylinder with rods protruding out from both ends. Double-rod cylinders possess the unique mathematical property of differential flatness due to their symmetry, which is exploited to execute the inversion for estimating the compensation for oil compressibility (Kock et al. 2012; Kim et al. 2015; Kemmetmuller et al. 2007). However, for a single-rod asymmetric cylinder the flatness property cannot be maintained properly. For the compressible flow model, designing a flat feedforward controller for the single-rod cylinder system as a straightforward extension of the existing inversion method for the double-rod system remains a challenge. Existing research for a cylinder with a single rod that avoids the inversion problem employs the numerical solution of a nonlinear differential equation (Tripathi & Sun, 2016). Incorporating the oil compressibility effect into the pressure dynamic model and further relaxing the incompressible flow model rendered the overall model numerically stiff. Other considerations for the development of the feedforward model assume no valve leakage, constant pump pressure, double-rod cylinders, and an incompressible flow model (Dasgupta & Watton, 2005; Tripathi & Sun, 2016). Of course, each of the assumptions has the corresponding penalty of restriction to low-pressure, slow applications and a higher space requirement when using large-deadband proportional valves or high-cost servovalves, respectively, with poorer energy efficiency. Use of a variable-displacement pump that provides pump flow variation matched to the actuation demand increases the energy efficiency of EHAS in general (Daher & Ivantysynova, 2014). Improving the energy efficiency of electrohydraulic systems is a significant requirement, as the energy efficiency of conventional hydraulic systems with fixed-displacement pump and standard relief valve pairs is quite inadequate (Du et al., 2017). This is a result of the

flow throttling losses in the main control valves and bypassing relief valves (Mattila et al. 2017; Saeedzadeh et al. 2018; Wang et al. 2018). Conventionally, a relief valve ensures constant pump pressure at the highest value that the system needs, and the metering of the main control allows required flow to the actuator together with damping of the unwanted actuation oscillations. The energy saving investigations attempt to establish variation of the pump pressure or discharge to match with the actuation requirement of the payload. For achieving the pressure matching, the relief valve was endowed with either proportional or switched control (Baghestan et al. 2015; Tivay et al. 2014). In order to achieve the discharge matching, either variable-displacement or variable-speed pumps were used (Daher & Ivantysynova, 2014; Du et al. 2017) by retaining the relief valve only as a safety ploy against accidental over-pressurization. Like static friction of the actuator, the variation of pump pressure renders additional source of disturbance in the system models that are routinely used for designing controllers.

From the above discussion, it can be concluded that combined feedforward and feedback control is an effective way to significantly improve performance over simple feedback control whenever there is a major disturbance or frequent change in command signals that can be measured before it affects the process output. In the most ideal situation, feedforward control can entirely eliminate the effect of the measured disturbance on the process output. Even when there are modeling errors, feedforward control can often reduce the effect of the measured disturbance on the output better than feedback control alone. However, feedforward control is always used along with feedback control because a feedback control system is required to track set-point changes and suppress unmeasured disturbances that are always present in any real process.

### **1.3 Classification of Robotic Manipulators**

Robotic manipulators in the form of robotic arms (mostly stationary) are extensively used in modern industries for various automation applications like assembly, different manufacturing operations processing, material handling, etc. Several research projects based on advanced mobile robotic systems are also gaining vast attention for running self-driving cars in the automotive industries, to develop unmanned mobile robots to be used in defense for load ferrying purposes in hazardous and unstructured environments (Mattila et al. 2017; Semini et al. 2011), for space exploration, in medical surgery (Truong, Maxon & Goh 2019), etc. However, the classification of different manipulators is based on several

criteria, viz., degree of freedom (DOF), kinematic structure, mode of actuation, different control methods, workspace, and different characteristics of motion, that are normally useful to determine a suitable manipulator to perform a given task. A brief idea regarding the classifications of robotic manipulator have been described below.

*a. Degree of Freedom (DOF):* Normally, for a robotic manipulator, several links are connected with each other by joints to form a kinematic chain of an open or closed type. The number of joints, however, provides information about the number of independent constraints on motion of the manipulator, and thus the degrees of freedom (DOF) of a robotic manipulator can be defined as the total number of freedoms of the rigid bodies minus the number of constraints on their motion coming from the joints. As a result, the robotic manipulator can be further classified based on the degrees of freedom (DOF) available as a general manipulator with normally having six DOF, a redundant manipulator with a greater number of DOF than required, a deficient manipulator with less than six DOF, and a flexible manipulator, which has flexible links rather than rigid links as evident in the other three cases.

*b. Kinematic Structures:* In terms of characteristics of the mechanism of the manipulators, three types of architecture may exist, termed "**serial**," "**parallel**," and "**serial-parallel**." A serial manipulator with an open loop kinematic chain has a large workspace and moves like a human arm. It has many uses in the automation industry, but it still has high precision positioning errors and bends easily because of its cantilever structure (Dasgupta & Mruthyunjaya, 2000). On the other hand, parallel manipulators, also called closed loop kinematic chains, have a high load carrying capacity, higher stiffness, and high precision work (Chaudhuri et al. 2020b), but they have a small workspace (Dasgupta and Mruthyunjaya 2000; Pashkevich, Chablat, and Wenger 2008; Pashkevich, Klimchik, and Chablat 2011). However, both manipulators have their own merits and demerits regarding fields of application, load-carrying capacity, etc. The idea of combining the two architectures into a single design has the potential benefits of each manipulator in terms of rigidity and workspace (Tanev, 2000). This type of manipulator is often referred as "hybrid" manipulator in robotic research. For popular appreciation, it is referred in this study as a serial-parallel manipulator, reflecting its combination of

both open and closed chain mechanisms where both serial and parallel architectures are integrated in a single arrangement to obtain a higher number of degrees of freedom (DOF) (Waldron, Raghavan, & Roth 1989), to meet a variety of operational requirements.

- c. **Different Modes of Actuation:*** Choosing the right actuation systems is an important part of making a robotic manipulator. Actuators are usually power sources that send power to the end effector through a series of rigid or flexible links that are part of the manipulator. According to the mode of actuation, manipulators can be classified into three ways: electrically actuated (where AC and DC servo motors are popularly used to drive the robot) for having an excellent level of accuracy and controllability (Caldwell et al. 1995; Truong, Maxon & Goh, 2019); pneumatically actuated for having a high power-to-weight and power-to-volume ratio (Chiag & Chen 2017); and electrohydraulically actuated (for having a high power-to-weight ratio and high stiffness (Truong, Maxon, & Goh 2019; Chaudhuri et al. 2020) in order to negotiate heavy loads with increased speed of response and torque (Hollerbach et al. 1992).
- d. **Different Control Methods:*** Robotic manipulators based on control method can be classified into two types: **non-servo manipulators** and **servo-controlled manipulators**. Earlier versions of robotic manipulators come under the non-servo category with a simple structure and are normally used for material handling purposes, viz., pick and place operations. This manipulator system is normally of the open-loop type, to do some specific job in less quantity. Servo-controlled manipulators use a closed-loop control system where the controller guides the motion of the end effector to perform a task in an efficient manner. Servo-controlled robots are further classified as **point-to-point** and **continuous-path** robots based on the guidance provided by the controller to the end effector. The reprogrammable feature of the closed loop system makes the manipulator multitasker.
- e. **Workspace:*** Another crucial factor that determines the maximum limit of the movement of any industrial manipulator is known as workspace, which is further defined as the total volume swept by the end effector during execution of all possible motion for a particular manipulator. Based on the workspace, most industrial robotic manipulators can be further classified as: **Cartesian** (with **3** prismatic joints), **Cylindrical** (with **1** revolute and **2** prismatic joints), **Spherical**

(with **2** revolute and **1** prismatic joint), **Selective Compliance Assembly Robot Arm (SCARA)** (having **3** revolute and **1** prismatic joint) and **Articulated** (with **3** revolute joints).

- f. Nature of Motion:* Robotic manipulators can be classified based on the nature or characteristics of motion as well. Based on the motion criteria, manipulators can be further classified as "**planer manipulators,**" where all the links move in a plane that is parallel to each other, **Spherical manipulator:** when the links associated with the manipulator perform spherical motions and **Spatial Manipulator:** If at least one link of the manipulator possesses 3-dimensional spatial motion during execution of any task.

Based on the above discussions, it can be said that different classifications of robotic manipulators ultimately depend on various industrial applications to perform with good dynamic performance and precise positioning (Dasgupta & Mruthyunjaya 2000).

### **1.3.1 Applications of Serial, Parallel and Combined Serial-Parallel Manipulators**

In the scope of this work, the two most important ways to classify robotic manipulators are by their mode of action and their kinematic structure. No matter what the actuation system is, every manipulator can be described by its kinematic structure as either having an open loop (serial manipulator), a closed loop (parallel manipulator), or a combination of both (serial-parallel manipulator). But in modern industries, each of these structures does a different job, so the fields of use for each manipulator are also vastly different. A brief idea of the different applications of these individual manipulators is given below.

- a. Applications of Serial Manipulator:* The most generic form of robotic manipulator used in industries are serial manipulators, where a number of rigid or flexible links are connected with joints (either prismatic or revolute) to form the manipulator. For serial joints, the first joint usually has a fixed link, which is called the base, and the last link, which is called the end effector, is free to move in space. This makes a structure that looks like an arm, which is called a "robotic arm." The serial manipulators are widely used in the automotive industries to perform several operations like welding through an electric arc and shielding gas (Garriz et al. 2019), spot welding of automobile bodies, or spray painting. Other operations

involved in these categories include grinding, polishing, etc. Serial manipulators are also widely used for material-handling purposes in order to pick objects from one conveyor and place them on another (Ramirez, Kotlarski, & Ortmaier 2016). Further, with the aid of a visual feedback system, serial manipulators are used in slaughterhouses for processing food (Wu et al. 2017). Serial manipulators, sometimes mounted on a mobile platform fitted with a camera at the platform and end effector, are used in hazardous and unfriendly environments, viz., nuclear plants for decommissioning, cleaning of nuclear waste, and grasping and pipe cutting using a dual-arm manipulator with vision-based feedback (Bandala et al. 2019).

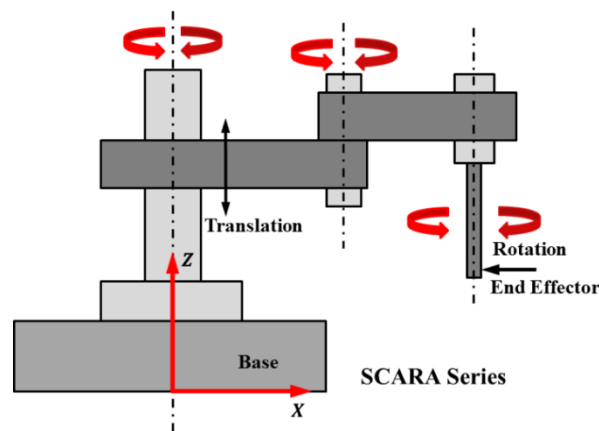


**Figure 1.11: Schematic of serial manipulator (SCARA Series) performing drilling operations**

These manipulators even proved themselves as an efficient system for assembling industrial parts (Rice & Schimmels 2018) like future vehicles in the automotive industry at the body shop (Garriz et al. 2019) and to perform automated detection of several defects and the corresponding location of the defects in large metal plates by non-destructive testing (NDT) methods (Lu et al. 2015; Hou et al. 2021). In the field of medical robotics, serial manipulators are extensively used for robot-assisted cardiac surgery and further reduce the mortality rate. (Yanagawa, Pérez, & Bell 2015) Several serial manipulators, viz., PUMA, SCARA, KUKA, etc., having different series, are popularly used in modern automation industries. Figure 1.11 clearly depicts the schematic representation of an electrically actuated serial manipulator that belongs to the SCARA series used in machine tool industries for performing drilling operations.

**b. Applications of Parallel Manipulator:** The applications of the parallel manipulator have also become widely popular in various fields, viz. precise manufacturing, space exploration, and medical science, due to several distinct advantages of high accuracy positioning, fast response speed, high system stiffness, and a high force-to-weight ratio as compared to serial manipulators (Dasgupta & Mruthyunjaya 2000; (Pashkevich, Chablat & Wenger 2008; Pi & Wang 2011). These are closed-loop kinematic chains where the end effectors, in the form of platforms, are linked to the base by an independent kinematic chain having parallel actuation (Patel & George 2012) to form a multi-DOF system. The parallel manipulators in the form of a 6-DOF Stewart-Gough platform or hexapod are used as a flight simulator motion system for research and training purposes (Pradipta et al. 2013; Huang et al. 2017). In automotive industries, the Stewart platform in canonical form is used as a pose sensor to measure 6-DOF motion (Jang, Lim & Kim 2018) and also as an active vibration isolator for space applications to reduce jitter induced through various sources of disturbance. (Chi et al. 2015; Li et al. 2018). In medical robotics to develop robotic teleoperation systems for high-precision microsurgeries, viz., endoscopy, cell implant, spine surgery, etc. (Zhao et al. 2019; Tendick et al. 1998; Wapler et al. 2003), and also for ankle telerehabilitation (Girone et al. 2001) in the form of a Stewart platform with manipulation in the submillimeter range.

Figure 1.12 shows a laboratory-scale electrohydraulically operated parallel manipulator in the form of the Stewart Platform, which consists of six double-acting single rod actuators that act as the six legs of the platform, where the cylinder end is hinged with the base fixed at the ground and the rod end holds a moving platform that acts as an end effector. The hydraulic energy is utilized here for the motion of the moving platform with respect to the fixed base.

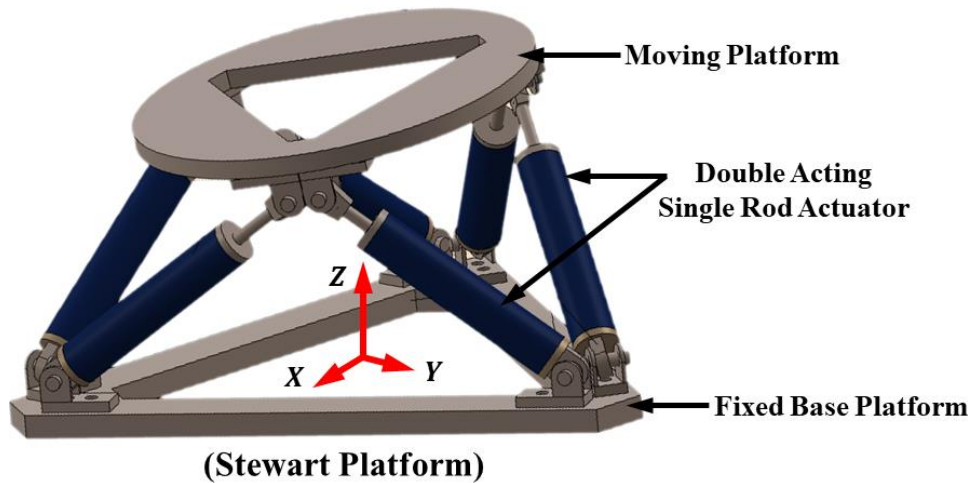


**Figure 1.12: Laboratory-scale electrohydraulic parallel manipulator in the form of a 6-DOF Stewart platform**

Another form of parallel manipulator, the delta robot, which contains 4-DOF, is widely used in several industries, viz., food processing for fast pick-and-place applications (Březina et al. 2013), food packaging, and also for weed control applications in organic farming (Hussmann et al. 2019). Recently, this kind of kinematic structure has been effectively used in additive manufacturing, also known as the 3-D printing technique, to obtain 3-D physical objects with complex geometry (Rodriguez & Alvares 2019).

*c. Applications of Serial-Parallel Manipulator:* As was said above, the serial-parallel type of manipulation system is a combination of both closed chain and open chain mechanisms. It has the benefits of both serial and parallel manipulators (Kang et al. 2011; Yeshmukhametov et al. 2017) in terms of rigidity, speed of response, and working with large workspaces. This manipulator can be used for a lot more things because it has both serial and parallel architectures in a single unit. Advance manufacturing industries use this architecture for multitasking processes, viz. milling, drilling, and grinding with more flexibility in the NC process (Lu, Hu & Yu 2009) and also ultra-precision machining like freeform polishing (Xu et al. 2020). A serial-parallel robotic arm with a hand is extensively used for forging operations, rescue missions, and testing and inspection (Lu et al. 2015). In the aerospace and automotive industries, this system is used as a spray-painting robot for surface coating at a stable speed in order to reduce severe corrosion (Liu et al. 2021). In medical robotics, serial-parallel manipulators are used as surgical robots



to perform minimally invasive surgery or (MIS), also known as **laparoscopic surgery** (Pisla et al. 2013).

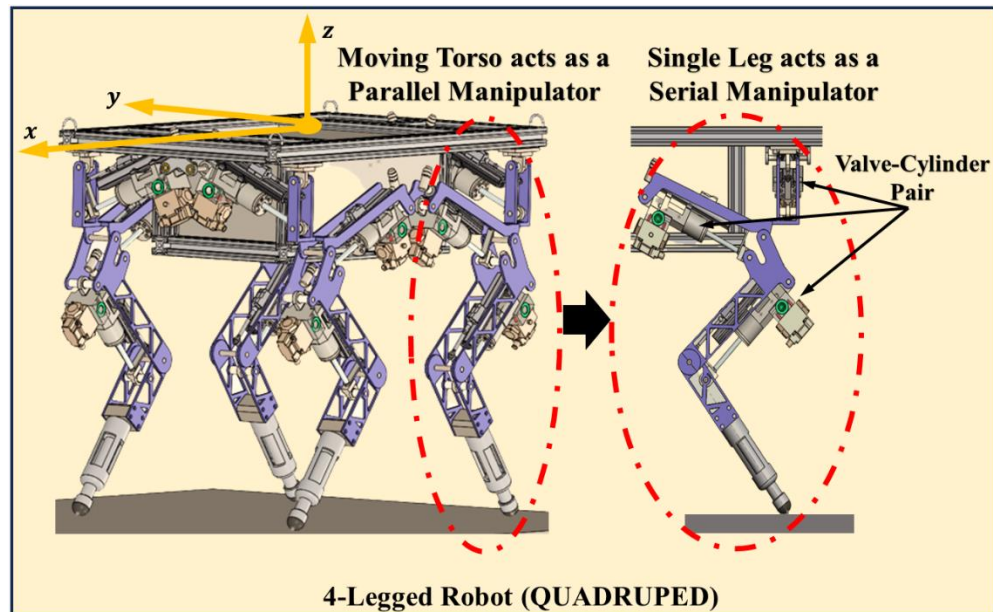


**Figure 1.13: Laboratory-scale electrohydraulic serial-parallel manipulator in the form of a Quadruped**

The manipulator architecture of mobile robots with legs is being used more and more in hazardous situations like firefighting, mine inspection (Biswal et al. 2020), and rough or soft unstructured terrain (Hutter et al. 2014). Legged robots have greater flexibility in obstacle negotiation and approach in such environments (Semini et al. 2011). Popularly known as quadrupeds, viz., Boston Dynamics BigDog (Raibert et al. 2008), Alpha Dog or (LS3) designed for military use (Biswal et al. 2020), ANYmal (Fankhauser et al. 2018) for industrial operation in challenging environments, and IIT's HYQ (Semini et al. 2011), these vehicles are very effective in accomplishing rescue operations, disaster management, and maintenance in situations, where any other means could be difficult to deploy, and human assistance could even be life-threatening. Battlefield, fire, flood, earthquake, and tsunami may unfold situations where these robots with remote human assistance could be highly effective for the initial restoration of the extensive damage and rescuing the trapped and endangered lives. Figure 1.13 depicts a laboratory-scale electrohydraulically operated serial-parallel manipulator in the form of a quadruped consisting of four legs and a torso. Each single-leg structure of the quadruped acts as a serial manipulator and has been shown

separately in the figure. The torso, or body, of the quadruped acts as a parallel manipulator, with four legs grounded.

While serial and parallel architectures find extensive use, it is evident that combined serial-parallel manipulators are often regarded as highly effective mechanisms for integration into modern industrial automation. This recognition extends across various industries, including manufacturing, process industries, aerospace, agriculture, mining, and medical science. These manipulators can accommodate the unique architectural limits of each manipulator since they were built using a combination of serial and parallel mechanisms in accordance with the tailored application's requirements. These manipulators have today gained widespread attention for application in mobile robotic systems, demonstrating their practical value.

### **1.3.2 Modelling Challenges for Different Manipulator Systems**

Robotic manipulators are being used for more and more tasks in modern automation industries. This calls for an advanced manipulator architecture that considers the specifics of each mechanism. Starting with serial and parallel mechanisms, more complicated and advanced kinematic structures that combine serial and parallel mechanisms are becoming more important in modern industries. However, system modeling of these kinematic structures during the development of the motion control systems is prone to several challenges and further complicates the control system's design. The design of the closed-loop control system for a robotic manipulator is thus considered to be the most challenging task and has become an open research problem in the field of robotics.

Despite the serial manipulator having several benefits, such as a large workspace and skilled maneuverability already stated above, it includes a number of links connected with joints in series to create a cantilever structure that is subject to bending under severe strain. (Patel et al. 2012). Moreover, the extra load on the system is caused by the actuator attached to each active joint of the architecture, which further causes the mass of the links to increase, making the system bulky. (Dasgupta & Mruthyunjaya 2000; Zhu et al. 2007). The overall dynamic behavior of the system, which is once again nonlinear in character, is greatly influenced by the presence of a significant amount of inertia. The system's linked nonlinear time-varying dynamics provide difficulties for manipulator dynamic modeling,

which is necessary for model-based controller design (Matilla et al. 2017; Delavari et al. 2010). Also, online computation time for solving model dynamic equations grows significantly for higher DOF manipulator systems and further increases computation complexity (Zhao et al. 2009).

The kinematics of all the kinematic structures of any manipulator, which map the relationship between joint space and workspace can be divided into two types: **inverse kinematics** and **forward kinematics**. For the motion control of robotic manipulators in real time, inverse kinematic modeling generates the actuation demand required to obtain the desired position of the end effector. Similarly, the forward kinematic model helps in predicting the end effector pose for specific actuation outputs. However, inverse kinematic modeling of redundant serial manipulators that possess a higher number of degrees of freedom (DOF) is quite complex, and its implementation in real time is also a challenging task (Ananthanarayanan & Ordóñez 2015). During construction of a redundant-type serial manipulator, the kinematic redundancy also adds complexity to the structural design. The manipulator, due to its structure, may also vibrate at a higher speed (Dasgupta & Mruthyunjaya 2000), which presents a challenge in system modeling for real-time control.

Other forms of closed-loop kinematic structures termed "parallel manipulators" also possess several advantages, including greater load carrying capacity, higher structural stiffness, higher operating speed, and low inertia of the moving parts, but at the cost of limited workspace, difficult mechanical design, a challenging forward kinematics problem, and a complex control algorithm (Matilla et al. 2017). The solution of the forward kinematic problem is the primary requirement for control purposes, motion plan design for the end effector, and also for calibration purposes. However, the forward kinematic model of a parallel manipulator is usually complex, forming a nonlinear set of complicated equations for pose variables that admit multiple solutions to the given problem, unlike the inverse kinematic model, which is normally very simple. The presence of unactuated passive joints, unlike serial manipulators, also brings complications when solving forward or direct kinematics problems during the elimination of passive joint variables (Patel et al. 2012). One of the most common challenges normally encountered during the modeling of a parallel manipulator involves the solving of complicated dynamic models for control purposes that involve solving forward kinematics by online solving of unknown dynamic parameters, which further increases the computational complexity of solving dynamic

models and reduces the potential benefits of the corresponding model (Bhattacharya, Hatwal, and Ghosh 1997; Abdellatif & Heimann 2005).

Another commonly encountered challenge experienced by both serial and parallel manipulators is termed as "singularity", which refers to a certain configuration of the manipulator where the motion of the end effector is blocked in a certain direction. During singularity at a specific orientation, a serial manipulator may have an unlimited number of solutions for its inverse kinematic position problem (Lai & Yang 1986). From a control perspective, this situation is important, as the robot's control is completely lost during this configuration. During singularity configuration, the serial manipulator may lose a single or multiple DOFs (Lai & Yang 1986; Gosselin & Angeles 1990; Dasgupta & Mruthyunjaya 2000).

Combined serial-parallel manipulators have the benefits of both serial and parallel mechanisms. They have a larger workspace than a parallel manipulator and better dynamic response and stiffness than a serial one (Kang et al. 2012). However, the modeling of this structure still involves complicated nonlinear forward kinematic equations with multiple solutions, in contrast to open and closed chain configurations. The kinematic and dynamic analysis are still challenging for this hybrid structure due to several constraints and singularities (Tanev 2000; Pisla et al. 2013).

Apart from all the challenges stated above for different manipulator configurations, the mode of actuation system also induces several other challenges, viz. different nonlinearities like friction, hysteresis, saturation with parametric uncertainties, which bring further challenges during overall system modeling (Matilla et al. 2017).

### **1.3.3 Mode of Actuators for Different Manipulator Systems**

Actuators supply motive power to drive the end effector of a robotic manipulator. The three modes of actuation systems, viz., electrical, pneumatic, and electrohydraulic, are commercially available on the market and are normally used to drive different manipulators, the corresponding use of which further depends on respective application areas. The most common form is by utilizing electrical power, which consists of a servo motor having low inertia and friction with high speed capability (Na et al. 2015). In the field of mobile robotics, several robots, viz. Honda's ASIMO (Sakagami, 2002), Sony's AIBO (Fujita and Kitano, 1998), and Little Dog (Kalakrishnan et al. 2011), where

electrically driven servo motors are used, The battery-driven motors with high gear-ratio reduction drives, though cheap and easy to use with high output torque and clean energy without detectable signatures and with dominantly linear characteristics, have poor back drivability due to increases in friction and mechanical impedance, which further complicate the dynamics of the system. Moreover, poor back drivability also reduces the maximum speed of the joints, with a further reduction in response time, poor controllability, and a loss in power due to friction (Na, Choi, & Kong 2015). The use of mechanical reduction gears (Byl & Tedrake 2009) is also susceptible to mechanical failure for high impact loading (Semini et al. 2011) or sudden torque reversal of high magnitude (Na, Choi & Kong 2015). The electrical drives have also limited operability after long durations of off-service battery recharging (Degrave et al. 2015). The thermal capacity of a servomotor is lower, and thus the operation of the motor is also limited by a rigid duty cycle or may be integrated with a forced air cooling system (Siciliano et al. 2016). There is also a possibility of sparks (Truong, Trinh, & Ahn 2019).

A pneumatic system is also used for developing robotic hands with artificial muscles and in mobile robotics. Pneumatic systems possess several advantages over electrical systems, including low cost, being less influenced by the environment, and being relatively safe in explosive environments (Siciliano & Khatib 2016) with quick response times (Truong, Trinh, & Ahn 2019). However, the use of pneumatic drive is limited due to difficulty in controlling the system in the presence of a high non-linear output force to contraction relation and large hysteresis (Caldwell, Medrano-Cerda, & Goodwin 1995) with intrinsic compliance (air compressibility) and a low power-to-weight ratio as compared to electrical and hydraulic actuation systems.

Electrohydraulic systems are another option to drive large electrohydraulic manipulators, which have found applications in harvesting (Papadopoulos, Bin, and Frenette 2003), mining (Cetinkunt et al. 2004), excavation (Feng et al. 2019; Zhang et al. 2019), and motion simulators (Gang et al. 2013). These systems are more compact than their electrical and pneumatic counterparts and can handle payloads much heavier than those tackled by electrical actuators. The fact that the system has a wider dynamic range, a high power-to-weight ratio, and is highly back-drivable arises from oil compressibility. The features of load handling capability along with better back-drivability compared to an electrical motor make electrohydraulic systems suitable for high-load applications, for instance in systems pertaining to manufacturing (Komsta, van Oijen, & Antoszkiewicz 2013), mobile

hydraulics (Yung, Vázquez, & Freidovich 2017; Semini et al. 2011), robotics (Koivumäki, Zhu, & Mattila 2019), and active suspension (Liu et al. 2020).

(Hunter, Hollerbach, and Ballantine 1992) note that electrohydraulic systems also exhibit a rapid time of response and precise controllability with a high bandwidth and a degree of inherent compliance. However, due to the presence of inherent hydraulic nonlinearities in the system, such as metered orifice flow, leakage flow, deadband in valves, cylinder friction, oil compressibility, etc. (Sarkar et al. 2013a, 2013b; Das et al. 2016), the modelling of electrohydraulic system becomes extremely difficult, as described in subsection 1.2.1, which further makes precision and faster tracking quite challenging, particularly for smaller manipulators, and can only be achieved by implementing an advanced controller, whose closed-loop design and stability analysis provide additional difficulties (Mattila et al. 2017).

#### **1.3.4 Motivations for Using Electrohydraulic Systems in Actuations of Manipulators**

The comparative study of different modes of actuation and their uses show that EHAS are best for manipulator systems that must deal with higher loads and torques. This is especially true for mobile (off-highway) machines like excavators, loaders, diggers, etc. that are used in construction, forestry, and mining. From the available literature survey, it is also evident that the emergence of more advanced EHAS driven robotic manipulators will reform these heavy industries in the near future. Articulated-structure mobile manipulators driven by EHAS are also proving their potential to handle a higher load with higher accuracy in motion. However, the presence of inherent nonlinearities in electrohydraulic systems associated with nonlinear complex dynamic behavior of multibody structures makes the controller design a challenging task, and moreover, the high precision motion demand can only be achieved with the use of an advanced controller that either considers both manipulator and actuator dynamic models or the individual dynamics of either actuator or the entire system in isolation, depending solely on the complexity of the system, computation time to solve the nonlinear dynamic equation and its complexity, the types of controller used, etc. Several research projects for the development of advanced and sophisticated controllers are still ongoing and can be considered an open problem statement in the field of electrohydraulically driven robotic research.

Another important and evolving need in present research is the improvement of energy efficiency in electrohydraulically driven mobile manipulators since the energy efficiency of conventional hydraulic systems with fixed-displacement pumps and standard relief valve pairs is very poor. Though for industrial stationary type manipulators, it is a secondary objective as compared to other design criteria, for mobile systems with onboard power sources, this efficiency term is very crucial. However, modern research exhibits that energy efficiency and control performance of robotic systems are reciprocal in nature and need to be optimized properly, as energy efficiency cannot be obtained at the cost of compromised control performance. Hence, achieving energy-efficient mobile hydraulic systems is again challenging and can be considered a crucial research domain.

The several advantages associated with the number of open challenges pertain to designing an energy-efficient electrohydraulic system while developing an advanced control algorithm to obtain precise controllability, which automatically led the researchers to choose this system as a primary driving unit for robotic manipulators.

### **1.3.5 Literature Survey on Control Strategies for Electrohydraulic Manipulators**

Many studies have used sophisticated controllers for straightforward single-degree-of-freedom systems with a single valve-cylinder pair, including sliding-mode controllers (SMC) (Gang et al. 2013), adaptive SMC (Dasmahapatra et al. 2015, 2018), and adaptive recurrent Hermite neural networks (Chaudhuri et al. 2020a). A greater number of valves are needed in manipulators for more sophisticated motion realization (Cetinkunt et al. 2004; Chaudhuri et al. 2020b; Cardozo & Weber 2017; Cai et al. 2021). In two previous investigations (Mohanty & Yao, 2011a & 2011b), only the arm of a three-cylinder serial manipulator was actuated, while the intermediate boom and tool-point stick remained unexcited. A PD controller with deadband compensation worked well in this situation with a 0.3Hz trapezoidal demand study. In another recent study with three actuation pairs in serial arrangement for the boom, the arm, and the bucket, actuations were only considered for the arm of a 23-ton excavator and the boom of a 6-ton excavator. (Feng et al. 2019; Zhang et al. 2019). One possible justification for activating only one among the multiple actuations in manipulators is the need to design controllers that allow for prior offline identification of most of its system parameters. Of course, a feedforward (FF) controller is a suitable choice in this regard (Sarkar et al. 2013a; Feng et al. 2019). However, due to the

difficulty in synchronizing many actuation pairs, only slowly fluctuating demands of up to 0.05Hz could be tracked well (Papadopoulos, Bin & Frenette 2003). In comparison to existing high-load applications, agricultural harvesting of tree branches of moderate to soft stiffness requires varying but much lower loads (Motokura et al. 2020). When branches remain less stiff, faster harvesting leads to better utilization of the installed power. By actuating all three cylinders in a serial manipulator, good tracking demand was only realized up to 0.1Hz for a moderate load of 475kg and the maximum displacement between 60 and 200mm (Koivumäki, Zhu & Mattila 2019).

One of the major limitations of implementing feedforward controllers in manipulators is their inability to handle multiple nonlinear issues like valve leakage and cylinder friction. In excavators, only friction compensations were offered by motion modeling of the cylinder (Feng et al. 2019), and only the discharge of a variable displacement pump was based on velocity demand, resulting in what was known as velocity feedforward. According to Zhang et al. (2019), the model-estimated delivery pump pressure was either implemented directly for pump control or through valve control (Li et al. 2019).

The feedforward technique is still inapplicable due to the challenge of building a flat model in a double-acting single-rod cylinder, or DASRC. However, these are far more abundant for their greater compactness than the double-rod type (Quan, Quan & Zhang 2014). Researchers used a block strict-feedback formulation with neural control (Guo & Chen 2021), back-stepping control (Guo, Zuo & Ding 2020), dynamic-surface control (Liu et al. 2020), and command-filtering control (Ye, Song & Ren 2020). A back-stepping controller necessitates the adjustment of numerous parameters. The dynamic-surface and command-filtering methods are sophisticated solutions to the parameter explosion issue. However, maintaining the parameters adjusted online within acceptable bounds produces new difficulties. A multi-aspect feedforward design for numerous actuators with DASRC could be a big step in this direction for utilizing the benefit of identifying FF parameters offline.

The ability of a controller architecture to reject disturbances that frequently cannot be modelled to make them amenable to FF compensation is another crucial aspect. Adding a simple PID controller to the feedback path with the FF structure is an alternative, of course, at the level of first evaluation. The formulation for adding the FF controller in an inverse manner for the estimation of the control command from the demand for the response (Astrom & Hagglund 2006) gives rise to an associated model of a linearized error dynamics that could provide the basis for implementing the PID controller. In reality, the PID



controller's implementation for linearized dynamics enables the computation of PID gains based on a fundamental stability analysis that is not dependent on a specific individual. However, the final setting of these gains in a PID-alone controller for a nonlinear system, on the other hand, depends on the user's expertise gained through experimenting with various settings. The backing of a fundamental analysis provides the PID part of the FFPID structure with a higher capability of disturbance rejection since a relatively low error following the FF compensation is handled in the FFPID setting in comparison to the uncompensated situation in the case of the PID-alone strategy (Sun et al. 2016; Sun & You 2021).

With the aging of valves and cylinders, the leakage through narrow clearances between the sliding surfaces increases. Good tracking with an older valve would require additional compensation to take care of the increased leakage through clearance passages within the valve handling very high pressure. Valve replacement would be required past a certain point. By using time-to-time identification trials, appropriate decisions may be made while updating feedforward parameter values. The observed deviation from the baseline values in a feedforward model handling multiple issues, including valve and cylinder leakages, could determine whether a component still remains fault-tolerant or not. This condition monitoring approach would indeed be more powerful than the recently proposed observer-based approach of detecting only valve leakage (Dao et al. 2021). Recently proposed constructions of data-driven feedforward controllers (Sun & You 2021; Djordjevic et al. 2022; Jiang et al. 2022) would be fault-tolerant but incapable of such condition monitoring.

## **1.4 Motivation of the Present Work**

It is quite apparent from the literature survey given in sections 1.1, 1.2, and 1.3 regarding the development of EHAS control and its corresponding application in robotic manipulators that a number of research works, both at the theoretical and experimental level, are already available. However, certain research gaps associated with electrohydraulically operated robotic manipulators, and their control can still be identified from the available literature study and may be properly addressed. A brief description of these research gaps is given below.

- I.* Already in section 1.2.2, it has been detailed that rugged proportional valve actuator pairs have been mostly preferred in electrohydraulic industries in recent decades for

their low cost and uninterrupted use compared to their sophisticated servo-grade counterparts, which can further enhance performance up to high precision levels with the aid of advanced controller design. Advanced controller design in order to extract servo-grade performance from a rugged valve-actuator pair is still considered an open research problem in the field of electrohydraulics.

2. From the available literature on feedforward controller design for electrohydraulic systems, it is clear that most of the study exploited a differentially flat system model to compensate for the known disturbances and nonlinear effects by using the standard system model of double-acting double-rod cylinders. However, development of the controller for double-acting single-rod cylinders, that has been widely used for their compactness, still remains a challenge due to the presence of asymmetric piston areas on each side of the hydraulic cylinder, causing a loss of flatness property. Though, some literature has considered an incompressible flow model with no valve leakage, constant pump pressure, and cylinder friction as a small part of an external load disturbance that may be neglected and is associated with a symmetric actuator configuration for the design of a feedforward controller. However, compensation of all the nonlinear effects in a single framework of feedforward controller design is still considered as a challenge.
3. Based on the available literature survey, it is also evident that incorporating variable pump flow as per the requirement of actuation demand in the feedforward controller design to obtain an energy-efficient electrohydraulic system is available at the cost of not considering several nonlinear effects, viz., compressibility and friction, which implies energy efficiency at the cost of non-optimal use of control performance.
4. The consideration of several nonlinear effects to account for the strong nonlinear feature of the electrohydraulic system in order to obtain good tracking performance of the output motion necessitates estimation of the unknown parameters associated with different nonlinear mathematical models, also known as system identification. Proper estimation of these parameters is required to obtain the control signal to excite the proportional valve. Several strategies have been used to find these parameters, either online with the use of additional flow and pressure sensors, by online parameter adaptation within reasonable bound or offline using appropriate optimization techniques. However, in order to achieve the optimized values of the

unknown parameters required to run the feedforward controller efficiently, a precise methodology in this regard must yet be investigated.

5. Implementation of electrohydraulic control in motion manipulators to obtain multi-DOF motion is challenging due to the presence of several nonlinearities in the hydraulic system associated with the nonlinear, complex multibody dynamics of the manipulator. Most of the available literature shows state-of-the-art research on servo motor-driven manipulators and their performance. However, research on electrohydraulically driven motion manipulators is extremely limited, and those available in open literature pertain to the low speed of response for end-effector motion. Despite the use of an advanced feedforward-PID or FFPID controller, achieving faster tracking still remains a challenge in the context of manipulators driven by EHAS.
6. The consideration of various nonlinearities, such as friction, compressibility, leakage, and so on, complicates the system modelling further, and the order of the system also increases, posing another challenge to obtaining a stability analysis of the closed-loop controller along with its design. The review of the literature reveals that there has been little research in the subject of stability-guaranteed controller design for EHAS when working with higher-order systems and multi-DOF robotic manipulators.

The open challenges in the field of EHAS and its control, associated with its limited real-time implementation in manipulators, motivate the present thesis work to address these primary issues in order to make a meaningful contribution in the domain of electrohydraulically actuated robotic manipulators.

## **1.5 Objectives of the Present Work**

Given the existing status of research in the field of electrohydraulically driven robotic manipulator systems and their control, detailed in the earlier sections, the overall objective of the present work has been set to design and implement a feedforward motion controller coupled with a PID-feedback in real time for the actuation of multi-DOF robotic manipulators, viz., serial, and serial-parallel types driven by EHAS. The goal of the present work also involves bridging the identified research gaps for EHAS driven manipulator design and its control obtained from different literature surveys given in sections 1.1, 1.2,

and 1.3 and precisely elaborated in section 1.4. However, the overall objective of the present work further involves individual tasks to be performed in order to meet the end goal.

To meet the overall objective of the present work, however, it is possible to design a feedforward controller algorithm capable of handling multiple nonlinearities and should be distinct from existing algorithms. The performance of the designed controller should be tested in real-time with PI feedback through rigorous experimental analysis, and it can be compared with performance of some existing feedforward controllers that must be designed separately for validation purpose. Additionally, the efficacy of the designed controller should be compared to that of some other sophisticated nonlinear controllers. For the purpose of validation of the proposed controller in real-time, a single DOF electrohydraulic system as a hardware that is simple in construction with large application areas can be chosen. Based on the performance of the designed controller, the feedforward controller should be selected and further extended to implement from a single to a multi-DOF electrohydraulic serial motion manipulator system for the realization of a more complex high-speed motion demand of its end effector in a two-dimensional plane suitable for fast and futuristic practical real-world applications.

The successful implementation of the designed feedforward controller coupled with PID feedback over an electrohydraulic serial manipulator provides the confidence to employ the controller over the entire electrohydraulic serial-parallel manipulator system in the form of a four-legged robot with twelve servo-proportional valve and cylinder pairs to achieve both serial and parallel actuation in real time.

## **1.6 Contributions of the Present Work**

Based on the end objectives stated in the previous section, a novel feedforward controller has been designed and proposed to be implemented in real time in the present work for an electrohydraulically driven robotic manipulator system with a higher number of degrees of freedom. The major contributions of the present thesis work are described below.

- 1.* Design and development of a generalized version of feedforward position controller as opposed to conventional approach. Two different approach of design algorithm have been studied in the present work: a conventional and a novel order separation approach that can be used in a wide range of applications for compressible and

incompressible flow, fixed-displacement and variable-displacement modes of pump operation, and proportional and servo-proportional valves connected to single-rod and double-rod double-acting cylinders. However, the approach of conventional design is further based on several restrictive features.

The controllers' feedforward and feedback parameters were identified offline using a simulation-guided GA optimization strategy, as opposed to the prior approach based on online trials that used additional sensors just for system identification.

The PI gain selection coupled with feedforward controllers in the feedback path is based on a rigorous stability analysis for linearized error dynamics with time varying coefficients by extending Routh criteria for a time-variant system.

Real-time implementation of designed controllers in a single-cylinder electrohydraulic test bench with energy efficient pump operation for testing the acceptability of the novel OSFFPI controller against CFFPI and also for validation of both the designed controller with classical PI only and against an existing nonlinear adaptive sliding-mode integral, or ASMIC, controller by conducting rigorous experimental analysis.

2. The acceptable and validated design of the novel OSFF controller in its modified version is combined with PID feedback to form OSFFPID and implemented in real time for a serial manipulator in the form of a single leg of a quadruped and a combined serial-parallel manipulator in the form of a four-legged structure with a torso that has multiple degrees of freedom (DOF) to meet a more complex high-speed motion demand in a two-dimensional plane suitable for real-life applications.

The novelty of the proposed formulation for robotic manipulators lies in handling multiple nonlinearities in a single framework with general applicability for different cylinders and consideration of translational dynamics for the feedforward formulation of the lower piston relative to that of the cylinder. The feedforward parameters and PID gain estimation have been done using a GA-based optimization technique. The effects of several assumptions that were not considered while formulating the controller have been validated numerically, and the stability analysis shows that the effect of D gain is a necessary part of the manipulator system's inertial terms that were not considered.

Precise and smoother tracking performance in real time up to 1.0 Hz, higher than existing manipulators, has been achieved for serial manipulators at the expense of lower control energy, where the application corresponds to agricultural harvesting.

3. The proposed formulation in real time has been applied to a serial-parallel manipulator system for the realization of platform or torso heaving on four grounded legs for the adjustment of platform height corresponding to the impending stride of a quadruped and also for the realization of a model static walk motion plan. All these real time studies thus form the basis for setting up a testing protocol and initializing the legs of a quadruped robot prior to executing a specific gait.

## **1.7 Organization of the Thesis**

Chapter 2 of the thesis gives a detailed description of the different modules of the laboratory-scale electrohydraulic setup where all of the experiments for the present work were done. This includes everything from a single-cylinder test bench to more complex manipulator architectures with single to complex multi-dimensional motion and their corresponding flow, pressure, and dynamic modeling for the development of the proposed feedforward model, which is considered to be the main contribution of the present work.

Chapter 3 describes the design and development of the feedforward controller, considered to be the core building block of the entire thesis, and its real-time implementation over a one-dimensional motion control system. Mainly, the corresponding chapter focuses on two design algorithms for the development and testing of the feedforward controller, viz., the conventional approach and the novel order separation approach. The consequent conventional model has been used to test the acceptability of the latter one. The selection of the designed controllers is based on the design algorithm, design considerations, and finally, the real-time experimental results, with considerations of several non-linearities addressed during the two designs and by including PI feedback with both the designed controllers formulated to take care of the modeling uncertainties and approximations. The PI gain selection has been done by a rigorous stability analysis of the linearized error equation by extending Routh criteria to a time-variant system involving the offline estimates of the GA-optimized system and feedforward parameters. Chapter 2 further disseminates the performance of the proposed controller with two existing established

controllers, viz., classical PI and a nonlinear adaptive sliding-mode integral controller, or ASMIC.

By increasing the demanded motion frequency from or below 0.1Hz in the existing studies to 1.0Hz, the newly designed feedforward controller based on novel order separation approach has been further implemented to a serial manipulator in form of a single leg of a walking quadruped in order to realize complex motion demand of its free point in two dimensional plane suitable for agricultural harvesting. These topics are covered in Chapter 4, which also provides a thorough description of the feedforward controller and PID's real-time implementation. The trials unambiguously demonstrate the suggested FFPID controller's advantages over a traditional PID-only controller in terms of better tracking and energy used. The function of the designed feedforward controller in terms of disturbance and instability rejection is also discussed in this chapter. The methodology of manipulator design with the use of feedforward formulation is also described in Chapter 4.

A further effort has been made to implement the feedforward controller in real-time for the entire serial-parallel configuration in the form of a four-legged walking robot to realise both serial-parallel combined actuation after the feedforward controller was successfully implemented on the serial manipulator. Demand has been made for the grounded quadruped to move its body and one foot tip forward in order to realise both serial and parallel actuation. Additionally, the body has provided a vertical reciprocating motion, termed as a heave motion, at a frequency of 0.1 and 0.2Hz, respectively, to realise the parallel actuation solely. With the aid of various sorts of demands taken into consideration in this chapter, Chapter 5 discusses the real-time implementation of the developed controller for this configuration and also illustrates the performance in comparison to a traditional PID-only controller.

The key findings are summarised in Chapter 6 with the real-time performances of the created controllers. The work's future scope has also been described here.









# CHAPTER 2

## System Description and Modeling

### 2.1 Introduction

**Electrohydraulic** actuation systems or (**EHAS**) are very popular for a wide range of rugged to sophisticated applications requiring high force or torque. Merritt (1967) pointed out the main features of these systems as high-power density and fast response that led to their applications in most modern industries for high precision motion and force controls. However, these systems have several nonlinear features that pose significant challenge to the controller design. (Eryilmaz et al. 1999) considered the aspect of nonlinearities associated with oil compressibility and oil leakage through control valves. Besides the oil leakage, (Hu et al. 2011; Na et.al. 2011) dealt with the effect of valve deadband, the range within which the actuation response remains sluggish. (Sha et al. 2002) provided compensation for the static and dynamic friction in the cylinder in their real-time motion-control experiments. The primary focus of the present work is to design and implement position controllers with a dominant feedforward part for compensating all these nonlinear effects. Several configurations with increasing complexities have been considered in the present study.

The first configuration considered is an existing **single-cylinder electrohydraulic test bench**, commissioned by (Sarkar et al. 2013a & b). An energy-saving hydraulic system has been utilized during the experiments. These experiments resemble the controlled working of many land-based stationary equipment. Fabrication of a motion-control setup has been undertaken during the course of the present study that has been utilized first as a **serial manipulator** and then as a **serial-parallel manipulator** with multiple degrees of freedom (**DOF**). Eventually, the setup would be upgraded to realize an autonomous walking quadruped as a group activity. A welcome feature for such mobile systems is low weight

for achieving longer uninterrupted operation. These systems are described in Sections 2.2 to 2.4.

From the viewpoint of controller development, the prime objective has been set as developing a suitable feedforward model for tackling the nonlinear motion dynamics at the system output emerging from its interaction with the valve flow. The major components of an existing single-cylinder electrohydraulic test bench are a proportional valve **PV** and an industry grade cylinder **C**. These components are cheaper in comparison to a servoproportional valve **SPV** used in pair with a low-friction cylinder in each of the actuation systems of the serial and serial-parallel manipulators. Despite the higher valve deadband and higher friction between the piston and the cylinder, these cheaper components are rugged providing long duration uninterrupted service without maintenance. For many mobile systems, this ruggedness is indeed a welcome feature.

The common nonlinear features of comparable level for both the cheaper and more sophisticated actuation systems are the square root pressure-discharge relation at the metered valve ports and oil compressibility. Of course, oil leakage in an **SPV** is higher than that in a **PV**. In a low-friction cylinder, higher valve leakage could result in alternate mode of motion dynamics of the piston that is unlikely in case of an industry-grade cylinder. The differences between an existing old system and a new system under realization leads to certain differences in their actuation system modeling. While the axial-piston pump in the old system has a passive hydro-mechanical pressure compensator capable of adjusting the flow according to the actuation requirement, the new system has a fixed-displacement gear pump of constant discharge.

The actuation models form the backbone for tackling the system nonlinearities by estimating a feedforward compensation corresponding to any stated output demand. Two different approaches have been taken. In the conventional mode of estimating a consolidated compensation for all the nonlinearities, the contribution of the present study involves the estimation in case a double-acting single-rod cylinder working at high pressure warranting the oil-flow treatment as compressible. Next, a novel order-separated approach of estimating multiple feedforward components has been developed so that it renders it the ability of diagnosing the location of any emerging fault. The two approaches have been compared in the single-cylinder workbench introduced. Section 2.5 pertains to the actuation modeling of this test bench corresponding to the two feedforward estimation approaches. In Section 2.6, the actuation models corresponding to the single test bench has been

extended in modelling of a serial manipulator driven by a pair of independent actuation systems.

In the single-cylinder test bench, the system output motion and load are identical to those at the output of the individual cylinders. However, the outputs at the task space of the manipulator are linked with the outputs of the two driving cylinders by suitable kinematic and dynamic models. The formulation of these kinematic and dynamic models that are discussed in Sections 2.7 and 2.8. Section 2.9 provides the closure of the overall modeling.

## 2.2 System Description of Single Cylinder Test Bench

In Figure 2.1, the single-cylinder test bench is shown, on which the present work has been carried out. Table 2.1 details the specification of the components. The overall setup was essentially realized by (Sarkar et al. 2013a & b). It has a **hydraulic power pack**, an **actuation system** involving an industry-grade double acting single-rod cylinder **C** and proportional valve **PV** apart from a **data acquisition and control system**.

### 2.2.1 Hydraulic Power Pack

A hydraulic power pack is the heart of the electrohydraulic actuation system **EHAS**. The existing setup has a variable-displacement axial-piston pump **P** driven by a 3-phase induction motor **M**. The pump sucks oil from a tank **T** through a filter **F** and supplies it to the system through a check valve **CV** installed at the pump outlet. This makes the pump flow unidirectional. The pump can either be operated in fixed or in variable displacement mode. In order to vary the volumetric displacement of the pump, the pump has a passive pressure-compensating arrangement. The conventional mode of fixed displacement type pump operation with relief valve **RV** setting provides very poor energy efficiency of the system. Though the **RV** ensures constant pump pressure at the highest value that the system needs, the pump discharge in excess of the actuation requirement is drained to the tank through the **RV** at the highest pressure required for the actuation. Thus, a loss of power arises that translates to substantial wastage of energy in systems requiring intermittent actuation, say by the electrohydraulic steering system of a car during its turning.

A variable mode of pump operation makes an energy efficient **EHAS**. The pressure compensator of such a pump adjusts the pump displacement to the level necessary for the actuation during its active period. Over the durations without any actuation requirement,

the delivery pressure rises to a high cut-off level and the pump displacement gets adjusted to meet only the internal flow through the pump necessary for lubricating its different parts. Between the higher cut-off and lower cut-in levels of the pressure, the displacement of the pump varies and below the cut-in level, nearly a constant discharge is maintained. A pressure relief valve **RV** is installed between pump outlet and the check valve **CV** for preventing accidental over-pressurization of the system. The **RV** pressure setting is kept well above the operating pressure zone. Clearly, this variable mode of pump operation makes the overall system energy efficient. At the outlet of the pump, there is a pressure transducer **PT** and a flowmeter **FM** to record the pump pressure and flow, respectively.

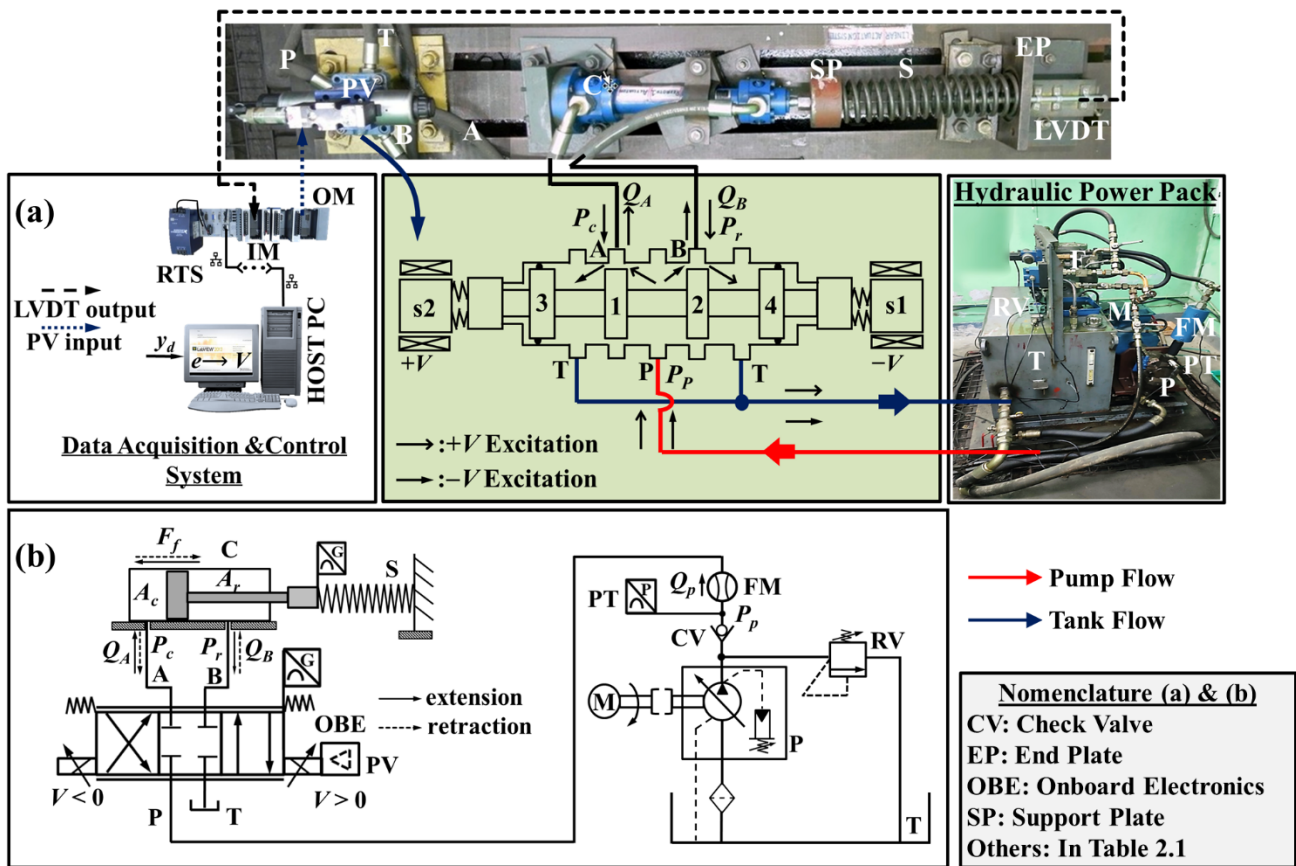


**Figure 2.1: Experimental setup for electrohydraulically actuated linear-motion study in (a) photographic view and (b) circuit diagram**

**Table 2.1 Component specifications of Single-Cylinder Test Bench**

Component	Make	Specifications
<b>Proportional valve PV</b>	Rexroth	4WREE 10 E50-23/G24K31/A1V
<b>Single-rod cylinder C</b>	Rexroth	Bore 40mm and rod 20mm in diameter, piston mass 2.5kg
<b>Variable-displacement pump P</b>	Rexroth	A10VSO 45DR/31; $4.5 \times 10^{-5} \text{m}^3$ nominal displacement; maximum discharge $8.3 \times 10^{-4} \text{m}^3 \text{s}^{-1}$
<b>Flowmeter FM</b>	Kral	Working pr. $0-2.5 \times 10^7$ Pa; flow $2-1.7 \times 10^{-3} \text{m}^3 \text{s}^{-1}$ ; maximum temp $120^\circ \text{C}$ ; accuracy $\pm 0.1\%$
<b>Input Module IM</b>	NI Systems	NI 9215 (4 Channel; $\pm 10$ V A/D, 16-bit simultaneous analog input)
<b>Linear variable differential transformer LVDT</b>	HBM	Plunger type; 0-0.200m range with 0.5-10V analog output; Nominal Sensitivity: 80mV/V
<b>Motor M</b>	ABB	3GBA201044-ADEIN; 3-phase; 2 pole: 37kW; 2945rpm
<b>Oil tank T</b>	Local	Dim.-1.0m x 0.6m x 0.5m; capacity-200L
<b>Output module OM</b>	NI Systems	NI 9263 ( $\pm 10$ V D/A, 16-bit simultaneous analog output)
<b>Pressure Relief valve RV</b>	Yuken	EBG-03-H-11; $2.05 \times 10^7$ Pa
<b>Pressure Transducer PT</b>	Kistler	$0-2 \times 10^7$ Pa; temp: $-20$ to $85^\circ \text{C}$ ; linearity, hysteresis, and repeatability $\pm 0.25\%$
<b>Real-time system RTS</b>	NI Systems	1GHz, 32-bit NI-cRIO 9081, Sampling rate-100 KS/s
<b>Spring S</b>	Local	Stiffness $20 \text{ kNm}^{-1}$

### 2.2.2 Actuation System

With reference to Figure 2.1 and 2.2, the actuation system of the single-cylinder test bench is described. It has a proportional valve **PV** and a double-acting single-rod cylinder **C**. The valve controls the flow of pressurized oil supplied by the pump **P** for actuation purpose. Inside **C**, the piston divides the hollow cylinder into two chambers that could be at different pressures depending on the external load and the valve opening. The chambers corresponding to the piston side and the rod side end are referred as the cap-end chamber and the rod-end chamber, respectively. The corresponding areas of the chambers are shown in Figure 2.2 as  $A_c$  and  $A_r$ , respectively. The loading of the piston-rod by a compression spring **S** is evident from Figure 2.1. On a horizontal test bed, the cylinder **C** is clamped with its piston rod in line with the spring **S** and the rod of a linear variable differential

transformer **LVDT** that measures the piston displacement  $y(t)$ . The rods of the piston and the **LVDT** are screwed by a fastener in the end plate **EP**. For a displacement of the piston, the piston rod, **LVDT** and the **EP** move in unison. The spring **S** is supported between the floating **EP** and a stationary support plate **SP**, which is mounted rigidly to the base of the bench. Hence a movement of the piston causes a corresponding deflection of the spring.

The flow connectivity in the setup is highlighted in Figure 2.2. Of course, the **PV** is used to direct the flow from the pump to the cylinder for the motion of the piston in a definite direction. In the valve, there are four ports **P**, **T**, **A** and **B** – connected externally to the lines from the pump to the tank, with the cap-end chamber and with the rod-end chamber, respectively. While ports **A** and **B** are metered having rectangular cross-sections, the ports **P** and the **T** ports are unmetered.

The proportional valves are generally solenoid operated, driven by either voltage or current. In this set up the solenoid of the **PV** is voltage driven. In Figure 2.1, the valve is represented schematically. A solenoid integrated at each end the valve spool is represented schematically in both Figs. 2.1 and 2.2 by a small rectangle containing a slant line cut by an arrow of opposite slant across the box. The valve spool can slide coaxially, depending on the status of the solenoid excitation. When the solenoid of the **PV** is energized by a voltage  $V$ , an electromagnetic force acts on the armature-spool assembly, causing it to move.

Under the excitation voltage  $V > 0$ , the spool moves towards left and the pressurized oil from the pump port **P** enters the cap end side of the **C** through port **A**. Consequently, the piston of **C** extends to the right and low-pressure oil from the rod-end chamber enters the **PV** through port **B** and returns to the tank through port **T**. Similarly, for negative voltage  $V < 0$  the spool moves in the rightward direction and the fluid path of **P-B-A-T** is responsible for the retraction motion of the piston assembly.

In this set up, the spring is mounted in a manner so that the piston at the most retracted position keeps the spring nominally pre-compressed. At any extended position with respect to it, the compression load applied by the spring **S** on the piston rod increases. In other words, this load  $F_{sp}$  is a variable load proportional to the net spring compression comprised of the spring pre-compression and displacement  $y$  of the piston. The spring considered here is a linear one with a known stiffness of  $20 \text{ kNm}^{-1}$ .



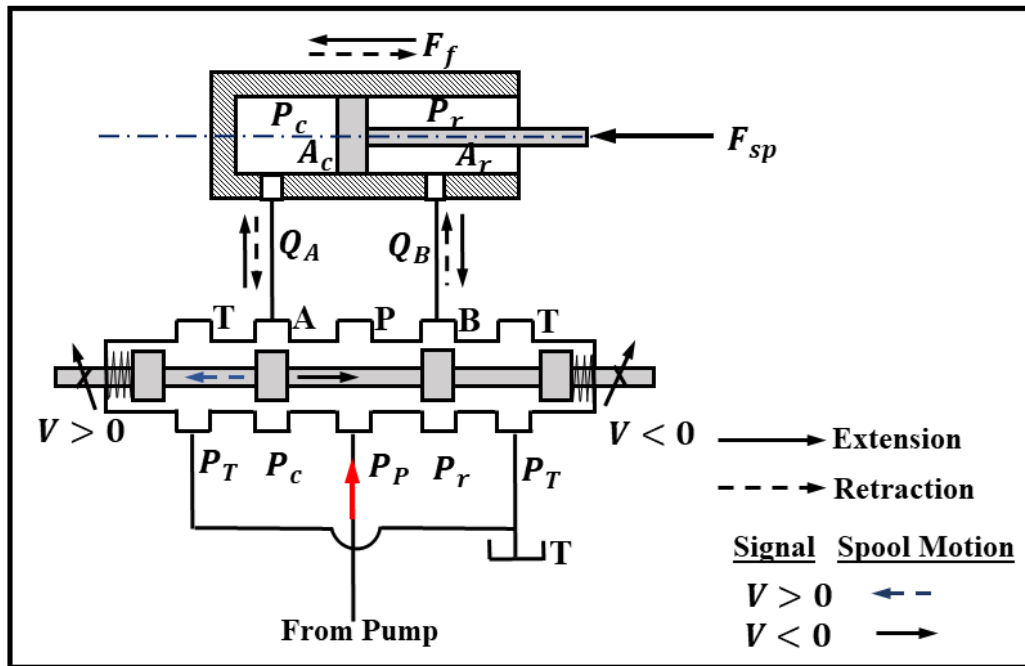


**Figure 2.2: EHAS with a double-acting single-rod cylinder and electrohydraulic valve**

The pump supplies pressurized oil at a rate of  $Q_p$  to the valve-cylinder combination. Ignoring any transmission loss in the lines and at the unmetered ports **P** and **T** with respect to the large losses in the metered ports **A** and **B**, the pressure is taken as constant at  $P_p$  from the outlet of the pump up to the connected chamber of the **PV** through the port **P**. Similarly, the pressure from the valve chamber up to the connected tank is another constant  $P_T$ . For an open tank, the tank pressure is set as zero-gauge pressure. Due to the significant pressure drops at the two metered ports **A** and **B**, which act as sharp-edged orifices, the pressure and flow to or from the cap-end chamber are set as  $P_c$  and  $Q_A$  respectively, while those at the rod-end chamber as  $P_r$  and  $Q_B$  respectively. Due to these pressures at the cylinder chambers, a net thrust acts on the piston resulting in its extension or retraction. In turn, the spring compression increases or decreases.

During both extension and retraction stroke of the piston, the spring remains engaged within the end-plate cup at one end. At the other end, the spring rests on the front face of a support plate **SP** that is rigidly mounted on the test bench, as shown in the Figure 2.1, through a central hole in the **SP**, the **LVDT** rod enters the **LVDT** body from the front side. The front and bottom of the **LVDT** body are respectively supported at the back side of the **SP**, clamped to the test bed. Hence the end plate, the **LVDT** rod and the piston can move as a single unit.

### 2.2.3 Data Acquisition and Control System

It has been already mentioned during elaboration of Figure 2.1 that the instantaneous position of the piston  $y(t)$  is measured with the position transducer **LVDT**. The pressure transducer **PT** and flow meter **FM** at the pump delivery line that measure the pump pressure  $P_p$  and discharge  $Q_p$  respectively. From these analog sensors, the voltage signals are sampled in real time by the input module **IM** of the real-time system **RTS**. Of course, the **IM** contains corresponding analog-to-digital (A/D) converters and signal conditioners. The **RTS** is connected with **HOST PC** through an ethernet cable. In the **PC**, the control algorithms are executed in a software platform to generate the control signal. This control signal is then passed to the integrated control electronics **ICE** card via a digital-to- analog (D/A) converter at the output module **OM** of the **RTS**. The **ICE**, based on the control signal generates the voltage signal, within the hardware range of  $\pm V_{\max}$  with  $V_{\max}$  equal to 10V, which is used to drive the solenoid of the **PV**.

## 2.3 Serial Manipulator Test Bench

With reference to Figure 2.3, the 2-DOF serial electrohydraulic manipulator structure used for the experimental study has been described here. The term serial is used by considering the loop formed involving each electrohydraulic linear actuator joining two members across it by a passive pin joint by taking it as an equivalent system of the two members joined by a rotary actuator instead of the pin joint. A parallel arrangement of four such manipulators would eventually be used for quadruped walking. While Table 2.2 lists the major constructional details, Table 2.3 provides the component specifications, which are depicted in Figure 2.4 symbolically. Figure 2.4 also shows the significant internal features of a valve used in each of the two actuation systems of the manipulator.

In Figure 2.3 (a) and (b), the manipulator pose is shown at two different instants. The initial pose at time  $t$  equal to 0 is shown in greater detail in Figure 2.3(a) and by dashed lines in Figure 2.3(b). In both the figures, the continuous line indicates the pose at a time  $t > 0$ . With reference to a fixed coordinate system  $(x, z)$  attached to an anchor point  $a(0,0)$ , the output positions of the free end of the manipulator are shown as  $f(x_f, z_f)$  at time  $t$  moving from an initial point  $f_0(x_{f0}, z_{f0})$  at  $t = 0$ . The subscript 0 corresponds to coordinates at the initial time. The anchor and the suspending point  $h(x_h, z_h)$  of the manipulator remain stationary. At the point  $k(x_k, z_k)$ , the lower and upper members of the manipulator are

joined by a horizontal pin with axis orthogonal to the  $xz$  plane. With respect to the vertical direction  $z$  at  $k$ , the lower and upper members make acute angles  $\alpha$  and  $\beta$  respectively.

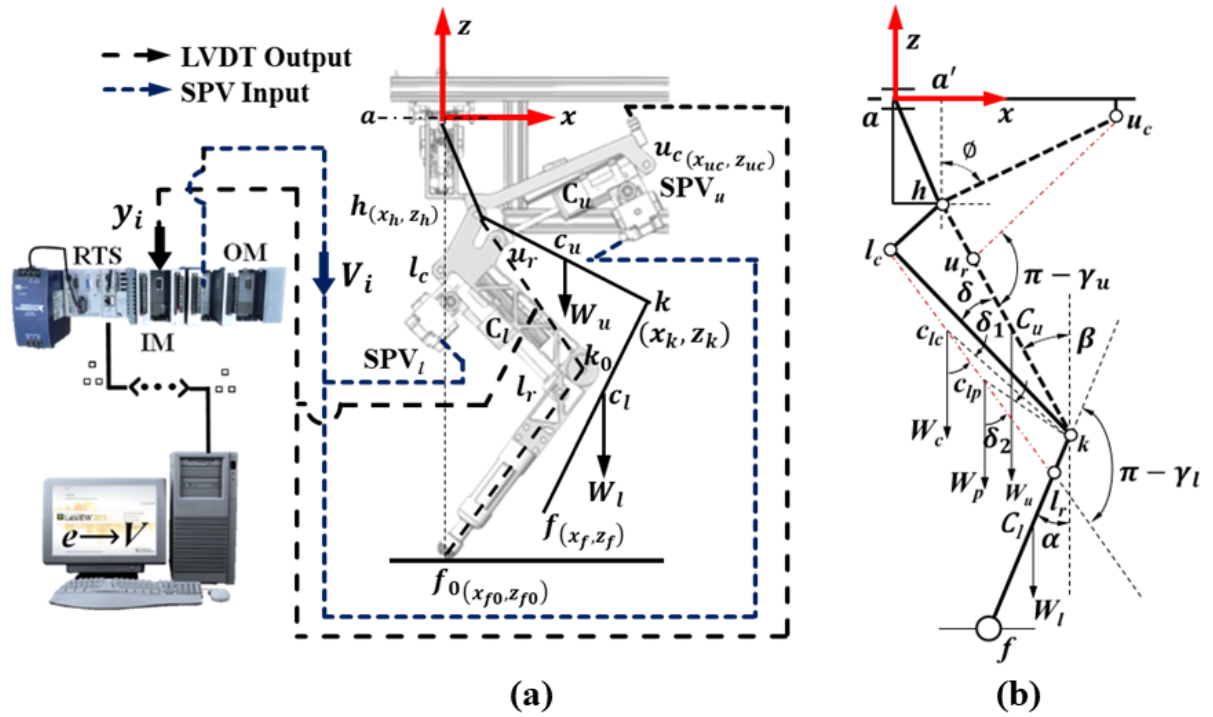


Figure 2.3: Schematic of experimental setup of a serial manipulator

Table 2.2: Lengths in mm, weights in N and angles in  $^\circ$  for Manipulator Components

$\overline{hk}$	$\overline{kf}$	$\overline{hl}_c$	$\overline{hu}_c$	$\overline{hu}_r$	$\overline{kl}_c$	$\overline{kl}_r$	$(x_h: \overline{aa'}, z_h)$	$\overline{a'u}_c$	$\overline{l_c l_r} _c$
350	470	125	330	60	320	60	(65,175)	212	280
$\overline{l_c c_{lc}}$	$\overline{l_r c_{lp}}$	$\overline{kc}_l$	$\overline{hc}_u$	$W_c$	$W_l$	$W_u$	$W_p$	$\alpha_0$	$\beta_0$
114	185	134	157	3.6	2.5	2.4	0.4	26.6	37

Besides the **hydraulic power pack** with a marking **P** for the pump and **M** for the motor, Figure 2.4 shows an **actuation system** with the components bearing a general subscript  $i$ , which are related by  $l$  for the lower system and  $u$  for the upper system in Figure 2.3. The **data acquisition system** for all three test benches remains the system. Only the number of channels differ corresponding to the number of actuation systems used in each. In the next subsections, these **modules** are detailed. The differences of these modules with those in the single-cylinder test bench are also indicated.

**Table 2.3 Component specifications of Manipulators Power Pack**

Component	Make	Specifications
Filter F	Stauff	Maximum working pressure $4.2 \times 10^7$ Pa
Fixed-displacement pump P	Dowty	Series P3146, $10^{-3} \text{m}^3/\text{s}$ at 1500rpm, max continuous pressure 17.7MPa
Input Module IM	NI Systems	$\pm 10$ VA/D, 9215 module, Sampling rate 100KS/s
Linear variable differential transformer LVDT	Gefran	Stroke 0.2m; resolution $\pm 5 \times 10^{-6}$ m
Motor M	ABB	3-phase; 30kW; 1470rpm
Oil tank T	Local	Capacity $0.2 \text{m}^3$
Output module OM	NI Systems	$\pm 10$ V D/A, 9263 module, Sampling rate-100KS/s
Pressure Relief valve RV	Rexroth	DBW10 A2-5X/315 6E W230 N9K4; $3.5 \times 10^7$ Pa
Real-time system RTS	NI Systems	1GHz, 32-bit NI-cRIO 9076, Sampling rate 100KS/s
Servo-proportional valve PV	EATON	SM4-10(10)38-20/200-10, mass 6.5kg
Single-rod cylinder C	EATON	Bore 25mm and rod 12mm in diameter, stroke 60mm, 2.5kg

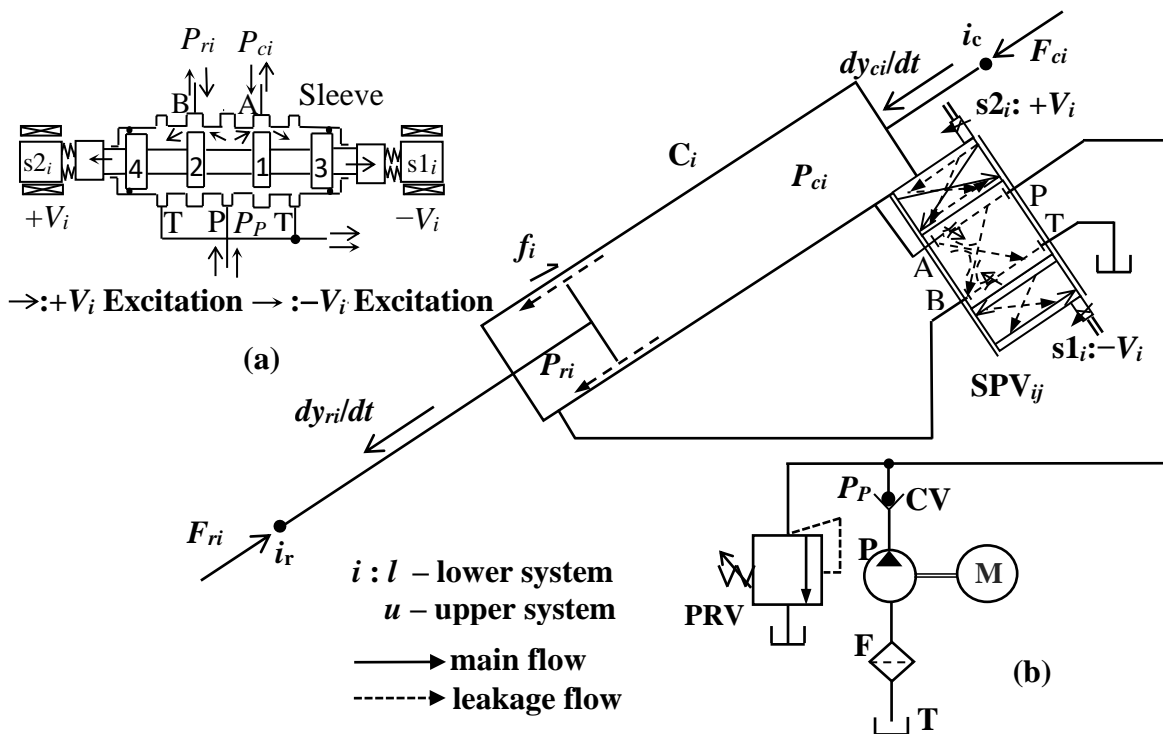


**Figure 2.4: Schematic of (a) valve details and (b) its role in electrohydraulic circuit for serial manipulator**

### 2.3.1 Hydraulic Power Pack

The hydraulic power pack used for the manipulator has a common fixed displacement type gear pump **P** of 60lpm capacity, driven by an induction motor **M**. The pump draws oil from a hydraulic tank **T** through the filter **F** to supply the flow through a check valve **CV** to two servo-proportional valves **SPV<sub>u</sub>** and **SPV<sub>l</sub>** which are connected to the upper and lower cylinders – **C<sub>u</sub>** and **C<sub>l</sub>** respectively. A relief valve **RV** is installed at the pump outlet which maintains a nearly constant pressure at the pump delivery when the total flow to both the cylinders is less than the pump flow. The **RV** is essential to protect the system from over-pressurization.

### 2.3.2 Actuation Systems

Each of the two actuation pairs of the serial manipulator has a servoproportional valve paired with a single-rod double-acting hydraulic cylinder. Such a valve resembles a servovalve for having nearly zero lap in the unexcited neutral or null state and relatively wider radial clearance like a proportional valve. A proportional valve remains sluggish within its deadband range of excitation. However, the near-zero valve lap renders a servoproportional valve the potential to perform as fast as a servovalve over the entire range of excitation. Of course, the combination of the lap and radial clearance respectively one-order lower and higher than a proportional valve makes the null leakage in a servoproportional the highest. Hence, for achieving performance closely matching a servovalve, adequate compensation in the form of additional voltage might be necessary for a servoproportional valve. Such compensation in a good controller should be significantly lower than the deadband range of a corresponding proportional valve. The cylinders of the system have low-friction seals allowing good lubrication even for a low relative speed of the piston. The hydraulic cylinder-valve pairs for the upper and lower systems are labelled in Figure 2.3 as **C<sub>u</sub> – SPV<sub>u</sub>** and **C<sub>l</sub> – SPV<sub>l</sub>** respectively

In Figure 2.4, the same general subscript notations for the actuation systems have been extended for the variables too. Hence, *i* stands for both *u* and *l* with  $P_{ci}$  and  $P_{ri}$  referring to pressures in the cap and protruding rod sides of the  $i^{th}$  cylinder, respectively. In Table 2.2,  $i_1 i_2 |_c$  indicates the closed length of each pair with the piston rod most retracted inside the cylinder. A servoproportional valve monitors the oil supply in the paired cylinder and the coordinated actuation of the two pistons within the respective cylinders results in the

output motion of the free end  $f$  of the manipulator in the vertical plane  $xz$ . Any motion of the piston in  $C_l$  causes a rotation of the lower member about a horizontal axis through  $k$ , while that of  $C_u$  induces rotation of both the members about a horizontal axis through  $h$ .

The hydraulic circuit of the serial manipulator is depicted in Figure 2.4, with the  $i^{th}$  valve-cylinder pair being supplied by the pump. There are 4 ports in the valve, indicated by the symbols **P**, **A**, **B** and **T**, in the central block of the valve  $SPV_i$ . Port **P** is connected with the pump delivery, while ports **A** and **B** communicate respectively with the cap and rod side chambers within  $C_i$ . Port **T** takes the return flow back to the tank. **P** and **T** are the unmetered ports of fixed openings. Each of port **A** and **B** is a metered port monitoring the cylinder flow through a variable-area orifice, shown crossed by an inclined arrow. In the setup depicted in Figure 2.6, the piston rods of the upper and lower cylinders have been respectively connected with the upper member at  $u_r$  and the lower member at  $l_r$ . Each of these is at a lower height than the respective cap end connections at  $u_c$  or  $l_c$ . From Figure 2.7 the dashed lines in the valve symbol show the leakage paths with two fixed-area orifices shown at the central block corresponding to no excitation to either of Solenoids **s1** and **s2**. The flow connectivity for negative excitation to **s1** or positive excitation to **s2**, are shown on the opposite sides of the neutral block with respect to the excited solenoid.

### 2.3.3 Data Acquisition and Control System

The excitation voltage to either of the solenoids is provided from the output module **OM** of the real time system **RTS** shown in Fig 2.3(i). There are position sensors  $S_u$  and  $S_l$  that are linear variable differential transformers, or **LVDT**, sending the feedback of piston displacements of the upper and lower cylinders, respectively. These signals are received by the input module **IM** of the **RTS**. This module is an A/D converter producing digital signals corresponding to the analog signals fed by the **LVDT**. By comparing this signal with that corresponding to the user defined demand, an error is computed that is processed by a D/A converter in the output module, or **OM**, to produce an output voltage. Any control algorithm developed in LabVIEW software environment inside **Host PC** with the objective of minimizing the error should be loaded on a real-time processor of **RTS**. Of course, the output voltage produced within the limit of  $\pm V_{max}$  is sent to the designated one between the two solenoids of each servoproportional valve. The hardware limit of  $V_{max}$  is equal to 10V. Both **IM** and **OM** are equipped with appropriate filters for signal conditioning.

## 2.4 Serial-Parallel Manipulator Test Bench

A parallel arrangement of four serial manipulators shown in Figure 2.5 suspended under a common body with rectangular cross section has been used as a serial-parallel manipulator or precisely a quadruped in this study. In a rectangular coordinate system  $xyz$  shown in the respective figure,  $z$  is the vertical upward direction and the horizontal plane on the rectangular body frame involves  $x$  from left **L** to right **R** and  $-Y$  from front **F** to back **B**. In the arrangement each serial manipulator forms a leg system that is connected by individual hip and actuation systems with the common body. Figure 2.5 along with Tables 2.3 and 2.4 describe the entire quadruped test bench. Each component or variable associated shown in Figure 2.5 with any one of the four serial manipulators representing the legs, is denoted by an index  $j$  having values 1 to 4. Three actuation systems fitted with each leg are denoted by subscripts  $l$ ,  $t$ , and  $u$  for the lower, transverse, and upper locations, respectively. While reading Table 2.3 and Figure 2.4 with each  $i$  denoting  $l$ ,  $t$  or  $u$  should be read as  $ij$  for each Leg  $j$  equal to 1 to 4 for the quadruped.

Since one end of each leg assembly is anchored with the body and the free end can move in space, the leg assembly acts as an open loop kinematic chain. This further implies that each leg assembly, in isolation, behaves like a serial manipulator. From the application point of view, a serial manipulator can be used as robotic arm to perform welding operation, painting, material handling and so on. However, if all the four legs remain grounded, and the free point of all the legs remain stationary then the body acts as moving platform on a fixed support base rendering the mechanism a close loop kinematic chain character. The body of such a parallel manipulator can be used for lifting heavy load with high precision and accuracy and generate complex motion for aircraft or ship-motion simulator. For a walking quadruped, the free points of the legs form a floating support base. For their ability to negotiate unstructured terrains, these could be especially useful as human-assist system in the initial phase of a disaster management to clear and repair the track for the restoration of the normalcy. In the face of any post-disaster radiation hazard, an autonomous quadruped could be extremely useful.

The body of the quadruped consists of a frame made from extruded aluminum channel. These frames are connected to each other by two aluminum cross girder with holes for fixing the links and payloads as appropriate. A revolute joint with axis coincident with  $t_{cj}$  connects the body with Hip System  $H_j$  of Leg  $j$  that also has an upper limb  $U_j$ , a middle

limb  $M_j$  and a lower limb  $L_j$ . Limb  $U_j$  and  $H_j$  have a rigid connection. Point  $a_j$  lies at the intersection of  $t_{cj}$  and the cylinder axis. The hip of a leg formed by a revolute joint  $h_j$  connects  $H_j$  and  $M_j$ . Another revolute joint  $k_j$  corresponding to the knee of a leg connects  $M_j$  and  $L_j$ . At the free end of  $L_j$  that is the foot tip  $f_j$  of a leg, there is a rubber pad.  $L_j$  and  $M_j$  are connected by the lower actuation pair  $C_{lj}$ - $SPV_{lj}$ , Limb  $M_j$  and  $U_j$  by  $C_{uj}$ - $SPV_{uj}$  and the body with  $H_j$  by  $C_{ij}$ - $SPV_{ij}$ , where  $C$  and  $SPV$  designate a cylinder and servo-proportional valve, respectively.  $C_{uj}$  and  $U_j$  are connected by a revolute joint at the cap end  $u_{cj}$  of the cylinder. The piston rod protruding out of  $C_{uj}$  is attached to  $M_j$  at another revolute joint  $u_{rj}$ . The cap end of  $C_{lj}$  relates to  $M_j$  at a joint  $l_{cj}$  and the end of the piston rod connected to  $L_j$  at the joint  $l_{rj}$ .

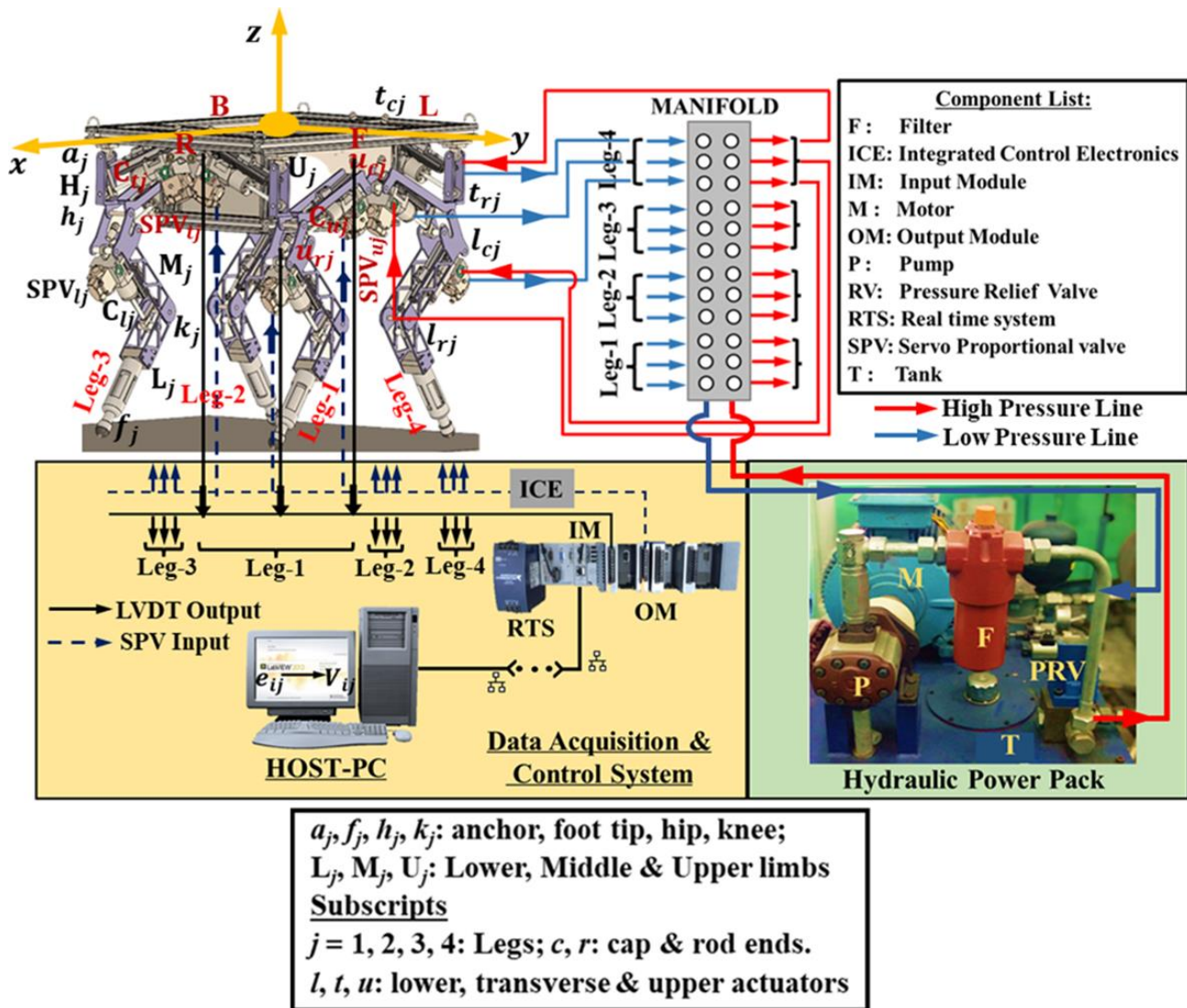


Figure 2.5: Schematic of experimental setup of serial-parallel manipulator with component list



## **2.5 Actuation System Modeling for Single Cylinder Test Bench**

As mentioned earlier, an existing test bench commissioned by (Sarkar et al. 2013a & b) with a double-acting-single-rod cylinder has been used in this study. A stiff compression spring coaxial with the industry-grade hydraulic cylinder has been used to load the piston for achieving a desired translation of the piston that has demanded the pressure at the pump delivery to rise above 20MPa. In view of such high system pressure, oil compressibility effect has been considered for the system modeling. Besides exploiting the energy-saving potential of the pump of the setup, incorporating the compressibility effect for a double-rod single-acting cylinder forms a notable contribution for the feedforward model to be developed on the basis of the system modeling presented next. Different considerations employed for developing the model are

- oil is compressible.
- transmission loss of fluid is negligible.
- leakage through the valve ports is not insignificant.
- spool dynamics is much faster than the piston dynamics.
- the friction between piston and cylinder has strong nonlinear features.
- the effect of valve deadband has been absorbed as a part of the excitation necessary to overcome the large static friction of the cylinder.
- variable displacement mode of pump operation is considered on the basis of its experimentally determined characteristic curve.

The overall model is presented next following the sequence modeling of

**A) Piston motion dynamics**

**B) Cylinder friction**

**C) Valve leakage**

**D) Metered valve flows and pressure dynamics in cylinder chambers**

**E) Pump characteristics and its flow coupling with valve and cylinder.**

### 2.5.1 Piston Motion Dynamics

From Figure 2.1 and 2.2, it is evident that during extension stroke of the piston against the spring loading, the pump port **P** is connected with the cap end side of the cylinder through port **A** of the **PV** and the rod end side relates to the tank port **T** through port **B**. During retraction of piston aided by the relaxation of the spring compression, port **B** directs the pump flow to the cylinder and port **B** routs the cylinder flow to the tank. The consequent pressures  $P_c$  and  $P_r$  at the cap and rod end chambers generate a thrust on the piston causing it to move against a friction force  $F_f$  and spring force  $ky$  exerted by the spring of stiffness  $k$ . If the total moving mass of the assembly is  $m$ , then the consequent dynamics of the piston can be expressed as

$$\dot{y} = v, \quad (2.1a)$$

$$\text{and } \dot{v} = \ddot{y} = (P_c A_c - P_r A_r - ky - F_f)/m, \quad (2.1b)$$

$$\text{where } A_c = \pi d_c^2/4 \text{ and } A_r = \pi(d_c^2 - d_r^2)/4. \quad (2.1c)$$

In the above equations,  $y$ ,  $\dot{y} = v$  and  $\ddot{y} = \dot{v}$  are the displacement, velocity, and acceleration of the piston respectively and  $d_c$  and  $d_r$  are the cylinder bore diameter and piston rod diameter respectively. In the catalogues of Bosch Rexroth AG Hydraulics (2012, 2017), the cylinder and valve masses are specified respectively as 2.5kg and 6.5kg. As apparent from the valve schematic in Figure 2.4(a). the spool strokes within a sleeve that in turn is housed inside a much bigger body containing all the flow passages. Also, a pair of solenoids and the associated electronics implies the mass of the tiny spool to be much lower than actuated mass together with the piston. Following the existing studies like those by (Du et al. 2017; Fliss et al. 1995; Sahoo et al. 2018; Faessler et al. 2018; Sira-Ramírez et al. 2017), the spool dynamics has been neglected.

### 2.5.2 Cylinder friction

The friction force  $F_f$  arises between the piston seals and the cylinder bore during the motion of the piston or its onset. (Sarkar et al. 2013a; Tran et al. 2014; Huang et al. 2019) for instance, discussed some existing models. A friction model that conforms to the development of the targeted feedforward model involving **static friction**  $F_s$ , **Coulomb friction**  $F_c$ , **coefficient of viscous or dynamic friction**  $\alpha_v$  and **Stribeck velocity**  $v_s$  is expressed as

$$F_f = \{F_c + (F_s - F_c) \exp\{- (\dot{y}/v_s)^2\} \text{sgn}(\dot{y}) + \alpha_v \dot{y}, \quad (2.2a)$$

or by an even simpler version

$$F_f = \{F_c\} \text{sgn}(\dot{y}) + \alpha_v \dot{y}, \quad (2.2b)$$

A notable feature of (2.2a) is that with increase in the piston speed the friction force magnitude initially drops and then increases. The decrease of friction with piston velocity in the low-velocity regime assumes importance, say in the context of grounded legs of a walking robot.

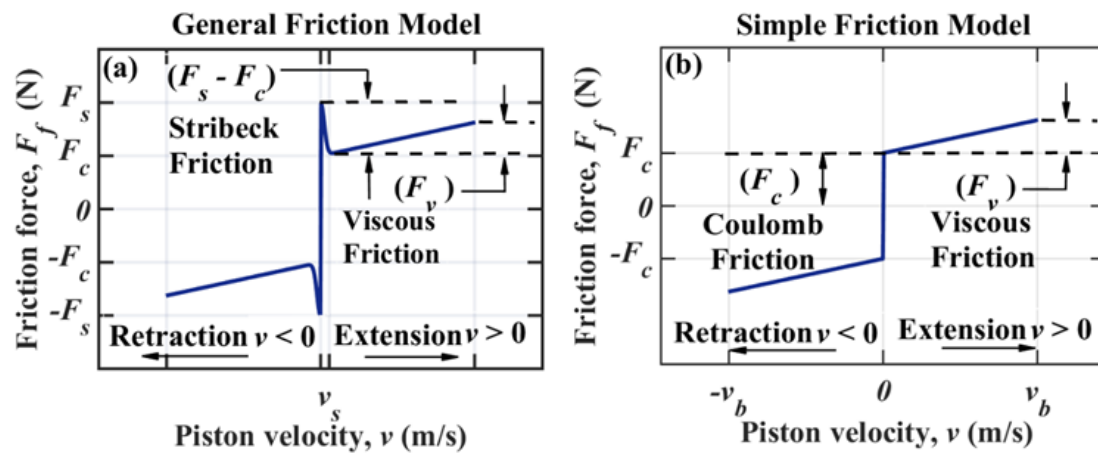


**Figure 2.6: Cylinder friction (a) with Stribeck variation and (b) in simplified form**

### 2.5.3 Valve Leakage

Oil leakage takes place through the radial clearance between the spool land and the sleeve at the valve ports **A** and **B**. Two different models of the leakage flow have been proposed in the present work. The first model is an improvisation corresponding to that proposed by (Eryilmaz et al. 1999) on the basis of their experimental results. This model indicates the valve leakage to be the maximum at the neutral spool position of the spool and decays through a bell-shaped variation with spool displacement away from the null. Consistent with this observation, a model shown in Figure 2.7 is proposed here by using  $l$  for leakage as subscript or superscript leading to

$$Q_l = Q_A^l + Q_B^l = 2Q_{l0}[\exp(-\alpha_l\{(1 - P_c/P_r)/(1 + P_c/P_r)\}^2)] + Q_{l1}, \quad (2.3a)$$

$$\text{along with } Q_A^l = \sqrt{P_c} Q_l / (\sqrt{P_c} + \sqrt{P_r}) \text{ and } Q_B^l = \sqrt{P_r} Q_l / (\sqrt{P_c} + \sqrt{P_r}), \quad (2.3b)$$

where Ports **A** and **B** in Figure 2.2 respectively involve subscripts  $A$  and  $B$  and leakage parameters are  $Q_{l0}$ ,  $Q_{l1}$  and  $\alpha_l$ . This model envisages the valve leakage to arise under the forcing by the pressure in each cylinder chamber through the orifice-like valve leakage

paths in the form of annular sectors that return the flow to the open tank taken to be at zero-gauge pressure.

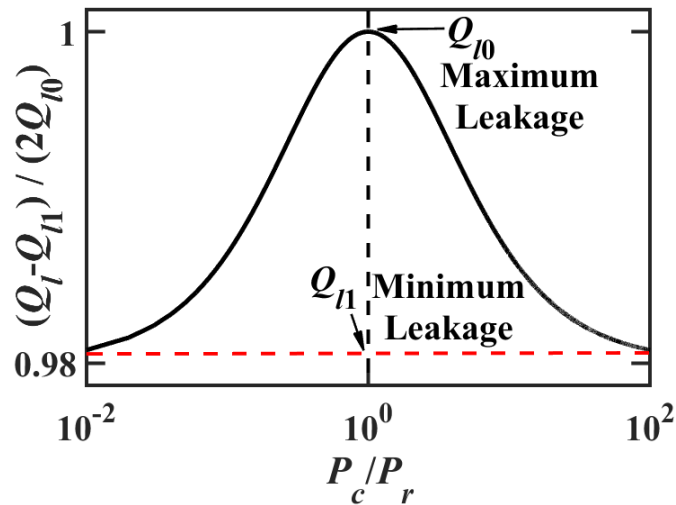


**Figure 2.7: Bell-shaped leakage between spool land and bush**

In the second approach, the leakage at Ports **A** and **B** are modelled as orifice flows through the constant-area radial clearance at the side of the spool land that moves under the sleeve. In Figure 2.2, the metering lands at Ports **A** and **B** are shown at the neutral position. At this position, the higher width of a spool land than the width of the corresponding port cut in a proportional valve with deadband constitutes two short radial clearances ending at the right and left edges of each these lands. Between the positions shown in Figure 2.2 and Figure 2.4(a), the spool movement creates an opening on one side through a preceding stage of shortening of the length of the radial clearance. The shortening of the length ends, when the moving circular edge of the spool land comes just under the edges of the sleeve cuts, each of which is a circular arc. In Figure 2.4(a), two orifice openings are apparent in the vicinity of each metering land. On the axially opposite side of the same land, the radial clearance keeps on getting longer throughout the spool movement without any increase in the flow area across the clearance. These clearances are responsible for the oil leakage. In comparison to the pressure drops in all these orifices, all other pressure losses in a continuous flow path remain negligible. In terms of usual orifice discharge relation proportional to square-root of pressure drop, a leakage model is proposed as

$$Q_l = \sum_{i=A}^B Q_i^l = Q_A^l + Q_B^l = c_{lA} \sqrt{P_c} + c_{lB} \sqrt{P_p - P_r} \text{ for } \dot{y} \geq 0, \quad (2.3c)$$

$$\text{and } Q_l = \sum_{i=A}^B Q_i^l = Q_A^l + Q_B^l = c_{lA} \sqrt{P_p - P_c} + c_{lB} \sqrt{P_r} \text{ for } \dot{y} < 0, \quad (2.3d)$$

where  $c_{lA}$  and  $c_{lB}$  are the leakage constants at Ports A and B respectively. While writing the above relations, the pump pressure is denoted by  $P_p$  and the oil tank open to the ambient is taken to be at zero-gauge pressure.

The oil flow through the orifices getting opened under the voltage excitation to one of the valve solenoids induces a pressure dynamics in the connected cylinder chambers due to accumulation and depletion of oil in the two chambers. Eventually, the pressure difference developing across the piston sets it in motion. This model is elaborated in the next subsection.

#### 2.5.4 Metered Valve Flows and Pressure Dynamics in Cylinder Chambers

Taking bulk modulus of the hydraulic fluid as  $\beta$ , the equations for the cap end and rod end pressure dynamics can be written as

$$\dot{P}_c = \beta(Q_A - A_c v)/(V_{0c} + A_c y), \quad (2.4a)$$

$$\text{and } \dot{P}_r = \beta(A_r v - Q_B)/(V_{0r} - A_r y), \quad (2.4b)$$

where  $V_{0c}$  and  $V_{0r}$  are the oil volumes respectively at the cap and rod end sides of **C** with the piston most retracted and  $Q_A$  and  $Q_B$  are the discharges respectively through ports **A** and **B** of **PV**. Each of the discharges through the metered ports has two parts. The first part is induced by the piston motion and is proportional to the voltage  $V$ , valve coefficient  $c_{vi}$  and the square root of the pressure drop across the port. From this part, a second part  $Q_i^l$  due to the leakage, is subtracted to obtain the net flow  $Q_i$  entering or leaving the corresponding cylinder chamber. The leakage  $Q_i^l$  can either be modeled as bell-shaped leakage model or by orifice flow leakage model involving a leakage coefficient  $c_{li}$  as discussed above in the leakage modeling section. Using either the bell-shaped leakage model (2.3a) and (2.3b) or the orifice flow leakage model (2.3c) and (2.3d), the overall flow-pressure model for the metered ports is hence expressed as

$$Q_A = c_{vA} V \sqrt{P_P - P_c} - Q_{lA} \text{ for } \dot{y} \geq 0, \quad (2.4c)$$

$$\text{or, } Q_A = c_{vA} V \sqrt{P_c} - Q_{lA} \text{ for } \dot{y} < 0, \quad (2.4d)$$

$$Q_B = c_{vB} V \sqrt{P_r} - Q_{lB} \text{ for } \dot{y} \geq 0, \quad (2.4e)$$

$$\text{or, } Q_B = c_{vB} V \sqrt{P_P - P_r} - Q_{lB} \text{ for } \dot{y} < 0. \quad (2.4f)$$

where  $P_p$  is the pressure at the pump port **P** of **PV** and the generalized branch leakage through the valve is expressed for the bell-shaped model (2.3a) and (2.3b) as

$$Q_{lA} = Q_A^l \quad \text{and} \quad Q_{lB} = Q_B^l \quad (2.4g)$$

and for the orifice model as

$$Q_{lA} = c_{lA}\sqrt{P_c} \quad \text{for } \dot{y} \geq 0 \quad \text{and} \quad c_{lA}\sqrt{P_p - P_c} \quad \text{for } \dot{y} < 0, \quad (2.4h)$$

$$\text{and } Q_{lB} = c_{lB}\sqrt{P_p - P_r} \quad \text{for } \dot{y} \geq 0 \quad \text{and} \quad c_{lB}\sqrt{P_r} \quad \text{for } \dot{y} < 0. \quad (2.4i)$$

The different subscripts  $A$  and  $B$  has been used for the coefficients, in view of different lengths of the peripheral cuts in the sleeves communicating flow respectively with the larger cap-end area and smaller rod-end area of the cylinder chambers, respectively. A valve-cylinder pairing of the form

$$\lambda = c_{vB}/c_{vA} = c_{lB}/c_{lA} = A_r/A_c, \quad (2.4j)$$

makes the pressure drops at the metered ports nearly equal for the domination of the motion-inducing discharge proportional to the piston velocity over the leakage expressed by (2.4c) to (2.4j) and the compressibility effect captured by (2.4a) and (2.4b). Under these assumptions, (2.4c) to (2.4i) yield

$$P_p - P_c = P_r \quad \text{for } \dot{y} \geq 0, \quad (2.4k)$$

$$P_p - P_r = P_c \quad \text{for } \dot{y} < 0, \quad (2.4l)$$

$$P_r = P_p/\Omega^2 - P_c/\Omega^2 \quad \text{for } \dot{y} \geq 0, \quad (2.4m)$$

$$P_r = P_p - P_c/\Omega^2 \quad \text{for } \dot{y} < 0, \quad (2.4n)$$

$$\text{where } \Omega = c_{vB}/(\lambda c_{vA}). \quad (2.4o)$$

Equal pressure drops at the paired metering ports of a proportional valve like the one shown in Figure 2.4(a) implies matched response of pressure change in these ports during any transient. Unequal drops would have led to different transient durations induced by the variation of pressures in the flow through the two ports. Consequently, the overall transient time would be longer. A transient process could set in through change of the external loading on the piston or the delivery pressure of the pump working in variable-displacement mode. The flow coupling of such a pump with the valve and cylinder are detailed next.

### 2.5.5 Pump Characteristics and its Flow Coupling with Valve and Cylinder

In the present work, a variable displacement pump has been considered for exploring the energy efficiency possibility together with precise control. A pressure compensated swash plate type axial piston pump is used here with pressure-discharge characteristics given by Figure 2.8. In such a pump, the pressure compensation mechanism consists of a control spool valve, which senses the pressure at the pump delivery line. When this pressure exceeds the cut-in pressure  $P_{ci}$  the spool of this valve moves against a pre-compressed spring. The cut-in pressure is set by the pre-compression of this spring. Once the spool moves, a flow is initiated to a stroking cylinder, whose piston moves the swash plate against another piston-cylinder arrangement called the rate cylinder. The movement of the swash plate causes a reduction of the swashing angle resulting in a reduction of the pump flow  $Q_p$ . In a variable-displacement pump, both the discharge and delivery pressure vary over a range. Below the cut-in pressure  $P_{ci}$  the swashing angle remains fixed at the nominal value resulting in a constant flow  $Q_{p0}$ . In the present set up  $Q_{p0}$  is equal to  $8.3 \times 10^{-4} \text{m}^3/\text{s}$ , as evident from Table 2.1. Above this pressure, the discharge decreases steeply and becomes zero at the cut-off pressure  $P_{p0}$ . Based on the above discussion a reasonable model for such characteristics of pump is proposed here based on the experiments conducted by (Mondal et al. 2019) as

$$P_p \equiv f_1(Q_p) = P_{ci}[2 + \coth\{(Q_p - Q_{p0})/Q_c\}]. \quad (2.5a)$$

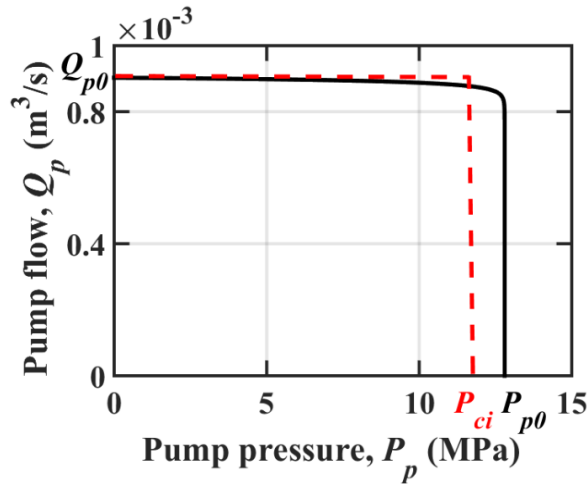


**Figure 2.8: Characteristics of a variable-displacement swash-plate axial-piston pump**

where  $Q_c$  is a characteristic flow and  $Q_p$  is the total pump discharge. The cut-in pressure  $P_{ci}$ , and the characteristic flow  $Q_c$  are unknown parameters of the pump model whose

values can be found from a parameter identification technique explained in the controller development chapter. This model reveals a static characteristic curve of the pump which gives a relationship between the pump pressure  $P_p$  and the discharge  $Q_p$ . Moreover, any sluggishness of the pump is expected to get compensated by the much faster valve dynamics by the corrective feedback voltage. The pump characteristics curve (2.5a) is depicted in Figure 2.5. The optimized value of the cut-off pressure  $P_{p0}$  for this set up is 128bar as shown in Fig 2.5. It is evident from the figure that the discharge  $Q_p$  is nearly constant at  $Q_{p0}$  equal to 52lpm up to pressure  $P_{ci}$  of 120bar. Beyond this pressure, the flow decreases sharply and become zero at  $P_{p0}$ .

The pump flow enters the valve through Port **P** as shown in Figure 2.2. This is routed through Ports **A** and **B**, one of which in the active state of a solenoid remains open and the other provides a leakage path. Hence, the pump flow through the proportional valve can also be expressed as

$$Q_P \equiv f_2(V, P_p, P_c, P_r) = V_{c_{vA}}\sqrt{P_p - P_c} + Q_{lB} \text{ for } \dot{y} \geq 0, \quad (2.5b)$$

$$\text{or } Q_P \equiv f_2(V, P_p, P_c, P_r) = V_{c_{vB}}\sqrt{P_p - P_r} + Q_{lA} \text{ for } \dot{y} < 0. \quad (2.5c)$$

As is evident from the last two expressions, the pump flow is governed by the pressures in the two-cylinder chambers corresponding to the external spring loading evident in Figure 2.1 for the system under study. Under the spring loading and use of (2.2a) and (2.2b) as friction model respectively for the conventional and order-separated models, use of (2.4m) and (2.4n) in (2.1b) yields the expressions for pressures in the two-cylinder chambers as

$$P_c \equiv f_3(P_p, \ddot{y}, \dot{y}, y) \\ = \{(P_p/\Omega^2)\lambda A_c + m\ddot{y} + ky + F_f\} / \{A_c(1 + \lambda/\Omega^2)\} \text{ for } \dot{y} \geq 0, \quad (2.5d)$$

$$\text{or } \{(P_p)\lambda A_c + m\ddot{y} + ky - F_f\} / \{A_c(1 + \lambda/\Omega^2)\} \text{ for } \dot{y} < 0, \quad (2.5e)$$

$$\text{and } P_r \equiv f_4(P_p, \ddot{y}, \dot{y}, y)$$

$$= \{(P_p/\Omega^2)A_c - (m\ddot{y} + ky + F_f)/\Omega^2\} / \{A_c(1 + \lambda/\Omega^2)\} \text{ for } \dot{y} \geq 0, \quad (2.5f)$$

$$\text{or } \{(P_p)A_c - (m\ddot{y} + ky - F_f)/\Omega^2\} / \{A_c(1 + \lambda/\Omega^2)\} \text{ for } \dot{y} < 0. \quad (2.5g)$$

The expressions for the pressure transients in the cylinder chambers can be rewritten by using (2.4c) to (2.4f) in (2.4a) and (2.4b) respectively as

$$\dot{P}_c|_{\dot{y} \geq 0} = \beta[c_{vA}V\sqrt{P_p - P_c} - Q_{lA} - A_c\dot{y}] / (V_{0c} + A_c y), \quad (2.5h)$$



$$\text{or } \dot{P}_c|_{\dot{y}<0} = \beta[c_{vA}V\sqrt{P_c} - Q_{lA}] - A_c\dot{y}/(V_{0c} + A_c y), \quad (2.5i)$$

$$\text{and } \dot{P}_r|_{\dot{y}\geq 0} = \beta[\lambda A_c\dot{y} - c_{vB}V\sqrt{P_r} + Q_{lB}]/(V_{0r} - \lambda A_c y), \quad (2.5j)$$

$$\text{or } \dot{P}_r|_{\dot{y}<0} = \beta[\lambda A_c\dot{y} - c_{vB}V\sqrt{P_p - P_r} + Q_{lB}]/(V_{0r} - \lambda A_c y). \quad (2.5k)$$

Finally, by differentiating (2.1b) and using (2.5h) to (2.5k), it can be written that

$$\begin{aligned} \ddot{y} &\equiv f_5(\dot{y}, \dot{y}, y, V, P_p, P_c, P_r) \\ &= \{\beta A_c(c_{vA}V\sqrt{P_p - P_c} - Q_{lA} - A_c\dot{y})/(V_{0c} + A_c y) - \beta\lambda A_c(\lambda A_c\dot{y} - \\ &\quad c_{vB}V\sqrt{P_r} + Q_{lB})/(V_{0r} - \lambda A_c y) - k\dot{y} - \alpha_v\ddot{y}\}/m \text{ for } \dot{y} \geq 0, \end{aligned} \quad (2.5l)$$

$$\begin{aligned} \text{or } &\{\beta A_c(c_{vA}V\sqrt{P_c} - Q_{lA} - A_c\dot{y})/(V_{0c} + A_c y) - \beta\lambda A_c(\lambda A_c\dot{y} - \\ &\quad c_{vB}V\sqrt{P_p - P_r} + Q_{lB})/(V_{0r} - \lambda A_c y) - k\dot{y} - \alpha_v\ddot{y}\}/m \text{ for } \dot{y} < 0. \end{aligned} \quad (2.5m)$$

It is evident from (2.5l, m) that the third-order piston motion dynamics is set in by the high-pressure flow delivered by the pump through the proportional valve to the cylinder and back to the open tank. It may be noted that the variation of pump pressure in a variable-displacement pump in this test bench gives rise to a system transient that do not arise in case of a fixed-displacement pump. In the face of coupling between hydraulic nonlinearities and complex motion of the manipulator mechanism, a fixed-displacement pump has been used in the manipulator setup. In the next subsection, the modeling of the actuation systems of the manipulators are detailed.

## 2.6 Actuation System Modeling for Manipulators

The mathematical modeling of the actuation system considered here, viz. a serial and a serial-parallel manipulator can be further subdivided into three parts-

- A) Dynamic modeling of the cylinder rods,**
- B) Cylinder-valve pressure and flow modeling** and the
- C) Kinematic modeling** that generates a connectivity between the cylinder space and the task space for executing the motion of the free point in the vertical plane for a serial manipulator and motion of the Centre-of-mass for the serial-parallel manipulator, corresponding displacements of the cylinder rods.

The mathematical modeling of the manipulators is based on several considerations which are different from those that have been taken during the mathematical modeling for

Configuration- I. These differences are due to the differences in the system hardware and their corresponding working conditions. Both the serial manipulator and the parallel arrangement of 4 serial manipulators considered here are driven by a fixed displacement type gear pump, along with servo category valve-cylinder pairs. Hence the considerations that has been used for the Configuration I, which deals with variable displacement pump along with industry grade valve-cylinder pair will not be consistent with these configurations. Following are the several issues that have been considered during the development of the mathematical modeling of the different manipulators.

- From the specification Table 2.3 for the two configurations considered here, it is observed that the piston cap end and rod end diameters are 25mm and 12mm respectively and the corresponding stroke is 60mm. So, one can conclude that within this small geometry the volume of fluid will be quite small and hence the compressibility effect of hydraulic oil will not be prominent, which thus can be neglected.
- Fixed displacement mode of pump operation is considered.
- Friction force  $F_f$  between the piston seal and the servo-grade cylinder can be considered or neglected. This consideration is based on the facts that the cylinders are servo grade, and the setup is quite new.
- The suspended weight  $F_w$  and the mass actuated  $m_p$  by each piston and piston rod- are neglected in the present work. The rationale behind these considerations has been explained clearly in chapter 4. However, the neglected inertial effect further simplifies the control algorithm for driving the manipulators. Any inaccuracy due to these considerations will be compensated by the feedback controller.
- The servo category valve that has been used here is zero lapped. Thus, the leakage at valve ports is evident and hence the leakage past the valve port can be considered in this analysis.
- The oil leakage flows between the piston-cylinder radial clearances, due to the difference in pressures  $P_{ci}$  and  $P_{ri}$  are neglected.

### 2.6.1 Dynamic Modeling of Actuators

Based on the above assumptions neglecting the friction between piston rings and the inner cylinder surface for the servo-grade cylinders, the oil leakage flows between the piston-cylinder radial clearances along with inertial effect of the moving masses of the pistons and with zero load on the actuators, a simple dynamic model of the actuators can be obtained here from the force balance equation, and can be written as

$$(P_{ci}A_{ci} - P_{ri}A_{ri}) = 0 \quad (2.6a)$$

$$\text{with, } A_{ci} = \pi d_{ci}^2/4 \text{ and } A_{ri} = \pi(d_{ci}^2 - d_{ri}^2)/4. \quad (2.6b)$$

where  $P_{ci}$  and  $A_{ci}$  are the cap end pressure and areas respectively,  $P_{ri}$  and  $A_{ri}$  are their rod end counterparts.  $d_{ci}$  and  $d_{ri}$  are the bore and rod diameters of the cylinders.

### 2.6.2 Pressure and Flow Modeling

As has been stated in the previous section, the valve -cylinder pair that have been used here are servo-grade. Such valves mostly have nearly zero lap resulting in almost zero dead band. Furthermore, the servo-grade cylinders have negligible frictional effects. Hence the usual hard nonlinearities associated with these effects are negligible in the present configurations. Also, from the geometry of the valve-cylinder pair, the fluid flow is considered to be incompressible. But as the valve spool are critically lapped therefore an appreciable amount of leakage will occur at the valve ports **A** and **B**. Finally for using a fixed displacement pump in the present configuration, the pump port pressure always remains constant at the **RV** setting.

From these considerations of no dead band in the valve, no stiction zone, no compressibility effect with appreciable amount of leakage, the flow at the control ports can be expressed as,

$$Q_{ci} = A_c \dot{y}_i = c_{vA} V_i \sqrt{P_P - P_{ci}} - Q_{lAi} \quad \text{for } \dot{y}_i \geq 0, \quad (2.7a)$$

$$Q_{ri} = A_r \dot{y}_i = c_{vB} V_i \sqrt{P_{ri}} - Q_{lBi} \quad \text{for } \dot{y}_i \geq 0, \quad (2.7b)$$

$$Q_{ci} = A_r \dot{y}_i = c_{vA} V_i \sqrt{P_{ci}} - Q_{lAi} \quad \text{for } \dot{y}_i < 0, \quad (2.7c)$$

$$\text{and } Q_{ri} = A_c \dot{y}_i = c_{vB} V_i \sqrt{P_P - P_{ri}} - Q_{lBi} \quad \text{for } \dot{y}_i < 0. \quad (2.7d)$$

where  $Q_c$  and  $Q_r$  are the flow through ports **A** and **B** respectively,  $c_{vA}$  and  $c_{vB}$  are the valve coefficients in ports **A** and **B** respectively,  $V$  is the control voltage of **SPV**<sub>*i*</sub>,  $Q_{lA}$  and  $Q_{lB}$  are the leakages at **A** and **B** respectively and  $\dot{y}_i$  represents the piston velocity.

By extending the above equations (2.7a) to (2.7d), and considering incompressible flow and ignoring the leakage flows, from Continuity Equation, the approximate cylinder chamber pressures for both extension and retraction can be written in the form

$$P_{ci} | \dot{y}_i \geq 0 = P_p - \{A_c \dot{y}_i / c_{vA} V\}^2, \quad (2.8a)$$

$$P_{ri} | \dot{y}_i \geq 0 = \{A_r \dot{y}_i / c_{vB} V\}^2, \quad (2.8b)$$

$$P_{ci} | \dot{y}_i < 0 = \{A_c \dot{y}_i / c_{vA} V\}^2, \quad (2.8c)$$

$$\text{and } P_{ri} | \dot{y}_i < 0 = P_p - \{A_r \dot{y}_i / c_{vB} V\}^2. \quad (2.8d)$$

The above equations shown here are representative for one valve-cylinder set, which forms the basis for the formulation of the feedforward controller for the 2-DOF serial and the serial-parallel manipulator. A reasonable controller formulation with proper notation for the two sets of valves and actuators will be explained in the subsequent chapter during controller formulation of the serial manipulator. However, it is not the out of place to mention that from the choice of the two designed feedforward controllers, the most efficient one will be implemented here in a modified manner based on the considerations for the serial manipulator.

### 2.6.3. Kinematic Modeling for Serial Manipulator

The kinematic model forms the basis for the relationship among the linear motions of the actuators or cylinder pistons, the rotation of the 2 segments of the manipulator and the movement of the free point of the manipulator in the vertical plane. Hence, with respect to Figure 2.3, the kinematic model leads to a set of equations relating (a) the instantaneous end-to-end lengths of the piston-cylinders –  $l_c l_r$  or  $u_c u_r$  – in the *actuation space*, (b) the joint angles of the manipulator segments  $\alpha$  and  $\beta$  in the *joint space* and (c) the coordinates  $(x_f, z_f)$ , of the free point or the end-effector of the manipulator in the *task space*.

Depending on the use of the kinematic relations, the model is termed *forward kinematic model* or *inverse kinematic model*. This has been shown in Figure 2.9 below. The former refers to the model-based predictions of the task space motion with the actuator space motion as the input. On the other hand, specifically for controller implementations, one

needs to identify the actuator space demands for a known motion plan in the task space. This is called the inverse kinematic model. In the present section, the forward kinematics is discussed. The inverse model will be stated in a subsequent chapter in the context of designing the controller for specified motion plans.

For instantaneous displacements  $y_l$  and  $y_u$  of the upper and lower pistons respectively, the end-to-end lengths of the two piston cylinder arrangements at any instant can be expressed as

$$l_c l_r = y_l + l_c l_r|_c, \quad (2.9a)$$

$$u_c u_r = y_u + u_c u_r|_c, \quad (2.9b)$$

where,  $l_c l_r|_c$  and  $u_c u_r|_c$  refer to the closed lengths of the corresponding piston-cylinders.

Then with reference to Figure 2.6, using the cosine law,

$$\phi = \cos^{-1}[\{(z_h)^2 + (hu_c)^2 - (a'u_c)^2\}/\{2(z_h)(hu_c)\}], \quad (2.9c)$$

$$\text{and } \beta = \pi - \phi - \cos^{-1}[\{(hu_c)^2 + (hu_r)^2 - (u_c u_r)^2\}/\{2(hu_c)(hu_r)\}], \quad (2.9d)$$

$$\text{Also, } \delta = \cos^{-1}[\{(hk)^2 + (kl_c)^2 - (hl_c)^2\}/\{2(kl_c)(hk)\}], \quad (2.9e)$$

$$\text{and } \alpha = \pi - \delta - \beta - \cos^{-1}[\{(kl_c)^2 + (kl_r)^2 - (l_c l_r)^2\}/\{2(kl_c)(kl_r)\}], \quad (2.9f)$$

Finally, the coordinates of the free point can be expressed as

$$x_f = (hk)\sin\beta + x_h - (kf)\sin\alpha, \quad (2.10a)$$

$$\text{and } z_f = z_h - (hk)\cos\beta - (kf)\cos\alpha. \quad (2.10b)$$

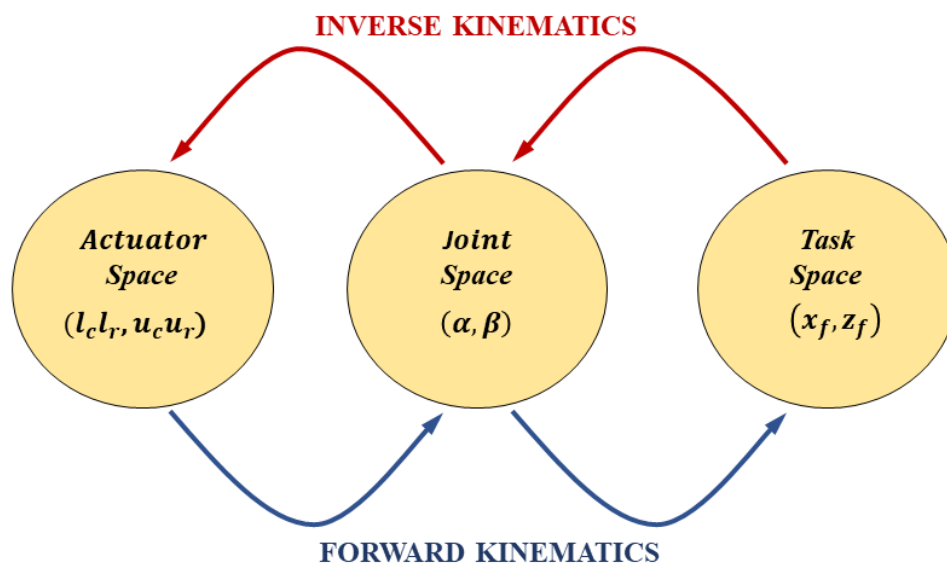


**Figure 2.9: Kinematic relations of the 2-DOF serial manipulator**

## 2.7 Kinematic Modeling for Serial-Parallel Manipulator

From the above discussion, it is apparent that the end goal of the present work is to drive electrohydraulically actuated manipulators in real time with the help of a suitably designed feedforward position controller. As the feedforward controller design is model based, the background work for the development of the controller is proper mathematical modeling of the systems. The above discussions also reveal that the system modeling for serial manipulator forms the core of the serial-parallel manipulator, where four serial manipulators have been arranged in parallel to support a body or platform. Same hydraulic power pack has been used to drive both the manipulators individually. Hence the dynamic modeling of the actuators, chamber pressures and flow modeling and finally the kinematic modeling for both serial and serial-parallel serial manipulator remains same. The kinematic modeling for serial and serial-parallel manipulator is further based on several motion demands. For the serial manipulator in form of a single leg of a quadruped the anchor  $\mathbf{a}$  and the hanging point  $\mathbf{h}$  is considered to be fixed and several motion demands are given to the free point  $\mathbf{f}$ . Whereas for the entire quadruped the hanging point  $\mathbf{h}$ , also termed as heave joint, and the corresponding anchor point where four legs are fitted with the body, are in relative motion with respect to the foot tips  $\mathbf{f}$ . The free point  $\mathbf{f}$  for serial manipulator, is termed as foot tip  $\mathbf{f}$  for serial-parallel manipulator. The motion demand of the free point for serial manipulator is somewhat simple as compared to serial-parallel manipulator and has been explained clearly in chapter 4. However, for the realization of serial-parallel actuation of the manipulators a combined motion of body or platform followed by the motion of the individual leg is required. The sequential motion of the body followed by the motion of the individual leg ensuring speed and stability of the system is termed as motion plan design. The next section provides a brief idea about the mathematical modeling that represents the motion of the foot tips along with the motion of the body in order to develop a stable motion plan also termed as gait.

### 2.7.1. Design of Foottip and Body Motion for Serial-Parallel Manipulator

Based on the photographic representation of serial-parallel manipulator or quadruped given in Figure 2.5, a schematic line diagram depicting the front, side, and top view of the same in Figs 2.10 (a), (b) and (c) respectively, the motion of which is analyzed with respect to a coordinate system  $\mathbf{XYZ}$ , parallel to the body fixed coordinate system  $\mathbf{xyz}$  and fixed on

earth. For the analysis of the motion of quadruped, the mass of the overall system has been considered to be concentrated at the geometric center of the overall system termed as center of mass COM ( $\mathbf{C}$ ) whose projection on the ground coincides with the origin of the earth fixed coordinate system  $\mathbf{XYZ}$  and referred as ( $\mathbf{C}'$ ). It has been considered that the vertical projection of the geometric center ( $\mathbf{C}'$ ) and the four-foot tips moves sequentially along the  $\mathbf{X}$  direction as shown in the Figure 2.10. for the purpose of the locomotion. The combined motions of lower and upper cylinders of each leg having all the foot tips grounded, is responsible for the translational motion of the body along positive  $\mathbf{X}$  and  $\mathbf{Z}$  direction known as surge and heave motion, respectively. The transverse actuators fitted with the body on the other hand provides translation of the body along  $\mathbf{Y}$  axis known as sway. Under all these conditions of motion of the body of the quadruped keeping the foot tip grounded is said to be operated as a parallel manipulator. On the other hand, if the body remains stationary and the foot tip is given motion along ( $\mathbf{XZ}$ ) plane, then the system is said to be act as a serial manipulator. However, the sequential motion of the body, followed by the corresponding motion of the foot tips of each leg is referred as hybrid actuation of combined serial-parallel manipulator.

The initial rest position of the quadruped with respect to the earth fixed coordinate system  $\mathbf{XYZ}$  is such that the four-foot tips lie slightly offset outward along the transverse direction from their four corresponding anchor points  $a_j$ , at a particular coordinate of  $(x_{f0j}, y_{f0j}, z_{f0j} = 0)$  as shown in Figure 2.10 (a), (b) and (c) respectively. The initial position of the system has been represented by using suffix 0. Table 2.2 lists the important parametric values of the system during the initial condition. The offset length of the four-foot tips from their corresponding anchor point along the transverse direction is given by  $\pm b/2$ , where the longitudinal distance between the two anchor points is  $S_0$ , as shown in the below figure. The initial offset length of the four foot-tips are normally provided to maintain the static stability of the center of mass COM during execution of any motion plans.

The foottip of each leg and their corresponding anchor point fitted with the body are numbered following the sequence **1** for right-front (**RF**), **2** for left-back (**LB**), **3** for right-back (**RB**) and **4** for left-front (**LF**). With reference to Figure 2.10, the initial coordinates of the foot tips – **1**, **2**, **3** and **4** – can be respectively expressed as  $(S_0/2, (B + b)/2, 0)$ ,  $(-S_0/2, -(B + b)/2, 0)$ ,  $(S_0/2, -(B + b)/2, 0)$ ,  $(-S_0/2, (B + b)/2, 0)$ .

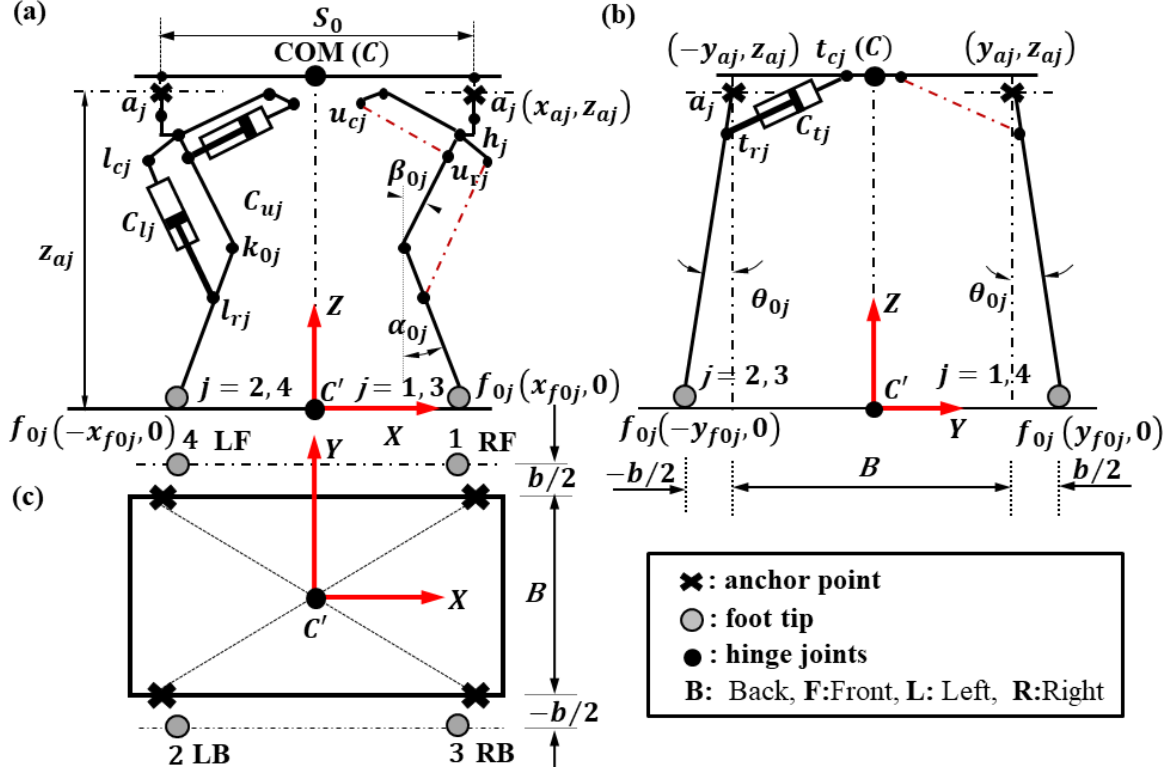


**Figure 2.10: Schematic of initial leg configuration of 6 DOF serial-parallel manipulator**

For the locomotion of the entire quadruped in a definite direction the four foot-tips ( $f_j$ ) and the projection of the COM ( $C'$ ) on the ground must move in a particular sequence. Specifying the sequence of motions of the ( $f_j$ ) and ( $C'$ ), along with the ( $f_j$ ) and ( $C'$ ) trajectories is known as the motion plan and depends upon the gait for which the motion is designed. The motion of a particular foot-tip in the swing phase is expressed with reference to a coordinate system  $x_f - y_f - z_f$ , parallel to the earth-fixed coordinate system but with its origin coinciding with the position of the particular foot-tip on the ground just before its lift-off. A foot tip during execution of a particular gait will either swing in the air, also known as the swing phase, or will remain grounded. For the locomotion of the total system in the forward  $X$  direction, the motion of the foot tips, in the swing phase, will be confined in the  $(XZ)$  plane. The trajectory of a swinging foot tip in either the  $x_f$  or  $z_f$  direction,



represented respectively by  $x_{fj}(t)$  and  $z_{fj}(t)$  – can be designed to be a linear function of time, a sinusoidal function of time or a combination of both. The choice of the motion plan for a foot tip depends on two things. The first is the maximum allowable speed of the foot tip which decides the maximum slewing rates of the hydraulic cylinders and hence the flow requirement from the pump. The second issue to be considered is the speed of touchdown of the foot tip after completion of the swing phase, which will decide the extent of the impact loading on the leg structure. The total stride to be covered by each foot tip in the  $x_f$  direction during the swing phase of its motion, in a time period of  $T$  starting from lift off to touchdown is denoted by  $s_f$ . For complete locomotion of the whole system, over the time period  $T$ , each foot tip along with body must cover this distance  $s_f$ . However, the time required to cover the same distance by the foot tips and the body will not be same – as they move at different speeds. These velocities should be adjusted in such a way that at every instant, the stability of the overall system can be maintained by ensuring that the point ( $C'$ ) always lies inside the support polygon formed by joining the grounded foot tips. The tuning of the velocities of the foot tips and body, during locomotion in order to maintain the stability of the system, is also a part of the motion plan design. The equation of motion that can be developed to describe the motion of a swinging foot-tip and body are given below.

The motion of a swinging foot tip along  $x_f$  direction can be designed with a set of equations representing the variation of the foot tip coordinate with time as  $x_{fj}(t)$ . The equation can be adjusted by a parameter  $a_f$  such that for  $a_f$  value very close to zero,  $x_{fj}$  varies linearly with time and for  $a_f = 0.5$ ,  $x_{fj}$  varies with time in a sinusoid manner. For  $0 < a_f < 0.5$ , the motion is a combination of linear and sinusoidal variations. Also, it can be seen, that the factor  $a_f$  affects both the maximum speed as well as the touchdown speed of a particular foot tip.

Considering, the total time for swing phase of the foot tip to be  $T$ . For the case where the foot tip has a combined linear and sinusoidal motion from lift off to touchdown the ground, this time  $T$ , is divided into three phases. The initial phase consists of a sinusoid variation over time  $T_s/2$ , followed by a linear motion over time  $T_c$  and finally again a sinusoidal motion for the remaining time  $(T - T_c - T_s/2)$ . The total time period  $T$  thus can be written as,

$$T = T_s + T_c \quad (2.11a)$$

$$\text{with, } T_s = \pi T a_f / \{1 + (\pi - 2)a_f\}. \quad (2.11b)$$

Equation (2.11b) indicates that if  $a_f = 0$ , then  $T_s = 0$  implying that there will be linear motion over the entire time  $T$ . Similarly, for  $a_f = 0.5$ , then  $T_s = T_c$  implying that there will be sinusoid motion over the entire time  $T$ .

Thus, the three phases of motion along  $x_f$  direction can be written as-

$$x_{fj}(t) = a_f s_f \{1 - \cos(\pi t / T_s)\} \text{ for } 0 \leq t \leq T_s / 2, \quad (2.11c)$$

$$x_{fj}(t) = a_f s_f \{1 + (\pi / T_s)(t - T_s / 2)\} \text{ for } T_s / 2 < t \leq T_s / 2 + T_c, \quad (2.11d)$$

$$\text{and, } x_{fj}(t) = a_f s_f \{1 + (\pi T_c / T_s) - \cos[\pi(t - T_c) / T_s]\} \text{ for } T_s / 2 + T_c < t \leq T. \quad (2.11e)$$

The above equations reveal that from the starting of motion, the foot tip moves in the forward direction sinusoidally up to a period of  $T_s/2$ . From  $T_s/2$  to  $T_c$  the foot tip moves with uniform motion, followed by the next half of  $T_s/2$  from  $T_c$  where again the foot tip moves sinusoidally. The effect of using each trajectory can be best understood with the help of the following Figure 2.11 (a) and (b) – which show the variations of  $x_{fj}$  and corresponding foot tip velocities  $v_{fj}$  for 3 different values of  $a_f$ .

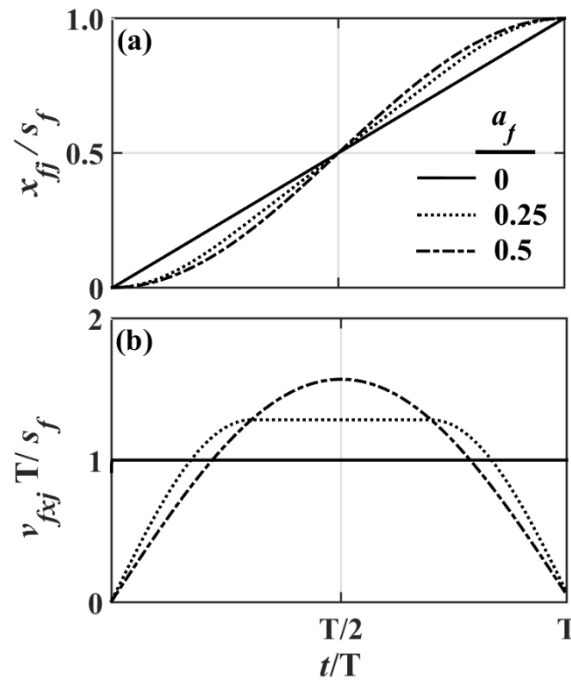


**Figure 2.11: Effect of variation of  $a_f$  on foot tip (a) displacement and (b) velocity along  $x_f$  direction**

Figure 2.11(a) and (b) reveal that when the value of  $a_f = 0.5$ , the full stride will be covered by sinusoidal motion that would ensure lowest impact of touchdown of the foot tip on rough terrain, but the at the cost of highest value of maximum piston velocity. For  $a_f = 0.25$ , 50% of the stride will be covered by sinusoidal motion that has been designed to ensure low-impact touchdown on rough terrain and a moderate maximum piston velocity. For  $a_f = 0$ , the foot tip will move with constant velocity for the entire stride and an impact will occur during a touchdown with a velocity of  $s_f/T$  under all conditions.

The foot tip also has a component of motion along  $\mathbf{z}_f$  direction as stated above, the motion of the foot tip along  $\mathbf{z}_f$  direction can be considered as pure linear or sinusoid and can be expressed as

$$z_{fj}(t) = 2s_v(t/T), \text{ for } 0 \leq t \leq T/2 \quad (2.11f)$$

$$\text{and } z_{fj}(t) = s_v - 2s_v/T (t - T/2) \text{ for } T/2 \leq t \leq T. \quad (2.11g)$$

for pure linear motion, and for sinusoidal motion of the foot tips the expressions corresponding expressions can be written as-

$$z_{fj}(t) = 0.5s_v\{1 - \cos(2\pi t/T)\} \text{ for } 0 \leq t \leq T. \quad (2.11h)$$

where  $s_v$  is termed as maximum vertical stride along  $\mathbf{z}_f$  direction. Considering pure linear and sinusoidal variation of foottip motion along  $\mathbf{z}_f$  direction the variation of  $z_{fj}$  and corresponding foot tip velocity  $v_{fzj}$  plots are shown in the below figure below.

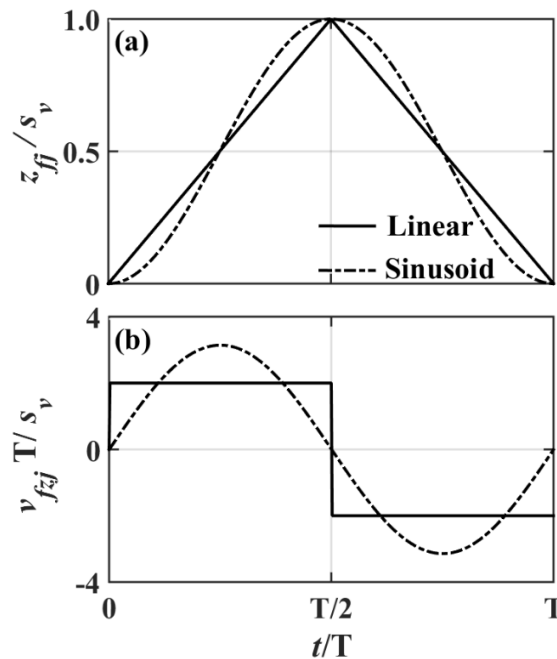


**Figure 2.12: (a) Displacement and (b) velocity of foot tip along  $\mathbf{z}_f$  direction**

Figure 2.12(a) and (b) shows the non-dimensional displacement and velocity profile of foot tip along  $\mathbf{z}_f$  direction for both linear and sinusoidal motion. From the velocity plot 2.12(b) at the end of the swing phase, the foot tip velocity for linear variation is non-zero. This situation further implies higher force of impact during touch-down of foottip, and thereby maximizing the chance of any mechanical damage, unlike sinusoidal motion where at the end of swing phase the foottip velocity reduces to zero. Comparing both the velocities of foot tip along  $\mathbf{x}_f$  and  $\mathbf{z}_f$  direction obtained from the plot 2.11(b) and 2.12(b) it can be concluded that pure linear variation of motion to the foottip along  $\mathbf{x}_f$  and  $\mathbf{z}_f$  direction will provide non-zero touchdown velocity and higher impact force. Also, pure linear motion demand further makes the foottip motion jerky. The touchdown velocity and hence effect of impact force is minimum when pure sinusoidal and combination of sinusoid and linear motion demand is given to the foottip along  $\mathbf{x}_f$  direction and pure sinusoidal motion along  $\mathbf{z}_f$  direction. However, the maximum velocity during swing phase along  $\mathbf{x}_f$  direction is less for combined sinusoidal motion coupled with constant velocity phase compared to the corresponding maximum velocity of motion in the  $\mathbf{z}_f$  direction having pure sinusoid variation. The combined motion not only reduce the touchdown velocity and impact force, but also reduces the flow requirement and consequently the hydraulic power requirement during the swing phase motion. In this context it should also be noted that the hydraulic power requirement during swing phase motion of legs is much higher compared to the stance phase of grounded legs, when the body weight is negotiated by the legs.

Based on the above discussions about different foot tip motions during swing phase along  $\mathbf{x}_f$  and  $\mathbf{z}_f$  direction, the different possible foot tip trajectories can now be shown in Figure 2.13. The figure reveals that initially the foot tip is at the ground, and the initial foot tip coordinate along  $(\mathbf{x}_f - \mathbf{z}_f)$  plane is  $(x_{fj}, z_{fj}) = (x_{fj0}, 0)$ . From this position the foot tip is taking both horizontal and vertical stride of  $s_f$  and  $s_v$  respectively along  $(\mathbf{x}_f - \mathbf{z}_f)$  plane. Considering pure linear motion along  $(\mathbf{x}_f - \mathbf{z}_f)$  plane will produce triangular or trapezoidal trajectory of foottip. Pure sinusoidal motion and combination of both linear and sinusoid motion of foottip along both the axes can either produce sinusoidal trajectory or trapezoidal trajectory.

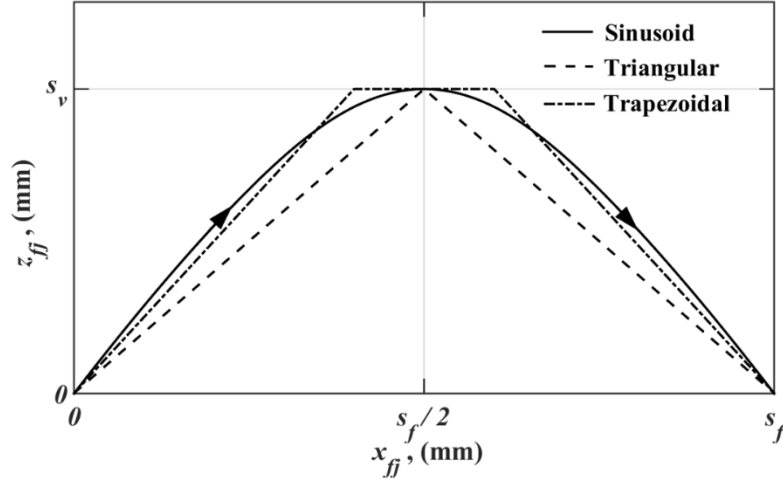


**Figure 2.13: Foot tip trajectories in  $(x_f - z_f)$  plane**

As discussed about several foottip motions along  $x_f$  and  $z_f$  directions, the motion plan for serial-parallel manipulator also demands the corresponding motion of the body. During the motion, the body will also advance sequentially by maintaining the stability of the system. Based on the discussion regarding the ground projection of COM ( $C'$ ) in motion plan design, its motion in the  $X$  direction, termed as  $x_{C'}(t)$  can be designed either a sinusoidal or linear function of time. However, in order to reduce the velocity of the body COM and hence overall hydraulic flow requirement during the entire motion of the system a combination of linear and sinusoid motion can be given to ( $C'$ ) following the equations 2.11(c) to 2.11(e). Figure 2.14 illustrates the motion variation of the projection of COM ( $C'$ ) along the positive  $X$  direction with time, and the corresponding velocities.

The three phases of motion of ( $C'$ ) along  $X$  direction can be written as-

$$x_{C'}(t) = x_{COM} = a_f s_f \{1 - \cos(\pi t / T_s)\} \text{ for } 0 \leq t \leq T_s / 2, \quad (2.11i)$$

$$x_{C'}(t) = x_{COM} = a_f s_f \{1 + (\pi / T_s)(t - T_s / 2)\} \text{ for } T_s / 2 < t \leq T_s / 2 + T_c, \quad (2.11j)$$

$$\text{and, } x_{C'}(t) = x_{COM} = a_f s_f \{1 + (\pi T_c / T_s) - \cos[\pi(t - T_c) / T_s]\} \text{ for } T_s / 2 + T_c < t \leq T. \quad (2.11k)$$

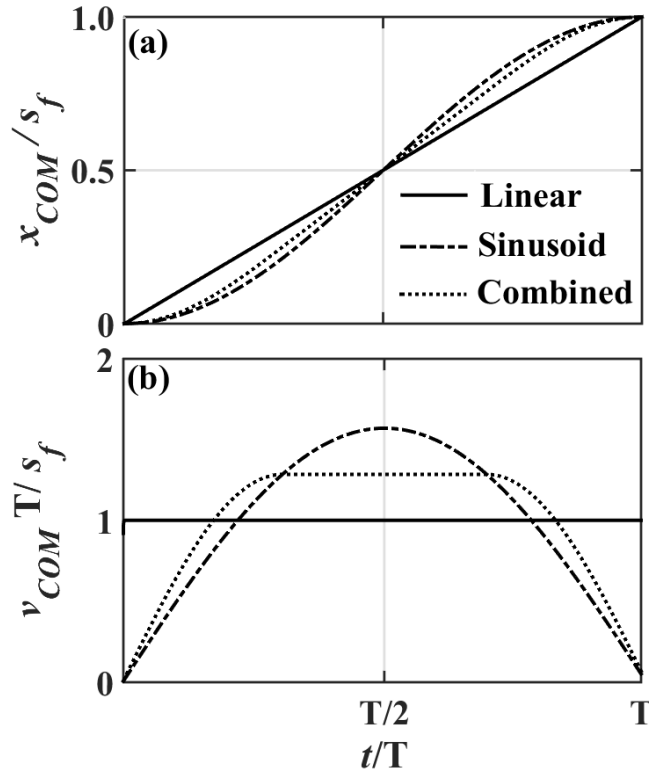


**Figure 2.14: (a) Displacement and (b) velocity of COM along positive  $X$  direction**

### 2.7.2 Proposed Motion Plan Sequence for Serial-Parallel Manipulator

After designing suitable motion demand for both foot tips and body COM of the quadruped configuration, the next part of work is to develop a suitable sequential motion plan for the COM and foot tips in order to realize the serial-parallel actuation. The motion plan must be designed in such a manner that the legs and the body of the system can be moved in a sequential manner by ensuring the speed and stability during motion. The design of sequential foot tip motions coupled with motion of center-of-mass (COM) of the body is also known as a gait. From the point of view of stability, the walking gaits of a quadruped are classified into “static walk” and “dynamic walk” (Hirose & Yoneda 1993; Kurazume, Hirose & Yoneda 2002). Walking is accomplished in a static gait at a constant body speed with at least three legs on the ground called the stance legs with the vertical projection of the COM ( $C'$ ) always being contained inside the support polygon formed by the three grounded foot tips. The following gait is called static because at every instant of the body maintains the static equilibrium. Such a motion plan calls for features of a discontinuous gait where there may exist some periods of body motion without any leg swings. The gait, though stable, is not suitable for high-speed locomotion.

Based on the above discussion a model static walking (SW) gait can be proposed here, whose one cycle consists of 6 motions as is shown in Figure 2.15. below. The figure depicts that starting from the rectangular posture of the four-foot tips at the ground, orientation of the four-foot tips should form a parallelogram. The geometric formation of the four-foot tips should be such that static stability at every instant can be ensured properly throughout the gait. The figure clearly exhibits the discontinuous motion of COM over entire cycle, which occurs during 1<sup>st</sup> and 4<sup>th</sup> phase, followed by the motion of the four-foot tips in the sequence of 4-1-2-3 during 2<sup>nd</sup>, 3<sup>rd</sup>, 5<sup>th</sup>, and 6<sup>th</sup> phase of the entire cycle. The motion of the foot tips further implies that one foot tip in the swing phase at a time and other three remains grounded.

To maintain the static stability, the vertical projection of COM ( $C'$ ) will always lie inside the support polygon formed by the three grounded legs. Here  $T_{SW}$  is the total cycle time for SW gait, and the body moves by a distance of  $S_f/2$  at a time of  $T_{SW}/6$  during each phase of its motion. On the other hand, each foot tip moves by a distance of  $S_f$  at the same time. There is no lateral sway of the body is considered during this gait and the COM travels at a constant speed of  $3S_f/T_{SW}$ .

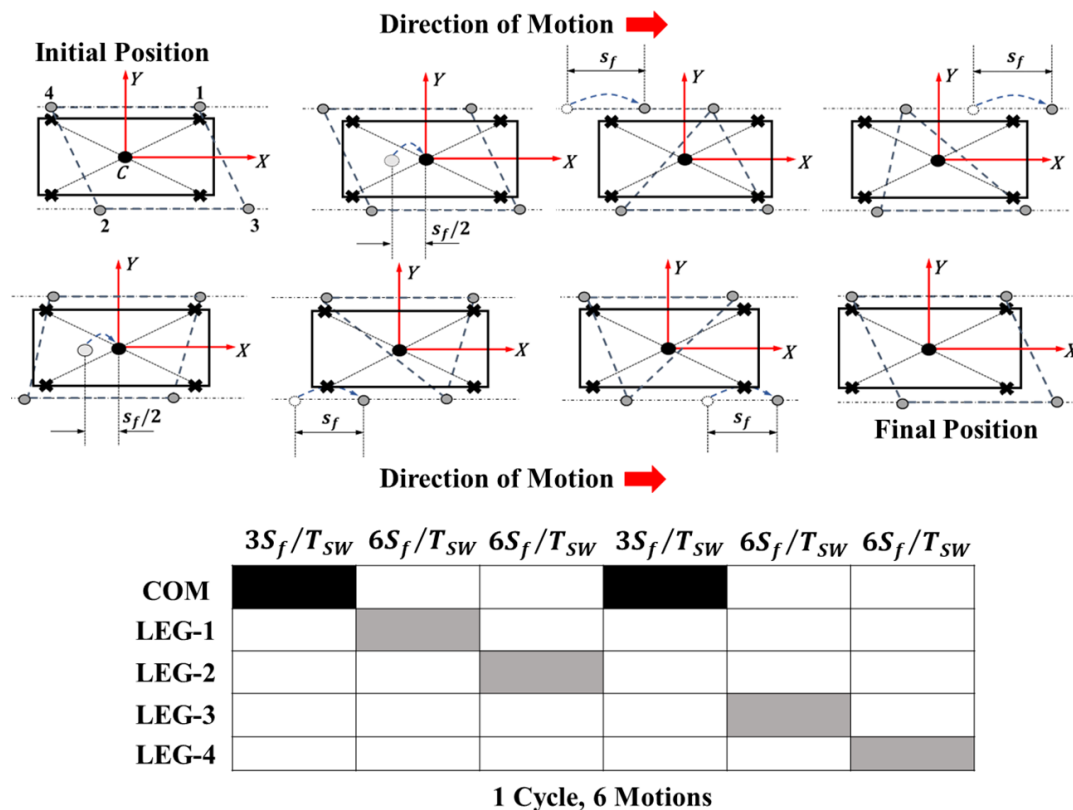


**Figure 2.15: Sequence of proposed static walk (SW) motion plan for serial-parallel manipulator**

### 2.7.3 Kinematic Model

After the design of a suitable motion plan, the kinematic model refers to the relationship among the linear motions of the actuators inside the cylinders for a particular motion of the individual foot tips and the body or torso of the serial-parallel manipulator. As the legs relate to the body at their corresponding anchor points, so the relative displacement between the foot tips of a particular leg with respect to their corresponding anchor points provides the connection to generate individual cylinder displacements of the corresponding legs. The relative displacement of the foot tips with respect to their corresponding anchor points can be expressed as,

$$x_{faj} = x_{fj} - x_{aj} \quad (2.12a)$$

$$y_{faj} = y_{fj} - y_{aj} \quad (2.12b)$$

$$z_{faj} = z_{fj} - z_{aj} \quad (2.12c)$$

For the serial manipulator stated above, the anchor point is always remains stationary, and the motion of the free point  $f$  is considered with respect to the fixed anchor  $a$ , where the origin of the coordinate system is fixed to analyze the motion of the free point along  $(xz)$  plane, where the coordinate of the free point at any instant for the activation of the kinematic model is denoted by  $(x_f, z_f)$ . However, in the present configuration as the body has also a motion, so also the individual anchor points  $(a_j)$ . Hence, the expressions (2.12a) and (2.12c) can be used in place of  $x_f$  and  $z_f$  in the kinematic model of serial manipulator.

The lower, upper, and transverse cylinder instantaneous piston positions for each leg can be thus obtained as  $(l_c l_r)_j, (u_c u_r)_j$  and  $(t_c t_r)_j$  respectively from the geometric configuration as discussed in context of Configuration II in Section 2.6.

From Figure 2.16 (a) and (b) the expression of  $\alpha_j, \beta_j$  and  $\theta_j$  can be written as-

$$\alpha_j = \pi - \delta_j - \beta_j - \cos^{-1}[\{(k_j l_{cj})^2 + (k_j l_{rj})^2 - (l_{cj} l_{rj})^2\} / \{2(k_j l_{cj})(k_j l_{rj})\}], \quad (2.13a)$$

$$\text{And } \beta_j = \pi - \phi_j - \cos^{-1}[\{(h_j u_{cj})^2 + (h_j u_{rj})^2 - (u_{cj} u_{rj})^2\} / \{2(h_j u_{cj})(h_j u_{rj})\}] \quad (2.13b)$$

$$\theta_j = \cos^{-1}[\{(a_j t_{cj})^2 + (a_j t_{rj})^2 - (t_{cj} t_{rj})^2\} / \{2(a_j t_{cj})(a_j t_{rj})\}] - \pi/2 \quad (2.13c)$$

From the above expression of  $\alpha_j, \beta_j$  and  $\theta_j$  the actual coordinate of the foot tip relative to the anchor point at any instant denoted by  $(x_{faj}, y_{faj}, z_{faj})$ , can be found from the below equations.



$$x_{faj} = (h_j k_j) \sin \beta_j + x_{hj} - (k_j f_j) \sin \alpha_j, \quad (2.14a)$$

Also, the height of the anchor points from the ground denoted by  $z_{aj}$  can be given as -

$$z_{aj} = z_{hj} - (h_j k_j) \cos \beta_j - (k_j f_j) \cos \alpha_j. \quad (2.14b)$$

The  $Y$  coordinate of the foot tip can be obtained after calculating the height of the anchor point  $z_{aj}$  with respect to the ground as

$$y_{faj} = -z_{aj} \tan \theta_j \quad (2.14c)$$

The height of the anchor point for all the legs are same, as the plane of the body is always remain horizontal with respect to the ground. The instantaneous height of the anchor from the ground is necessary to calculate the foot tip coordinates in the lateral direction given by the equation 2.14(c), the value of which for the motion plan stated above will become a constant and equal to  $b/2$ .

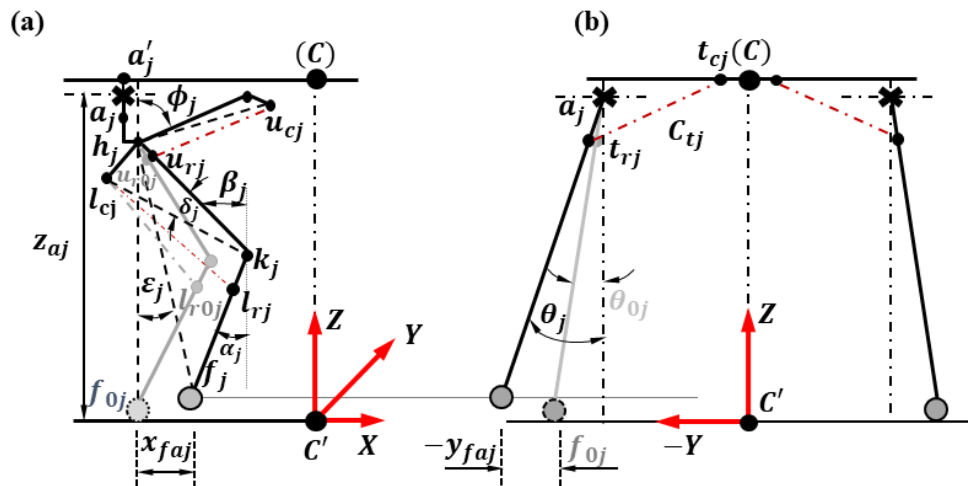


**Figure 2.16: Line diagram of initial and displaced leg configuration for serial-parallel manipulator**

## 2.8 Summary

The electrohydraulic flow model inducing piston motion detailed here for the three systems introduced above are used in three separate chapters for developing the proposed feedforward models. These models form the core contributions of the present work. With aging of the system, evolving internal changes call for reassessing several modeling parameters. Hence, an identification-based feedforward model has been constructed for the single-cylinder test bench. Chapter 3 contains its details of the corresponding feedforward

model. On the other hand, the necessary parameters in the new setup have been extracted from the relevant catalogue. A novel order-separated feedforward controller has been proposed not only for achieving good control performance, but also utilizing it for condition monitoring of the system through time-to-time identification experiments. For each of manipulator system, the multi-DOF kinematic formulations presented above have been exploited in the inverse form for extracting the demands in the actuation spaces corresponding to the specified output motions. In each of Chapters 4 and 5, the kinematics have been employed in the forward path for constructing the actual output from the real time actuation response.



# CHAPTER 3

## Controller Design and Real Time Analysis for Single Cylinder System

### 3.1 Introduction

The present chapter deals with design of feedforward position controller for an electrohydraulic motion actuation system and its real-time implementation along with PI feedback in a single-cylinder test bench depicted in Figure 2.1. In this chapter, the models developed in the last chapter have been utilized to formulate feedforward controllers, one following the conventional approach and another by a novel order-separated approach. Prior to executing the controller for performance analysis, a simple experiment has been carried out and parameters of both the feedforward models have been identified by carrying out an optimizer guided number of numerical simulations.

A feedforward controller is developed on the basis of a mathematical system model that can be manipulated to arrive at an explicit algebraic formulation of the command signal in terms of the demand and its derivatives. Such a system model is referred as differentially flat and the manipulation process is termed as the model inversion for instance by (Fliess et al. 1995; Kock and Ferrari 2012; Sira-Ramírez 2017). A differentially flat model allows a feedforward controller to compensate for the known disturbances and nonlinear effects. (Du et al. 2017; Fliss et al. 1995; Sahoo et al. 2018; Faessler et al. 2018; Sira-Ramírez et al. 2017) considered the variation of the pump pressure. Faessler et al. (2018) accounted for the rotor drag. But construction of a flat model is often not straight forward. In some recent investigations, model-free controllers were employed for electrohydraulic motion control. (Na et al. 2011) used a neural-network controller by training it on the basis of the available input-output data to extract the command input at the implementation stage corresponding to the desired response. (Mandal et al. 2016) developed a fuzzy controller that mimicks the operating procedure of a skilled worker. Such controllers cannot use the

command signal in an optimal manner for lacking the physical basis of model-based controllers. Some notable existing model-based controllers are the robust controller due to (Plummer 2007),  $H_\infty$  control with input linearization due to (Fales et al. 2009), pole-placement control due to (Daher & Ivantysynova 2014) and sliding-mode control due to (Dasmahapatra et al. 2018) and (Kaya and Bilgin 2019). Most of the flat models involves simplifying assumptions and approximations. Hence, a feedback part is combined with a dominating feedforward part. The domination yields a linearized equation for the error dynamics that can be exploited to undertake stability related decision for the overall controller. Such a stability analysis is hard and mostly not possible to carry out for model-free controllers.

A double-acting hydraulic cylinder is extremely popular in case both the extension and retraction strokes of the output motion require to follow a demand track. In a spring-loaded single-acting cylinder, only one of the strokes could be command controlled along with uncontrolled reversal under the forcing by the spring. Available feedforward models for double-acting cylinders in electrohydraulic systems developed for instance by (Kemmetmuller et al. 2007; Kock and Ferrari 2012; Kim et al. 2015) pertain to double-rod cylinders and fixed-displacement pumps. (Kock and Ferrari 2012; Kim et al. 2015) considered the cylinder friction to be a small part of the external load disturbance. (Kemmetmuller et al. 2007) compensated for the effect of oil compressibility but used an an additional impedance-matching scheme for compensating friction. Of course, the friction compensation improves the tracking capability of the controller, and the compressibility effect assumes greater importance at higher pressure in fast-response applications.

(Tripathi et al. 2016) used numerical solution of a nonlinear differential equation for a single-rod cylinder that worked well, as long as oil was taken as incompressible. But the consideration of oil compressibility made the overall model numerically stiff. (Destro & Negri 2018) could arrive at a common analytical frame for both single and double-rod cylinders, only for flow areas bearing a ratio matched with the ratio of the circumferential lengths of the valve ports metering the flows in the corresponding cylinder chambers. In real-life situations like the one investigated by (Chenoweth and Slaugh 1985), such matching may not exist. Oil leakage was ignored in all these models. (Sarkar et al. 2013a & b); Yao et al. 2017 & Feng et al. 2019) are among the researchers, who used existing friction models to estimate a compensation in terms of the motion demand for both single

and double-acting cylinders.

In comparison to a double-rod cylinder, a single-rod cylinder requires smaller space to accommodate the extension or retraction of the piston rod from one end of the cylinder, whereas the other end remains fully capped. In a review, (Quan et al. 2014) noted the compactness to be reason for the use of single-rod systems in 80% cases. (Mattila et al. 2017 & Du et al. 2017) used such cylinders for robotic systems. Though (Guo et al. 2019) obtained a strict feedback state-space model recently, its flatness has not been exploited yet to ascertain if it would resolve the stiffness issue faced by (Tripathi et al. 2016). (Daher & Ivantysynova 2014) used passive hydromechanical compensation arrangement in a variable-displacement pump providing matching pump flow with varying actuation requirement. Such an operation makes the system energy efficient. A feedforward controller was developed by (Du et al. 2017) in a system with such a pump by ignoring the effects of oil compressibility and cylinder friction.

The difficulty of compensating all the effects together by a differentially flat single feedforward model led to the development of advanced adaptive controllers, some of which are due to (Shi et al. 2015); Liu et al. 2020; Cheng et al. 2020 & Dao et al. 2021). In the combined feedforward-feedback controller employed by (Kemmetmuller et al. 2007; Kock and Ferrari 2012 & Kim et al. 2015), the feedforward compensates the known effects that in most cases dominate over the uncertainties and approximations tackled by the feedback part. Such a decoupled handling is more likely to be optimal than the adaptive controllers. Identification experiments necessary for estimating the feedforward parameters could be of different forms. Dedicated flow and pressure sensors were used by (Sarkar et al. 2013a & Feng et al. 2019) to characterize the individual feedforward models for the cylinder friction and pressure losses in the flow lines and the valve ports. In another approach, the same displacement sensor was used by (Sarkar et al. 2013b) & Faessler et al. 2018) both for the identification and providing the feedback to the motion controller.

In the light of the above discussions, the main objective of the present work has been set as designing feedforward controllers by a conventional approach and a novel-order separated scheme. The former controller has been developed for testing the acceptability of the novel controller, in which several restrictive features of the conventional design could be removed. A PI feedback has been added in both the cases. While the first design is referred hereafter as **CFFPI**, the latter one is referred as **OSFFPI**. Section 3.2 mentions the compositional differences between the two models and Sections 3.3 and 3.4 detail the

respective formulations. The adaptation of an existing **RCGA** optimizer that has been employed for extracting the feedforward parameters has been explained in Section 3.5. Section 3.6 details the estimation results for the two controllers. In Section 3.7, the stability conditions of these controllers are derived. The stability results are presented in Section 3.8. The performance of the two controllers is compared in Section 3.9. Section 3.10 summarizes the outcome and the mode of continuation of the remaining investigations.

## 3.2 Basic Controller Structure

An FFPI position controller depicted schematically in Figure 3.1 has been developed for a system with variable-displacement pump and low-cost as well as rugged pair of a single-rod double-acting cylinder and a proportional valve. If  $y_d$  is the position demand fed to the system in real time and  $y$  is the corresponding response obtained, the controller targets minimizing the error defined as

$$e = y_d - y. \quad (3.1a)$$

The control voltages for the FFPI controllers are evaluated as

$$V = V_f + v_b: v_b \ll V_f, \quad (3.1b)$$

where  $V_f$  and  $v_b$  are the feedforward and feedback parts with the latter obtained as

$$v_b = k_p e + k_i \int e dt, \quad (3.1c)$$

in terms a proportional (P) gain  $k_p$  and an integral (I) gain  $k_i$ . In the CFFPI scheme, a consolidated voltage  $V_f$  is directly estimated, as shown in Figure 3.2 unlike OSFFPI which considers a motive part  $V_{f0}$  that imparts oil flow between the paired valve and cylinder as the dominating part along with lower-order other parts. By representing the relatively smaller voltages  $v_{fl}$  to compensate for the valve leakage and  $v_{f\beta}$  linked with the compensating discharges for compressibility with respect to  $V_{f0}$ , the overall OSFFPI model as shown below in Figure 3.3 can be expressed as

$$V_f = V_{f0} + v_{fl} + v_{f\beta}. \quad (3.1d)$$

A major limitation of the CFFPI approach is the constraint on the ratio of oil-flow area within the cylinder bore across the piston. It is accepted the ratio is closely equal with the ratio of the peripheral lengths at the corresponding metering ports of the valve. This assumption in the real-life systems is often close, but not exact. The OSFFPI model is

neither constrained by the matching area-ratio assumption, nor whether the cylinder is of single or double-rod type. Both the models are based on a number of common system models. These are the piston dynamic model (2.1a) to (2.1c), the pressure dynamic model (2.4a) and (2.4b) in the two cylinder chambers and the pump-flow model (2.5a). Where the non-linear friction model given in (2.2a) corresponds to CFFPI model and even much simpler version (2.2b) conforms to OSFFPI. The model of oil through the valve ports to the respective cylinder chambers corresponding to the CFFPI model is given by (2.4c) to (2.4g), whereas those for the OSFFPI have been proposed as (2.4c) to (2.4f) along with (2.4h) and (2.4i). While the bell-shaped oil leakage model (2.3a) and (2.3b) at the valve has been used in the CFFPI scheme, the leakage model (2.3c) and (2.3d) in the OSFFPI scheme is an integral part of the flow model for the metered orifice.

Using (3.1a) in the piston dynamic model (2.1a), it is rewritten as

$$\dot{v}_d - \dot{e} = \ddot{y}_d - \ddot{e} = \{P_{cf}A_c - P_{rf}A_r - k(y_d - e) - F_f\}/m, \quad (3.2a)$$

where  $P_{1f}$  and  $P_{2f}$  are the chamber pressures respectively at the cap and rod-end chambers of the cylinder that would be estimated from the evolving model.

The nonlinear friction model (2.2a) used in the CFFPI controller is rendered by (3.1a) to the form

$$F_f = \{F_c + (F_s - F_c) \exp[-\{(\dot{y}_d - \dot{e})/v_s\}^2]\} \operatorname{sgn}(\dot{y}_d) + \alpha_v(\dot{y}_d - \dot{e}), \quad (3.2b)$$

The simpler model (2.2b) used in the OSFFPI controller yields

$$F_f = F_c \operatorname{sgn}(\dot{y}_d) + \alpha_v(\dot{y}_d - \dot{e}). \quad (3.2c)$$

The branch leakages (2.3b) corresponding to the bell-shaped leakage model (2.3a) particular to the CFFPI scheme is expressed in terms of feedforward pressures as

$$Q_{ld} = 2Q_{l0}[\exp(-\alpha_l\{(1 - P_{cf}/P_{rf})/(1 + P_{cf}/P_{rf})\}^2)] + Q_{l1}, \quad (3.2d)$$

$$Q_{Ad}^l = \sqrt{P_{cf}}Q_{ld}/(\sqrt{P_{cf}} + \sqrt{P_{rf}}) \text{ and } Q_{Bd}^l = \sqrt{P_{rf}}Q_{ld}/(\sqrt{P_{cf}} + \sqrt{P_{rf}}), \quad (3.2e)$$

And in terms of usual orifice discharge relation proportional to square-root of pressure drop, the leakage model corresponding to (2.3c) and (2.3d) can be expressed in terms of feedforward pressures as

$$Q_{ld} = Q_{Ad}^l + Q_{Bd}^l : Q_{Ad}^l = c_{lA}\sqrt{P_{cf}} \text{ and } Q_{Bd}^l = c_{lB}\sqrt{P_{pf} - P_{rf}} \text{ for } \dot{y} \geq 0, \quad (3.2f)$$

$$\text{and } Q_{ld} = Q_{Ad}^l + Q_{Bd}^l : Q_{Ad}^l = c_{lA}\sqrt{P_{pf} - P_{cf}} \text{ and } Q_{Bd}^l = c_{lB}\sqrt{P_{rf}} \text{ for } \dot{y} < 0, \quad (3.2g)$$



where  $c_{lA}$  and  $c_{lB}$  are the leakage constants at Ports **A** and **B**, respectively.

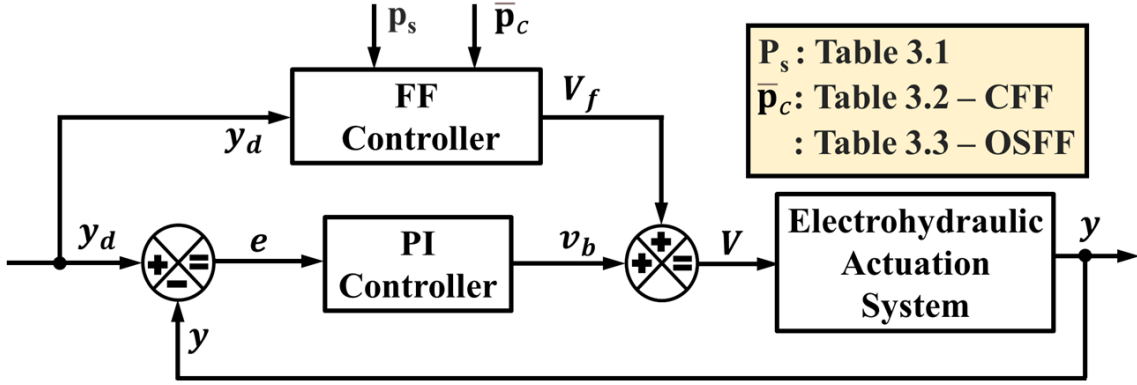


**Figure 3.1: Schematic illustration of the FFPI control structure**

Use of (3.1a) and the feedforward pressures in the pressure dynamic model (2.4a) and (2.4b) yields

$$\dot{P}_{cf} = \beta\{Q_A - A_c(\dot{y}_d - \dot{e})\}/\{V_{0c} + A_c(y_d - e)\}, \quad (3.2h)$$

$$\text{and } \dot{P}_{rf} = \beta\{A_r(\dot{y}_d - \dot{e}) - Q_B\}/\{V_{0r} - A_r(y_d - e)\}. \quad (3.2i)$$

By using both (3.1a) and (3.1b) along with the feedforward pressures, the flow through the metered orifices in the CFFPI model are expressed from (2.4c) to (2.4g) as

$$Q_{Af} = c_{vA}(V_f + v_b)\sqrt{P_{Pf} - P_{cf}} - Q_{Ad}^l \text{ for } \dot{y}_d \geq 0, \quad (3.2j)$$

$$\text{or, } Q_{Af} = c_{vA}(V_f + v_b)\sqrt{P_{cf}} - Q_{Ad}^l \text{ for } \dot{y}_d < 0, \quad (3.2k)$$

$$Q_{Bf} = c_{vB}(V_f + v_b)\sqrt{P_{rf}} - Q_{Bd}^l \text{ for } \dot{y}_d \geq 0, \quad (3.2l)$$

$$\text{or, } Q_{Bf} = c_{vB}(V_f + v_b)\sqrt{P_{Pf} - P_{rf}} - Q_{Bd}^l \text{ for } \dot{y}_d < 0. \quad (3.2m)$$

From (2.4c) to (2.4f) along with (2.4h) and (2.4i), the corresponding expressions for the OSFFPI model are obtained by putting (3.1a) and (3.1d) as

$$Q_{Af} = c_{vA}(V_{f0} + v_{fl} + v_{f\beta})\sqrt{P_{pf} - P_{cf}} - c_{lA}\sqrt{P_{1f}} \text{ for } \dot{y}_d \geq 0, \quad (3.2n)$$

$$\text{or } Q_{Af} = c_{vA}(V_{f0} + v_{fl} + v_{f\beta})\sqrt{P_{cf}} - c_{lA}\sqrt{P_{pf} - P_{cf}} \text{ for } \dot{y}_d < 0, \quad (3.2o)$$

$$\text{and } Q_{Bf} = c_{vB}(V_{f0} + v_{fl} + v_{f\beta})\sqrt{P_{rf}} - c_{lB}\sqrt{P_{pf} - P_{rf}} \text{ for } \dot{y}_d \geq 0, \quad (3.2p)$$

$$\text{or } Q_{Bf} = c_{vB}(V_{f0} + v_{fl} + v_{f\beta})\sqrt{P_{pf} - P_{rf}} - c_{lB}\sqrt{P_r} \text{ for } \dot{y}_d < 0. \quad (3.2q)$$

Finally, the feedforward pump pressure for both the models are expressed from (2.5a) as

$$P_{pf} = P_{ci}[2 + \coth\{(Q_{a\dot{y}_d} + Q_{a\beta} + Q_l - Q_{P0})/Q_c\}], \quad (3.2r)$$

Where for both the controller model pump discharge can be modeled as

$$Q_P = Q_{a\dot{y}_d} + Q_{a\beta} + Q_l; Q_{a\beta} \ll Q_{a\dot{y}_d}, Q_l \ll Q_{a\dot{y}_d}, \quad (3.2s)$$

comprised of a motive discharge imparting the piston motion given by

$$Q_{a\dot{y}_d} = A_c \max(\dot{y}_d, 0) - A_r \min(\dot{y}_d, 0), \quad (3.2t)$$

the compressibility related discharge in the cylinder chambers expressed as

$$Q_{a\beta} = \{\max(\dot{y}_d, 0)\dot{P}_{cf}(V_{0c} + A_c y_d) - \min(\dot{y}_d, 0)\dot{P}_{rf}(V_{0r} - A_r y_d)\}/\beta. \quad (3.2u)$$

On the basis of the above feedforward expressions, the controller design for the two feedforward models is taken up in the next two sections.

### 3.3 Conventional Feedforward Controller Design

Figure 3.2 corresponds to CFF control structure, the design algorithm of which is based upon a restrictive assumption for the ratio  $\lambda$  introduced in (2.4j). Since both the oil leakage through the valve and the compressibility-compensating discharges in the cylinder chambers are much lower than the total discharges at the metered ports, (3.2h) to (3.2k) can be approximated as

$$A_c \dot{y}_d = Q_{Af} = c_{vA} V_f \sqrt{P_{Pf} - P_{cf}} \text{ for } \dot{y}_d \geq 0, \quad (3.3a)$$

$$\text{or, } A_c \dot{y}_d = Q_{Af} = c_{vA} V_f \sqrt{P_{cf}} \text{ for } \dot{y}_d < 0, \quad (3.3b)$$

$$A_r \dot{y}_d = Q_{Bf} = c_{vB} V_f \sqrt{P_{rf}} \text{ for } \dot{y}_d \geq 0, \quad (3.3c)$$

$$\text{or, } A_r \dot{y}_d = Q_{Bf} = c_{vB} V_f \sqrt{P_{Pf} - P_{rf}} \text{ for } \dot{y}_d < 0. \quad (3.3d)$$

Last five expressions lead to the condition of equal pressure drop at the metered ports given by

$$P_{pf} - P_{cf} = P_{rf}. \quad (3.3e)$$

By combining the dominant parts of (3.2a) and (3.2b) with the pertinent pair among (3.3a) to (3.3d) together with using (3.3e), the feedforward voltage model is derived as

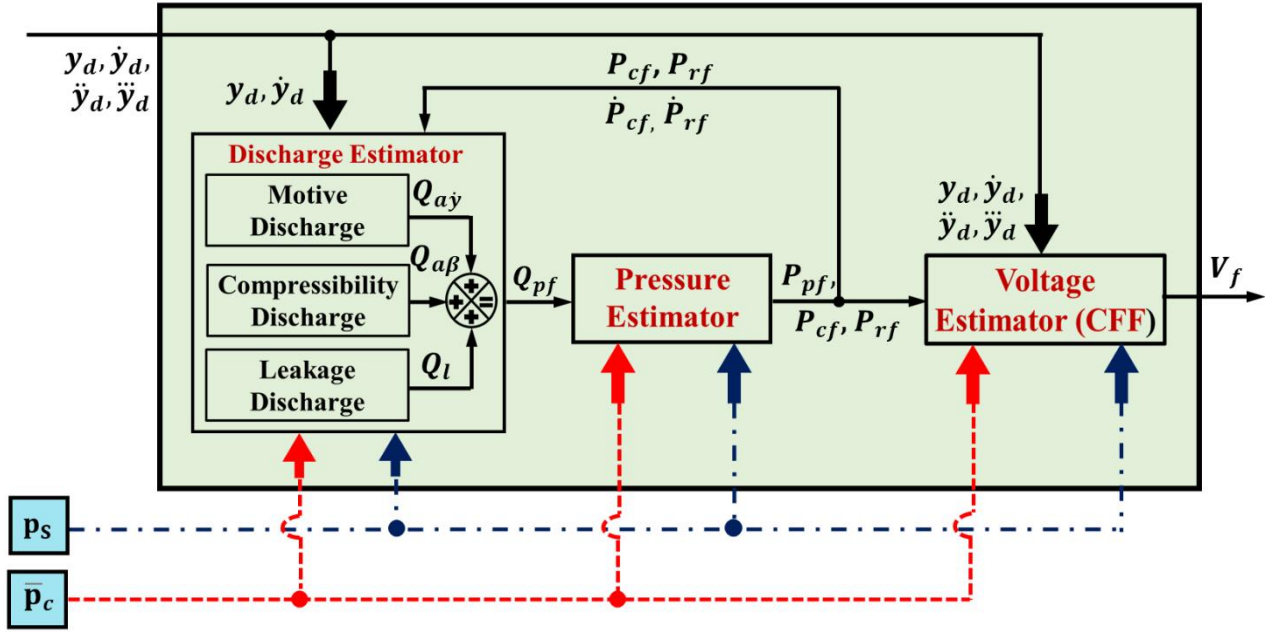


**Figure 3.2: Schematic illustration of conventional FFPI control structure**

$$V_f = [m\ddot{y}_d - \{2\dot{y}_d\dot{y}_d(F_s - F_c)/v_s^2\} \exp(-\dot{y}_d^2/v_s^2) \operatorname{sgn}(\dot{y}_d) + \alpha_v\dot{y}_d + k\dot{y}_d + \beta\dot{y}_d\{A_c^2/(V_{0c} + A_c y_d) + A_r^2/(V_{0r} - A_r y_d)\} + \beta A_c\{Q_A^l/(V_{0c} + A_c y_d) + \lambda Q_B^l/(V_{0r} - A_r y_d)\}]/$$

$$[\beta A_c c_{vA}\{1/(V_{0c} + A_c y_d) + \lambda^2/(V_{0r} - A_r y_d)\}] \times$$

$$\{\max \langle \operatorname{sgn}(\dot{y}_d), 0 \rangle (P_{Pf} - P_{cf}) + \min \langle \operatorname{sgn}(\dot{y}_d), 0 \rangle P_{cf}\}^{1/2}, \quad (3.4a)$$

where  $P_{cf} = [m\dot{y}_d + k y_d + \{F_s + (F_s - F_c) \exp(-\dot{y}_d^2/v_s^2) \operatorname{sgn}(\dot{y}_d) + \alpha_v \dot{y}_d + P_P A_r\}] \times$

$$(A_c + A_r)^{-1}, \quad (3.4b)$$

and  $P_{rf} = [P_{Pf} A_c - m\dot{y}_d - k y_d - \{F_s + (F_s - F_c) \exp(-\dot{y}_d^2/v_s^2) \operatorname{sgn}(\dot{y}_d) - \alpha_v \dot{y}_d\}] \times$

$$(A_c + A_r)^{-1}. \quad (3.4c)$$

By using (3.3e), the initial conditions of (3.2h) and (3.2i) at no load are set as

$$P_{cf0} = P_{pf0} A_r / (A_c + A_r) \text{ and } P_{rf0} = P_{pf0} A_c / (A_c + A_r). \quad (3.5a)$$

Starting from the initial time  $t$  equal to zero and using the updated pressures from (3.4b) and (3.4c) after every  $\delta t$  time, the pressure derivatives are easily computed as

$$\dot{P}_{cf} = (P_{cf}|_t - P_{cf}|_{t-\delta t})/\delta t, \quad (3.5b)$$

$$\text{and } \dot{P}_{rf} = (P_{pf} - P_{cf} - P_{rf})/\delta t. \quad (3.5c)$$

These updated pressures are the required inputs for (3.2u) for estimating the compressibility-compensating discharges. With this expression, the closure of the voltage

updating procedure is obtained.

In terms of a flowchart the Figure 3.2 has been represented for extracting the feedforward voltage from the formulation developed above for the CFFPI scheme. The figure clearly depicts three distinct module, viz. **Discharge Estimator**, **Pressure Estimator** and **Voltage Estimator**. The inputs of which are the actuator states comprised of the demand and its derivatives ( $y_d, \dot{y}_d, \ddot{y}_d, \ddot{y}_d$ ) and the model parameters, which are grouped in two parts. One part contains the known parameters ( $A_c, \lambda, \beta, m, k, c_{vA}, \Omega, Q_{P0}$ ) termed as system parameter  $\mathbf{p}_s$  the values of which are given in Table 3.1. The other part are the unknown parameters, grouped as hydraulic parameters ( $V_{0c}, V_{0r}, Q_{l0}, Q_{l1}, \alpha_l, P_{ci}, Q_c$ ) and cylinder friction parameters ( $F_s, F_c, v_s, \alpha_v$ ), together denoted as  $\mathbf{p}|_{\text{CFFPI}}$  given in (3.12b), needs to be identified by implementing some optimization routine in order to run the **CFFPI** model in real time.

Identification of these parameters have been accomplished here by adapting an existing offline optimization technique of real-coded genetic algorithm, or **RCGA**, employed earlier by Sarkar et al. (2013b). Table 3.2 given in section 3.6 shows the converged values of these unknown system parameters for **CFFPI** model after the execution of **RCGA** routine. The **Discharge Estimator** in Figure 3.2 pertains to the pump discharge model (3.2s) comprised of (3.2t) for the discharge sustaining the piston motion, (3.2u) for compensating oil compressibility and (3.2d) for the leakage through the valve. The **Pressure Estimator** in the diagram corresponds to (3.2r) for calculating pump pressure along with (3.4b) and (3.4c) for cylinder chamber pressures. The output of these modules is utilized in the manner depicted in the flowchart to estimate the feedforward voltage from (3.4a). This voltage together with a PI part evaluated from (3.1c) form the **CFFPI** controller voltage schematically shown by Figure 3.1 in a general manner. As the **CFFPI** controller has been developed in the conventional manner, it is prudent to utilize this for acceptability testing of the proposed order-separated feedforward controller. The formulation of the proposed model is given in the next section.

### 3.4 Order-Separated Feedforward Controller Design

The motivation for developing the order-separated feedforward controller arises from relaxing the restrictions imposed on developing a feedforward controller in a conventional manner involving a consolidated estimate of the feedforward compensation. In the

proposed model, the novelty pertains to the exploitation of the natural order-separated form for the oil discharge, the major part which sustains the piston motion as the motive discharge. With its respect, each of the other effects like discharges corresponding to the oil compressibility, leakage and the piston friction are of lower order. The strength of this non-iterative algebraic sequential estimation algorithm over the conventional scheme is its general applicability for any double-acting cylinder irrespective of whether it is single-rod or double-rod type. In fact, the model can be easily extended for a dual-tandem cylinder having back-to-back single and double-rod arrangements considered by (Shi et al. 2015).

The overall arrangement of the **OSFFPI** scheme is shown in Figure 3.3. Instead of (3.1a) to (3.1c) used for developing the **CFFPI** scheme, (3.1b) is replaced by (3.1d) in formulating the **OSFFPI**. A matched composition of the feedforward voltage in (3.4a) is assumed to be dominated by the flow-inducing major voltage  $V_{f0}$  and relatively smaller voltages  $v_{fl}$  to compensate for the valve leakage and  $v_{f\beta}$  linked with the compensating discharges  $Q_{A\beta}$  and  $Q_{B\beta}$  at the cap and rod-side chambers of the cylinder. The overall model is expressed as

$$V_f = V_{f0} + v_{fl} + v_{f\beta}, \quad (3.6a)$$

$$Q_{Af} = A_c \dot{y}_d + Q_{A\beta}, \quad (3.6b)$$

$$\text{and } Q_{Bf} = \lambda A_c \dot{y}_d + Q_{B\beta}. \quad (3.6c)$$

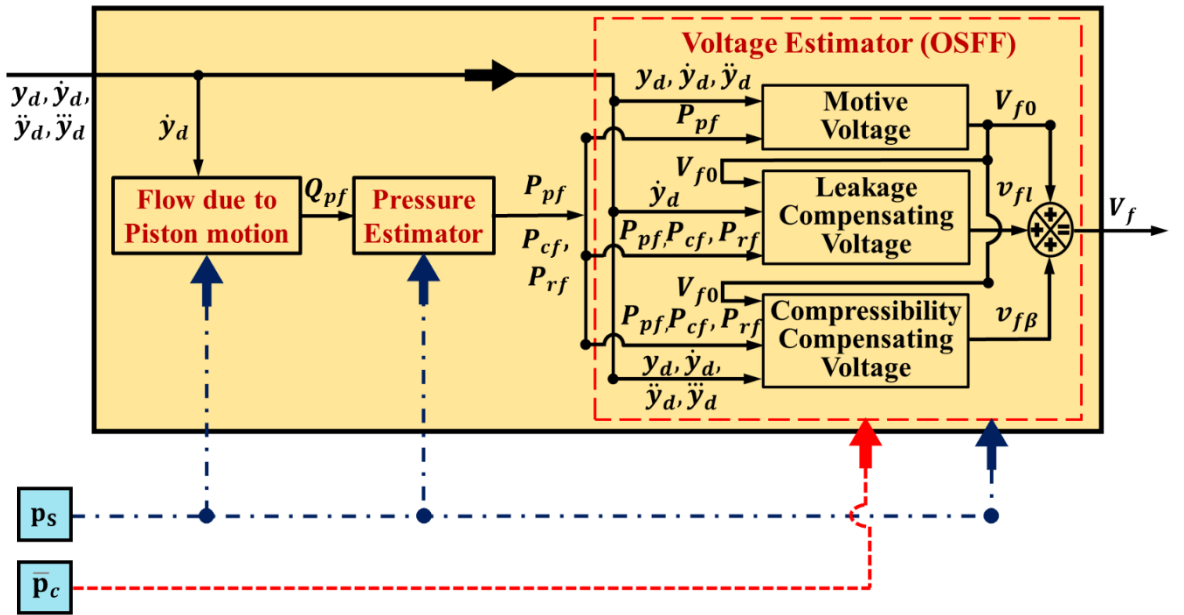


Figure 3.3: Schematic illustration of order separated FFPI control structure

Use of (3.6a) to (3.6c) allows (2.4c) to (2.4f) along with (2.4h) and (2.4i) to be rewritten respectively as

$$Q_{Af} = A_c \dot{y}_d + Q_{A\beta} = c_{vA}(V_{f0} + v_{fl} + v_{f\beta})\sqrt{P_{pf} - P_{cf}} - c_{lA}\sqrt{P_{cf}} \text{ for } \dot{y}_d \geq 0, \quad (3.7a)$$

$$Q_{Bf} = \lambda A_c \dot{y}_d + Q_{B\beta} = c_{vB}(V_{f0} + v_{fl} + v_{f\beta})\sqrt{P_{rf}} - c_{lB}\sqrt{P_{pf} - P_{rf}} \text{ for } \dot{y}_d \geq 0, \quad (3.7b)$$

$$Q_{Af} = A_c \dot{y}_d + Q_{A\beta} = c_{vA}(V_{f0} + v_{fl} + v_{f\beta})\sqrt{P_{cf}} - c_{lA}\sqrt{P_{pf} - P_{cf}} \text{ for } \dot{y}_d < 0, \quad (3.7c)$$

$$\text{and } Q_{Bf} = \lambda A_c \dot{y}_d + Q_{B\beta} = c_{vB}(V_{f0} + v_{fl} + v_{f\beta})\sqrt{P_{pf} - P_{rf}} - c_{lB}\sqrt{P_{rf}} \text{ for } \dot{y}_d < 0. \quad (3.7d)$$

By invoking (3.6b) and (3.6c) for negligible oil leakage and compressibility, the dominating feedforward model for the pump flow in (2.5b), (2.5c) and (2.5a) respectively emerge as

$$Q_{Pf} = A_c \dot{y}_d \text{ and } \lambda A_c \dot{y}_d \text{ respectively for } \dot{y}_d \geq 0 \text{ and } \dot{y}_d < 0, \quad (3.7e)$$

$$\text{and } P_{pf} = P_{ci}[2 + \coth\{(Q_{Pf} - Q_{P0})/Q_c\}]. \quad (3.7f)$$

The collection of the dominant terms in (3.7a) to (3.7d) yield

$$\dot{y}_d = (c_{vA}/A_c)V_{f0}\sqrt{P_{pf} - P_{cf}} = (c_{vB}/\lambda A_c)V_{f0}\sqrt{P_{rf}} \text{ for } \dot{y}_d \geq 0, \quad (3.8a)$$

$$\text{and } \dot{y}_d = (c_{vA}/A_c)V_{f0}\sqrt{P_{cf}} = (c_{vB}/\lambda A_c)V_{f0}\sqrt{P_{pf} - P_{rf}} \text{ for } \dot{y}_d < 0. \quad (3.8b)$$

On the basis of the above stated model for **OSFF**, the estimator blocks depicted in Figure 3.3 are constructed. The estimations corresponding to the different modules of the Figure 3.3 are explained below.

### 3.4.1 Estimation of Motion-Inducing Voltage and Chamber Pressures in the Cylinder

Use of (3.2a) and (3.2c) in (3.8a) and (3.8b) yields the expressions for the basic part of the feedforward voltage as

$$V_{f0}|_{\dot{y}_d \geq 0} = +A_c^3[\{\dot{y}_d^2(1/(c_{vA}^2) + \lambda^3/c_{vB}^2)\}/(P_{pf}A_c - m\ddot{y}_d - ky_d - F_c - \alpha_v\dot{y}_d)]^{1/2}, \quad (3.9a)$$

$$\text{or } V_{f0}|_{\dot{y}_d < 0} = -A_c^3[\{\dot{y}_d^2(1/(c_{vA}^2) + \lambda^3/c_{vB}^2)\}/(m\dot{y}_d + ky_d + F_c + \alpha_v\dot{y}_d - P_{pf}\lambda A_c)]^{1/2}.$$

$$(3.9b)$$

The pair (3.8a) and (3.9a) yields the feedforward estimates of the pressures in the cylinder chambers during the extension demand as

$$P_{cf}|_{\dot{y}_d \geq 0} = P_{pf} - \{\dot{y}_d A_c / c_{vA} V_{f0}\}^2, \quad (3.9c)$$

$$\text{and } P_{rf}|_{\dot{y}_d \geq 0} = \{\dot{y}_d \lambda A_c / c_{vB} V_{f0}\}^2. \quad (3.9d)$$

During the retraction demand phase, the pair (3.8b) and (3.9b) provides the estimates of the same variables as

$$P_{cf}|_{\dot{y}_d < 0} = \{\dot{y}_d A_c / c_{vA} V_{f0}\}^2, \quad (3.9e)$$

$$\text{and } P_{rf}|_{\dot{y}_d < 0} = P_{Pf} - \{\dot{y}_d \lambda A_c / c_{vB} V_{f0}\}^2. \quad (3.9f)$$

### 3.4.2 Estimation of Leakage-Compensating Voltage

By grouping the leakage dependent terms in (3.6a) and (3.7a) to (3.7d) along with using the pertinent pressures from (3.9c) to (3.9f), the leakage-compensating voltage is obtained as

$$v_{fl}|_{\dot{y}_d \geq 0} = \{(c_{lA}/c_{vA})\sqrt{P_{cf}}/\sqrt{P_{Pf} - P_{cf}} + (c_{lB}/c_{vB})\sqrt{P_{Pf} - P_{rf}}/\sqrt{P_{rf}}\}/2, \quad (3.10a)$$

$$\text{and } v_{fl}|_{\dot{y}_d < 0} = \{(c_{lA}/c_{vA})\sqrt{P_{Pf} - P_{cf}}/\sqrt{P_{cf}} + (c_{lB}/c_{vB})\sqrt{P_{rf}}/\sqrt{P_{Pf} - P_{rf}}\}/2. \quad (3.10b)$$

### 3.4.3 Estimation of Compressibility-Compensating Voltage

By substituting (3.6a) to (3.6c) in (3.7a) and (3.7b) and then use of (2.5l) leads to the expression for the compressibility-compensating voltage during the extension demand phase as

$$v_{f\beta}|_{\dot{y}_d \geq 0} = (m\ddot{y}_d + k\dot{y}_d + \alpha_v \dot{y}_d) / \{\beta(c_{vA} A_c \sqrt{P_{Pf} - P_{cf}}) / (V_{0c} + A_c y_d) + (c_{vB} \lambda A_c \sqrt{P_{rf} - P_T}) / (V_{0r} - \lambda A_c y_d)\}. \quad (3.11a)$$

The expression for the same voltage during the retraction demand phase is obtained by substituting (3.6a) to (3.6c) in (3.7c) and (3.7d) followed by using (2.5m) as

$$v_{f\beta}|_{\dot{y}_d < 0} = -(m\ddot{y}_d + k\dot{y}_d + \alpha_v \dot{y}_d) / \{\beta(c_{vA} A_c \sqrt{P_{cf} - P_T}) / (V_{0c} + A_c y_d) + (c_{vB} \lambda A_c \sqrt{P_{Pf} - P_{rf}}) / (V_{0r} - \lambda A_c y_d)\}. \quad (3.11b)$$

It is clear from (3.9a) to (3.9f), (3.10a), (3.10b), (3.11a) and (3.11b) that for implementation of **OSFFPI** model in real time, the known system parameters  $\mathbf{p}_s$  given in Table 3.1 are required and the unknown parameters  $\mathbf{p}|_{\text{OSFFPI}}$  as given in (3.12c) should be known beforehand like **CFPI**. Table 3.3 provides the optimized values of these unknown parameters for **OSFFPI**. A procedure for identifying such unknown parameters for both

**CFF** and **OSFF** is detailed in the next section in a general manner. In Sections 3.6 and 3.7, the estimation results for **CFFPI** and **OSFFPI** are given.

### 3.5 Parameter Identification Procedure

Optimization is an integral part of modern design for finding the globally best solution minimizing an objective function within certain constraints. A nonlinear system has multiple feasible solutions that are locally optimal. A real-coded genetic algorithm, or **RCGA**, earlier used by (Sarkar et al. 2013b) has been used here for estimating the global optimum solution defined in terms of the difference of the performance indices, one obtained by using the response of an experiment and the other predicted on the basis of numerical simulation. The experiment involves only a PI controller and a sinusoidal position demand of frequency  $f$  and amplitude  $a$  resulting in

$$y_d = a \sin(2\pi ft + 3\pi/2) + a. \quad (3.12a)$$

A P gain of 180V/m, I gain of 100V/(m-s),  $a$  of 20mm and  $f$  of 1.5Hz have used in the experiment.

The simulation uses the pertinent feedforward model in open loop involving a parameter vector  $\mathbf{p}$  and the variation of the input command identical to the experiment. Table 3.1 lists the values of the known parameters used in all the simulation runs. The vector corresponding to the conventional and the order-separated feedforward models respectively are

$$\mathbf{p}|_{\text{CFFPI}} = (F_s, F_c, v_s, \alpha_v, V_{0c}, V_{0r}, Q_{10}, Q_{11}, \alpha_l, P_{ci}, Q_c)^T, \quad (3.12b)$$

$$\text{and } \mathbf{p}|_{\text{OSFFPI}} = (F_c, \alpha_v, V_{0c}, V_{0r}, Q_c, P_{ci})^T. \quad (3.12c)$$

Genetic algorithms are heuristic search algorithms that mimic the process of evolution of biological species based on survival of the fittest theory. In the present scenario, the difference of the performance indices to be minimized is defined as

$$I_\delta = \int_0^{nT} |y_p(t) - y(t)| dt, \quad (3.12d)$$

Where Figure 3.4 shows  $y(t)$  is the displacement of the piston in the real-time experiment and  $y_p(t)$  is the open loop simulation-predicted response obtained as output from the numerical simulator corresponding to the same voltage variation  $V$ , noted in the experiment. For the computation of  $I_\delta$ , three consecutive demand cycles have been



considered. In other words,  $n$  has been set as 3 in (3.12d).

The **RCGA**-guided prediction executes a search between the specified lower bound  $\mathbf{p}_1$  and upper bound  $\mathbf{p}_2$  beginning with the first generation consisting of ten set of values of the parameters selected randomly between the vector bounds. Subsequent generations are obtained through three steps. The first step pertains to the selection of the fittest candidates by Roulette wheel selection method. A parameter vector, which is called a candidate or offspring in general terms, stands higher probability of selection for multiple times, if it returns the lowest  $I_\delta$  through (3.12d).

In the next step of **BLX- $\alpha$**  crossover that has been randomly executed by setting  $\alpha$  equal to 0.5, five pairs are randomly formed out of the ten-candidate surviving the fitness test. The random execution is enabled, if a random value selected falls above the crossover-enabling set value of 0.6. For an enabled pair, the **BLX- $\alpha$**  crossover expands the parameter range on each side by half of the difference of the respective scalar values in the vector pair subjected to the constraint of the lower and upper bounds. The crossover is executed in terms of two selected random values, each returning an interpolated parameter value within the expanded range. A **non-uniform mutation** is executed in the third step, with its probability of execution reducing as the solution progresses over generations to convergence as the change of minimum  $I_\delta$  falls below a limit termed as  $\varepsilon_1$ .

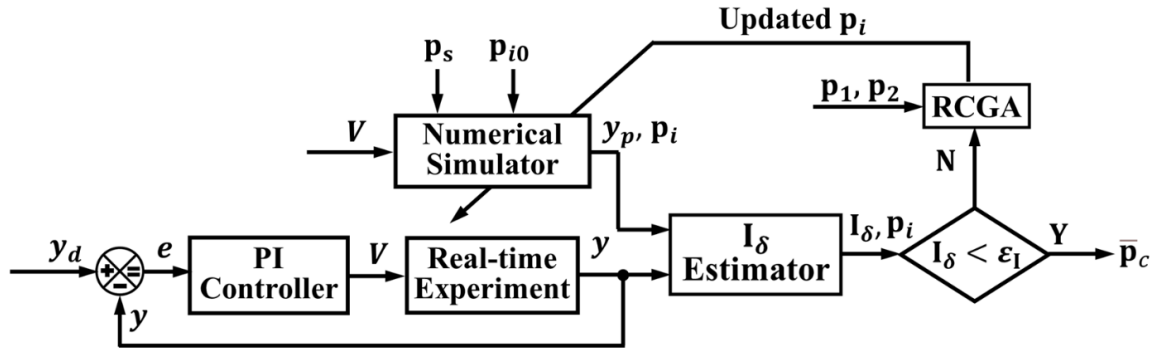


**Figure 3.4 Block diagram for RCGA based parameter Identification**

The simulation runs have been performed in **Matlab-Simulink** with *ODE1 Euler solver* with a time step of  $10^{-6}$ s. By carrying out the minimization for fifty times, the converged parameter sets along with their mean and standard deviation have been found out respectively as

$$\mathbf{p}_{ci} = \min_{\mathbf{p} \in (\mathbf{p}_1, \mathbf{p}_2)} I_\delta \text{ for } i = 1 \text{ to } 50, \quad (3.12e)$$

$$\bar{\mathbf{p}}_c = (\sum_{i=1}^{50} \mathbf{p}_{ci})/50, \quad (3.12f)$$

$$\text{and } \mathbf{SD} = 100[\{\sum_{i=1}^{50}(\mathbf{p}_{ci} - \bar{\mathbf{p}}_c)(\mathbf{p}_{ci} - \bar{\mathbf{p}}_c)^T\}/50]^{1/2}/\bar{\mathbf{p}}_c. \quad (3.12g)$$

**Table 3.1** Specified System Parameters  $\mathbf{p}_s$

Symbol	$A_c$	$\lambda$	$\beta$	$m$	$k$	$c_{vA} = 2c_{vB}$	$c_{lA} = 2c_{lB}$	$\Omega$	$Q_{P0}$
Unit	$10^{-3}$ m <sup>2</sup>	-	$10^9$ MPa	kg	N/mm	$10^{-8}$ m <sup>3.5</sup> V <sup>-1</sup> kg <sup>-1/2</sup>	$10^{-9}$ m <sup>3.5</sup> kg <sup>-1/2</sup>	-	$10^{-4}$ m <sup>3</sup> s <sup>-1</sup>
Value	1.256	0.75	1.3	2.5	20	3.46	3.8	0.66	8.3

The initial bounds for  $F_s$ ,  $F_c$ ,  $v_s$  and  $\alpha_v$  have been set from an earlier work by Sarkar et al. (2013b). Experimental data available in the work of (Mondal et al. 2019) have been used to set the bounds of  $V_{0c}$ ,  $V_{0r}$ ,  $P_{ci}$  and  $Q_c$ . The bounds for the valve coefficients and the leakage coefficients have been set by consulting the catalogue of (Bosch Rexroth AG Hydraulics 2012). In the present work, the entire optimization process has clearly been executed in the offline mode. The corresponding results are discussed in the next two sections.

### 3.6 Estimation of Feedforward Parameters

Within the lower bound  $\mathbf{p}_1$  and the upper bound  $\mathbf{p}_2$  given in Tables 3.2 and 3.3, Figure 3.4 shows the process of convergence of the minimum  $I_\delta$  value defined by (3.12d) for both the conventional and order-separated feedforward parameter sets given respectively by (3.12b) and (3.12c). These tables also contain the converged parameter mean  $\bar{\mathbf{p}}_c$  defined by (3.12f). The initial fluctuation of  $I_\delta$  in the figure may be attributed to the **non-uniform mutation** employed here, whose probability of relocating a parameter away from the expected good locations after crossover keeps on reducing over later generations. Relatively higher enablement of mutation during the initial stage allows exploring newer part of the domain containing the global optimum. However, the occasional increase in  $I_\delta$  in a later generation suggest the relocation to yield poorer solutions prior to coming to a matured stage. Much faster convergence evident in Figure 3.5 for the OSFF model in comparison to the **CFF** model is presumably due to the involvement of only six parameters in (3.12c) against eleven parameters in (3.12b) for the conventional scheme.

The outcome of the identification study are the converged values and the standard deviation defined in (3.12f) and (3.12g) that are also listed in Tables 3.3 and 3.4. Despite the differences in the parameter sets in (3.12b) and (3.12c) for the two feedforward schemes, similar converged values of  $Q_c$  and  $P_{ci}$  related to the pump and  $V_{0c}$  and  $V_{0r}$  for the volumes

of the cylinder chambers do not differ much. The differences are quite acceptable in a multi-parameter setting of a nonlinear system. Of course, the PI controller in the feedback loop evident in Figure 3.1 takes care of such minor differences and uncertainties in the estimation of the feedforward parameters.

In a simulation run, the mean of the lower and upper bounds given in Table 3.3 for each parameter has been used to predict the time variation  $y_p$  for the piston displacement. These plots are presented in Figure 3.6 for the three widely differing gain combinations. Clearly, the predictions remain bounded well within safe limit of 200mm strokes of both the cylinder and the LVDT of the setup shown in Figure 2.1. A safe containment of the stroking demonstrated in the figure provides confidence for executing an experimental identification run in real time by using those gain values. Despite a better mean-parameter prediction revealed in the figure for a higher proportional gain of 5000V/m, the lower proportional gain of 180V/m in combination 100V/(m-s) integral gain has been used as the default setting so as to avoid any voltage saturation during the stability analysis and the detailed experimental study. The other reason of the choice is its prediction emerging much closer to the best combination of 5000V/m and 100V/(m-s) than that predicted for the combination of 180V/m and 1V/(m-s).

**Table 3.2** Bounds and converged system parameters for **CFF** model

<b>Symbol</b>	$F_c$	$F_s$	$\alpha_v$	$v_s$	$V_{0c}$	$V_{0r}$	$Q_{10}$	$Q_{11}$	$\alpha_l$	$Q_c$	$P_{ci}$
<b>Unit</b>	N	N	N- s/m	mm/s	$10^{-4}$ m <sup>3</sup>	$10^{-4}$ m <sup>3</sup>	$10^{-5}$ m <sup>3</sup> /s	$10^{-5}$ m <sup>3</sup> /s	-	$10^{-5}$ m <sup>3</sup> /s	MPa
<b>p<sub>1</sub></b>	45.0	70.0	400.0	1.0	3.00	2.80	2.50	0.415	0.0008	1.25	12.00
<b>p<sub>2</sub></b>	60.0	90.0	550.0	7.0	3.50	3.20	4.17	1.250	0.0020	3.45	13.00
<b>p<sub>c</sub></b>	<b>55.0</b>	<b>85.0</b>	<b>482.0</b>	<b>5.17</b>	<b>3.40</b>	<b>3.10</b>	<b>3.72</b>	<b>1.150</b>	<b>0.0015</b>	<b>2.50</b>	<b>12.77</b>
<b>SD</b>	2.92	2.85	13.17	0.453	0.2437	0.1382	0.16	0.00296	0.00023	0.167	0.153
<b>SD</b> <b>(%mean)</b>	<b>4.69</b>	<b>3.35</b>	<b>2.73</b>	<b>8.31</b>	<b>7.17</b>	<b>4.45</b>	<b>4.30</b>	<b>0.257</b>	<b>15.33</b>	<b>6.68</b>	<b>1.19</b>

**Table 3.3** Bounds and converged system parameters for OSFF model

Symbol	$F_c$	$\alpha_v$	$V_{0c}$	$V_{0r}$	$Q_c$	$P_{ci}$
Unit	N	N-s/m	$10^{-4}$ m <sup>3</sup>	$10^{-4}$ m <sup>3</sup>	$10^{-5}$ m <sup>3</sup> s <sup>-1</sup>	MPa
Lower bound, $p_1$	45	400	3.0	2.8	1.25	12
Upper bound, $p_2$	60	550	3.5	3.2	3.45	13
Converged mean, $\bar{p}_c$	<b>53.1</b>	<b>461.6</b>	<b>3.30</b>	<b>3.05</b>	<b>1.7</b>	<b>12.8</b>
SD	2.75	14.77	0.115	0.163	0.172	0.132
SD (%mean)	<b>5.14</b>	<b>3.2</b>	<b>3.68</b>	<b>5.25</b>	<b>8.6</b>	<b>1.03</b>

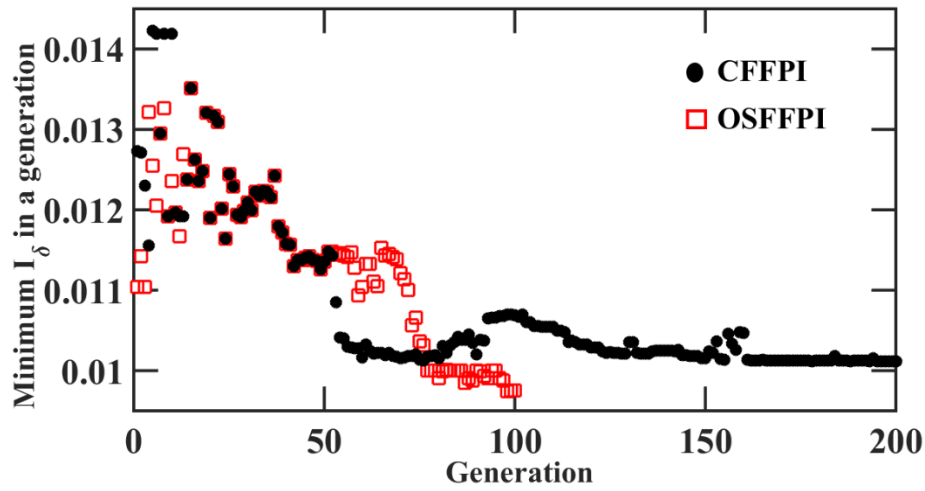


**Figure 3.5:** Parameter estimation for the proposed feedforward models

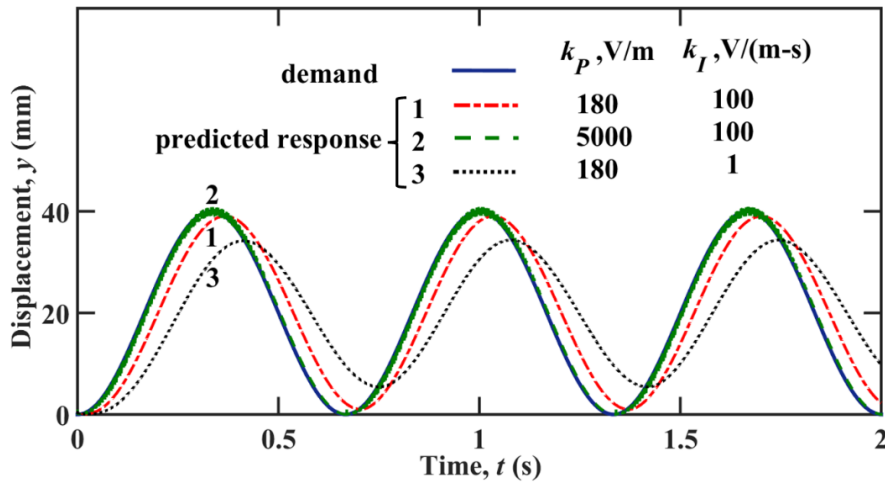


**Figure 3.6:** Predicted variations of responses with time for different gains and fixed parameter values

The overall system attains a fourth-order structure due to the third-order motion dynamics evident in (2.51) and (2.5m) and the PI controller. Any order greater than two requires a

stability analysis over and above the positivity coefficients. The next section details the proposed stability approach for the CFFPI and OSFFPI controllers.

### 3.7 Proposed methodology for Controller Stability Assessment

The backbone of the stability analysis is formed by the functions  $f_i$  with  $i$  equal to 1 to 5, where (2.5a) contains  $f_1$ , the pair (2.5b) and (2.5c)  $f_2$ , the pair (2.5d) and (2.5e)  $f_3$ , the pair (2.5f) and (2.5g)  $f_4$  and the pair (2.5l) and (2.5m)  $f_5$ . Their generalized derivative is expressed as

$$f_{i_x} = \partial f_i / \partial x |_{(y_d, \dot{y}_d, \ddot{y}_d, P_{Pf}, P_{cf}, P_{rf}, V_f)} \text{ with } x = y, \dot{y}, \ddot{y}, P_p, P_c, P_r \text{ and } V, \quad (3.13a)$$

for composing a linearized model about any operating point  $(y_d, \dot{y}_d, \ddot{y}_d, P_{Pf}, P_{cf}, P_{rf}, V_f)$  by neglecting the terms beyond the first order in Taylor series expansion of (3.13a). Of course, the first order derivatives are related to the perturbation about the demand in case of error (3.1a) and about the feedforward component for the other variables. These expansions are given next.

From (2.5l) and (2.5m), the equation for the error dynamics is thus expressed as

$$\ddot{e} \approx \ddot{y}_d - \ddot{y} = f_{5_{\ddot{y}}} \ddot{e} + f_{5_{\dot{y}}} \dot{e} + f_{5_y} e + f_{5_V} v_b + f_{5_{P_p}} p_p + f_{5_{P_c}} p_c + f_{5_{P_r}} p_r. \quad (3.13b)$$

Similar treatment for the pair (2.5b) and (2.5c) and then for (2.5a) yield the perturbation of the discharge and pressure at the pump delivery as

$$q_p \equiv Q_p - Q_{Pf} \approx f_{2_V} v_b + f_{2_{P_p}} p_p + f_{2_{P_c}} p_c + f_{2_{P_r}} p_r, \quad (3.13c)$$

$$\text{and } p_p = P_p - P_{Pf} \approx f_{1_{Q_p}} q_p. \quad (3.13d)$$

In the same manner, the pressure perturbations in the cylinder are obtained from the pair (2.5d) and (2.5e) for the cap-end chamber and from the pair (2.5f) and (2.5g) for the rod-end chamber respectively as

$$p_c = P_c - P_{cf} \approx f_{3_{P_p}} p_p - f_{3_{\ddot{y}}} \ddot{e} - f_{3_{\dot{y}}} \dot{e} - f_{3_y} e, \quad (3.13e)$$

$$\text{and } p_r = P_r - P_{rf} \approx f_{4_{P_p}} p_p - f_{4_{\ddot{y}}} \ddot{e} - f_{4_{\dot{y}}} \dot{e} - f_{4_y} e. \quad (3.13f)$$

Elimination of  $v_b$ ,  $p_p$ ,  $p_c$ ,  $p_r$  and from (3.13b) by using (3.1a) and (3.13d) to (3.13f), the error dynamics is expressed as

$$f(t) \equiv \ddot{e} + a_2 \dot{e} + a_1 e + a_0 e + a_{-1} \int e dt = \delta, \quad (3.14a)$$

where the expressions for the coefficients  $a_2, a_1, a_0$  and  $a_{-1}$  respectively with dimensions  $s^{-1}, s^{-2}, s^{-3}$  and  $s^{-4}$  are given in the APPENDIX and  $\delta$  stands for the neglected higher order terms. **Laplace transform** of the above equation yields the characteristic polynomial and the characteristic equation respectively as

$$\int f(t)\exp(-st)dt \equiv F(s)[\int\{(\int edt)\exp(-st)\}dt], \quad (3.14b)$$

$$\text{and } F(s) \equiv s^4 + a_2s^3 + a_1s^2 + a_0s + a_{-1} = 0 \text{ with } (a_2, a_1, a_0, a_{-1}) > 0, \quad (3.14c)$$

$$\text{where } s = \sigma + j\omega \text{ with } j = \sqrt{-1}, \quad (3.14d)$$

along with the conditions in (3.14c) need to be fulfilled by positive values for the coefficients at every operating point. The characteristic equation (3.14c) is of fourth order, Routh array for which is expressed as

$$R = [r_{ij}] \text{ with } i= 1 \text{ to } n \text{ and } j= 1 \text{ to } (n + 2)/2, \quad (3.14e)$$

with  $n$  equal to 4 in (3.14e). The coefficients in the first two rows of (3.14e) are used to form an even and odd pair of polynomials respectively as

$$F_4(s) = s^4 + a_1s^2 + a_{-1}s^0, \quad (3.14f)$$

$$\text{and } F_3(s) = a_2s^3 + a_0s. \quad (3.14g)$$

Next, the coefficients of the subsequent alternate even and odd polynomials of reducing orders of  $s$  are written in the manner, for instance to that of (Meinsma 1995), as

$$r_{kj}(s) = r_{k-2,2} - (r_{k-2,1}/r_{k-1,1})r_{k-1,2} \text{ for } 3 \leq k \leq (n + 1) \text{ and } 1 \leq j \leq (n + 2)/2, \quad (3.14h)$$

along with the corresponding polynomials for each  $k$  in one of the conditions above

$$F_{n-k+1}(s) = \sum_{j=1}^{(n+2)/2} [r_{k-2,2} - (r_{k-2,1}/r_{k-1,1})r_{k-1,2}]s^{n-k+3-2j}, \quad (3.14i)$$

and the complete Routh table as

$$\left. \begin{array}{l} F_4(s) \equiv O(s^4): \quad r_{11} = 1 \quad r_{12} = a_1 \quad r_{13} = a_{-1}, \\ F_3(s) \equiv O(s^3): \quad r_{21} = a_2 \quad r_{22} = a_0 \quad r_{23} = 0, \\ F_2(s) \equiv O(s^2): \quad r_{31} = a_1 - a_0/a_2 \quad r_{32} = a_{-1} \quad r_{33} = 0, \\ F_1(s) \equiv O(s^1): \quad r_{41} = a_0 - a_2a_{-1}/r_{31} \quad r_{42} = 0 \quad r_{43} = 0, \\ F_0(s) \equiv O(s^0): \quad r_{51} = a_{-1} \quad r_{52} = 0 \quad r_{53} = 0, \end{array} \right\} \quad (3.14j)$$

by adding zeros, wherever necessary so as to have equal number of coefficients in all the rows.

The polynomial form (3.14c) could be achieved by recombining (3.14f) and (3.14g) as one particular outcome  $Q_{1,0}(s)$  with  $k$  equal to 1 and  $\mu$  equal to 0 of in the family described in terms of the integer  $k$  and the real-valued  $\mu$  defining

$$Q_{k,\mu}(s) = F_{n-k+1}(s) + (1 - \mu s)F_{n-k}(s) \text{ with } 1 \leq k \leq n \text{ and } \mu \in R. \quad (3.15a)$$

In the family (3.15a),  $Q_{k,0}(s)$  represents a branch with  $\mu$  equal to zero signifying the addition of two successive polynomials yielding

$$Q_{k,0}(s) = F_{n-k+1}(s) + F_{n-k}(s), \quad (3.15b)$$

in which first summation  $Q_{1,0}(s)$  of successive odd-even polynomials leads to (3.14c). Of course, any characteristics polynomial with positive coefficients can be viewed to be composed of factors that contain the highest power of  $s$  either equal to 1 or 2 with positive real coefficients and the solution of the quadratic factor equal to zero yields complex conjugate roots. The factor with the highest power  $s$  equal to one and positive coefficients indeed gives rise to a negative zero of the polynomial (3.14c) implying its stability. Hence, the quadratic factors with positive coefficients and complex conjugate roots need attention for the assessment of the stability behavior.

Clearly, the order of polynomial  $Q_{k,\mu_{ck}}(s)$  for

$$\mu_{ck} = r_{k1}/r_{k+1,1}, \quad (3.15c)$$

is one less than to that of  $Q_{k,0}(s)$  that is induced in view of (3.14i) by the subtractive term in (3.15a) for the value (3.15c) along with the additive terms in (3.15a) forming the polynomial (3.15b). In other words, the orders of  $Q_{k+1,\mu_{ck}}(s)$  and  $Q_{k,0}(s)$  are identical. Hence, the entire process of reduction of  $k$  from  $n$  in steps of 1 to 0 through the branch  $Q_{k,\mu}(s)$  with continuous change of  $\mu$  from 0 to  $\mu_{ck}$  given by (3.15c) for each  $k$  is indeed continuous. The approach to  $Q_{k+1,\mu_{ck}}(s)$  can viewed as the coefficient of the leading quadratic factor in  $Q_{k+1,\mu}(s)$  approaching zero through a small  $\epsilon$ . By rewriting the quadratic factor in the limit of a small  $\epsilon$  and processing it shown below as

$$\epsilon s^2 + bs + c = 0 \approx \epsilon s^2 + (b + \epsilon c/b)s + c = 0 \Rightarrow s = -c/b, -b/\epsilon, \quad (3.15d)$$

the movement of the second root to infinity through the left-half of  $\sigma$ - $\omega$  plane can be appreciated if the ratio in (3.15d) is positive. This implies migration of one zero in a

quadratic factor with negative real parts through the left-half plane all along. The pair  $F_{n-k+1}(s)$  and  $F_{n-k}(s)$  in (3.15a) always remains an even-odd combination of successive orders and their common zeros are zeros of  $Q_{k,\mu}(s)$  and  $Q_{k,0}(s)$  too. Consequent to the order reduction of  $Q_{k,\mu}(s)$  to  $Q_{k+1,\mu}(s)$  at their connection point at  $\mu_{ck} = r_{k1}/r_{k+1,1}$ , a continuous variation of  $\mu$  with occasional discrete increase of  $k$  from one to  $n$  at  $\mu_{ck}$  eventually yields a polynomial of order one with negative zero. Of course, a negative zero in a first-order characteristic equation implies a stable system. The form of (3.15c) indicates that all migration takes place through the left-half plane for a positive coefficient vector involving those in the first column of (3.14j) represented as

$$C_1 \equiv (1 \quad a_2 \quad r_{31} \quad r_{41} \quad a_{-1})^T > \mathbf{0}^T. \quad (3.15e)$$

Such a migration was envisaged by (Meinsma 1995) as a process within a continuous family. The compliance with (3.15d) for (3.14c) implies it to represent a stable system with all the zeros containing a negative real part. This continuity argument is extended now for the linear time-varying form of (3.14c) to involve shift of the operating point as well at close intervals. This shift could be viewed as a continuous change in the coefficient values in (3.14c) from one constant set to another at a rate slower than that of  $\mu$ . As long as (3.15e) is not violated, (3.14c) clearly remains stable. This is an important finding of the analysis presented here. Over and above the positive coefficients in condition statements under (3.14c), the compliance with (3.15e) raises additional constraints from (3.14j) found as

$$0 < r_{31} < a_1 \text{ and } 0 < r_{41} < a_0. \quad (3.15f)$$

Based on the formulation given above, the stability assessment begins with deriving the expressions for the coefficients  $a_2$ ,  $a_1$ ,  $a_0$  and  $a_{-1}$  in (3.14c) in terms of the differentials of five functions appearing in the right side of (3.13a). The function  $f_1$  pertains to the pump characteristics given by (2.5a). Each of the other functions are expressed as a pair depending on the sign of the excitation voltage that in turn is related to the opposite sign of the displacement demand corresponding to the power connections set to the valve solenoids. It may be noted that the function  $f_2$  in (2.5b) and (2.5c) involves the leakage term that in case of CFFPI is given by (2.4g) and for OSFFPI by (2.4h) and (2.4i). The function  $f_3$  is introduced in (2.5d) and (2.5e),  $f_4$  is in (2.5f) and (2.5g) and  $f_5$  is in (2.5l) and (2.5m). A look in the Appendix makes it evident that the involvement of  $f_2$  in  $D$  expressed by (A9) makes the coefficient values determined from (A1) to (A4) different for the two FFPI models. The task of the stability assessment is finally accomplished by



evaluating  $r_{31}$  and  $r_{41}$  from (3.14g) and testing their compliance to (3.15f). Results of this test for the two controllers are discussed in the next section.

### 3.8 Controller Stability for CFFPI and OSFFPI Controllers

The controller stability is ensured by positive coefficients in (3.14c) that comply with (3.15e) and (3.15f). Of course,  $a_2$  and  $a_1$  could be maintained positive over a certain range of frequencies in the demand form (3.12a). For its values between 0.1Hz and 3Hz, the variations of the stability coefficients are evaluated over a cycle with 20mm amplitude. These results are depicted in Figs. 3.7 to 3.9 for the **CFFPI** and **OSFFPI** controllers. Of course, the different nature of variations for the two controllers are justifiable due to the use of different friction models (3.2b) and (3.2c) in the **CFFPI** and **OSFFPI** controllers respectively along with leakage models (3.2d) and (3.2e) for the **CFFPI** case and (3.2f) and (3.2g) for the **OSFFPI** case.

In all the figures, the variation of the coefficients beyond the initial time appears greater than zero for the combination of P gain of 180V/m and I gain of 100V/(m-s) indicating the fulfilment of the stability criteria.

In Figs. 3.7a and 3.7b, pertaining to the **CFFPI** controller, the strong influence of the friction model (3.2b) on  $a_2$  and  $a_1$  is evident corresponding to the sharp rise of the static friction over a phase about each velocity reversal in the demand (3.12a) that are apparent in Figure 3.6 at the beginning, middle and end of a cycle. With increase in the frequency, the variation over these phases clearly becomes sharper. The subsequent changes of the trend observed in Figure 3.7a in case of the three highest frequencies are consistent with the decreasing Stribeck friction involving the exponential term in (3.2b) followed by linearly increasing fully lubricated viscous friction with increase in the piston speed Sarkar et al.(2013). In Figure 3.7b, the influence of Stribeck friction appears weaker and the viscous friction non-existent presumably under the greater influence of the shifting operating point.

In Figure 3.7e, the variation of  $a_2$  under the **OSFFPI** controller seems to be sensitive to the interaction of the forces. A look at Figure 2.1 reveals that the extension stroke is aided by the net thrust on the piston and opposed by the compression spring, whereas the retraction stroke is aided by both of these forces. The net effect is manifested in Figure 3.7e as frequency-independent variation during the extension phase and progressive increase of

the amplitude yielding lower minimum value up to 2Hz frequency during the retraction phase. A comparison of Figs. 3.7b and 3.7f reveals the superimposition of the additional effect in Figure 3.7b arising from the exponential Stribeck term in (3.2b) for the **CFPI** controller with respect to the friction model (3.2c) of the **OSFFPI** controller.

In Figures 3.7c and 3.7d, the variations of  $a_0$  and  $a_{-1}$  under the **CFPI** controller appear to be frequency independent. These trends could be due to the strong influence remaining mute for keeping P gain constant in Figure 3.7c and I gain in Figure 3.7d, whereas (A3) and (A7) in the Appendix reveal direct influence of P gain on  $a_0$  and (A4) shows a similar effect of I gain on  $a_{-1}$ . In Figures. 3.7g and 3.7h, the influence of the variation of the operating point seems to have surfaced for the same selected gains in case of the **OSFFPI** controller. This is acceptable in view of the difference in the two formulations.

It is evident from (A3) and (A4) that higher positive  $a_0$  and  $a_{-1}$  are attainable by higher choices of P and I gain, respectively. By inspecting (3.14a) it can be inferred that in absence of I gain, the steady error would be equal to  $\delta/a_0$  that would be lower for higher  $a_0$  achievable with higher P gain beyond a threshold. The incentive of employing I gain embedded within  $a_{-1}$  could be identified from (3.14a) as achieving zero steady error despite the uncertainties embodied within  $\delta$  by simultaneous fulfillment of

$$a_{-1} \int_0^{t \geq t_s} e dt = \delta \text{ and } e|_{t_s} = 0 \text{ for any } t \geq t_s, \quad (3.16)$$

where  $t_s$  stands for the settling time. Since the predicted performance in Figure 3.5 reveals much improved performance for I gain of 100V/(m-s) in comparison to 1V/(m-s), the higher of the two I gain seems to be the choice for performing the real-time experiments. Hence, the effect of different P gains on the coefficients in (3.15f) is studied next.

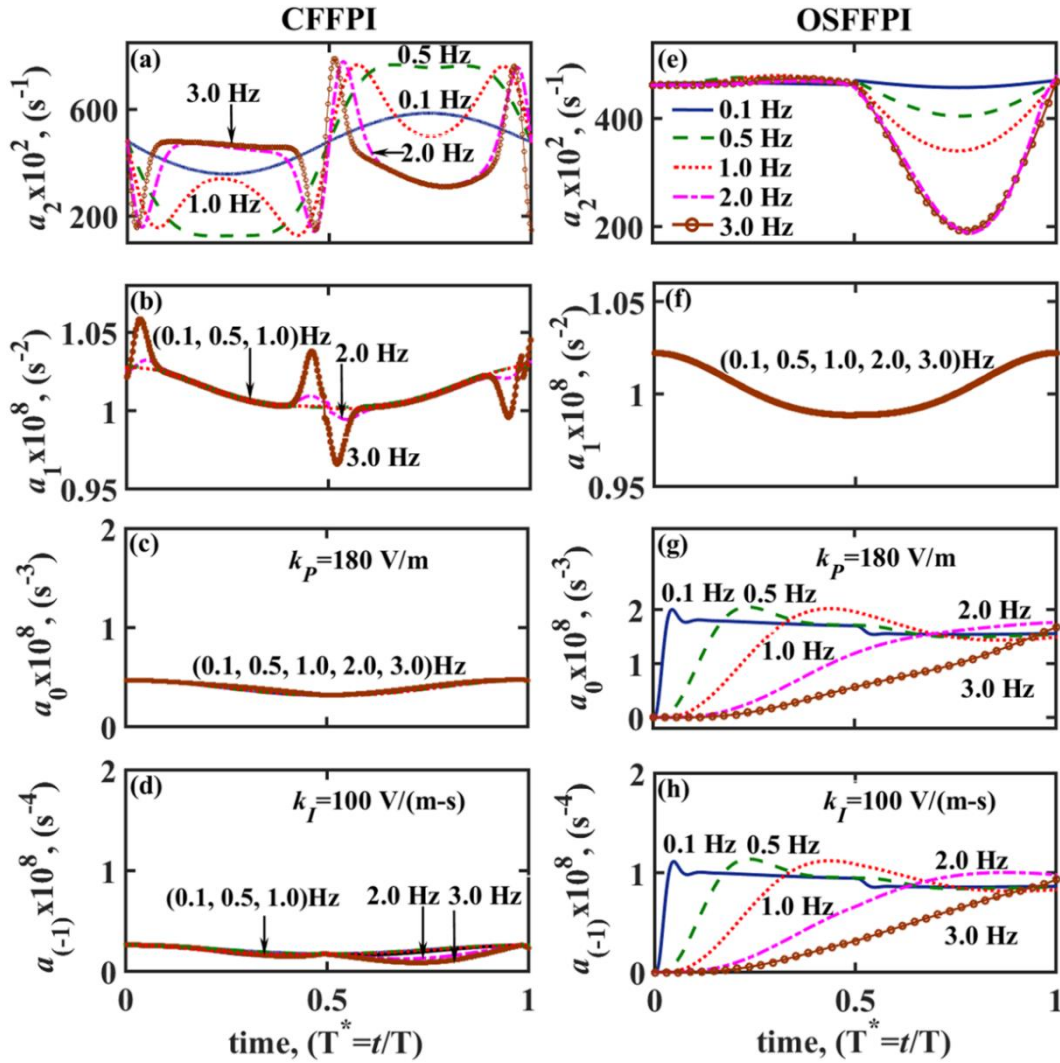


Figure 3.7. Variation of coefficients of characteristic equations over sinusoidal demand cycles of different frequencies for CFFPI in (a) to (d) and OSFFPI in (e) to (h)

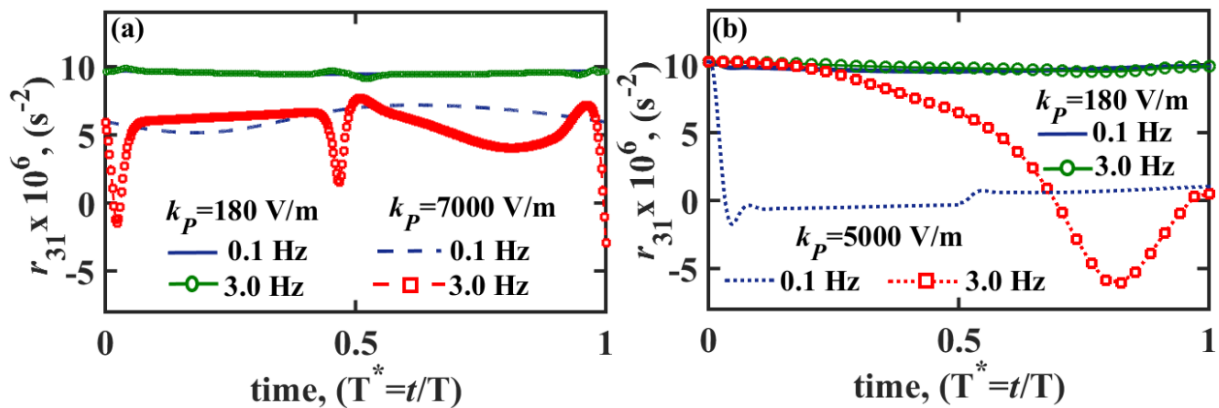
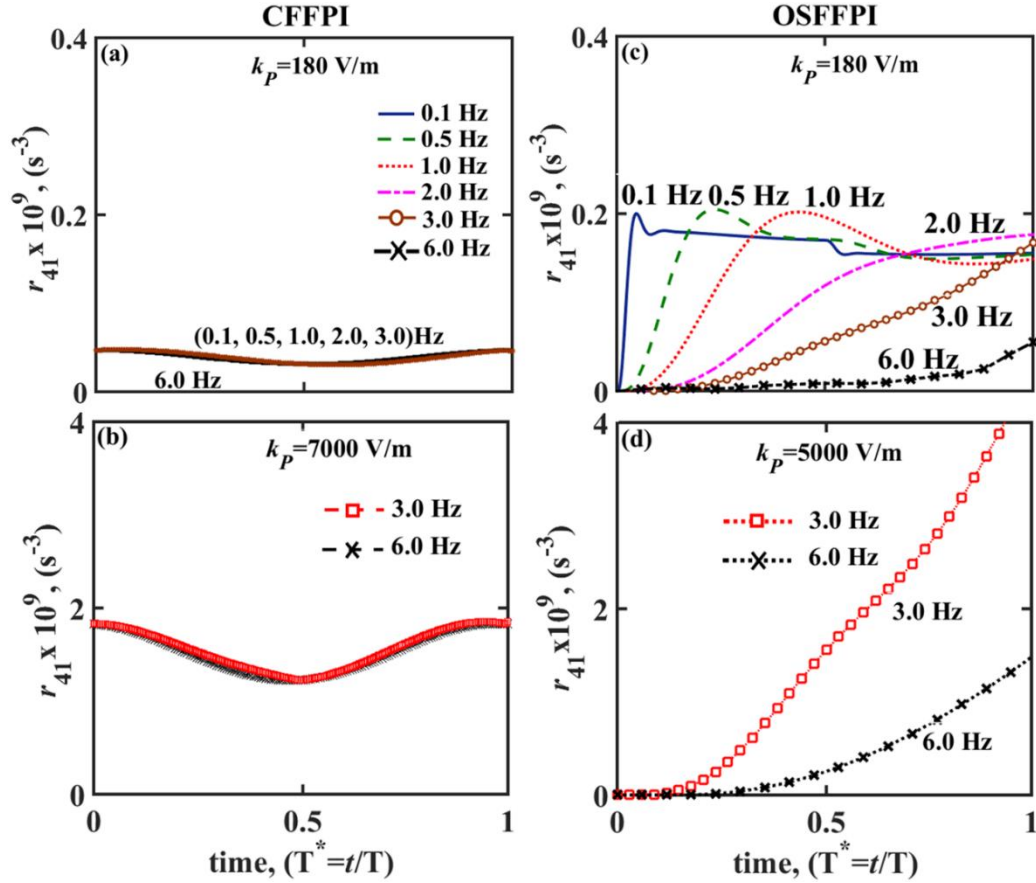


Figure 3.8. Effect of proportional gain variation on  $r_{31}$  under (a) CFFPI and (b) OSFFPI controllers



**Figure 3.9. Variation of  $r_{41}$  over a cycle for 100V/(m-s) I gain and P gains of (a) 180V/m and (b) 7000V/m under CFFPI controller and (c) 180V/m and (d) 5000V/m under OSFFPI controller**

The variation of  $r_{31}$  over a cycle shown in Figure 3.8 clearly shows the coefficient assuming negative values for high P gain for both the controllers. In Figure 3.9,  $r_{41}$  remains positive throughout for both the gains. Hence for the sake of stability, the lower P gain of 180V/m has been employed in all real-time experiments, the results of which are discussed in the next section.

### 3.9 Results and Discussions

Results of the experiments performed for sinusoidal position tracking demand (3.12a) with 20mm amplitude over frequency range from 0.1Hz to 9Hz are presented in the setup of linear actuation system as shown in Figure 2.1, are given in Figures 3.10 to 3.18 and Table 3.4 for the parameter values listed in Tables 3.1 to 3.3 for both the **CFFPI** and **OSFFPI** controllers. A major motivation of the study is to carry out an acceptability test for the novel

**OSFFPI** controller against the **CFFPI**, controller. The notable aspect of both the models are accounting for the variable pump pressure by incorporating the compressibility effect of oil that becomes significant at high pressure. There are additional reasons for having the initial confidence on the **OSFFPI** controller. First the formulation is based on naturally emerging order-separated effects with the motion-inducing flow requiring the major voltage contribution in the overall sense. Secondly, the model provides a broad-based framework for any double-acting cylinder irrespective of the ratio of the flow area across the piston. In fact, the applicability of the model is even broader for having no restriction on the number of compensations that would remain minor, yet important either for achieving better performance or for locating an emerging fault precisely.

The real time study includes comparison of **OSFFPI** controller with the **CFFPI** controller, and with two existing advanced controllers designed by (Dasmahapatra et al. 2018) and (Chaudhuri et al.2020a). The two controller design includes, an advanced adaptive sliding-mode integral controller, or **ASMIC**, and an adaptive recurrent neuro sliding-mode controller with adaptive bias **ARHNNSMC-AB** is also implemented in real-time and compared with presently designed feedforward controllers as shown in Figure 3.10. The validation of the designed controllers is also compared with a simple **PI** alone controller. Of course, implementation of **PI** controllers is easier than all these models. In order to bring out the motivation for using a controller more advanced than the most popular **PID** controller or its variant, the comparison also involves the results of a **PI** controller. The corresponding results are given in Figures 3.11 to 3.16 and Table 3.4. Finally, the energy saving potential of the designed controllers have been demonstrated with reference to Figure 3.17. by operating the pump in fixed displacement mode for **ASMIC** and **ARHNNSMC-AB**, and in variable-displacement mode for the other three controllers. Table 3.4 lists the values of different performance index, viz. integral absolute error

$$\mathbf{IAE} = (\int_0^{nT} |e|dt)/(anT), \quad (3.17a)$$

integral square control effort

$$\mathbf{ISCE} = (\int_0^{nT} V^2 dt)/(V_{\max}^2 nT), \quad (3.17b)$$

integral absolute derivative error

$$\mathbf{IADE} = (\int_0^{nT} |\frac{de}{dt}|dt)/a, \quad (3.17c)$$

and the integral absolute derivative control effort

$$\mathbf{IADCE} = (\int_0^{nT} |\frac{dV}{dt}| dt) / V_{max} \quad (3.17d)$$

For the sinusoidal demand stated above having amplitude  $a= 20\text{mm}$  with frequency range limited to (0.1- 7.0) Hz estimated over a period of three consecutive cycles by setting  $n$  equal to 3. The lower and upper limit of the control signal  $V_{max}$  varies within  $\pm 10V$ . Average power saved under both the **OSFFPI** and **CFFPI** controllers are shown in Figure 3.17 that have been achieved by operating the pump in the variable-displacement mode in comparison to the fixed displacement mode maintaining the pump delivery at the relief valve pressure  $P_{RV}$ . The saving is calculated as

$$\bar{P}_s = Q_{p0}P_{RV} - (\int_0^T (Q_p P_p) dt / T). \quad (3.17e)$$

In terms of these results, the contribution of the present work is explained next.

A demonstration of the acceptability of the **OSFFPI** controller is evident in Figure 3.10 from the variations against the excitation frequency showing marginally lower deviation of the output amplitude from the demand and closely matching phase lag achieved under the **CFFPI** controller. Over the demand range between 0.4Hz and 5Hz, both the controllers exhibit lower amplitude deviation in comparison to that achieved under the existing **ASMIC**. While operating at lower frequencies, the amplitude deviation of the designed controllers is comparable to nonlinear **ARHNNSMC-AB** (Chaudhuri et al.2020a), which is particularly well suited for low velocity regime operation of **EHAS**. Up to about 3Hz demand, the lower phase shift achieved by both the proposed controllers is indeed an achievement offsetting the good effect of the marginally lower phase deviation under the **ASMIC**. Figure 3.10 clearly shows superior performance of the designed controllers in terms of amplitude and phase fluctuation when compared to **ARHNNSMC-AB**. More oscillatory **ASMIC** and **ARHNNSMC-AB** response than the designed controllers apparent in Figures. 3.11 to 3.16 is indeed a weakness of the existing **ASMIC** and **ARHNNSMC-AB** controllers.

The voltage oscillation in **ASMIC** and **ARHNNSMC-AB** evident in Figure 3.11 is intrinsic due to the time-to-time switching off and on of the SMC in the vicinity of low error implemented for chattering attenuation in the existing controller (Kim et al. 2015). This oscillation is of much lower frequency in comparison to the chattering produced by a simple **SMC**. However, under the effect of this voltage oscillation of the **ASMIC** and **ARHNNSMC-AB**, Figures 3.12 to 3.16 reveals corresponding oscillations in the response

too.

**Table 3.4: Variation of performance indices with frequency for different controllers**

Demand Frequency	Controllers				
	CFFPI	OSFFPI	ARHNNSMC-AB	ASMIC	PI
	<b>IAE</b>				
0.1Hz	<b>0.126</b>	<b>0.124</b>	0.048	0.124	0.253
0.5Hz	<b>0.110</b>	<b>0.086</b>	0.062	0.133	0.214
1.0Hz	<b>0.210</b>	<b>0.182</b>	0.098	0.142	0.482
2.0Hz	<b>0.135</b>	<b>0.107</b>	0.429	0.197	0.253
3.0Hz	<b>0.220</b>	<b>0.212</b>	0.747	0.232	0.714
4.0Hz	<b>0.468</b>	<b>0.267</b>	0.856	0.270	0.810
5.0Hz	<b>0.965</b>	<b>0.884</b>	1.123	0.532	1.050
7.0Hz	<b>1.840</b>	<b>1.835</b>	1.923	2.157	1.856
	<b>ISCE</b>				
0.1Hz	<b>0.0074</b>	<b>0.0045</b>	0.0134	0.0491	0.0064
0.5Hz	<b>0.0184</b>	<b>0.0148</b>	0.0205	0.0543	0.0014
1.0Hz	<b>0.0310</b>	<b>0.0246</b>	0.0316	0.0673	0.0187
2.0Hz	<b>0.1045</b>	<b>0.0795</b>	0.0541	0.1102	0.0025
3.0Hz	<b>0.3821</b>	<b>0.1546</b>	0.0647	0.1694	0.0353
4.0Hz	<b>0.4123</b>	<b>0.2662</b>	0.0985	0.3273	0.0543
5.0Hz	<b>0.7517</b>	<b>0.6213</b>	0.1216	0.5653	0.0733
7.0Hz	<b>0.8450</b>	<b>1.2463</b>	0.1665	0.9035	0.1672
	<b>IADE</b>				
0.1Hz	<b>25.89</b>	<b>12.89</b>	49.69	1012	04.17
0.5Hz	<b>11.26</b>	<b>3.813</b>	12.19	222.7	12.41
1.0Hz	<b>08.75</b>	<b>08.63</b>	08.34	103.8	08.02
2.0Hz	<b>09.73</b>	<b>08.75</b>	08.98	45.75	05.84
3.0Hz	<b>10.12</b>	<b>09.49</b>	13.12	38.66	13.57
4.0Hz	<b>12.57</b>	<b>11.36</b>	15.56	32.65	15.68
5.0Hz	<b>15.70</b>	<b>13.56</b>	21.04	27.32	17.23
7.0Hz	<b>18.38</b>	<b>17.73</b>	15.75	32.53	20.02
	<b>IADCE</b>				
0.1Hz	<b>15.42</b>	<b>02.94</b>	60.28	1722	17.88
0.5Hz	<b>04.56</b>	<b>01.95</b>	13.02	376.4	04.53
1.0Hz	<b>03.12</b>	<b>02.61</b>	05.48	179.5	02.91
2.0Hz	<b>04.45</b>	<b>03.75</b>	07.35	80.96	03.78
3.0Hz	<b>06.54</b>	<b>05.79</b>	05.71	70.13	04.78
4.0Hz	<b>10.35</b>	<b>07.86</b>	06.35	43.64	05.21
5.0Hz	<b>13.12</b>	<b>11.20</b>	08.21	28.81	05.88
7.0Hz	<b>12.38</b>	<b>12.60</b>	04.24	12.53	06.45

The oscillation-free excitation and response achieved under both the proposed **FFPI** scheme along with their lower **IAE** is indeed a notable contribution. The higher magnitude of **IAE** in case of the **PI**-only controller for all the frequencies apparent in Table 3.4 with

correspondingly the largest error variation with time exhibited in the Figures 3.12 to 3.16 justifies the use of more advanced controllers despite their higher implementation complexities. In terms of **IAE** in Table 3.4 and the corresponding error variations with time given in Figure 3.11 and 3.16, the controller **ARHNSMC-AB** provides superior performance up to a frequency of 1.0Hz, after which its performance degrades progressively.

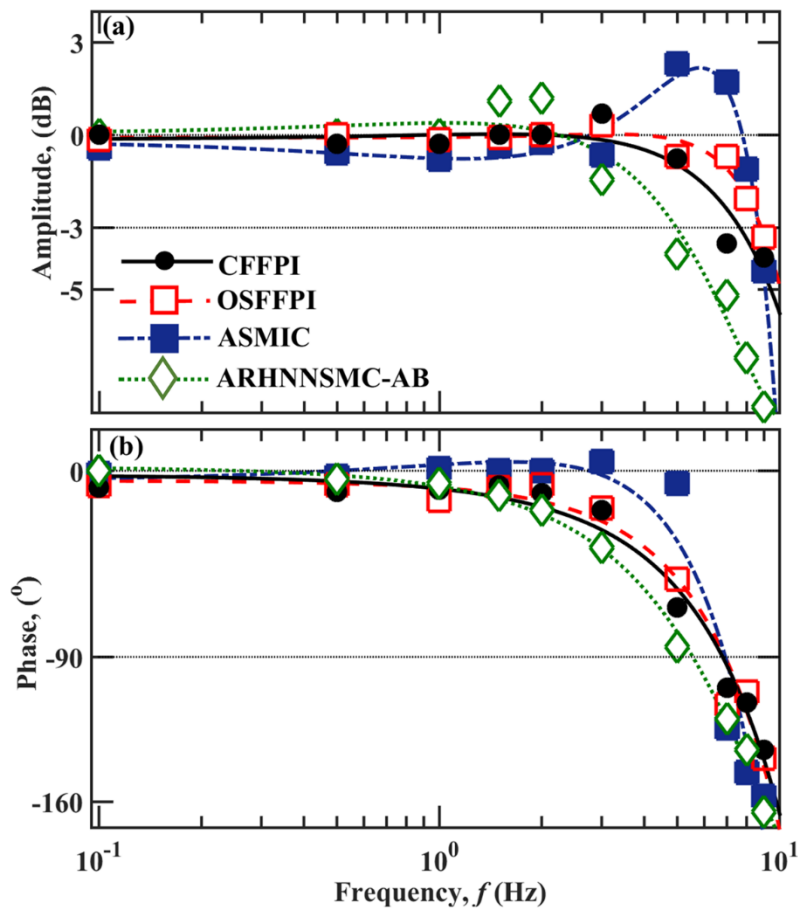


**Figure 3.10. Comparison of frequency responses of CFFPI, OSFFPI with existing ASMIC and ARHNSMC-AB controllers**

The lower magnitude of **IAE** up to 1Hz noted in Table 3.4 in case of **ARHNSMC-AB** seems to have arisen under the domination of the effect of significantly lower amplitude deviation than the other three controllers, offsetting the effect of its marginally lower phase-lag effect as apparent in Figure 3.10. Near 2Hz demand, all the three controllers other than **ARHNSMC-AB** in Figure 3.10 exhibit insignificant amplitude difference between the output and the demand. Despite the least phase deviation of **ASMIC** in this case, its **IAE** in Table 3.4 appears higher than the **IAE** of each of the proposed two **FFPI** controllers. This higher **IAE** could be attributed to the significantly large-amplitude oscillatory



response of the **ASMIC** evident in Figures 3.11 to 3.16. It is logical to accept the oscillations of much lower amplitude observed in Figures 3.11 to 3.16 for the two **FFPI** controllers as the usual overshoots and undershoots about the demand track arising under, I gain.

The lowest **IAE** under **ASMIC**, listed in Table 3.4 at 5Hz with Figure 3.10 exhibiting similar phase lag in all the cases could be surmised as the domination of the effect of significantly lower amplitude deviation than the other three controllers offsetting the effect of more oscillatory **ASMIC** response. Figure 3.10 reveals that all three controllers besides **ARHNNSMC-AB** have a bandwidth of approximately 8Hz, which corresponds to a 3db amplitude reduction and a 90 degree phase offset, respectively. However, the corresponding figure for **ARHNNSMC-AB** shows a bandwidth of approximately 5 Hz for 3db amplitude reduction and 90 degree phase offset.

Table 3.4 clearly reveals a strength of the **OSFFPI** controller by its either nearly equal or lower **IAE** than those under **CFPI** over the entire bandwidth range. Such an achievement at the expense of lower **ISCE** up to 5Hz by the **OSFFPI** controller indeed establishes its superiority over the **CFPI** controller.

In most cases of the frequency demand presented in Table 3.4, the expense of **ISCE** under the two **FFPI** controllers arising lower than the **ASMIC** is a testimony of the soundness of the feedforward models. In the Lyapunov function-based adaptation deployed in the **ASMIC** (Dasmahapatra et al. 2018), only the minimization of the tracking error gets emphasized instead of the model-based estimation of the feedforward voltage in (3.1b). Achieving the lowest **IAE** at the cost of the lowest **ISCE** by the **ASMIC** only at 5Hz frequency is only fortuitous. In the existing **SMC**-based scheme (Dasmahapatra et al. 2018), the adaptation of the **SMC** parameters is kept suspended near the origin of the phase plane comprised of the error (3.1a) and its rate for mitigating the chattering effect. Such a scheme would have eliminated the chatter if the trajectory would have remained contained within the stipulated bound forever after its first progression into the bound. But the uncertain disturbances would make the error to hover around zero and larger disturbances would have pushed the error outside the bound giving rise to a spike in the voltage excitation as well as in the response in each case. Such occurrences must have been low at 5Hz leading to the corresponding best performance among all the controllers studied.

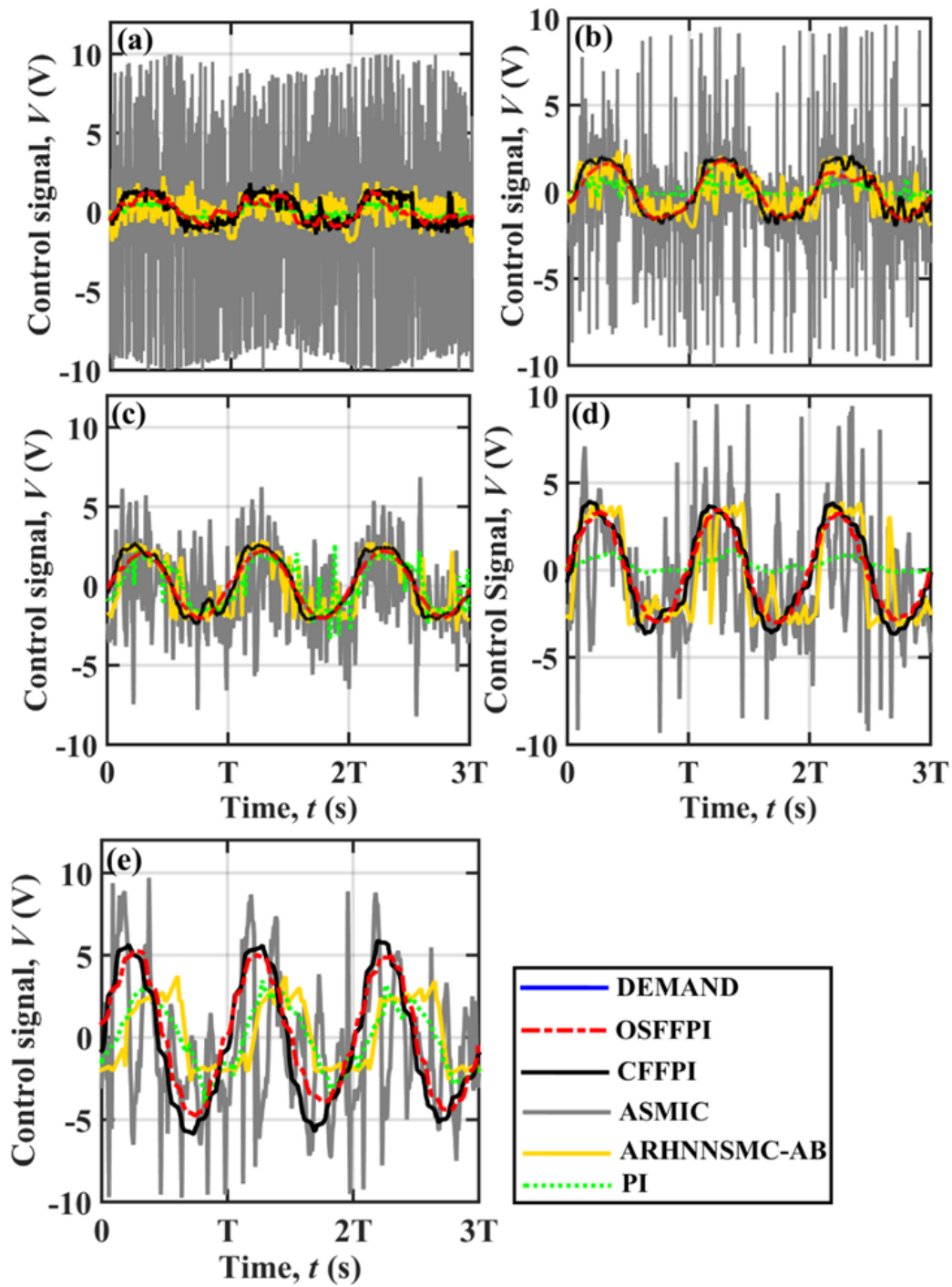


**Figure 3.11. Comparison of PI, CFFPI, OSFFPI, ASMIC and ARHNSMC-AB controllers for time variation of excitation voltage for a sinusoidal demand at frequency of (a) 0.1Hz, (b) 0.5Hz, (c) 1Hz, (d) 2Hz and (e) 3Hz**

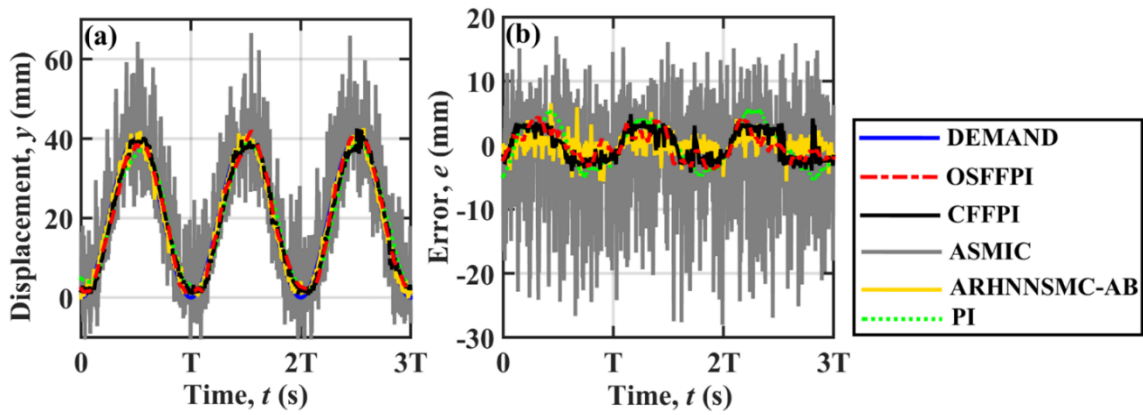


Figure 3.12. Comparison for PI, CFFPI, OSFFPI, ASMIC and ARHNNSMC-AB controllers at 0.1Hz frequency of a sinusoidal demand for the (a) response and (b) error

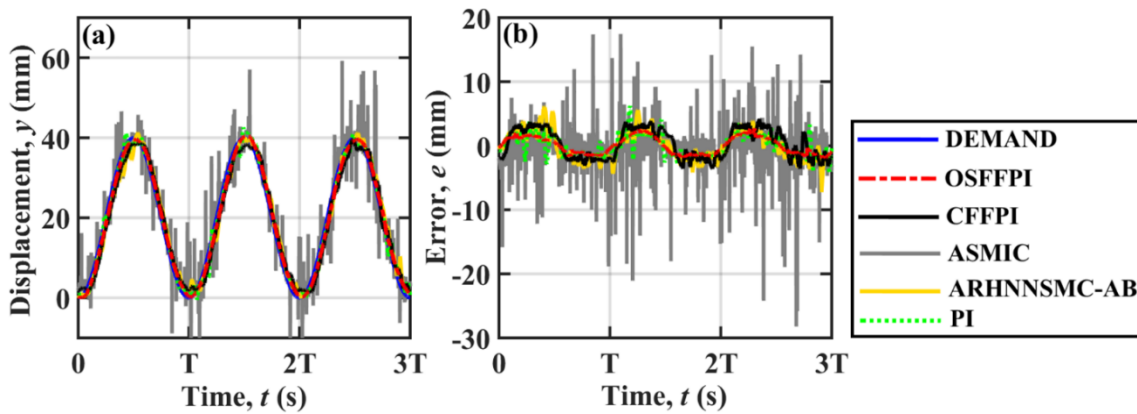


Figure 3.13. Comparison for PI, CFFPI, OSFFPI, ASMIC and ARHNNSMC-AB controllers at 0.5Hz frequency of a sinusoidal demand for the (a) response and (b) error

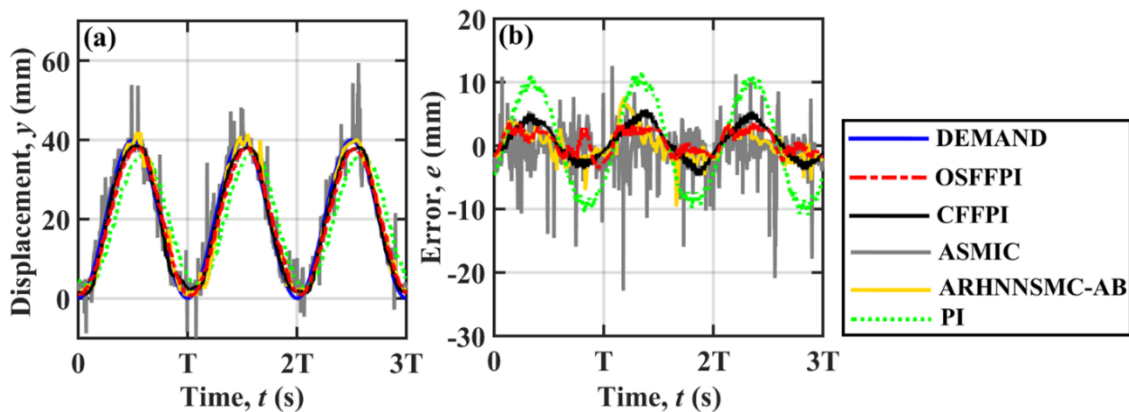
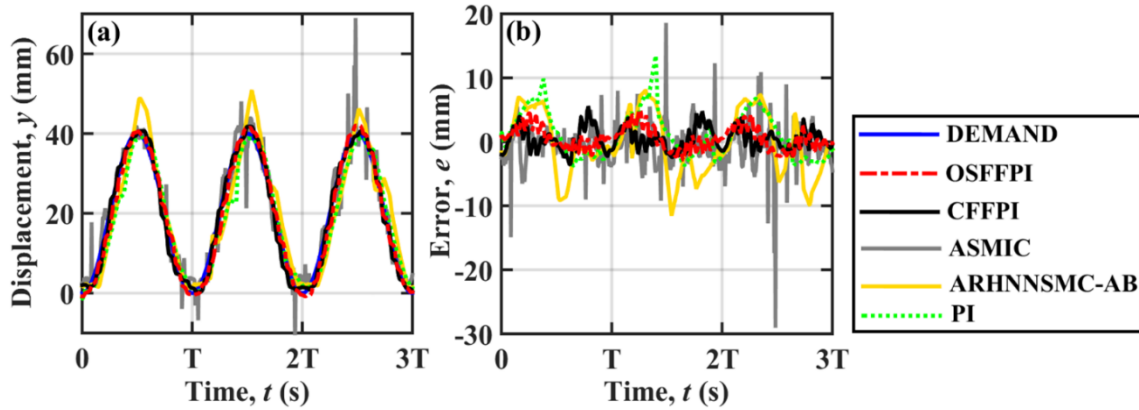
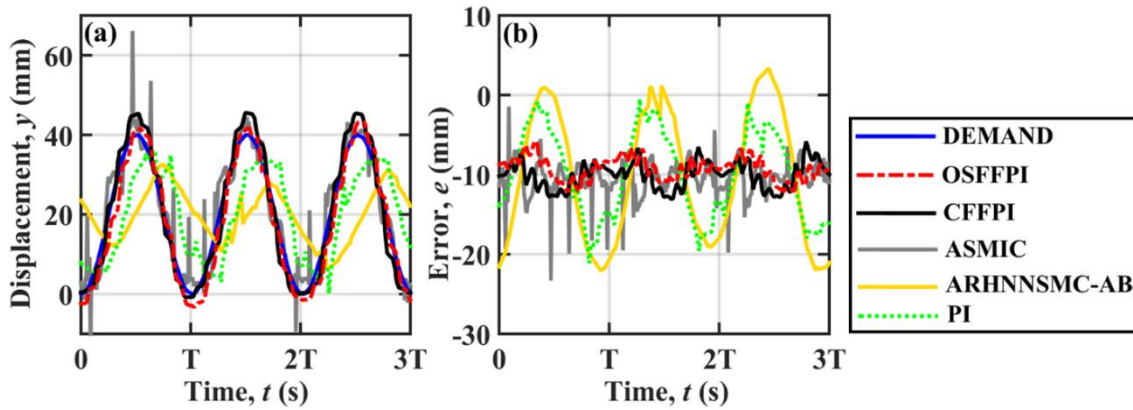


Figure 3.14. Comparison for PI, CFFPI, OSFFPI, ASMIC and ARHNNSMC-AB controllers at 1Hz frequency of a sinusoidal demand for the (a) response and (b) error



**Figure 3.15.** Comparison for PI, CFFPI, OSFFPI, ASMIC and ARHNNSMC-AB controllers at 2Hz frequency of a sinusoidal demand for the (a) response and (b) error



**Figure 3.16.** Comparison for PI, CFFPI, OSFFPI, ASMIC and ARHNNSMC-AB controllers at 3Hz frequency of a sinusoidal demand for the (a) response and (b) error

Table 3.4 demonstrates distinctly that, in comparison to all other controllers, **ARHNNSMC-AB** exhibits a reduced magnitude of **ISCE** across the entire frequency range, which increases with increasing frequency. The **ISCE** for the **OSFFPI** controller is substantially less than that of the **CFFPI** controller across the entire frequency range, and it remains less for the **ASMIC** controller up to 4Hz. The designed **OSFFPI** and **CFFPI** controller also exhibits a lower **ISCE** up to frequency range of 2Hz and 1Hz respectively compared to **ARHNNSMC-AB**. Beyond this frequency, despite the higher values of **ISCE** for both the feedforward controllers, the corresponding magnitude of **IAE** remains substantially lower than **ARHNNSMC-AB**, ensuring superior tracking performance in comparison to **ARHNNSMC-AB**.

To quantify the chattering of **ARHNNSMC-AB** and **ASMIC** with regard to the designed feedforward controllers and the tracking performance, two additional performance indices, **IADCE** and **IADCE**, were calculated using equations 3.17(c) and 3.17(d). Table 3.4 illustrates the magnitude of these two indices, which are based on the absolute time derivative of the tracking error and the control law for each controller. The preceding table plainly demonstrates that the magnitude of the aforementioned indices is greatest for **ASMIC**, followed by **ARHNNSMC-AB**, resulting in a substantial amount of chattering that ultimately affects the control performance. **OSFFPI**'s indices have the smallest magnitude compared to those of other feedforward controllers **CFFPI** and existing nonlinear **ASMIC** and **ARHNNSMC-AB**.

One of the important aspect of power saving achieved by operating the pump in variable-displacement, or **VD**, mode in comparison to fixed-displacement, or **FD**, pumping is shown in Figure 3.17 for the two designed **FFPI** controllers corresponding to the demand given in (3.12a). Figure (3.17a) depicts the variations of delivery pressure and discharge of the pump operating at both **FD** and **VD** modes over a full cycle for 1Hz frequency demand are shown. For **FD** operation, the relief valve pressure  $P_{RV}$  has been set at 12.8MPa very near to the identified cut-in value of the pump given in Table 4 along with lowering of the cut-in setting of the pre-compression spring of the pressure compensator valve of the pump so as to raise the cut-in value above the relief valve setting. The observed variations in Figure (3.17a) reveals nearly constant discharge  $Q_{p0}$  equal to  $8.3 \times 10^{-4} \text{m}^3/\text{s}$  and pressure of 12.8MPa along with low-amplitude ripples typical of **FD** operation without accumulator. These amplitudes are indeed insignificant with respect to those apparent during the executed two **VD**-mode operations.

For a **VD** mode operation, it is evident that during retraction stroke over half cycle of a motion demand the cylinder requires lower pump discharge to the rod-end chamber than during the extension stroking over each of the prior and next half cycles to the larger-area cap-end chamber. The discharge variation clearly exhibits a phase delay of about  $45^\circ$  with respect to the motion demand. In other words, it can be said that the variation of discharge at the beginning of the fourth pumping cycle shown in the figure matches with ongoing later-phase piston retraction in the third cycle.

Another issue of interest at the beginning of the fourth cycle, can also be observed in Figure 3.17a, which corresponds to the falling trend of pump discharge along with the mostly falling trend of pump pressure variation. However, during this phase of operation,

the discharge requirement for the cylinder keeps increasing. It seems that the requirements of lower compensation for the motive discharge in the cylinder against oil compressibility and leakage due to the falling pressure enable the piston to assist the motion demand quite well despite the falling trend of pump discharge. Also, a reasonably good tracking at 1 Hz frequency is evident in Figure 3.10b in terms of a lower phase lag of the piston response with respect to the demand as compared to the phase difference between the pump discharge and the demanded requirement apparent in Figure 3.17a. The observed variation of the discharges in Figure 3.17a for the two controllers explains the higher tracking error for the CFFPI controller apparent in Figure 3.14b with respect to the OSFFPI controller.

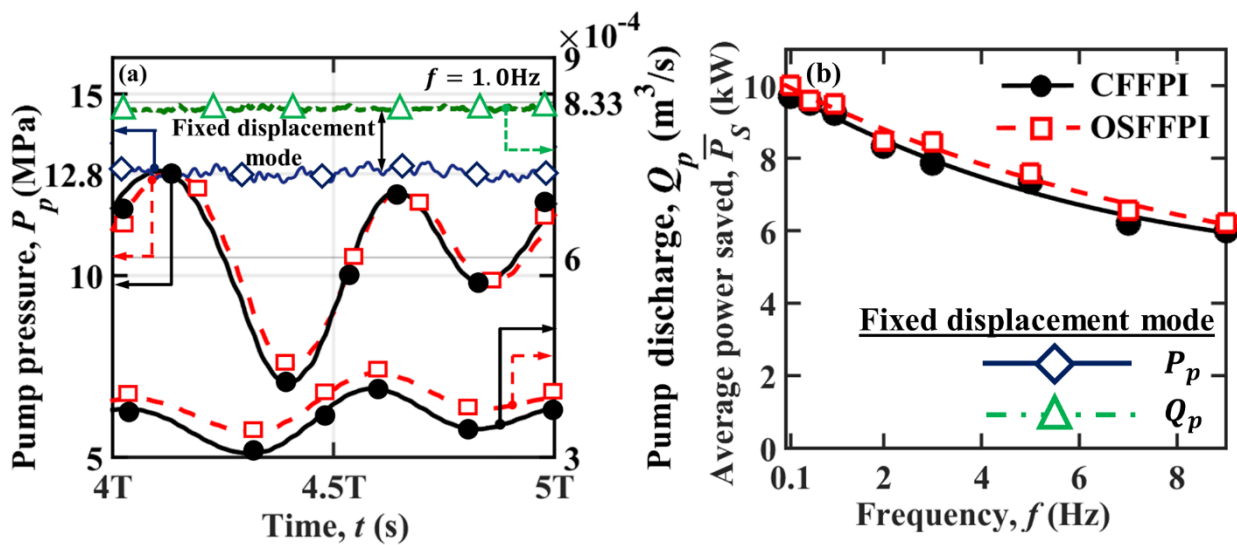


**Figure 3.17. Comparison of CFFPI and OSFFPI controllers on variable-displacement pump for (a) pressure and discharge variations over a cycle and (b) power saving over fixed displacement working**

The lower variation of the command signal during the retraction stroking, as depicted in Figure 3.11c compared to the extension stroking, indicates smaller opening of the metered port pair of the valve with a consequence of higher pressure drop. This drop seems to have counteracted the effect of the compression spring force in (3.2a) by opposing the extension stroking and facilitating the retraction stroking. Even though the rod-end chamber of the cylinder has a lower retracting discharge, the larger variation in pump pressure that can be seen in Figure 3.17a makes up for this. Obviously, the small orifice-like openings of the metered ports cause a significant pressure drop. At the same time, a small variation of the excitation signal gives rise to a fast-response pressure variation making it necessary to maintain high-frequency motion demands. The pressure dynamics of the pump appears to

be more sensitive than the discharge from the observed minimum pressure of about 7.5MPa that is well below the cut-in limit of 12.8MPa as noted in Table 3.2 despite a continued discharge variation in apparent contradiction of the steady-state characteristics Mondal et al. (2019).

The observed average power saved shown in Figure 3.17b for **VD** pumping arises from the elimination of the loss in the relief valve pressure in the **FD** mode. By ignoring the ripple effects as minor as apparent in Figure 3.17a, the **FD**-mode power is calculated in the first part of (3.17c) as equal to 10.6kW corresponding to the nearly constant discharge  $Q_{p0}$  equal to  $8.3 \times 10^{-4} \text{m}^3/\text{s}$  and the relief valve set at a pressure  $P_{RV}$  of 12.8MPa. The difference from this power in the estimation by (3.17c) determines the average power saved by pumping in **VD** mode that is observed at the identified cut-in value of 12.8MPa in Figure 3.17(b) to be comparable for both the proposed schemes. In fact, the relief valve setting for the pump operation in the **FD** mode has been set consistent with the converged  $P_{ci}$  values given in Table 3.3 of the identification exercise is also evident in Figure 3.17a is a testimony of the achievement of such manual setting so as to avoid penalization of the FD mode power by unduly high setting of the relief valve pressure. During the **VD** mode operation, the relief valve setting has been raised to a higher level so as to keep it closed during normal operation and allow it to provide protection only in case of any accidental overpressurization of the system.

Naturally, the absence of a return flow to the tank through the relief valve, which continues to increase with a decrease in frequency demand, implying a lower flow requirement for motion actuation, is the primary source of the savings in **VD** mode. As a result, as can be seen in Figure 3.17(b), the average amount of power saved in the VD mode decreases as frequency demand rises. The observed power savings of about 9kW at 1Hz demand and 6kW at 9Hz demand imply the pumping power requirements in the **VD** mode to be respectively just 15 and **44% of 10.6kW** required in the **FD** mode. Higher power saving achieved by the more generalized **OSFFPI** scheme except for very low-frequency demand uncovers another strength of this scheme.

### 3.10 Summary

The present chapter represents the core building block of the entire thesis, which deals with design and development of a feedforward position controller to drive electrohydraulic

motion control system comprised of a double-acting single rod cylinder, a solenoid-operated valve, and a pump. In a laboratory set up with an industry-grade cylinder, a low-cost proportional valve, and a pressure-compensated variable-displacement pump. Mainly two design algorithms have been focussed for the development and testing of the two-feedforward controller, viz. conventional approach and novel Order Separation approach. Starting from an explicit method to design the above-mentioned system that has been done in conventional approach a more generalized version of design has been proposed here also. The most notable aspect of the latter design with respect to the previous one is its wide range of applicability for compressible and incompressible flow, for fixed-displacement to pressure-compensated pumps, proportional and servo proportional valves as well as single and double-rod double-acting cylinders. Where the flatness-based controller design is the outcome of conventional technique, the novelty of the second approach for feedforward design lies in exploiting the natural order-separated form of the oil flow, leading to a non-iterative algebraic sequential estimation algorithm. A **PI** feedback has been included with both the above designed controller formulated to take care the modeling uncertainties and approximations. For both the design approach, prior to the real-time experimentations, the PI gains have been selected by a rigorous stability analysis of the linearized error equation by extending **Routh criteria** to a time variant system involving the offline estimates of **GA**-optimized system and feedforward parameters. The simulation-guided identification delineated here would help performing future identification experiments more safely than an existing identification approach relying only on experiments without any prior assessment of the stability at this stage.

The performance testing of the designed controllers has been done in real-time by considering several non-linearities which has been addressed during the design of both the controllers with different approaches. Based on the design algorithm, design considerations and finally with the results of real-time experiments the two controllers have been compared and the design based on Novel Order Separation Technique algorithm exhibits the most efficient one to be used for further studies.

The performance of the proposed controller is also compared in real-time with previously established controllers viz, classical **PI**, an adaptive recurrent neuro sliding-mode controller with adaptive bias **ARHNNSMC-AB** and a nonlinear adaptive sliding-mode integral controller or **ASMIC**, which demonstrates superior tracking performance of the designed controller in comparison to classical **PI** and **ARHNNSMC-AB**, and an equivalent tracking



performance with respect to **ASMIC** at the expense of much lower control effort. The significant energy-saving potentials of the controller with respect to working in the fixed-displacement mode of pump has also been quantified.

The above discussions clearly reveal the strength of the proposed **FFPI** controller based on Novel Order Separation Technique, and also provides approval to be used further with other configurations viz. a serial manipulator in form of a single leg of a quadruped and a combined serial/parallel manipulator in form of 4 leg structure with a torso, that has been described clearly in the previous chapter and referred as configuration-2 and configuration-3 respectively.



# CHAPTER 4

## Controller Design and Real-time Analysis for Serial Manipulator

### 4.1 Introduction

The acceptance of a novel order-separated feedforward controller with a PI-feedback, or **OSFFPI** controller, has been established in Chapter 3 through a rigorous experimental analysis. In a simple set up comprised of an industry-grade double-acting single-rod cylinder, or DASRC, paired with a proportional valve, the experiments have been carried out. A number of linear displacement-tracking experiments performed in the setup has also demonstrated the novel controller to be more precise and energy-efficient than another one that has been developed conventionally and employed as a substitute feedforward model. Motivated by the success of **OSFF** design, an **OSFFPID** has been implemented next in an electrohydraulic serial manipulator in order to meet the demand of its free point. The manipulator has a pair of low-friction DASRC, each equipped with a servoproportional valve, or SPV, along with members connected by the cylinders. The description of the manipulator setup and the mathematical modeling are detailed respectively in Sections 2.3 and 2.6 of Chapter 2.

In the next section, the inverse kinematic and dynamic models of the manipulator are detailed that extract the actuation demands for a specified motion plan of the free point. The **OSFF** formulation corresponding to these demands is elaborated next in Section 4.3. Section 4.4 details a forward kinematic formulation for composing the motion of the free point in terms of the LVDT-captured displacement tracks of the pistons, one each in the two cylinders of the manipulator. In Section 4.5, a numerical study is discussed for justifying the use of a simplified feedforward model implementable in controllers of moderate processing speed. The results of the real-time **OSFFPID** controller experiments are detailed in Section 4.6 along with highlighting its capability of avoiding instability-related transient oscillations that could arise in case of the PID-alone controller for the

manipulator system with complex nonlinear dynamics. The scope of using the feedforward formulation in designing the manipulator system is outlined in Section 4.7. A summary of this work is given in Section 4.8.

## 4.2 Inverse Kinematic and Dynamic Modeling

With reference to Figure 2.3(b) the inverse kinematic modeling of the serial manipulator has been developed which provides the actuation demands based on the motion demand of the free point  $f$  of the serial manipulator in the vertical plane  $xz$  shown in Figure 4.1. The figure clearly depicts the motion plans studied here by showing the corresponding trajectories. The subscript  $f_0$  in the figure corresponds to the initial values for all the motion plans studied here and given in Table 2.2. Different angles, viz. the knee angles  $\alpha$  and  $\beta$  and the angle made by free point  $f$  etc. pertains to the development of inverse kinematic and dynamic model are clearly identifiable in Figure 4.1. By attaching the origin of the coordinate system  $(x, z)$  at the stationary anchor point  $a$ , the variation of the displacement of the free point  $f(x_f(t), z_f(t))$  with time  $t$  over only this plane is considered here. The inverse dynamic modeling provides the estimate of the actuation force along the common axis of each of the lower and upper cylinder-piston pairs. Based on these inputs, a feedforward model has been constructed for a specified demand to obtain the requirements of the actuator displacements, velocities and voltage excitations for the valve solenoids along with the discharge and the hydraulic power requirement from the common pump to sustain the actuation motion.

Based on the kinematic diagram, the corresponding line diagram showing all the essential angles in Figure 4.1(a) and (b) and the position demand  $f(x_{fd}(t), z_{fd}(t))$  of free point of the single leg, the inverse model has been developed by denoting using either a subscript  $d$  or an identifier  $|_d$  to certain variables related with the specified demand. By combining the projections of the length  $\overline{hf}$  on the coordinate axes shown in Figure 4.1, it is obtained that

$$\varepsilon_d = -\tan^{-1}\{(x_{fd} - x_h)/(z_h - z_{fd})\}, \quad (4.1a)$$

$$\text{and } \overline{hf} = [(x_{fd} - x_h)^2 + (z_h - z_{fd})^2]^{1/2}. \quad (4.1b)$$

Next, by using the cosine rule for an angle in  $\Delta hfk$  one can obtain

$$\alpha_d = [\cos^{-1}\{(\overline{hf})^2 + (\overline{kf})^2 - (\overline{hk})^2\}/(2\overline{hf}\overline{kf})] - \varepsilon_d. \quad (4.1c)$$

Since the projection of Link  $kf$  along  $x$  axis is given by  $(\overline{kf}) \sin \alpha_d$ , this expression together with the known length of Link  $hk$  further gives

$$\beta_d = \sin^{-1}\{(x_{fd} - x_h + (\overline{kf}) \sin \alpha_d)/(\overline{hk})\}. \quad (4.1d)$$

Again, the cosine rule for an angle in each of  $\Delta hkl_c$ ,  $\Delta kcl_r$ ,  $\Delta ha'u_c$  and  $\Delta hu_cu_r$  further provides

$$\delta = \cos^{-1}\{\overline{hk}^2 + \overline{kl}_c^2 - \overline{hl}_c^2\}/(2 \overline{hk} \overline{kl}_c)\}, \quad (4.1e)$$

$$\overline{l}_cl_r|_d = [\overline{kl}_c^2 + \overline{kl}_r^2 - 2\overline{kl}_c \overline{kl}_r \cos \{\pi - (\alpha_d + \beta_d) - \delta\}]^{1/2}, \quad (4.1f)$$

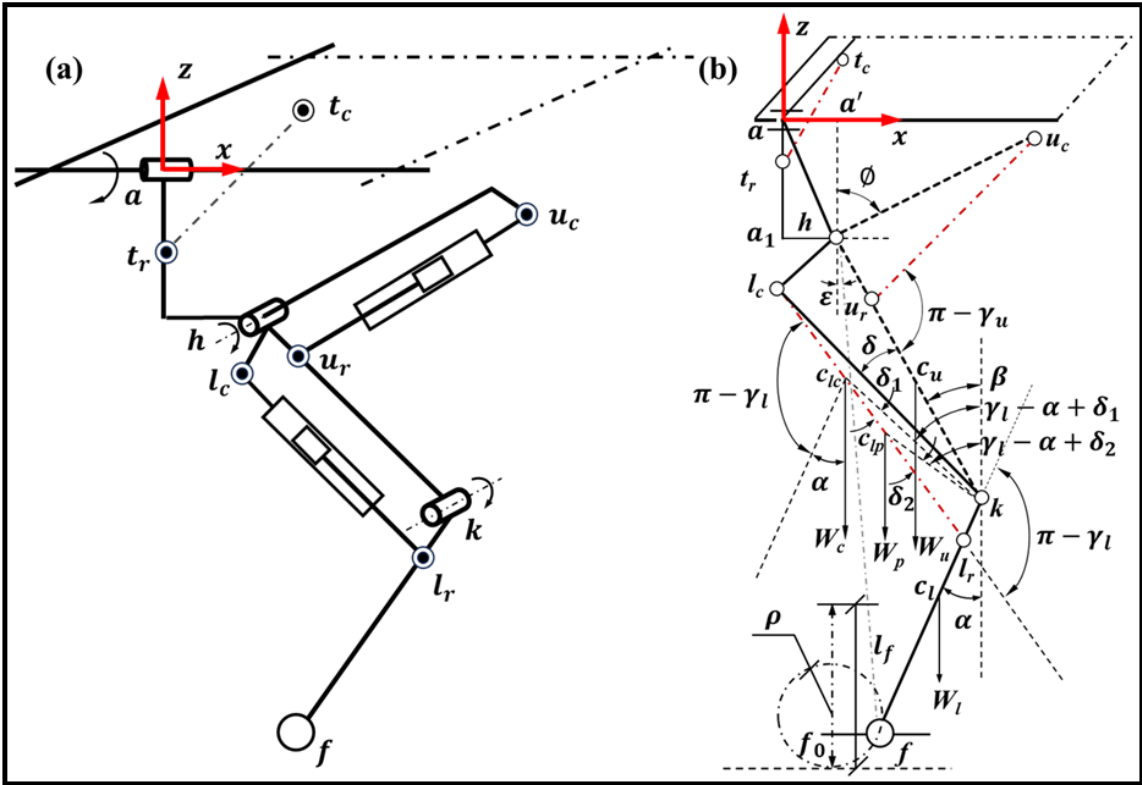


**Figure 4.1: (a) Kinematic diagram (b) Schematic line diagram of a single leg structure**

$$\phi = \cos^{-1}\{(z_h^2 + \overline{hu}_c^2 - \overline{a'u}_c^2)/(2z_h \overline{hu}_c)\}, \quad (4.1g)$$

$$\text{and } \overline{u}_cu_r|_d = \{\overline{hu}_c^2 + \overline{hu}_r^2 - 2\overline{hu}_c \overline{hu}_r \cos (\pi - \beta_d - \phi)\}^{1/2}. \quad (4.1h)$$

The displacement demands of the lower and upper actuating pistons relative to the corresponding cylinders at any instant thus can be obtained from the below relationship as

$$y_{dl} = \overline{l}_cl_r|_d - \overline{l}_cl_r|_c, \quad (4.1i)$$

$$\text{and } y_{du} = \overline{u}_cu_r|_d - \overline{u}_cu_r|_c, \quad (4.1j)$$

where  $\overline{l_c l_r}|_c$  and  $\overline{u_c u_r}|_c$  represents the closed lengths of the lower and upper actuating piston respectively. The above two displacements represent the primary outputs of the inverse kinematic model. Like the inverse kinematic model for obtaining the motion demand of the actuating pistons with respect to their corresponding cylinders, an inverse dynamic model is also necessary for the estimation of the forces along the axes of the piston-cylinder pairs for these actuated members undergoing translation. It is evident from Figure 2.3 given in Chapter 2 that the lower piston and cylinder and the upper piston could be in translation, whereas the anchoring of the upper cylinder permits only its rotation. Of course, the force estimation would call for estimating some angles further which make the inverse dynamic and kinematic models coupled to each other. However, the external forces that must be negotiated during the motion of the free point by the actuated members in linear acceleration arise from the suspended weights below the hinge points of the respective members. Taking moments about Point  $k$  for only the weight  $W_l$  of the lower member acting through  $c_l$ , the force on the lower piston along its axis are estimated as

$$F_{rl_d} = W_l \overline{k c_l} \sin \alpha_d / (\overline{k l_r} \sin \gamma_{ld}), \quad (4.2a)$$

$$\text{where } \gamma_{ld} = \cos^{-1} \{ (\overline{l_c l_r}|_d)^2 + \overline{k l_r}^2 - \overline{k l_c}^2 / (2 \overline{l_c l_r}|_d \overline{k l_r}) \}. \quad (4.2b)$$

The moment about Point  $k$  yet again for the weight  $W_l$  together with  $W_c$  for the lower cylinder acting through the point  $c_{lc}$  and  $W_p$  for the lower piston acting through  $c_{lp}$  yields the estimation of the lower cylinder force along its axis as

$$F_{cld} = [W_l \overline{k c_l} \sin \alpha_d + W_c \overline{c_{lc} k} \sin(\gamma_{ld} - \alpha_d + \delta_{1d}) + W_p \overline{c_{lp} k} \sin(\gamma_{ld} - \alpha_d + \delta_{2d})] / (\overline{k l_r} \sin \gamma_{ld}), \quad (4.2c)$$

$$\text{where } \overline{c_{lc} k} = [\overline{c_{lc} l_r}|_d^2 + \overline{k l_r}^2 - 2 \overline{c_{lc} l_r}|_d \overline{k l_r} \cos \gamma_{ld}]^{1/2}, \quad (4.2d)$$

$$\overline{c_{lc} l_r}|_d = [\overline{l_c l_r}|_d - \overline{l_c c_{lc}}], \quad (4.2e)$$

$$\overline{c_{lp} k} = [\overline{c_{lp} l_r}^2 + \overline{k l_r}^2 - 2 \overline{c_{lp} l_r} \overline{k l_r} \cos \gamma_{ld}]^{1/2}, \quad (4.2f)$$

$$\text{and } \delta_{1d} = \sin^{-1} [\overline{k l_r} \sin \gamma_{ld} / \overline{c_{lc} k}] \text{ and } \delta_{2d} = \sin^{-1} [\overline{k l_r} \sin \gamma_{ld} / \overline{c_{lp} k}]. \quad (4.2g)$$

By considering the weight of the upper member denoted by  $W_u$  acting along the point  $c_u$  besides the weights appearing in the last expression, the expression for the force along the axis of the upper piston is obtained by taking moment about  $h$  as

$$F_{rud} = [W_u \overline{hc_u} \sin \beta_d + W_l (\overline{hk} \sin \beta_d - \overline{kc_l} \sin \alpha_d) + W_c \{ \overline{hk} \sin \beta_d - \overline{c_{lc}k} \sin (\gamma_{ld} - \alpha_d + \delta_{1d}) \} + W_p \{ \overline{hk} \sin \beta_d - \overline{c_{lp}k} \sin (\gamma_{ld} - \alpha_d + \delta_{2d}) \}] / (\overline{hu_2} \sin \gamma_{ud}), \quad (4.2h)$$

$$\text{where } \gamma_{ud} = \cos^{-1} \{ (\overline{u_c u_r |}_d)^2 + \overline{hu_r}^2 - \overline{hu_c}^2 \} / (2 \overline{u_c u_r |}_d \overline{hu_r}). \quad (4.2i)$$

The inverse formulations described above provide the necessary inputs for execution of the controller structure proposed next.

### 4.3 Design of Order-Separated Feedforward Controller

The formulation of the **OSFF** model developed for simple linear motion demand in Chapter 3 is extended here for tracking more complex motions over a vertical plane for the free end of a serial manipulator involving lower and upper actuation systems. Besides estimating the actuation voltage demands for the valve solenoids, which must lie within the corresponding hardware limits, the model has also been used for fabrication design of certain components and selection of some others. The design has been achieved by carrying out a sensitivity analysis of the variations of the lengths of the passive members of the manipulator on the stroke lengths and velocities of the pistons leading to the estimation of the actuation discharge and power requirements.

It is evident from the last section that the inverse kinematic model generates the motion demand  $y_{di}$  of each piston relative to its cylinder, where  $i$  denotes either the lower valve-cylinder pair  $l$  or the upper pair  $u$ . The inverse dynamic model resolves the weight components for the estimation of the forces along the axis of each piston-cylinder pair. By using these estimations as inputs, the **OSFF** model constructed next targets estimation of the output of feedforward voltage  $V_{fi}$  through a non-iterative algebraic process. A feedback voltage  $v_{bi}$  has been added to take care all the modelling uncertainties and approximations. Thus, the overall controller with a dominant feedforward part emerges as

$$V_i = V_{fi} + v_{bi} \text{ with } v_{bi} \ll V_{fi}. \quad (4.3a)$$

The LVDT measures the displacement  $y_i$  of the piston relative to its cylinder and the error with respect to the demand  $y_{di}$  is estimated by the controller as

$$e_i = y_{di} - y_i. \quad (4.3b)$$

A classical form of PID feedback controller is considered in this study and can be represented as

$$v_{bi} = k_p e_i + k_I \int e_i dt + k_D (de_i/dt), \quad (4.3c)$$

where  $k_p$ ,  $k_I$  and  $k_D$  are the proportional (P), integral (I) and derivative (D) gains, respectively.

The dominating parts of the proposed feedforward controller that has been considered here are feedforward voltages  $V_{f0i}$  to sustain the desired piston motions by communicating oil through the metered ports of each valve. Since the axial opening at any such port could range from only a few microns to the maximum mostly well below 1mm, substantial amount of pressure drop occurs there, which can be sustained by the correspondingly high voltage contribution during any motion actuation. Two separate compensation voltages  $v_{li}$  and  $v_{fi}$  that are lower in order than the dominating motion-inducing voltage are considered for sustaining respectively the flow leakages and cylinder friction. Hence, the overall feedforward voltage model is expressed as

$$V_{fi} = V_{f0i} + v_{li} + v_{fi} \text{ with } v_{li} \ll V_{f0i} \text{ and } v_{fi} \ll V_{f0i}. \quad (4.4)$$

The excitation voltages monitor the actuation flows through the paired valve-cylinder arrangements. It is evident from Figure 2.3 that the upper cylinder end is hinged to an extended arm of the body, which further makes this end stationary relative to the body. However, the corresponding end of the lower cylinder could rotate about Point  $h$ . One component of this rotation can be resolved as translation of the lower cylinder along its own axis. Based on the above discussion a simple model for the acceleration of each piston of rod diameter  $d_r$  and weight  $W_p$  relative to the low-friction cylinder bore having diameter  $d_c$  and weight  $W_c$  under the pressures  $P_{ci}$  at the cap end and  $P_{ri}$  at the rod end of the cylinder emerges as

$$\ddot{y}_{r/cu} \equiv \ddot{y}_{ru} = (g/W_p)\{P_{cu}A_c - P_{ru}A_r - F_{ru} - F_{su} \text{sgn}(\dot{y}_{r/cu}) - \alpha_{vu}\dot{y}_{r/cu}\}, \quad (4.5a)$$

$$\begin{aligned} \ddot{y}_{r/cl} \equiv \ddot{y}_{rl} - \ddot{y}_{cl} = g\{(P_{cl}A_c - P_{rl}A_r - F_{rl} - F_{sl} \text{sgn}(\dot{y}_{r/cl}) - \alpha_{vl}\dot{y}_{r/cl})/W_p + \\ (P_{cl}A_c - P_{rl}A_r - F_{cl} + F_{sl} \text{sgn}(\dot{y}_{r/cl}) + \alpha_{vl}\dot{y}_{r/cl})/W_c\}, \end{aligned} \quad (4.5b)$$

$$\text{where } A_c = \pi d_c^2/4 \text{ and } A_r = \pi(d_c^2 - d_r^2)/4, \quad (4.5c)$$



Referring equation (2.2b), a model of sliding friction  $F_{fi}$  between the piston and the cylinder bore is considered here that involves only a static or coulomb friction  $F_{si}$  and lubricated friction proportional to the relative sliding velocity together with a lubrication constant  $\alpha_{vi}$ . This model is simpler than Tustin model. Following (Niranjan et al. 2017), the model is written as

$$F_{fi} = F_{si}\text{sgn}(\dot{y}_{r/ci}) + \alpha_{vi}\dot{y}_{r/ci}. \quad (4.5d)$$

The unexcited valve holds its neutral position and leakage occurs around the periphery of both the flat sides of each of the metering spool lands, marked as 1 and 2 in Figure 2.4 (a) near Ports A and B respectively. As the valves used in this setup have specified zero lap, the length of the leakage paths between the land and the facing edge of each sleeve cut remains close to zero within the limit of the manufacturing tolerance that is usually kept positive for the land. Each set of sleeve cuts is located between a companion recess in the bush outside and the spool inside. Across a leakage path in each of Ports A and B, the pressure drops from pump pressure  $P_p$  to the pressure in the connected cylinder chamber. From this chamber pressure, leakage also occurs to the tank. For the open tank used in the setup, the gauge pressure is set as zero.

For the external loading of the cylinder, when equal pressure is maintained in its two chambers, the leakages through the valve completely bypass the cylinder. However, in most of the situations, the chamber pressures remain unequal, and a leakage occurs past the piston, which can be derived as a part of the valve leakage. This has been exploited in the setup to keep the cylinder friction low. However, friction is likely to become perceptible due to clogging of the narrow radial clearance between the sliding members. The clogging may arise after long use from the failure of the oil filter or due to the degradation of oil itself.

Under the excitation of valve solenoid, the displacement of the spool causes increase of axial length of one leakage path associated to each metering land. At the other side of the land, an orifice opening of increasing axial length communicates with the connected cylinder chamber a motive flow rendering the piston motion. In Figure 2.4(a), the motive flow and leakage flow through the valve have been shown by a series of wide-headed and narrow-headed arrows, respectively under the excitations of solenoid  $s_{1i}$  and  $s_{2i}$ . Many researchers like (Dao et al. 2021) used orifice-flow model for the valve discharges expressed as proportional to square root of pressure drop across the length of the respective

orifice. In view of negligible leakage across the much larger axial length of a metering spool land between any two adjacent window cuts in the sleeve with respect to much shorter axial length of a radial clearance from the curved edge of a cut, both the motive flow and the leakage flow are considered as proportional to the respective curved lengths at Ports A and B.

Similar to the single cylinder test bench described in the previous chapter, for the valve ports A and B of the serial manipulator test bench, constant leakage coefficients  $c_{lA}$  and  $c_{lB}$  along with constant valve coefficients  $c_{vA}$  and  $c_{vB}$  for the corresponding motive flow that excites motion of the piston inside the cylinder have been proposed here. An incompressible flow model makes this motive flow proportional to the piston velocity. For each zero-lap proportional valve used in the setup, the motive flow is also considered proportional to the main component of the feedforward excitation voltage  $V_{f0i}$  in (4.4). It is also evident that as long as the pump is running irrespective of the excitation state of the solenoids the leakage continues to take place. Hence, in the proposed model, it has been considered that any leakage flow is independent of the excitation voltage. Under the excited state, the leakage contribution is maintained along with the motive flow through the open orifice as a ploy to also sustain the leakage past the piston by the smaller voltage component  $v_{li}$  in (4.4). As the annular leakage path across the length of the piston is much greater than narrow radial clearance, (Dao et al. 2021) modelled the leakage as proportional to the pressure difference across the piston. A proportionality constant  $c_{lci}$  is used here to model the leakage discharge in Cylinder  $i$ .

The setup depicted in Figure 2.3 involves lifting of the free point from the worktable or floor in certain planned forms. Clearly, during the initial lifting phase of the free point of the pistons need to retract. The solenoid connections must be arranged in such a way to ensure extension demand  $\dot{y}_{di} \geq 0$  by giving negative excitation to  $s2_i$  and retracting demand  $\dot{y}_{di} < 0$  for positive voltage excitation to  $s1_i$ . Since the leakage between the cylinder chambers is equal to the discharge from the valve less by the rate of expansion of a chamber volume due to the piston motion, it can be expressed for both the chambers as

$$\begin{aligned}
 c_{lci}(P_{cfi} - P_{rfi}) &= \{c_{vA}(V_{f0i} + v_{li} + v_{fi}) + c_{lA}\}\sqrt{P_P - P_{cfi}} - c_{lA}\sqrt{P_{cfi}} - A_c\dot{y}_{di} \\
 &= \{c_{vB}(V_{f0i} + v_{li} + v_{fi}) + c_{lB}\}\sqrt{P_{rfi}} + c_{lB}\sqrt{P_P - P_{rfi}} - A_r\dot{y}_{di} \text{ for } \dot{y}_{di} \geq 0,
 \end{aligned}
 \tag{4.6a}$$

$$\begin{aligned}
c_{lci}(P_{rfi} - P_{cfi}) &= A_r \dot{y}_{di} - \{c_{vB}(V_{f0i} + v_{li} + v_{fi}) + c_{lB}\} \sqrt{P_p - P_{rfi}} + c_{lB} \sqrt{P_{rfi}} \\
&= A_c \dot{y}_{di} - \{c_{vA}(V_{f0i} + v_{li} + v_{fi}) + c_{lA}\} \sqrt{P_{cfi}} + c_{lA} \sqrt{P_p - P_{cfi}} \text{ for } \dot{y}_{di} < 0,
\end{aligned} \tag{4.6b}$$

$$\text{along with } v_{li} \ll V_{f0i}, v_{fi} \ll V_{f0i} \text{ and } c_{lA}/c_{lB} = c_{vA}/c_{vB}. \tag{4.6c}$$

In the first of the two steps of the feedforward formulation, the lower-order leakage term in (4.6a) and (4.6b) are neglected in view of the first part given in (4.6c). The resulting expressions for the chamber pressures are then substituted in (4.5a) and (4.5b) with inertia effects neglected for minimizing calculations. In the second stage, the second part of (4.6c) is then used and the terms not related to friction are collected as to form the higher-order expressions and the friction related terms are collected to form the lower-order expression. The higher-order expressions of the second stage of separation thus gives

$$\begin{aligned}
V_{f0i} &= -\dot{y}_{di} [(A_c^3/c_{vA}^2 + A_r^3/c_{vB}^2) / \{P_p \max\langle \text{sgn}(\dot{y}_{di}), 0 \rangle A_c\} \\
&\quad + P_p \max\langle \text{sgn}(-\dot{y}_{di}), 0 \rangle A_r\} \times f_{icp} - F_{id}]^{1/2},
\end{aligned} \tag{4.7a}$$

$$P_{cfi}|_{\dot{y}_{di} \geq 0} = P_p \{1 - (A_c^3/c_{vA}^2) / (A_c^3/c_{vA}^2 + A_r^3/c_{vB}^2)\}, \tag{4.7b}$$

$$P_{rfi}|_{\dot{y}_{di} \geq 0} = P_p (A_c A_r^2 / c_{vB}^2) / ((A_c^3/c_{vA}^2 + A_r^3/c_{vB}^2)), \tag{4.7c}$$

$$P_{cfi}|_{\dot{y}_{di} < 0} = P_p (A_r A_c^2 / c_{vA}^2) / ((A_c^3/c_{vA}^2 + A_r^3/c_{vB}^2)), \tag{4.7d}$$

$$\text{and } P_{rfi}|_{\dot{y}_{di} < 0} = P_p \{1 - (A_r^3/c_{vB}^2) / (A_c^3/c_{vA}^2 + A_r^3/c_{vB}^2)\}, \tag{4.7e}$$

$$\text{where } F_{id} = F_{rud} \text{ and } F_{rld} + F_{cld}(W_p/W_c) \text{ for } i = u \text{ and } l \text{ respectively,} \tag{4.7f}$$

$$\text{and } f_{icp} = 1 \text{ and } 1 + W_p/W_c \text{ for } i = u \text{ and } l \text{ respectively.} \tag{4.7g}$$

Next by equating the terms for the leakages in each of (4.6a) and (4.6b), the expression for the leakage compensating voltage  $v_{li}$  and the cylinder leakage constant  $c_{lc}$  are derived respectively as

$$\begin{aligned}
v_{li}|_{\dot{y}_{di} \geq 0} &= c_{lB} \{(P_{rfi}|_{\dot{y}_{di} \geq 0})^{1/2} - (P_p - P_{rfi}|_{\dot{y}_{di} \geq 0})^{1/2}\} - c_{lA} \{(P_p - P_{cfi}|_{\dot{y}_{di} \geq 0})^{1/2} - \\
&\quad (P_{cfi}|_{\dot{y}_{di} \geq 0})^{1/2}\} \times [\{c_{vA}(P_p - P_{cfi}|_{\dot{y}_{di} \geq 0})^{1/2} - c_{vB}(P_{rfi}|_{\dot{y}_{di} \geq 0})^{1/2}\}]^{-1},
\end{aligned} \tag{4.7h}$$

$$\begin{aligned}
v_{li}|_{\dot{y}_{di} < 0} &= c_{lA} \{(P_p - P_{cfi}|_{\dot{y}_{di} < 0})^{1/2} - (P_{cfi}|_{\dot{y}_{di} < 0})^{1/2}\} + c_{lB} \{(P_p - P_{rfi}|_{\dot{y}_{di} < 0})^{1/2} - \\
&\quad (P_{rfi}|_{\dot{y}_{di} < 0})^{1/2}\} \times [\{c_{vA}(P_{cfi}|_{\dot{y}_{di} < 0})^{1/2} - c_{vB}(P_p - P_{rfi}|_{\dot{y}_{di} < 0})^{1/2}\}]^{-1},
\end{aligned} \tag{4.7i}$$

$$c_{lci}|_{\dot{y}_{di} \geq 0} = \{(c_{vA} v_{li}|_{\dot{y}_{di} \geq 0} + c_{lA})(P_p - P_{cfi}|_{\dot{y}_{di} \geq 0})^{1/2} - c_{lA} P_{cfi}|_{\dot{y}_{di} \geq 0}\} \times$$

$$(P_{cfl}|_{\dot{y}_{di} \geq 0} - P_{rfl}|_{\dot{y}_{di} \geq 0})^{-1}, \quad (4.7j)$$

and  $c_{lci}|_{\dot{y}_{di} < 0} = -\{(c_{vA}v_{li}|_{\dot{y}_{di} < 0} + c_{lA})P_{cfl}|_{\dot{y}_{di} < 0} - c_{lA}(P_p - P_{cfl}|_{\dot{y}_{di} < 0})^{1/2}\} \times$

$$(P_{rfl}|_{\dot{y}_{di} < 0} - P_{cfl}|_{\dot{y}_{di} < 0})^{-1}. \quad (4.7k)$$

Finally, by equating the lower-order expression containing the friction terms in the second stage of separation, the friction compensating voltages for the valves is obtained as

$$v_{fu}|_{\dot{y}_{du} \geq 0} = 0.5V_{f0u}|_{\dot{y}_{du} \geq 0} - \{P_p A_c - F_{su} \text{sgn}(\dot{y}_{du}) - \alpha_{vu} \dot{y}_{du}\} \times (V_{f0u}^3 / 2\dot{y}_{du}^2) [(A_c^3 / c_{vA}^2) + (A_r^3 / c_{vB}^2)]^{-1}, \quad (4.7l)$$

$$v_{fu}|_{\dot{y}_{du} < 0} = 0.5V_{f0u}|_{\dot{y}_{du} < 0} - \{P_p A_c + F_{su} \text{sgn}(\dot{y}_{du}) + \alpha_{vu} \dot{y}_{du}\} \times (V_{f0u}^3 / 2\dot{y}_{du}^2) [(A_c^3 / c_{vA}^2) + (A_r^3 / c_{vB}^2)]^{-1}, \quad (4.7m)$$

$$v_{fl}|_{\dot{y}_{dl} \geq 0} = 0.5V_{f0l}|_{\dot{y}_{dl} \geq 0} - \{P_p A_c - F_{sl} \text{sgn}(\dot{y}_{dl}) + \alpha_{vl} \dot{y}_{dl}\} \times (V_{f0l}^3 / 2\dot{y}_{dl}^2) [(A_c^3 / c_{vA}^2) + (A_r^3 / c_{vB}^2)]^{-1}, \quad (4.7n)$$

$$\text{and } v_{fl}|_{\dot{y}_{dl} < 0} = 0.5V_{f0l}|_{\dot{y}_{dl} < 0} - \{P_p A_c + F_{sl} \text{sgn}(\dot{y}_{dl}) + \alpha_{vl} \dot{y}_{dl}\} \times (V_{f0l}^3 / 2\dot{y}_{dl}^2) [(A_c^3 / c_{vA}^2) + (A_r^3 / c_{vB}^2)]^{-1}. \quad (4.7o)$$

The above formulation is applicable for cylinders of both single and double-rod types. However, before using the feedforward expressions in real time an estimation of the parameters is usually necessary. The most convenient method of finding the feedforward parameters is to execute a real-time experiment for a simple demand and perform several numerical simulations with different parameter values for the full controller-integrated system model with identical voltage variation recorded in the experiment. The particular set of parameters that would yield a close matching of the variation between the predicted piston displacement and the experimental output would provide the desired estimate. Of course, an optimizer would be useful to set different parameter values for the simulation runs in a systematic manner. (Sarkar et al. 2013b & Dasmahapatra et al. 2018) used such an optimizer successfully in the past.

In view of the newness of the setup, the parameter values used in the experiments have been extracted directly from the catalogue SM4-10/12/15 of the valve manufacturer Vickers (Eaton), (-28). By using (4.7j) and (4.7k), the parameter for the cylinder leakage would be obtained. Also, as the cylinders deployed in the setup has lesser amount of friction its effect has been omitted while developing the feedforward model. However, the omitted

effect has been compensated by the feedback controller, much like the neglected inertia and suspended mass effects on the motion dynamics of the pistons. Under these circumstances, the real-time experiments have been carried out without any initial identification experiment. The identification experiments would be valuable for possible futuristic condition monitoring as described next.

Prolonged use of the manipulator would indeed lead to increasing contribution of the feedback voltages as well as the total voltages along with it. Beyond a level in the increase of the overall voltage requirement, identification experiments could be conducted for fresh estimation of all the parameters including that for the valve. Any substantial increase in the valve leakage coefficient, cylinder leakage coefficient or friction parameters would imply corresponding deterioration of the valve, the cylinder-piston radial clearance and the piston seals. In this way, the condition of the system along with pinpoint identification of the location of the emerging fault could be ascertained. Once the leakage coefficients are accepted from the identification experiment, their estimation from (4.7h) and (4.7i) is disregarded.

Once the necessary values of the feedforward parameters are available, the controller becomes ready for real-time use. The LVDT feedbacks would not only provide the control error (4.3b) but also the estimate of error with respect to the demanded displacement variation of the free point of the serial manipulator. A forward kinematic model would be useful in this regard.

#### 4.4 Forward Kinematic Modeling

For the single leg configuration, the forward kinematic model is used to extract the tracking performance of the feedforward controller by finding the position of the free point in the two-dimensional space. As one end of the leg hangs from a stationary anchor point  $a$ , the forward kinematic model has been formulated for finding the position of the free end with respect to the anchor. Between the forward and inverse kinematic models, the input and output are reversed. Hence, the inputs to the forward kinematic model are the LVDT readings for the combined axial length of the piston-cylinder pairs in the lower and upper systems. Corresponding to (4.1f), (4.1g), (4.1c) and (4.1d), the model is represented as

$$\overline{l_c l_r} = y_l + \overline{l_c l_r}|_c, \quad (4.8a)$$

$$\overline{u_c u_r} = y_u + \overline{u_c u_r}|_c, \quad (4.8b)$$

$$\alpha = \pi - \beta - \delta - \cos^{-1}\{(\overline{k l_c^2} + \overline{k l_r^2} - \overline{l_c l_r^2}) / (2\overline{k l_c} \overline{k l_r})\}, \quad (4.8c)$$

$$\text{and } \beta = \pi - \phi - \cos^{-1}\{(\overline{h u_c^2} + \overline{h u_r^2} - \overline{u_c u_r^2}) / (2\overline{h u_c} \overline{h u_r})\}, \quad (4.8d)$$

to finally obtain the actual coordinate of the free point as

$$x_f = \overline{h k} \sin \beta + x_h - \overline{k f} \sin \alpha, \quad (4.8e)$$

$$\text{and } z_f = z_h - \overline{h k} \cos \beta - \overline{k f} \cos \alpha. \quad (4.8f)$$

Of course, the deviations from a prescribed demand  $(x_{fd}, z_{fd})$  and the values given by at any instant by (4.8e) and (4.8f) depends on the performance of the controller employed in real time. Representative numerical and experimental results are presented next for two different motion plans. One motion plan

$$\dot{x}_{fd} = 0, z_{fd}(t) = z_{f0} + (l_f/2) \{\sin(2\pi t/T - \pi/2) + 1\}, \quad (4.9a)$$

is a linear vertical up and down reciprocating demand over length  $l_f$  and time period  $T$ . The other plan is a circular motion demand of radius  $\rho$  is expressed as

$$x_{fd}(t) = \rho \sin(2\pi t/T), z_{fd}(t) = z_{f0} + \rho \sin(2\pi t/T - \pi/2). \quad (4.9b)$$

## 4.5 Numerical Study and Stability Analysis of the Controller

A numerical study has been conducted first to justify the simplifications employed in (4.5a) and (4.5b) during their incorporation for developing the feedforward model (4.7a) to (4.7c). These results are presented in Figure 4.2 for only the circular motion plan given in (4.9b) for the frequencies of 0.5 and 1.0Hz. As estimated from feedforward pressure model (4.7b) to (4.7e), the variations of equal thrusts on each face of the same piston in the lower and upper systems are shown in Figure 4.2(a), The figure also shows variation of the net thrust on these pistons obtained from (4.5a) and (4.5b) by considering the effects of piston inertia and suspended weight under each actuator. Clearly, the net thrust is almost two-order lower than the feedforward thrust on one face. Hence, the numerical exercise validates the assumption of equal thrust on both sides of the piston that has been employed for making the feedforward calculation at the implementation stage faster.

In Figure 4.2(b), the variations of the inertia and suspended weights are depicted separately, which have been evaluated from (4.5a), (4.5c), (4.2h) and (4.2i) for the upper actuator and

(4.5b), (4.5c), (4.2a) and (4.2b) for the lower actuator. Since the multiplication factors of  $10^5$  and  $10^2$  respectively make the inertia and suspended weight comparable with the feedforward pressure (FF) thrust on one piston face, the former two effects are clearly negligible. Constancy of the pressure thrust over each half cycle for piston motion, as apparent in Figure 4.2(a), is consistent with the pressure model arising due to constant velocity to voltage ratio from (4.7a). As the inertia and the suspended weight have been neglected, (4.7b) to (4.7e) yield identical thrust over the corresponding half cycles of both the lower and upper actuators. The observed shift in Figure 4.2 between the duration of the half cycles for the two actuators for each type of force arises from the motion kinematics.

Figure 4.2(b) shows that the suspended load appears to be the chief contributor of the net thrust on each piston with respect to the inertia component, which provides almost three-order less contribution, respectively. As expected for the manipulator configuration of Figure 2.3, the suspended weight under the upper actuator apparent is significantly higher than that under the lower actuator. The inertia effect appears higher for the lower actuator possibly due to the translation of only the lower cylinder and arrested translation of the upper cylinder. Consideration of the relative translation of a piston relative to its cylinder is a notable aspect of the formulation (4.5b).

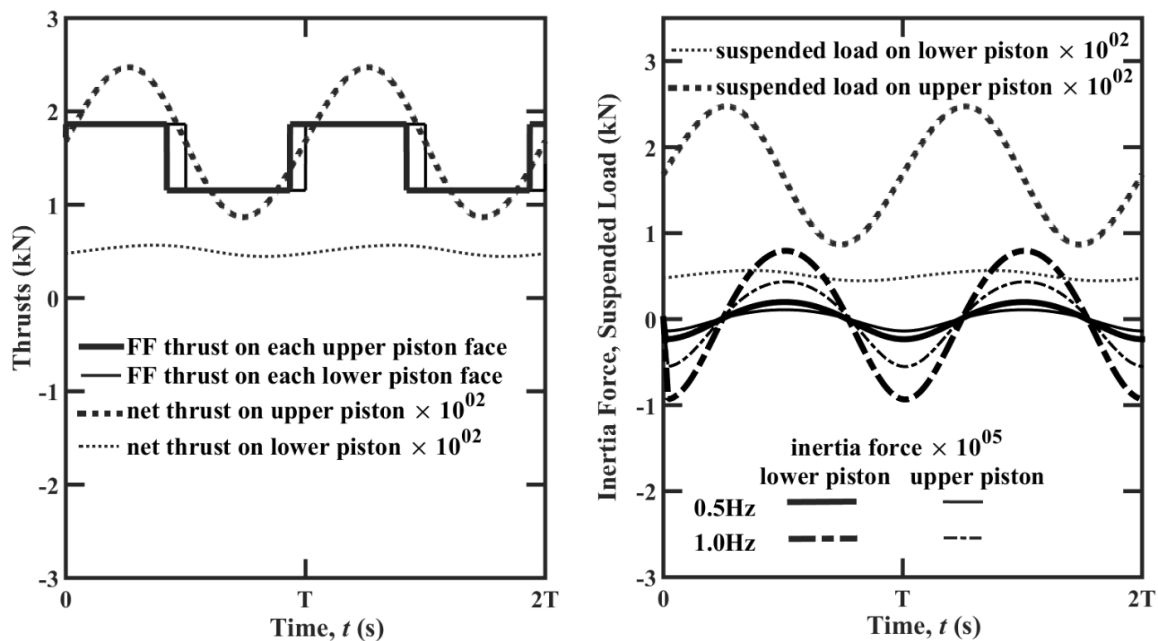


**Figure 4.2: Comparison of feedforward estimates of individual forces and computed net piston thrusts incorporating neglected effects in feedforward estimation.**

The consideration of imperceptible inertial effect simplifies the stability analysis of the overall **OSFFPID** controller formulation stated above where the **PID** feedback is normally

employed to take care of the controller error. During stability analysis of the above designed controller the actual flow with pressure in each cylinder chamber has been modeled properly as to have a dominating feedforward part along with a lower perturbation part yielding

$$P_{xi} = P_{xfi} + p_{xi} \text{ with } p_{xi} \ll P_{xfi} \text{ and } x = c \text{ and } r, \quad (4.10a)$$

together with equations (4.3b) and (4.6c) and subtracting from the ensuing model the pertinent **FF** equation between (4.6a) and (4.6b), it is obtained that

$$\left. \begin{aligned} p_{ci} &= 2v_{bi}(P_P - P_{cfi})/V_{f0i} + 2\sqrt{P_P - P_{cfi}}A_c\dot{e}_i/(c_{vA}V_{f0i}) \text{ for } \dot{y}_{di} \geq 0 \\ &= 2\sqrt{P_{cfi}}A_c\dot{e}_i/(c_{vA}V_{f0i}) - 2v_{bi}(P_{cfi})/V_{f0i} \text{ for } \dot{y}_{di} < 0 \end{aligned} \right\}, \quad (4.10b)$$

$$\text{and } \left. \begin{aligned} p_{ri} &= -2\sqrt{P_{rfi}}A_r\dot{e}_i/(c_{vB}V_{f0i}) - 2v_{bi}P_{rfi}/V_{f0i} \text{ for } \dot{y}_{di} \geq 0 \\ &= 2v_{bi}(P_P - P_{rfi})/V_{f0i} - 2\sqrt{P_P - P_{rfi}}A_r\dot{e}_i/(c_{vB}V_{f0i}) \text{ for } \dot{y}_{di} < 0 \end{aligned} \right\}, \quad (4.10c)$$

By dropping the insignificant terms from (4.5a) and (4.5b) based on the numerical results as depicted in Figure 4.2, the error dynamic equation can be deduced as

$$\dot{e}_i + a_1 e_i + a_0 \int e dt = 0, \quad (4.10d)$$

$$\text{where } a_1 = k_p F_f / a_2 \text{ and } a_0 = a_1 k_I / k_p, \quad (4.10e)$$

$$\text{with } \left. \begin{aligned} a_2 &= k_D F_f + 0.5\alpha_{li}|V_{f0i}| + \{\sqrt{P_P - P_{cfi}}A_c^2/c_{vA} + \sqrt{P_{rfi}}A_r^2/c_{vB}\} \text{ for } \dot{y}_{di} \geq 0 \\ &= k_D F_f - 0.5\alpha_{li}|V_{f0i}| - \{\sqrt{P_{cfi}}A_c^2/c_{vA} + \sqrt{P_P - P_{rfi}}A_r^2/c_{vB}\} \text{ for } \dot{y}_{di} < 0 \end{aligned} \right\} \quad (4.10f)$$

$$\text{and } \left. \begin{aligned} F_f &= A_c(P_P - P_{cfi}) + A_r P_{rfi} \text{ for } \dot{y}_{di} \geq 0 \\ &= A_c P_{cfi} + A_r(P_P - P_{rfi}) \text{ for } \dot{y}_{di} < 0 \end{aligned} \right\}, \quad (4.10g)$$

along with higher order FF voltage  $|V_{f0i}|$  used maintaining consistency with (4.7a). It is clearly apparent that beyond a certain value of the derivative ‘D’ gain, the controller emerges as stable in the light of all positive coefficients in the second-order linear dynamics of the integral of error in each actuation system. After performing this numerical study of the constructed FF model, another issue for identification of significant FF parameters has been taken up prior to the real-time implementation of the proposed **OSFFPID** controller. The **GA** based optimization technique that has been extensively used to find feedforward parameters during the development phase of feedforward controller, and already explained in section 3.5 and 3.6 of the previous chapter has been implemented here also for finding feedforward and feedback parameters of the present controller.



## 4.6 Identification of Feedforward Parameters & Condition

### Monitoring

The number of feedforward parameters includes four coefficients for each valve as evident from equation (4.6a) and (4.6b) and two friction coefficient as given in equation (4.5d). The valve parameters in (4.6a) and (4.6b) have been extracted from the catalogue of the manufacturer (Vickers (EATON); 1993) from the specified rated flow of  $6.34 \times 10^{-4} \text{m}^3/\text{s}$  and the maximum null leakage of  $2.34 \times 10^{-5} \text{m}^3/\text{s}$  at an excitation voltage of 4V and the total pressure drop of 7MPa across the two metered ports in series shorted by a line bypassing the cylinder. By using these values in (4.7j) and (4.7k), the valve coefficients  $c_{vA} = 2c_{vB}$  have been found as  $5.98 \times 10^{-8} \text{m}^{3.5} \text{V}^{-1} \text{kg}^{-1/2}$  and the leakage coefficients  $c_{lA} = 2c_{lB}$  as  $8.82 \times 10^{-9} \text{m}^{3.5} \text{kg}^{-1/2}$ . For finding the friction parameters as given in (4.5d) the **RCGA** based existing optimization algorithm has been used (Sarkar et al. 2013b), where the real-time response  $y(t)$  achieved for a sinusoidal demand with **PID** control has been compared with several numerical simulations of (4.5a) to (4.6b) yielding  $y_p(t)$  for different parameter set in (4.5d) with identical voltage variation recorded in the experiment. In Figure 4.3, the comparison is given corresponding to the converged set yielding low integral absolute error

$$\text{IAE} (\mathbf{I}_\delta) = \left( \int_0^T |y_p(t) - y(t)| dt \right) / T. \quad (4.11)$$

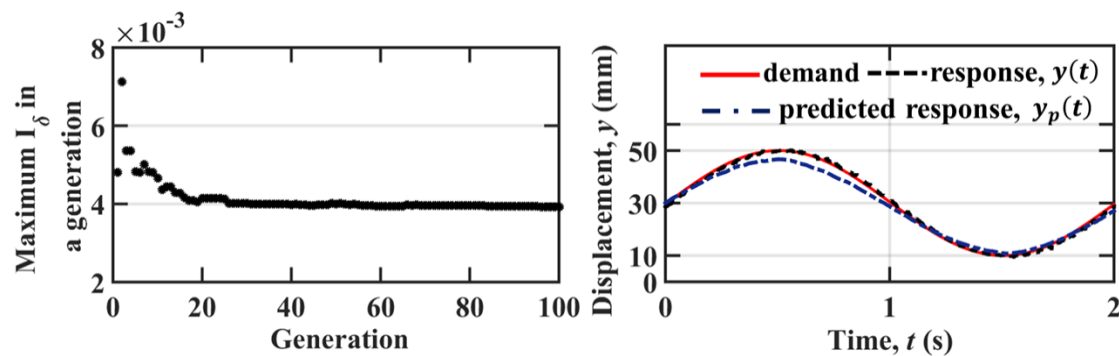


**Figure 4.3: Maximum IAE in a generations and predicted variations of response with time during friction parameter estimation**

The reduction of the maximum **IAE** in a generation to a converged level is apparent in Figure 4.3. After the end of the identification process the converged magnitude of static friction  $F_s$  and the lubrication constant  $\alpha_v$  is obtained as 22.5 N and 259.5 N-s/mm,

respectively. The matching of the predicted response with the given demand as shown in the figure makes these friction parameter values as acceptable.

After the justification study of the proposed feedforward model followed by the identification of feedforward parameters, the experimental scheme is discussed next with reference to Figure 4.4. The real-time results conducted for the motion demands (4.9a) and (4.9b) are presented in Figures 4.4 to 4.16.

## 4.7 Experimental Results and Discussion

### 4.7.1 Experimental Scheme and Performance Estimation Procedure

All the blocks except the performance estimation block shown in Figure 4.4 for the experimental scheme have been discussed in Section 4.3 separately. The leftmost block of the figure has been simplified to only the inverse kinematic model by the omission of the dynamic model, the acceptability of which has been already explained with the help of numerical results given in Figure 4.2. The performance estimation process begins with evaluation of the errors of the free point

$$e_f(t) = \{(x_{fd}(t) - x_f(t))^2 + (z_{fd}(t) - z_f(t))^2\}^{1/2}, \quad (4.12a)$$

$$\text{and } e_{f*}(t) = *_{fd}(t) - *_f(t) \text{ with } * = x \text{ or } z, \quad (4.12b)$$

in which  $e_{f_x}(t)$  identifies the unwanted cross-coupled horizontal component of the error. With the subscript  $d$  indicating the demand, another error composition given by

$$e_{f\rho}(t) = [\{x_{fd}(t)^2 + z_{fd}(t)^2\}^{1/2} - \{x_f(t)^2 + z_f(t)^2\}^{1/2}], \quad (4.12c)$$

computes the deviation of the trajectory from the demanded circular motion (4.9b).

At any instant, the target of the controller is minimization of the deviation of response with respect to the demand. A comparison between the **PID** and **OSFFPID** controllers is presented in Table 4.1 in terms of the integral absolute errors and root mean square errors for both the motion plans in the task space and actuation space along with and the control efforts and the total variation **TV** for both the actuators given respectively as

$$\mathbf{IAE}_i = (\int_0^{nT} |e_i| dt) / (nT) \text{ for } i = f, l \text{ and } u, \quad (4.12d)$$

$$\mathbf{RMSE}_i = \{(\int_0^{nT} e_i^2 dt) / (nT)\}^{1/2} \text{ for } i = f, l \text{ and } u \quad (4.12e)$$

$$\mathbf{CE}_i = (\int_0^{nT} V_i^2 dt) / (V_{\max}^2 nT), \quad (4.12f)$$

$$\text{and } \mathbf{TV}_i = (\int_0^{nT} |V_i| dt), \quad (4.12g)$$

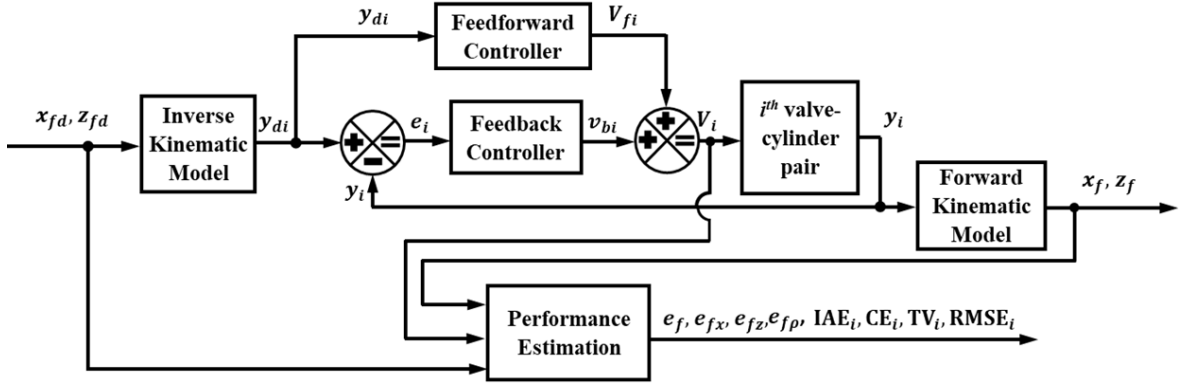


**Figure 4.4: Block diagram representation of experimental scheme**

where  $V_{\max}$  is taken equal to 2V and the amplitude  $a$  represents either half of the reciprocating length evident in (4.9a) or the radius  $\rho$  apparent in (4.9b). The performance index **IAE** given in (4.12d) corresponding to the free-point of the serial manipulator has been used here to tune the **PID** gains for both the **OSFFPID** and **PID** controllers excited for meeting the reciprocating motion demand given in equation (4.9a) with 70mm stroke length at 0.5Hz. The **RCGA** based minimization technique that has been described in section 4.6 with reference to Figure 4.3 to obtain feedforward parameters has been used here also in the same manner to obtain the converged gain values by using (4.12d) for the free-point. Subsequent experiments have been executed with these converged gains, unless mentioned otherwise.

Experimental results of Figures 4.5 to 4.17 have been obtained at a relief valve setting of 7MPa. Serial-mode reciprocating and circular motion demands of the free-point given respectively by (4.9a) and (4.9b) have been studied for frequencies of 0.1, 0.2, 0.5 and 1Hz. The length  $L_f$  equal to 70mm in (4.9a) and radius  $\rho$  equal to 40mm in (4.9b) has been considered for the current experiment. The **RCGA**-tuned proportional, integral and derivative gains have appeared respectively as 27V/m, 10.5V/(m-s) and 0.22V-s/m for the **PID** controller and as 9.5V/m, 3.8V/(m-s) and 0.14V-s/m for **OSFFPID** controller. Figure 4.17 shows the effect of gain variation significantly away from the tuned values. Besides comparing the performances of the two controllers and analysing the **OSFFPID** composition, the cause of the oscillatory behaviour of the **PID**-only controller have also been explained in a separate subsection.

#### 4.7.2 Comparison of Performance Indices for OSFFPID and PID Controllers

Table 4.1 contains the real-time performance of the proposed **OSFFPID** controller against a **PID** controller in terms of the performance index values estimated from (4.12d) to (4.12g) respectively— which clearly depicts lower **IAE** and **RMSE** for the proposed controller, and thus reveals its superiority over the **PID** controller. For both the reciprocation (4.9a) and the circular motion demand (4.9b), the  $\mathbf{IAE}_f$  appears lower by a factor of 1.5 to 3 for the **OSFFPID** controller. The superior performance of the proposed controller is presumably due to the inclusion of physics-based estimation of a significant part of each voltage excitation, on the basis of physical understanding of the oil flow and piston motion along with the acceptable approximations that has been revealed by the numerical results given in Figure 4.2. The **CE** requirement for the upper actuator appears to be higher in all the cases but one confirms the domination of the suspended weight over the inertia, which can also be clearly seen in the numerical results of Figure 4.2(b) that reveals about three-order lower inertia force even for 1.0Hz demand. Since the inertia force is proportional to the square of the frequency ratio, at lower frequencies, it would be further lower and in real time, these effects have been compensated by the **PID** feedback added in the **OSFFPID** controller

Table 4.1 also exhibits increase of **CE** with increase in frequency that clearly arises to meet the higher flow demand in the cylinder. With increase in the demanded frequency of the free-point motion, both  $\mathbf{IAE}_f$  and  $\mathbf{RMSE}_f$  show progressively increasing deviations under the **PID** controller that is more pronounced than observed under the **OSFFPID** controller. Better tracking has been realized by the **OSFFPID** controller mostly with lower control effort computed by (4.12f) and similar total variation obtained from (4.12g). Since the total variation is indicative of the expended energy from the battery that sustains the control electronics, better **OSFFPID** performance is even more encouraging.

With respect to the **RMSE** of 58.46mm under **PID** controller in an existing study at 0.05Hz, an **FFPID** controller resulted in much lower **RMSE** of 25.78mm for sinusoidal input motion demand at 0.05Hz for moving only the arm of a bigger system (Feng et al. 2019). Corresponding to this ratio of improvement of 2.27, Table 4.1 for the proposed order-separated **FFPID** scheme shows  $\mathbf{RMSE}_l$  reductions at 0.5Hz used for the gain tuning by a ratio of 3.22 for the reciprocation demand and 2.96 for the circular motion demand. For both the demands,  $\mathbf{RMSE}_u$  ratio has been generally lower than  $\mathbf{RMSE}_l$  ratio along with significant improvement in both  $\mathbf{RMSE}_u$  and  $\mathbf{RMSE}_l$  ratios at frequencies below 0.5Hz.

**Table 4.1 Comparison of performance indices for Serial Manipulator**

Performance Index	Reciprocation Demand (Hz)				Circular-motion Demand (Hz)			
	0.1	0.2	0.5	1.0	0.1	0.2	0.5	1.0
<b>OSFFPID IAE<sub>f</sub></b>	<b>0.59</b>	<b>0.62</b>	<b>0.67</b>	<b>0.72</b>	<b>0.60</b>	<b>0.61</b>	<b>0.61</b>	<b>0.64</b>
PID IAE <sub>f</sub>	0.92	1.15	2.00	2.26	1.11	1.33	1.89	2.17
<b>OSFFPID RMSE<sub>f</sub> (mm)</b>	<b>24.12</b>	<b>24.52</b>	<b>24.34</b>	<b>26.74</b>	<b>24.65</b>	<b>24.71</b>	<b>24.74</b>	<b>25.25</b>
PID RMSE <sub>f</sub> , mm	32.10	38.45	80.31	82.32	40.99	42.32	84.41	90.11
<b>OSFFPID IAE<sub>l</sub> × 10<sup>3</sup></b>	<b>5.88</b>	<b>12.56</b>	<b>25.59</b>	<b>70.8</b>	<b>8.32</b>	<b>9.68</b>	<b>27.6</b>	<b>6.315</b>
PID IAE <sub>l</sub> × 10 <sup>3</sup>	25.49	44.07	81.18	134.2	20.99	36.28	81.64	134.5
<b>OSFFPID RMSE<sub>l</sub> (mm)</b>	<b>0.26</b>	<b>0.49</b>	<b>0.98</b>	<b>1.74</b>	<b>0.38</b>	<b>0.43</b>	<b>1.23</b>	<b>1.29</b>
PID RMSE <sub>l</sub> (mm)	1.11	1.73	3.16	5.22	0.96	1.63	3.64	5.98
<b>OSFFPID IAE<sub>u</sub> × 10<sup>3</sup></b>	<b>5.83</b>	<b>4.64</b>	<b>12.86</b>	<b>33.24</b>	<b>1.44</b>	<b>1.5</b>	<b>18.21</b>	<b>6.23</b>
PID IAE <sub>u</sub> × 10 <sup>3</sup>	13.96	20.73	33.96	53.49	9.16	15.31	32.93	56.4
<b>OSFFPID RMSE<sub>u</sub> (mm)</b>	<b>0.23</b>	<b>0.17</b>	<b>0.50</b>	<b>1.29</b>	<b>0.07</b>	<b>0.08</b>	<b>0.82</b>	<b>0.29</b>
PID RMSE <sub>u</sub> (mm)	0.55	0.82	1.32	2.09	0.41	0.68	1.46	2.51
<b>OSFFPID CE<sub>l</sub> × 10<sup>3</sup></b>	<b>5.2</b>	<b>5.2</b>	<b>4.2</b>	<b>5.1</b>	<b>4.88</b>	<b>5.1</b>	<b>4.1</b>	<b>4.98</b>
PID CE <sub>l</sub> × 10 <sup>3</sup>	4.96	5.43	5.3	5.8	4.6	4.2	4.3	4.5
<b>OSFFPID CE<sub>u</sub> × 10<sup>3</sup></b>	<b>8.6</b>	<b>8.14</b>	<b>4.82</b>	<b>4.52</b>	<b>7.14</b>	<b>6.64</b>	<b>6.92</b>	<b>7.1</b>
PID CE <sub>u</sub> × 10 <sup>3</sup>	8.7	8.44	7.86	7.73	7.46	6.83	6.95	6.9
<b>OSFFPID TV<sub>l</sub> (V-s)</b>	<b>2.88</b>	<b>1.46</b>	<b>0.51</b>	<b>0.26</b>	<b>2.79</b>	<b>1.41</b>	<b>0.48</b>	<b>0.25</b>
PID TV <sub>l</sub> (V-s)	2.82	1.46	0.58	0.29	2.69	1.29	0.51	0.27
<b>OSFFPID TV<sub>u</sub> (V-s)</b>	<b>3.72</b>	<b>1.79</b>	<b>0.55</b>	<b>0.26</b>	<b>3.37</b>	<b>1.64</b>	<b>0.66</b>	<b>0.33</b>
PID TV <sub>u</sub> (V-s)	3.73	1.83	0.72	0.35	3.32	1.64	0.68	0.34

These results also clearly establish the strength of the proposed **OSFFPID** controller. It may be noted that the delivery pressure of the pump was set for the present experiment at only 7MPa in the serial manipulator setup shown in Figure 2.3 in comparison to 20MPa in the earlier study.

### 4.7.3 Time Domain Performance Comparison Between OSFFPID and PID Controllers

#### Controllers

Figures 4.5 and 4.6 represent the variations of the error in the free-point position with time for the reciprocating and circular motion demands, respectively. The increasing trend of free-point position error with increase in the demanded frequency is consistent with the corresponding integrated values, listed in the first four rows of Table 4.1. According to the expression given in (4.12a), the error values in these figures are always positive. The magnitude of error at any instant further depends on the actuation errors in the upper and lower systems that could have same or opposite signs at the same instant. The positive and negative signs of upper and lower actuation error as evident in Figures 4.7 and 4.8 are linked respectively with extravagant or insufficient excitation fed to the valves.

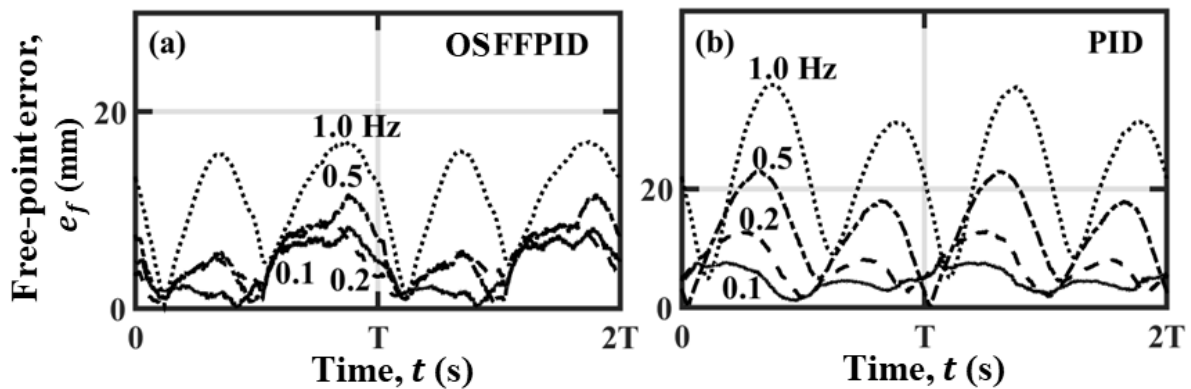


**Figure 4.5: Variations of free-point position error under OSFFPID and PID controllers at frequencies of 0.1, 0.2, 0.5 and 1.0Hz reciprocation demand**

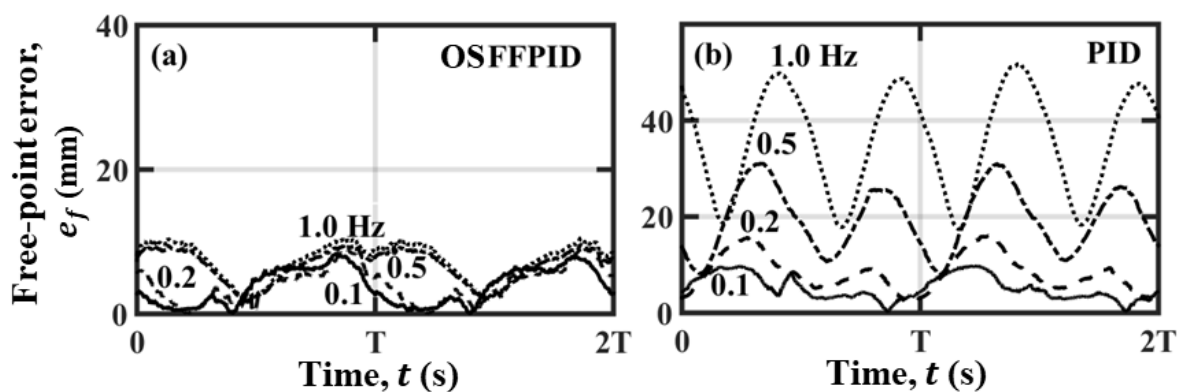


**Figure 4.6: Variations of free-point position error under OSFFPID and PID controllers at frequencies of 0.1, 0.2, 0.5 and 1.0Hz circular-motion demand**

Figures 4.9 and 4.10 depict the excitation voltage variations of the lower and upper valve for vertical reciprocation and circular motion, respectively. An insufficient excitation

voltage would produce an output lower than the demand which further leads to a positive actuation error given in (4.3b). On the other hand, extravagant use over a duration produces a negative error. Since the effect of the suspended weight and acceleration of the connected masses of the system have been neglected in (4.7a) in the feedforward model, the features of the feedback variations for the **OSFFPID** controller have appeared as qualitatively similar to that of the **PID**-only controller.

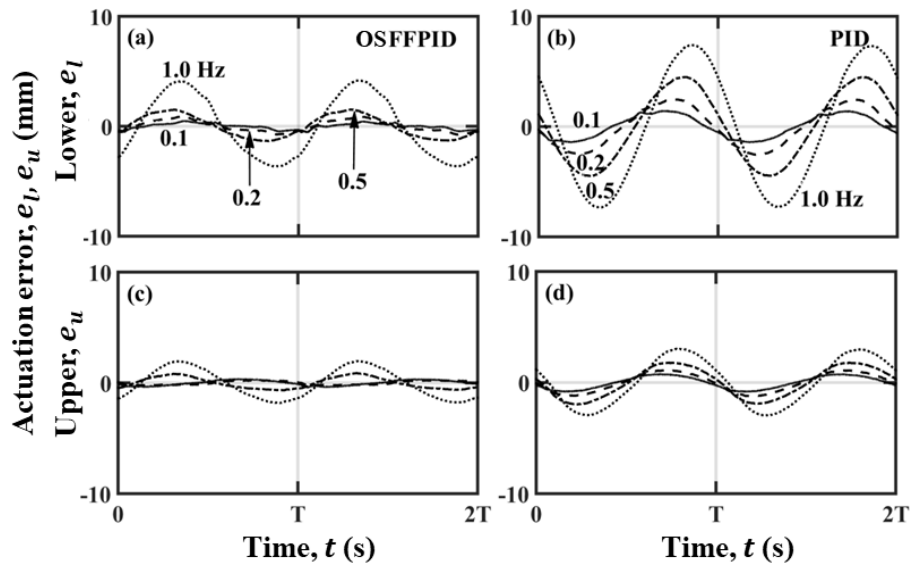


**Figure 4.7: Variations of actuation errors in lower and upper pistons under OSFFPID and PID controllers at frequencies of 0.1, 0.2, 0.5 and 1.0Hz reciprocation demand**

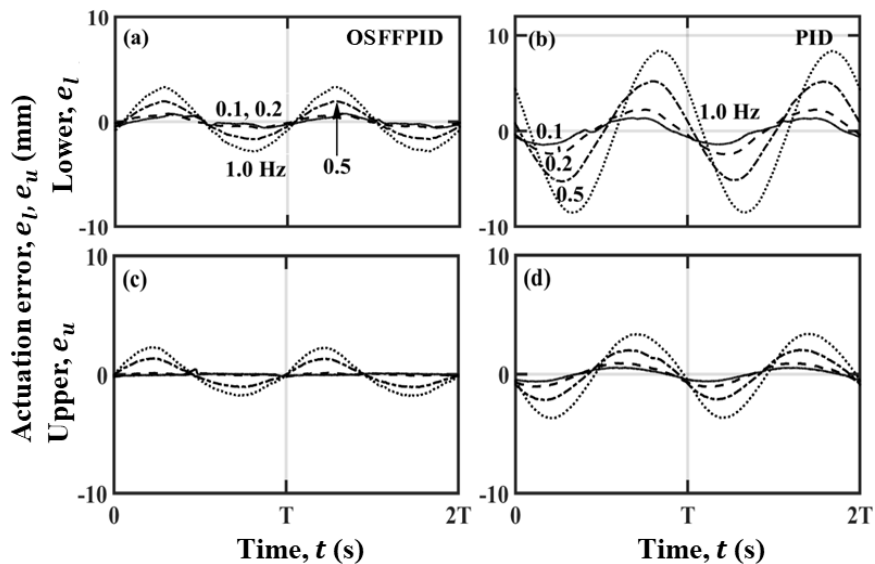


**Figure 4.8: Variations of actuation errors in lower and upper pistons under OSFFPID and PID controllers at frequencies of 0.1, 0.2, 0.5 and 1.0Hz circular-motion demand**

In Figures 4.9(b), 4.9(d), 4.10(b) and 4.10(d), an interesting feature of positive excitation voltage in both the upper and lower valves over the full cycle under the **PID-only** controller

is evident. The first half of each demand cycle represents upward motion of the free point followed by retraction of both the upper and lower pistons in the setup as depicted in Figure 2.3. During this half, a positive valve excitation has allowed metered pump flow to enter the rod-end chamber at the lower side of the cylinder and cause piston retraction in the expected manner.

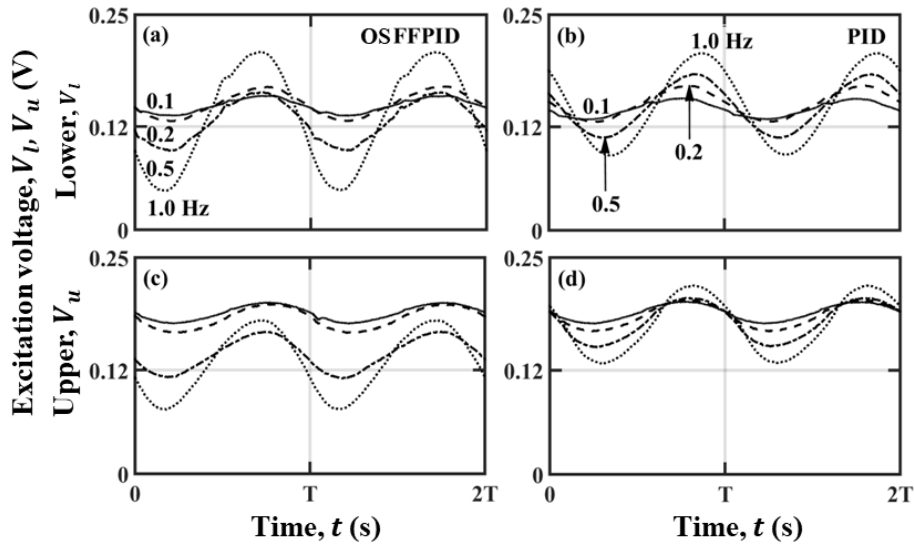


**Figure 4.9: Variations of excitation voltage in lower and upper valves under OSFFPID and PID controllers at frequencies of 0.1, 0.2, 0.5 and 1.0Hz reciprocation demand**

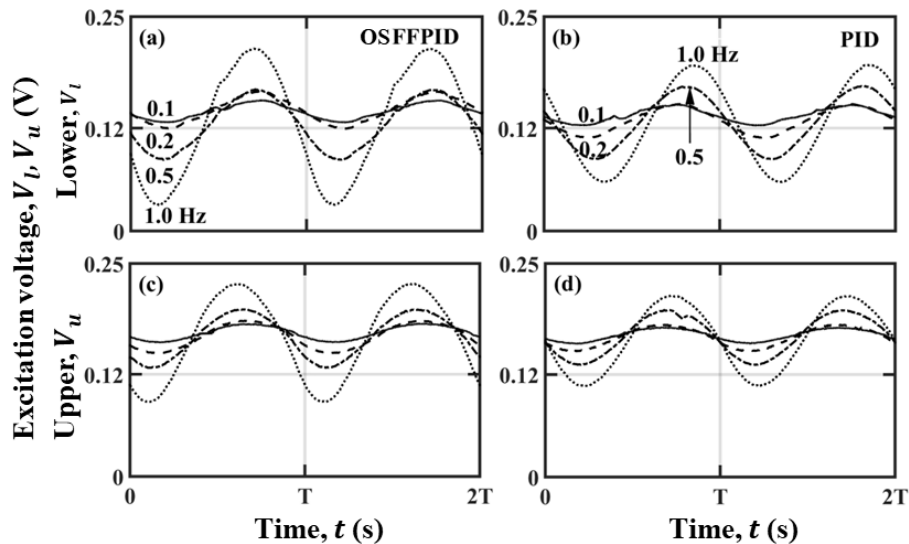


**Figure 4.10: Variations of excitation voltage in lower and upper valves under OSFFPID and PID controllers at frequencies of 0.1, 0.2, 0.5 and 1.0Hz circular-motion demand**

The produced thrust has been sufficient to lift the suspended weight under the piston rod by the higher pressure at the lower-area rod-side of the piston face. But positive excitation



causing the extension as well is unexpected.

During the second half of each cycle, the piston extension maintains the downward motion of the free point. At the unexcited neutral of the zero-lap valves in the setup, the flow path shown in Figures 2.4(a) through Ports A and B inducing the piston motion ideally remains blocked rendering the piston stationary. However, extension of the piston inside the bore of the low-friction cylinder could take place due to oil leakage to the upper chamber forced by the higher pressure at the rod-side chamber arising from the suspended weight under the action of piston rod. Even when the positive excitation to the valves is weak, the observed piston extension must occur by the leakage over a velocity range below the zero-excitation velocity. The positive excitation during the extension phase can be considered to be a carry-over effect of the I-gain that dominates over the P-gain. A sign reversal of error in (4.3b) immediately changes the sign of the proportional voltage contribution, whereas on the other hand the integral contribution takes time to change its sign. Higher errors in the lower system in comparison to the upper one as apparent from Figure 4.9 clearly indicates that the lower suspended weight under the lower piston is failing to produce the requisite leakage flow by a longer margin in comparison to that in the upper actuation system.

#### **4.7.4 Composition of OSFFPID Excitation Voltages**

In Figures 4.11 and 4.12, the individual components of voltages for the **OSFFPID** control are presented respectively for the vertical reciprocating and circular motion demands. The major feedforward part takes care of the motion of the piston by sustaining excitations for opening the valves, whereas the relatively much lower order part compensates friction in the cylinders and the flow leakages in the valves and the cylinders. These are termed as the basic voltage, friction compensation and leakage compensation voltage respectively in Figures 4.11 and 4.12. On the other hand, the **PID** feedback compensates the neglected effects of suspended weight and inertial effect of the moving mass along with other higher order terms in the feedforward formulation that have been neglected. In comparison to the upper piston, the lower suspended mass from the lower piston explains the comparatively lower compensation required in it.

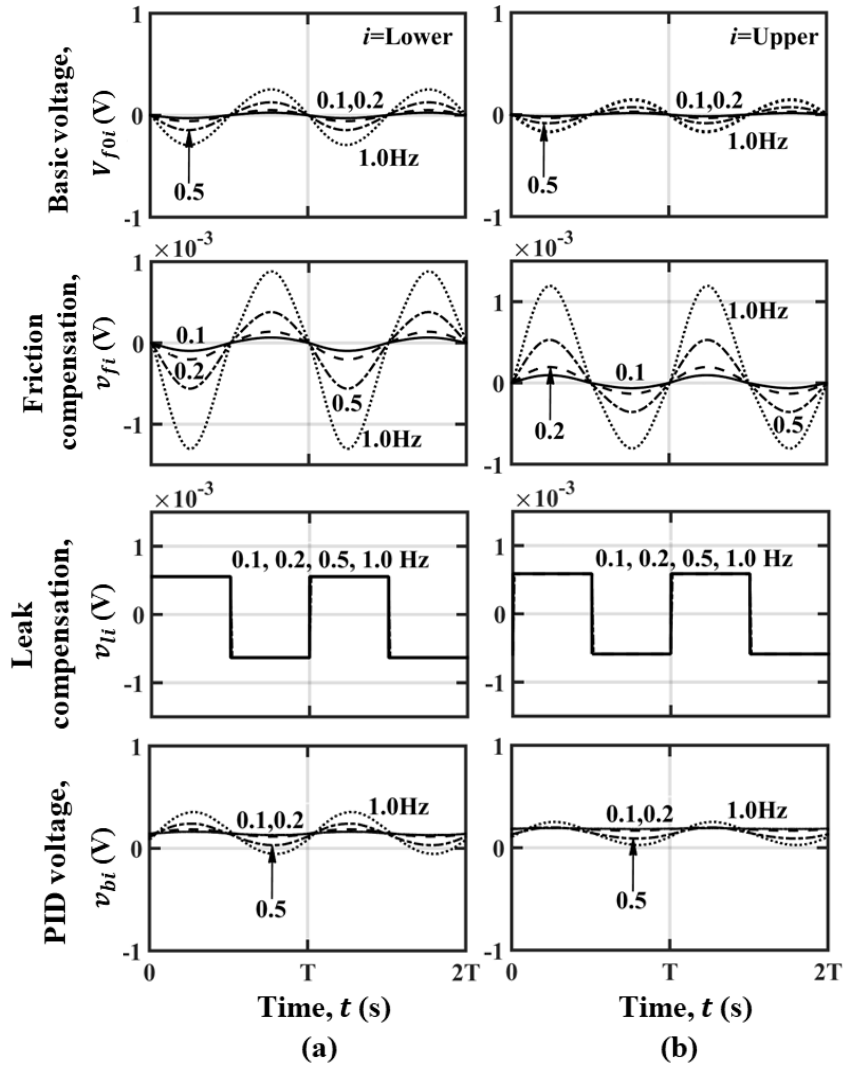


**Figure 4.11: OSFFPID voltage contributions for reciprocation demand at frequencies of 0.1, 0.2, 0.5 and 1.0Hz at (a) lower valve and (b) upper valve**

Figures 4.11 and 4.12 also clearly exhibit a nearly constant variation of the feedback voltage for the lowest frequency case of 0.1 and 0.2Hz, which might be attributed to the suspended weight. With increase in the demanded frequency, the rise in the amplitude of the voltage variation about the weight-sustaining voltage has indeed occurred due to the increasing inertial load along with the higher acceleration or deceleration of the connected members.

The additional feedforward voltage variations that are evident in Figures 4.11 and 4.12 in all the cases executed under the **OSFFPID** controller have directed to significant reduction of the position error with respect to the classical **PID-only** controller. This trend is also visible from the **IAE<sub>f</sub>** values of the respective cases. In case of the vertical reciprocation and circular motion demand, the **IAE<sub>f</sub>** for the **OSFFPID** controller is lower

by a factor of 1.5 to 3. Clearly, the improvement arises for compensating the pressure drops in the metered ports of the valves by its sound physical accounting in (4.5a) and (4.5b) of the feedforward model. It is indeed quite satisfactory to note from Table 4.1 that the noticeable improvement has been provided by the **OSFFPID** controller, which has been often accompanied with either comparable or lower control efforts.

For the motion plans given by the expression (4.9a) and (4.9b) when executed by the serial manipulator at the two lower frequencies, Figures 4.5 and 4.6 exhibit the bounds of the free-point position error  $e_f$  defined by (4.12a) as comparable. In case of the two higher frequency cases studied, the variation of error is seen to be kept similarly restrained in the case of the circular tracking demand executed with the **OSFFPID** controller. For the vertical reciprocation demand, the horizontal displacement that arises during the extension or retraction motion of the lower piston should ideally get exactly compensated by a matched extension or retraction motion of the upper piston. Under the **OSFFPID** controller, the observed variations of the errors establish the compensation not to be exact, but close.

An interesting observation in both the Figures 4.11 and 4.12, is the very similar magnitude of the leakage compensating voltage apparently insensitive to the frequency and the type of the demand. This is consistent with the finding of Figure 4.2 that minor pressure difference across a piston with respect to that across a metered port is sufficient to take care of the moving inertia and external force on the piston-cylinder pair. Moreover, the leakage compensating and friction compensating voltage appear to be negligible with respect to the other two voltage components. This is clearly understandable due to the commissioning of the set up with new valves only recently. Any significant future increase in the variation of the leakage and friction compensating voltage would be useful as a guide to undertake condition-monitoring identification study as explained in the discussion written after the expression (4.7o) in order to ascertain the acceptability of the valve.

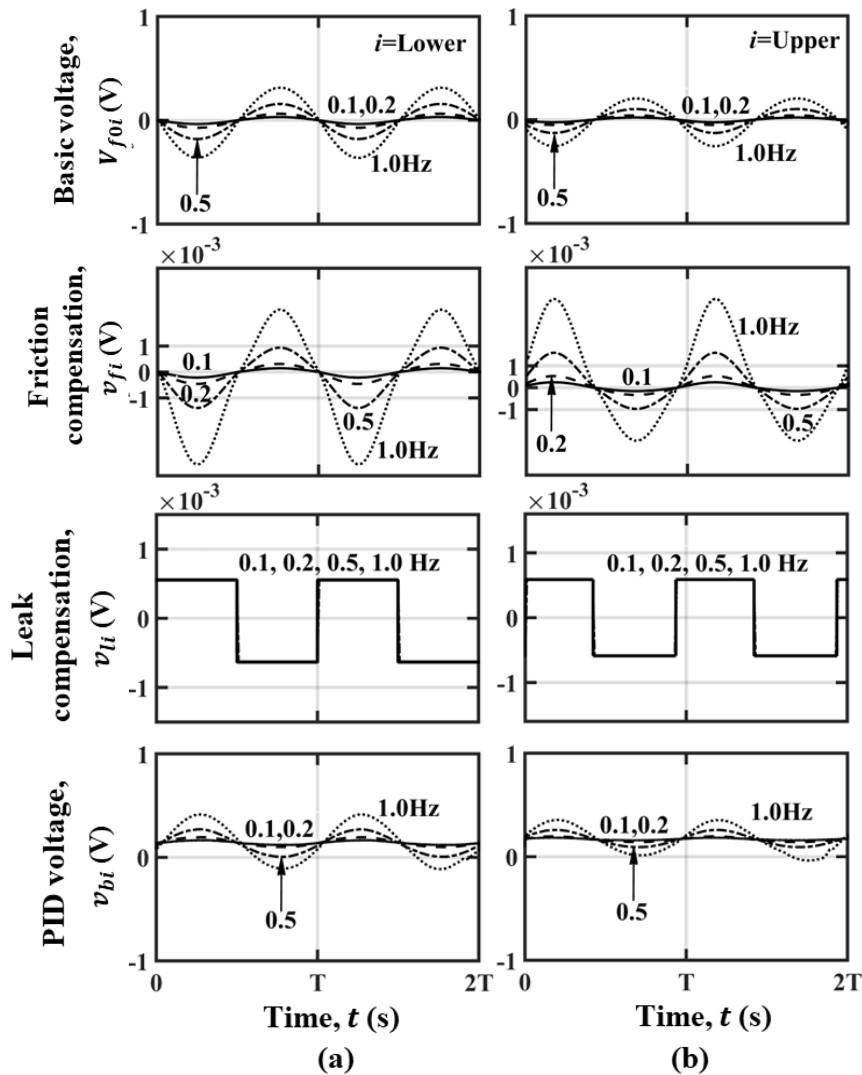


Figure 4.12: OSFFPID voltage contributions for circular motion demand at frequencies of 0.1, 0.2, 0.5 and 1.0Hz at (a) lower valve and (b) upper valve

#### 4.7.5 Free-point Trajectory and Error components for Vertical Reciprocation and Circular Motion Demand

Figures 4.13 to 4.14 exhibits the real-time free-point trajectory in two-dimensional plane for the vertical up-and-down reciprocation and the corresponding temporal variation of error components in these vertical and horizontal direction, respectively. The trajectory of the free-point in Figure 4.13 for the vertical reciprocating demand reveals unwanted cross-coupled horizontal motion. At higher frequency, the errors are clearly higher.

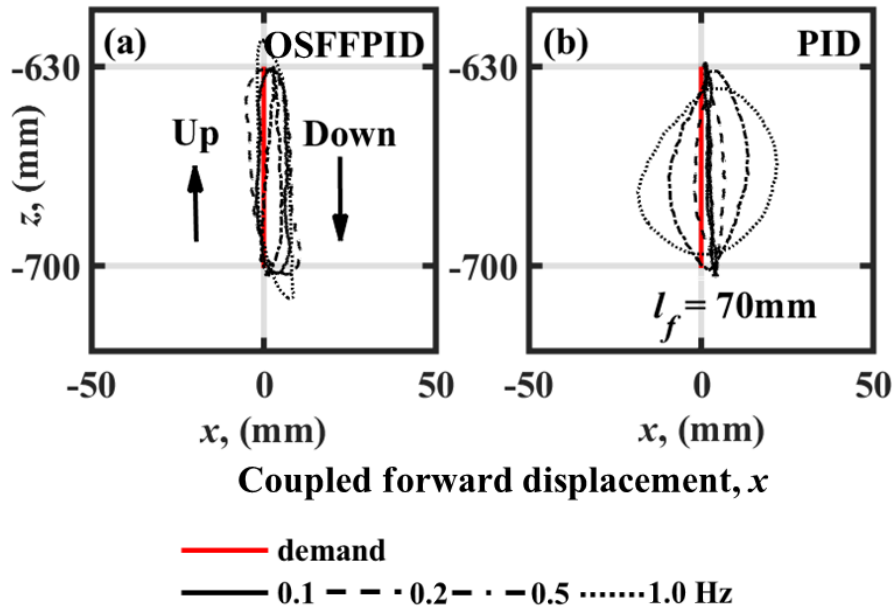


Figure 4.13: Tracking of free-point vertical reciprocating motion demand at frequencies of 0.1, 0.2, 0.5 and 1.0 Hz under OSFFPID and PID controllers

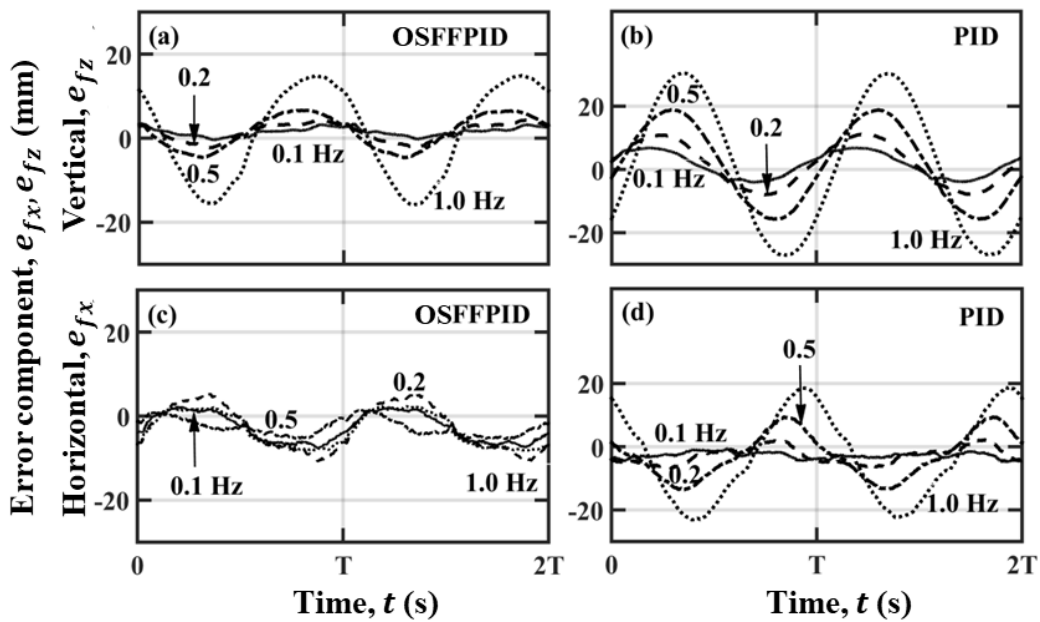


Figure 4.14: Variations of vertical and horizontal error components for free-point vertical reciprocation under OSFFPID and PID controllers at frequencies of 0.1, 0.2, 0.5 and 1.0 Hz

An error-free vertical reciprocation can be obtained through exact cancellation of the horizontal displacement during the extension or retraction motion of the lower piston respectively by a matched extension or retraction motion of the upper piston. Under the OSFFPID controller, the observed variations of the errors establish the compensation to

be not exact, but close and far better than achieved under the **PID-only** control. In comparison to the **PID** controller, superior tracking under the **OSFFPID** controller is also evident for the reciprocation demands above 0.2Hz.

It may be noted that for the cases of 0.1Hz and 0.2Hz vertical reciprocation demands, Figure 4.14 exhibits the relatively larger **PID** error with respect to the **OSFFPID** to be contributed dominantly by the vertical component. The corresponding appearance of higher  $IAE_f$  values noted in Table 4.1 are consistent in view of the comparable cross-coupled horizontal components apparent both in Figures 4.13 and 4.14. At the higher frequencies of 0.5 and 1Hz, the variations under the **OSFFPID** control exhibit significantly lower proportion of cross-coupled error with respect to the error in the vertical motion demand. In case an application requires very stringent low cross-coupled error, it needs to be investigated if incorporation of the effect of neglected inertia and suspended weight in the feedforward estimation provides the solution.

Figure 4.15 and 4.16 shows the free-point trajectory for circular motion demand and its corresponding radius error. The figures clearly exhibit significantly superior quality of tracking of the **OSFFPID** controller with respect to the **PID-only** controller up to 1Hz in terms of much lower deviation from the circular demand track with lower radius error. With respect to a **PID** controller, an existing **FFPID** controller study resulted in lower error variation over a cycle for sinusoidal input motion demand at 0.05Hz in case of a much bigger system (Feng et al. 2019). The noted improvement rendered by the **OSFFPID** controller in the smaller system is similar to that revealed in Figures 4.6 and 4.16 at a much higher frequency of 1Hz. Clearly, the proposed order-separated feedforward controller with **PID** feedback can be accepted as successful in achieving higher speed of response for low payload actuation. Of course, the difference of the pump pressures between 20MPa in the earlier and 7MPa in the present study is consistent with the difference of the payload in the two studies.

Insignificant trajectory deviation evident in Figure 4.15 about the circular motion demand irrespective of the frequencies is indeed a remarkable revelation, especially in view of substantial increase in the deviation with increase in frequency observed under the **PID-only** controller.

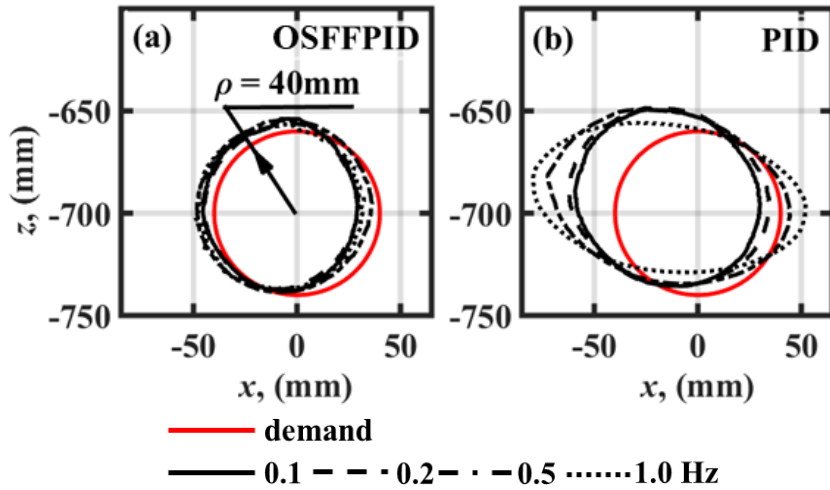


Figure 4.15: Tracking of free-point circular motion demand at frequencies of 0.1, 0.2, 0.5 and 1.0Hz under OSFFPID and PID controllers

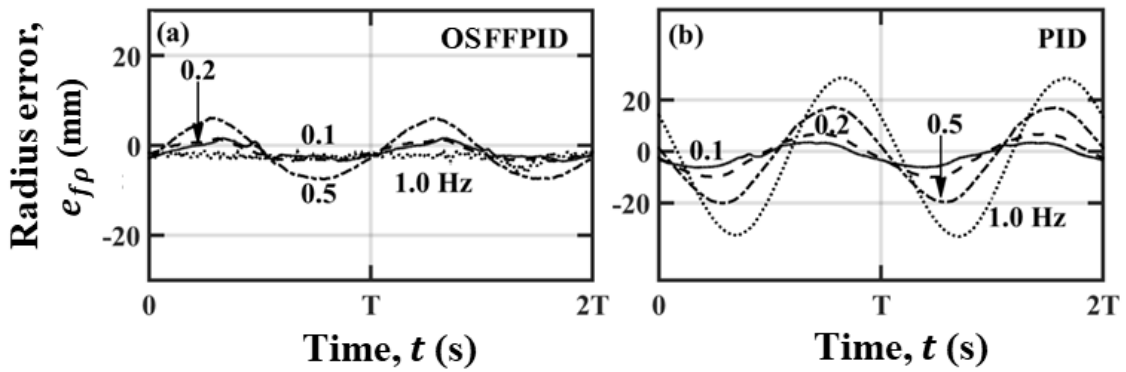


Figure 4.16: Variations of radius error of free-point for circular-motion demand under OSFFPID and PID controllers at frequencies of 0.1, 0.2, 0.5 and 1.0Hz

#### 4.7.6 Instability Mitigation Role of the Proposed OSFFPID Controller

Results in Figure 4.17 correspond to the vertical reciprocating motion demand (4.9a) of the free point at a frequency of 0.2Hz, for three proportional gains that has been used in the upper valve for both the **OSFFPID** and **PID** controllers. The reference gain is termed here as  $k_{p0}$  which corresponds to be the one that has been used in Figure 4.5. Three gain ratios  $k_p/k_{p0}$  of 1.0, 2.0 and 2.5 have been considered here to perform this experiment. The variations of the tracking error  $e_f$  defined by (4.12a) and the excitation voltages in the lower and upper valves over one cycle have been shown here. The results under the **PID** controller show much closer variations for the ratios of 1.0 and 2.0 in comparison to 2.5. In the latter case, the variations reveal much higher-amplitude oscillations in the realized motion leading to poor tracking. This oscillations with no voltage saturation could be surmised to

be the outcome of the transients set in by the hunting from one equilibrium state to another nearby state associated with the nonlinear dynamics of the system. In all the corresponding cases of the gain ratios, the **OSFFPID** controller does not reveal any undesirable large-amplitude oscillation.

Nearly imperceptible sensitivity of the proportional gain on the excitation voltages that is apparent in Figures 4.17(b) and (c) gives a clear indication of low contribution of the feedback in the overall excitation given by (4.3c) for the **OSFFPID** controller. Figure 4.17(a) clearly exhibits that even a small change in the feedback affects the corresponding error  $e_i$ , demonstrating the roles of the feedback to cover the limitations of the feedforward model without invoking the undesirable hunting.

On the other hand, under the **PID** controller, no significant effect of two-fold rise of the proportional gain from the reference value is apparent in any of the variations in Figure 4.17(b). However, a further 25% rise of the gain exhibits several higher order transient rises in these variations. These rises can be concluded as the onset of transient instabilities that is a well-known feature of a nonlinear dynamic system. Apart from the superior tracking mostly with lower control effort in comparison to those for the classical **PID** controller, the avoidance of the unstable operating zone revealed in Figure 4.17(a) is indeed a strong feature of the proposed **OSFFPID** controller.

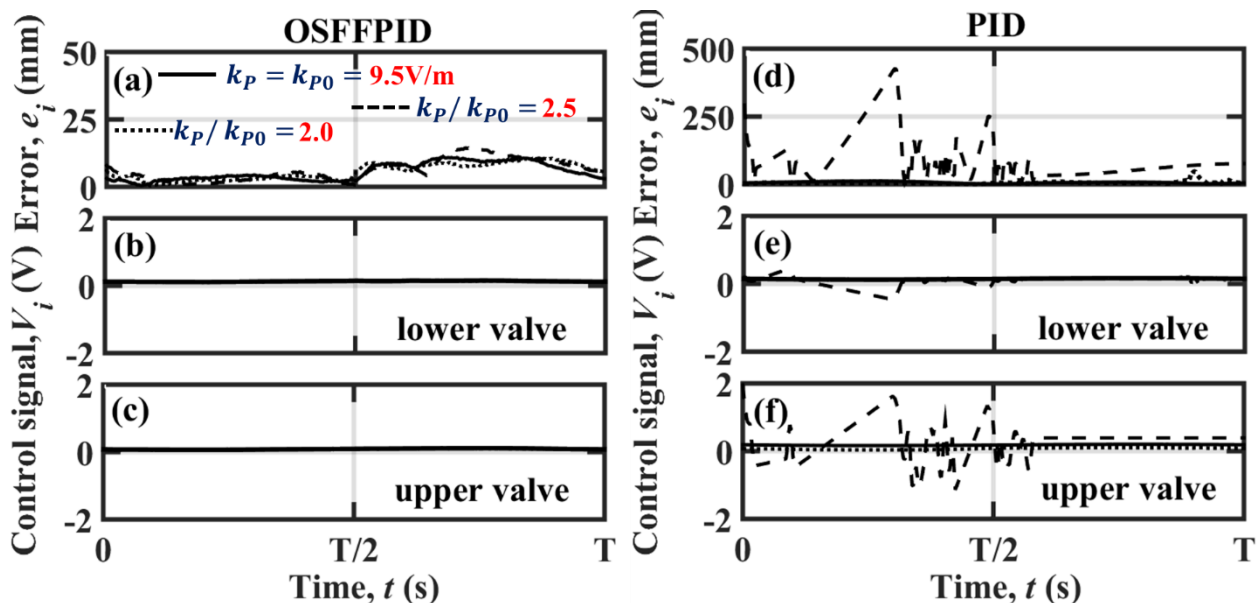


**Figure 4.17: Error and voltage variations at 0.2Hz for OSFFPID and PID controllers for different proportional gains in the upper valve**



Evidently, the transient effects have lasted longer and have been more oscillatory in the excitation voltage of the upper valve with respect to that in the lower one. This can be attributed to the bulkier suspended mass from the upper piston rod, inducing greater nonlinearity through higher leakage past the upper piston. Of course, the voltage oscillations have crept in through error oscillations despite no change in the gain setting of the lower valve. Besides demonstrating this instability mitigation role of the **OSFFPID** scheme, its prospective use at the design stage is outlined next.

## 4.8 Outlining the use of Feedforward Model for Manipulator

### Design

By exploiting the feedforward formulation developed in Section 4.3 along with the associated kinematics, a simulation program has been developed in **MATLAB-Simulink** environment for using it to design the lengths listed in Table 2.2 at the initial angles of the two members set as given in the table. The sensitivities on the variation of certain lengths are shown in Figures 4.18 to 4.29 for the lengths mentioned in the figures on the variations of the actuator displacements, velocities, and forces along with the total actuation discharge to both the cylinders obtained as

$$Q_s = \sum_{i=(l,u)} \{A_{ci} \max(\dot{y}_{di}, 0) + A_{ri} \max(-\dot{y}_{di}, 0)\}, \quad (4.13a)$$

and the corresponding expended actuation power as

$$P_s = P_p Q_s. \quad (4.13b)$$

In order to arrive at the power requirement (4.13b) in each design from the feedforward formulation, the ratio of the maximum actuation discharge requirement to the maximum pump discharge allocated to each system is estimated first. The higher of the two product terms in (4.13a) at the highest extension and retraction speeds yields the numerator of the ratio. Since different types of motion demands is sustained by different distributions of the pump flow to the actuation systems, the denominator of the ratio is simply taken as the specified pump discharge divided by the number of actuation systems in the manipulator. By allocating 50% of the maximum excitation voltage for the motive feedforward voltage expressed by (4.7a), the maximum voltage requirement in each design is evaluated by multiplying the ratio and the allocated 50% excitation.

As a further design-level simplification, the circular motion plan (4.9b) at a frequency of 1.0Hz is considered. Next, the combination of the maximum actuation velocity and the maximum effective actuation load  $F_{id}$  are put in (4.7a) by ignoring the phase difference between these two maxima. Under these simplifications, the maximum pump pressure requirement is estimated from (4.7a). Clearly, the chosen motion plan does not call for any flow to the transverse actuators. Hence, the relief valve should be set at the higher of the maximum pump pressures between the lower and upper actuation systems.

The estimation of the maximum effective actuation force in (4.7a) depends on the structure and material of the different parts of the leg system. Between the joints at the cap end of the cylinder and the rod-end of the piston, the piston-cylinder pair has a cap-end cover, an oil port on the cylinder periphery near the cap-end cover, the piston inside the cylinder bore and another oil port in the cylinder periphery near the rod-end cover. Both the piston and the rod-end cover must have sufficient length to ensure minimal oil leak. Hence, a piston length of 75mm and 50mm thick rod-end cover are considered initially for the design along with 25mm each for the two oil port diameters and the cap-end cover thickness. An outer diameter of 40mm for each joint clevis and 60mm piston stroke make the minimum center-to-center distance between the joints with the piston most retracted as 300mm.

Now, a look at Figure 4.1 makes it apparent that the lower actuator in this position would be nearly as long as the limb  $\overline{hk}$ , whereas the upper actuator marginally longer than the limb  $\overline{hu_c}$ . Hence, the design exploration has been carried out for the minimum lengths of  $\overline{hk}$  and  $\overline{hu_c}$  respectively equal to 300mm and 315mm. The mass of the cylinder-piston pair combined with the valve specified in Table 2.3 are 9kg, as extracted from the catalogues of Bosch Rexroth AG Hydraulics (2012, 2017). For each of the other limb lengths considered in the study, it has been assumed the combined weight pertains only to the additional length provided to the 12mm piston rod.

The weight of each limb corresponding to the length given in Table 2.2 have been calculated by **SOLIDWORKS** software package by accepting the structural material as **AISI316L**. For any other length of any general limb other than  $\overline{kf}$ , the weights of the two plates in each limb have been taken as proportional to their length and those for the pins as fixed. In case of  $\overline{kf}$ , the fixed part of the weight arises from the silicon rubber pad at the foot, the hemispherical foot, the spring along with the polyether polyol spacer and cover cylinder for the spring. The lengths of plate structure above the cover cylinder are taken as

different in different designs with the weights determined by following the same procedure as adopted for any other limb.

The sensitivity of the variation of the lengths being designed on the assessment parameters are shown in Figures 4.18 to 4.29, respectively for the lower and upper actuators, the sensitivities are shown for the variation of the limb length  $\overline{hk}$  on displacements in Figures 4.18 (a) and (c), on velocities in Figures 4.18 (b) and (d) and on forces in Figure 4.19 (a) and (b). For the same variations, the sensitivities on the actuation discharge (4.13a) and power (4.13b) are depicted in Figures 4.20 (a) and (b). Similar sensitivities are presented in Figures 4.21 to 4.23 for the variation of  $\overline{kf}$ , in Figures 4.24 to 4.26 for the variation of  $\overline{kl}_r$  and in Figures 4.27 to 4.29 for the variation of  $\overline{hu}_r$ . The middle of three values of each of the above lengths corresponds to that listed in Table 2.2 with the corresponding variations in each of the above figures shown by a continuous line.

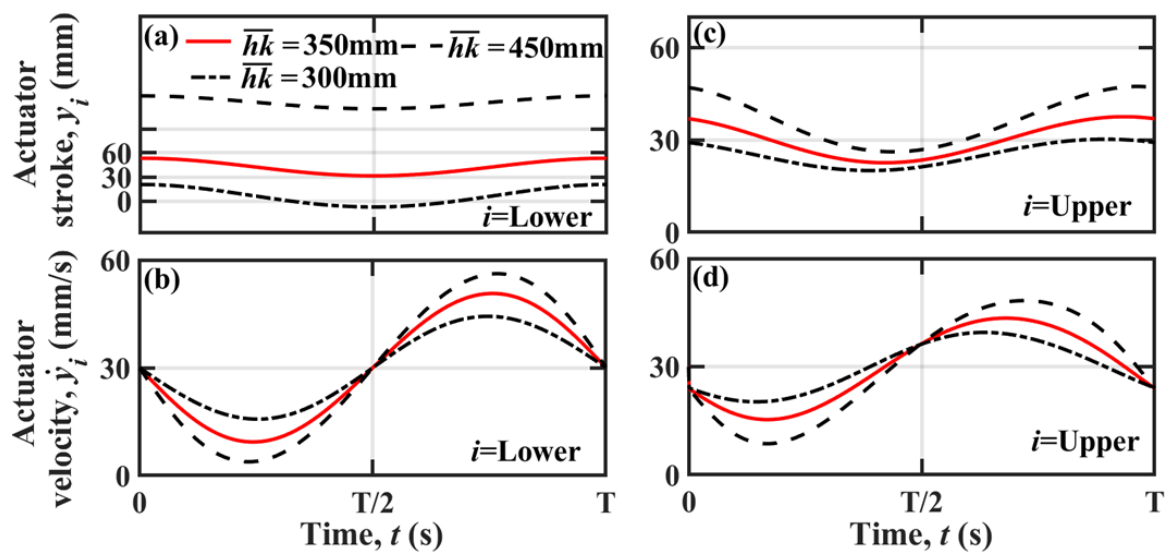


Figure 4.18: Effect of variation of  $\overline{hk}$  on actuator stroke and velocities

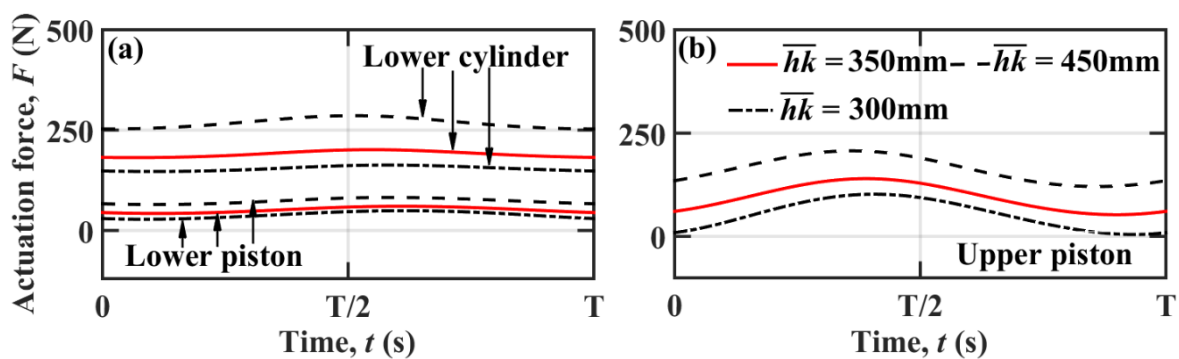


Figure 4.19: Effect of variation of  $\overline{hk}$  on actuation forces

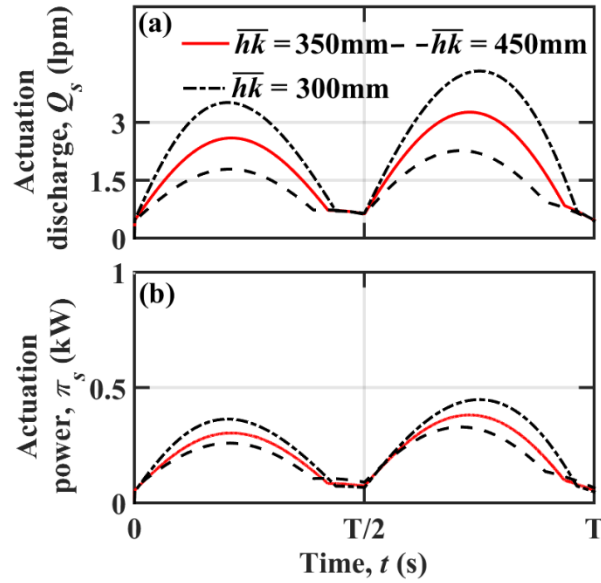


Figure 4.20: Effect of variation of  $\overline{hk}$  on actuation discharge and actuation power

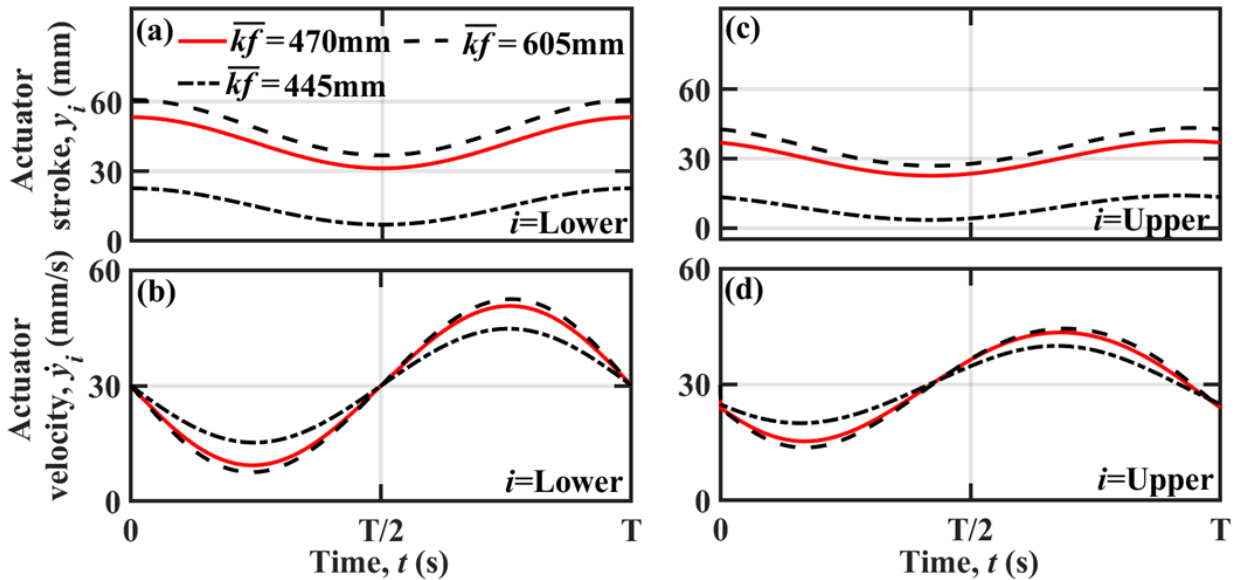


Figure 4.21: Effect of variation of  $\overline{kf}$  on actuator stroke and velocities

It is evident from Figures 4.18 and 4.21 that with increase in the limb length in each of  $\overline{hk}$  and  $\overline{kf}$ , the amplitude of stroke and velocity of both the lower and upper piston increases. From Figure 4.1, such increases clearly appear to be kinematic through larger displacement of the free-point through larger displacements of  $h$  for longer  $\overline{hk}$  induced by the upper actuator for its identical stroking and of  $k$  for longer  $\overline{kf}$  induced by the lower actuator for its identical stroking. Since a change of either  $\overline{kl}_r$  or  $\overline{hu}_r$  does not affect the upper or lower actuation respectively, the respective longer length only makes both the displacement and velocity amplitudes longer in Figure 4.24 or 4.27, respectively. As the stroking of any

actuator should remain between 0 and 60mm, any variation exhibiting out-of-range requirement implies an infeasible design. Such situations are apparent in Figure 4.18(a) for  $\overline{hk}$  equal to 300mm, in Figure 4.21(a) for  $\overline{kf}$  equal to 605mm and in Figure 4.24(a) for  $\overline{kl}_r$  equal to 78mm.

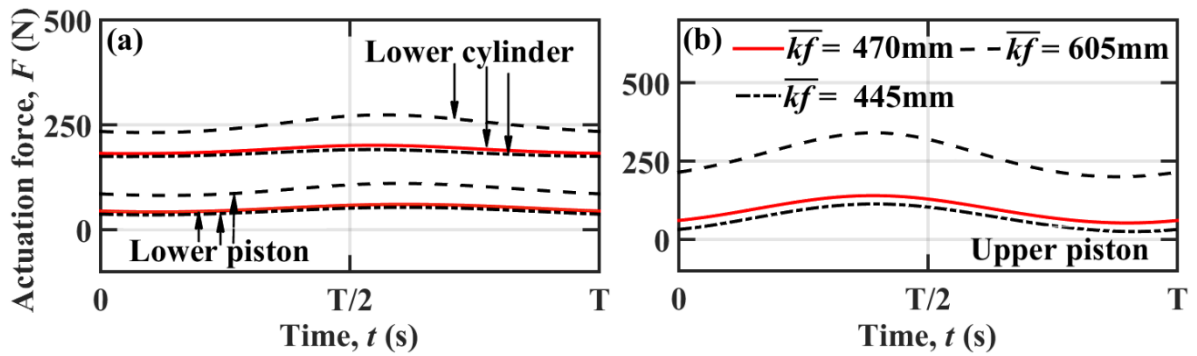


Figure 4.22: Effect of variation of  $\overline{kf}$  on actuation forces

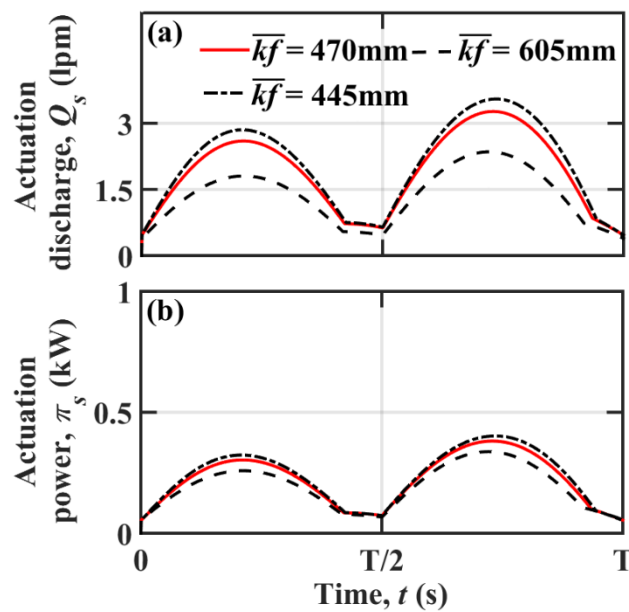


Figure 4.23: Effect of variation of  $\overline{kf}$  on actuation discharge and actuation power

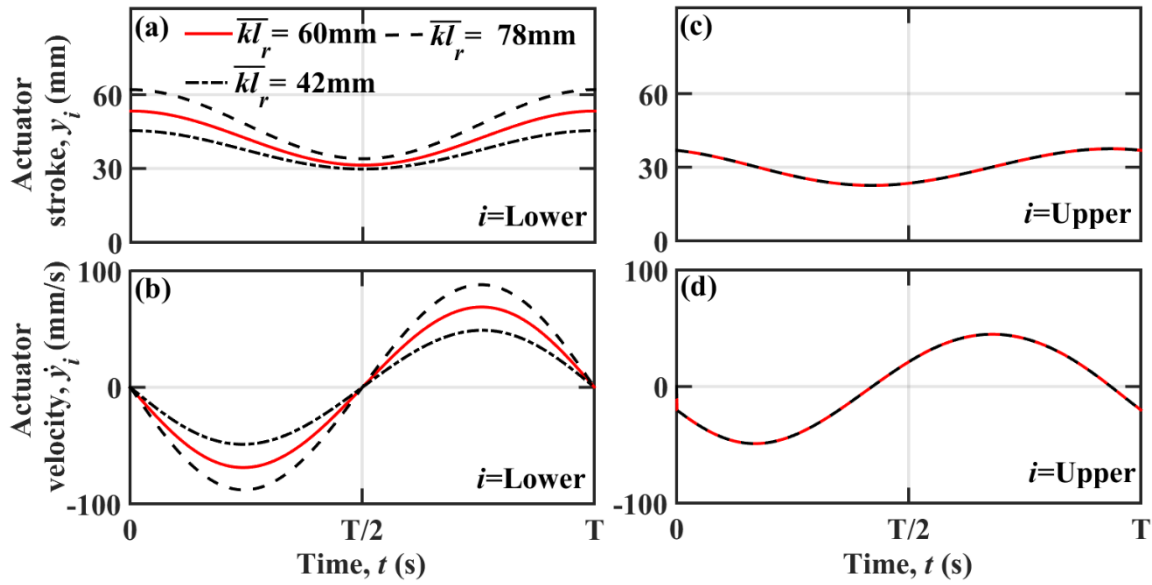


Figure 4.24: Effect of variation of  $\bar{k}l_r$  on actuator stroke and velocities

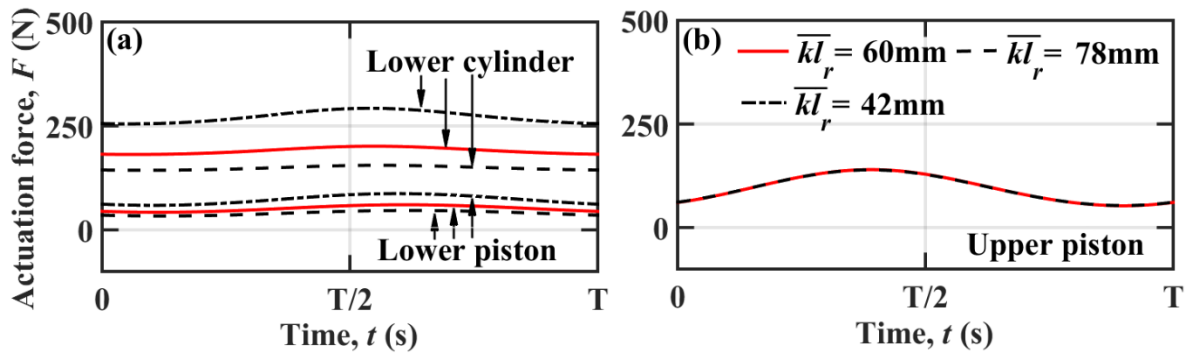


Figure 4.25: Effect of variation of  $\bar{k}l_r$  on actuation forces

The same motion demand of the foot tip in all the designs is reflected as lower actuation discharge (4.13a) in each of Figures 4.20, 4.23, 4.26 and 4.29, whenever a higher actuation velocity is achieved by increase of any of the four limb lengths considered in this study. It is understandable that a longer limb implies greater weight of the limb that pushes the maximum pressure requirement up in (4.13b). But qualitatively similar variations of discharge and power in the latter four figures indicates the effect of increased pump pressure in (4.13b) to remain dominated by the reduced discharge (4.13a). Such a trend in the actuation power requirement arises due to the domination of greater power loss in the valve for higher discharge through it over the increased requirement of the maximum pump pressure apparent in Figures 4.20 and 4.23 with increase in the limb length considered in each figure. The reduction of the moment arm about  $k$  for shorter  $\bar{k}l_r$  in Figure 4.25 or

about  $h$  for shorter  $\overline{hu}_r$  in Figure 4.28 for the same suspended weight in all the cases studied in each figure explains the correspondingly higher actuation force in the respective figure.

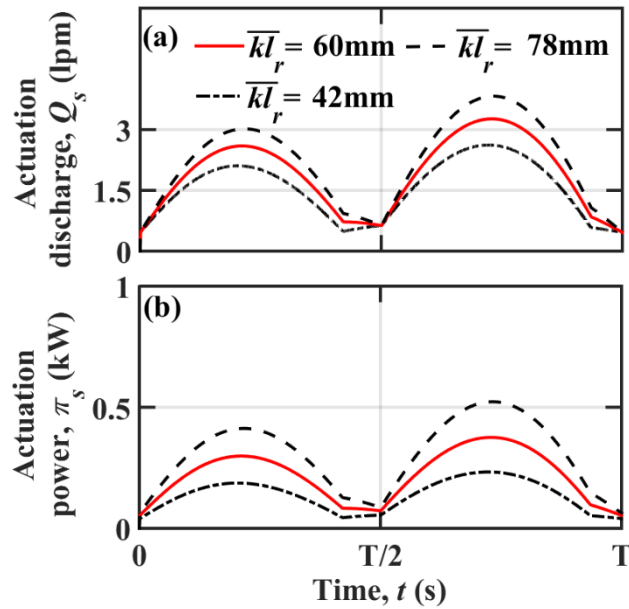


Figure 4.26: Effect of variation of  $\overline{kl}_r$  on actuation discharge and actuation power

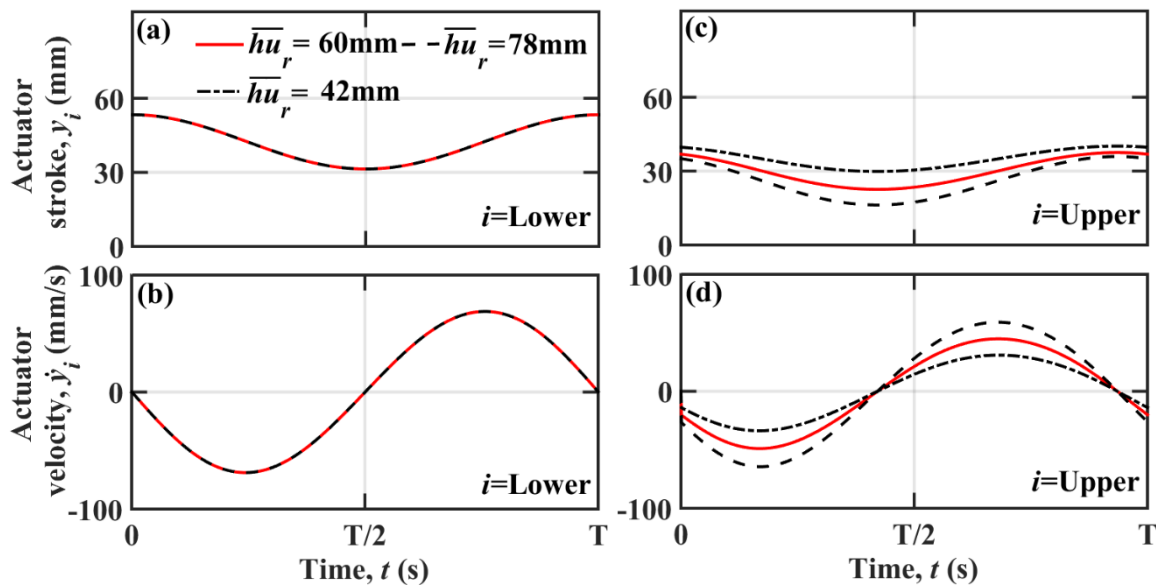


Figure 4.27: Effect of variation of  $\overline{hu}_r$  on actuator stroke and velocities

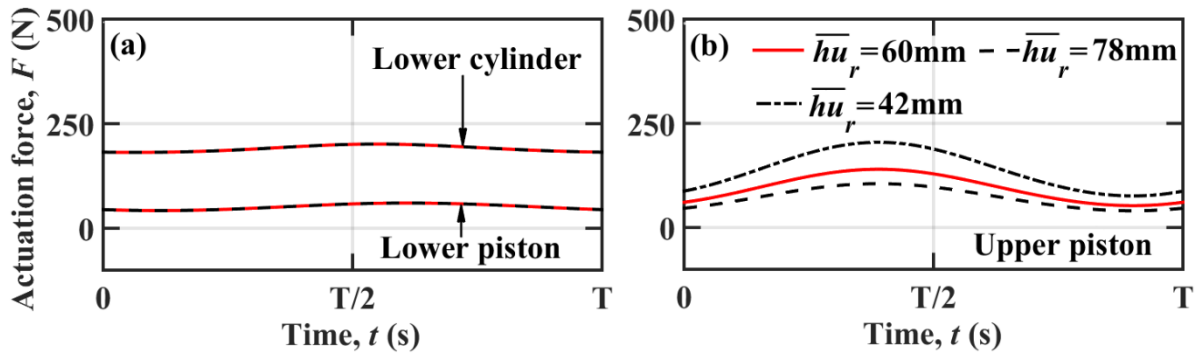


Figure 4.28: Effect of variation of  $\overline{hu}_r$  on actuation forces

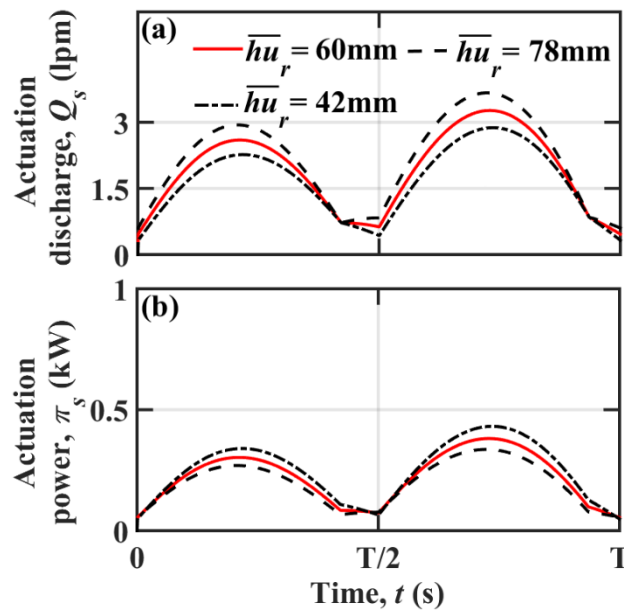


Figure 4.29: Effect of variation of  $\overline{hu}_r$  on actuation discharge and actuation power

Lower actuation power requirement for the longer upper and lower limbs respectively in Figures 4.20 and 4.23, each of which in turn makes the manipulator bigger, could appear as baffling despite the explanation given above in terms the lower discharge requirement dominating over the higher pressure requirement. Two strong reasons for this are the consideration of the same limb cross section irrespective of the maximum load that could be placed on the body and the same separating distance between the rightward and leftward manipulators. A larger manipulator corresponding to longer limb length would mean greater maximum load and longer separation implying longer body length from left to right. A strength analysis, which has been kept outside the purview of the present analysis, would have surely required larger limb cross section for the longer body supported on longer limbs. Hence, a complete optimized design analysis demands integration of the strength



analysis with the analysis presented corresponding to the feedforward formulation developed here.

## **4.9 Summary**

Design and real-time implementation of the order-separated feedforward position controller executed in the last chapter for a simple linear motion has been extended in this chapter for a serial manipulator. The demands in a vertical plane in the form of reciprocation and circular motion for the free point of the manipulator in a laboratory setup under development for a walking quadruped have been tracked by integrating a PID feedback. Instead of a proportional valve paired with an industry-grade high-friction double-acting single-rod cylinder employed for the linear-motion study, two servoproportional valves each paired with a low-friction cylinder have been used in the manipulator forming a single leg of the quadruped. Also, instead of a much costlier but energy-efficient variable-displacement pump, a fixed-displacement gear pump has been employed during the initial manipulator experiments.

One key aspect of the manipulator study is the use of inverse and forward kinematics and inverse dynamics with the feedforward formulation. A numerical study has been done to justify the rationale behind the assumptions of the neglected effects of actuator inertia and suspended weight of the leg members negotiated by the actuators during the laboratory experiments. Since one actuation pair in the manipulator involves the relative motion between the piston and the cylinder, the notable aspect of the kinematic formulation is its consideration contrasting the customary way of neglecting the cylinder motion. As indicated by the formulation, the incorporated effect is found to be indeed small for low ratio of the piston-to-cylinder weight in the pair.

In view of the newness of the setup and low-friction cylinders, the valve coefficients have been extracted from the manufacturers' catalogues and friction during the experiments has been ignored. The real-time experimental results clearly reveal the strength of the proposed FFPID controller over a classical PID controller, in terms of superior tracking along with lower or nearly equal spending of the control energy. A strong feature has been observed to be its ability to avoid instability-related transient oscillations of the response. Low PID feedback excitation under the feedforward guidance has been inferred as insufficient to

cause hopping among near-by permissible multiple solutions of the nonlinear system. Oil leakage through the valve and cylinder has been explained as one such nonlinear effect.

One of the major contributions of this study is successful tracking by extending the demanded motion frequency from or below 0.1Hz in the existing studies of serial manipulators to 1.0Hz. However, the present study also exhibits that incorporation of neglected effects in the proposed model might be necessary for reducing the unwanted cross-coupled error in the output motion at certain low-frequency demands.

At the feedforward formulation stage and then in terms of small leakage compensating voltage with respect to the motion-inducing feedforward part, a possible use of the model for condition monitoring of the valve and the cylinder has been explained. It has also been indicated that such a monitoring requires time-to-time execution of identification study by utilizing the valve voltage and the position-sensor feedbacks. In fact, the possibility of incorporating the cylinder friction in such an identification study has also been explained. Some results have been presented studying the sensitivity of changing certain lengths of the manipulator members in a numerical study involving the feedforward and kinematic models of the manipulator. A discussion of these results has indicated its prospective use at the pre-fabrication stage by integrating a strength analysis so as to achieve an optimized design.







# CHAPTER 5

## Controller Design and Real-time Analysis for Serial-Parallel Manipulator

### 5.1 Introduction

A novel order-separated feedforward controller, or **OSFF**, has been established as superior to a classical feedforward scheme, both tested on an electrohydraulic system comprising of a proportional valve and a double acting single rod cylinder, or **DASRC**, for linear motion tracking implemented in real time with **PID** feedback. Apart from a **DASRC**, this superior control scheme, henceforth termed as **OSFFPID** controller has been deployed successfully for motion control of a serial manipulator suspended from a stationary platform. This consists of serial arrangement of an upper and a lower actuation pairs, each having a low-friction **DASRC** and servoproportional valve or **SPV**. For executing the controlled motion of the free point of the manipulator an inverse kinematic model, as discussed in Section 4.2, has been used to transform the motion demand of the free point to the coupled actuation demands. With respect to the existing tracking control studies restricted to within 0.1Hz periodic demands, the proposed scheme has yielded good tracking control up to a speed of 1Hz. Following this success, a study has been taken up here for the coupled motion of a platform resting on four such serial manipulators working as a serial-parallel manipulator system – as discussed in Sections 2.4 and 2.7. These studies form the basis for setting up a testing protocol and initialization of the legs of a quadruped robot prior to executing a specific gait.

Each of the four serial manipulators acts as a leg of the quadruped, with its upper side, representing the hip joint, fastened to the platform, representing the body of the quadruped. The free point of each leg represents a foot tip that either remains grounded providing support to the body or executes a sequence of lifting from the ground, taking a stride and returning to the ground at a different point.

In the present chapter, two different motion demands are considered. The first one involves the forward motion of the platform on three grounded legs together with forward striding of the fourth leg. With reference to Figure 2.10 and 2.13 the quadruped configuration has been shown in Figure 5.1 for the development of the above stated motion demand. In Figure 5.1(a), the 4 foot tips are indicated as 1,2,3 and 4. The body lies in the horizontal plane  $XY$  where  $X$  represents the direction of motion of the quadruped. The horizontal plane on the rectangular body frame involves  $X$  from left  $L$  to right  $R$  and  $Y$  from front  $F$  to back  $B$ . The hip points are indicated by the 4 points  $h_1$  to  $h_4$  and the anchor points as  $a_1$  to  $a_4$ . For each serial manipulator system, the pair of **DASRC** axes are indicated by the dashed line – contained entirely in the vertical  $XZ$  plane. While Figure 5.1(a) represents the initial posture of the system, Figures 5.1(b), (c) and (d) represent, the system configuration after an initialization prior to taking a stride whereby foot-tips 2 and 3 are moved to 2' and 3' respectively, the stride pattern of foot tip 4 from 4 to 4' and forward motion of the body center  $C$  and the final configuration of the system after the completion of the stride.

The second motion demand involves the vertical movement of the platform along  $Z$  axis, with all the four foot tips grounded. This is also termed as heave motion of the body. The two actuation pairs in each leg have their demands conforming either to forward or heaving motion of the body. Hence, the nonzero motion demands for all the upper and lower actuation pairs in a single leg in case of the serial manipulator system investigated in the last chapter should be deployed for all four legs of the quadruped system.

The **OSFF** controller formulations corresponding to these demands are obtained from different equations given in Section 4.3. Section 4.4 details the forward kinematic formulation of the single leg for composing the relative motion of the foot-tip with respect to its corresponding anchor points in terms of the LVDT-captured displacements of the two-pistons fitted with lower and upper cylinder. This formulation has been used here for composing the synchronized tracking demand of the platform and the striding foot tip. The detailed mathematical formulation of the motion plan is explained in Section 5.2. Section 5.3 details the feedforward controller formulations. The results of the real-time experiments are detailed in Section 5.4 and finally a summary of this present work is given in Section 5.5.

## 5.2 Motion Plan Design for Serial-Parallel Manipulator

In the present work the effort has been made to design a portion of the static walk (SW) motion plan for the quadruped. From the proposed plan, it is clear that for execution of the portion of the gait, it is necessary that the 4 foot-tips in the ground before initiation of motion should form a parallelogram from an initial rectangular posture as shown in Figure 5.1(a). Also, the COM( $\mathbf{C}$ ) should maintain a definite height of ( $\mathbf{z}_a$ ) with respect to ground – which should be less than the maximum possible height of the platform to enable any foot-tip to take a nonzero stride in the  $\mathbf{X}$  direction. Conversion of initial rectangular posture of the foot-tips to parallelogram posture by maintaining a certain height of ( $\mathbf{C}$ ) with respect to ground is termed as initialization procedure, which can be considered of having following motion sequences – maintaining a fixed height ( $\mathbf{z}_a$ ) of the ( $\mathbf{C}$ ) from the ground, followed by movements of the leg pairs **2** and **3** to a certain distance of  $s_f/2$  so that the orientation of the 4-foot tips from the rectangle gets converted to a parallelogram as shown in Figure 5.1(b). Here  $s_f$  is the maximum stride of any foot-tip in the  $\mathbf{X}$  direction. This initialization phase occurs over a time  $T_I$ , known as initialization phase.

After the initialization phase, the portion of static walk motion plan has been initiated. After having initialization at first the COM ( $\mathbf{C}$ ) is displaced by an amount of  $s_f/2$  in the forward direction over a time period  $T_I < t \leq T$  with a sinusoidal motion, keeping all the foot-tips grounded. In this situation the overall system can be stated to be working as a parallel manipulator. In the second phase of motion the leg 4, will be in swing phase by making a horizontal and vertical stride of  $s_f$  and  $s_v$  respectively, with a combination of sinusoid and linear motion – this reveals the working of the system as a serial manipulator. As time of swing phase motion of the foot-tip 4 is also considered to be  $T_{SW}/6$ , the time segment for motion of the foot-tip 4 along forward direction is  $T_I + T < t \leq 2T$  where  $2T$  is the entire cycle time. During the motion of foot-tip 4 as it moves twice the displacement of the COM ( $\mathbf{C}$ ) within same period, the speed of the foot-tip will certainly become twice that of the body. Also, during the second phase of motion when leg 4 is in swing phase, the entire weight of body should be supported by the other three stance legs 1,2 and 3. In other words the vertical projection of the COM ( $\mathbf{C}'$ ) lies inside the support polygon made by the other three grounded legs, to maintain the static stability of the body. Further in order to maintain the static stability of the system, the magnitude of both body velocity  $v_{COM}$ , foot-tip 4 velocity  $v_{fx4}$  associated with horizontal stride  $s_f$  should be tuned accordingly.



One important consideration made while designing the motion plan is the absence of any lateral sway of the body during the execution of the motion. The sequence of motion of COM ( $\mathbf{C}$ ) and foot-tip 4 from the starting of initialization phase till the end of the entire cycle, are shown in the below Figure 5.1. The corresponding equations of motion for both COM ( $\mathbf{C}$ ) and the 4 foot-tips ( $\mathbf{f}_j$ ) with their coordinates are also stated below for individual phases. During formulation of motion plan for serial parallel actuation, the static walk period of each segment is represented by  $T$  here. Each mathematical expression of motion for both COM ( $\mathbf{C}$ ) and foot-tips ( $\mathbf{f}_j$ ) have been developed by using a subscript  $d$  in order to represent the demanded motion.

Figure 5.1(a) clearly depicts the initial rectangular posture of the four foot tips with COM ( $\mathbf{C}$ ) at a definite height ( $\mathbf{z}_a$ ) from the ground, before starting of the initialization phase at  $t = 0$ . This height ( $\mathbf{z}_a$ ) can also be termed as the relative distance between COM ( $\mathbf{C}$ ) and the four foot-tips. The rectangular orientation at  $t = 0$  should be converted to parallelogram during initialization phase. However, the coordinate of COM ( $\mathbf{C}$ ) at time  $t = 0$  can be written as,

$$x_{COMd} = 0, y_{COMd} = 0, z_{COMd} = z_a, \quad (5.1a)$$

Considering the sequence of four foot-tips as 4-1-2 and 3 the corresponding coordinates of the foot-tips can be written as,

$$x_{fd4} = -S_0/2, y_{fd4} = (B/2 + b/2), z_{fd4} = 0. \quad (5.1b)$$

$$x_{fd1} = +S_0/2, y_{fd1} = (B/2 + b/2), z_{fd1} = 0. \quad (5.1c)$$

$$x_{fd2} = -S_0/2, y_{fd2} = -(B/2 + b/2), z_{fd2} = 0. \quad (5.1d)$$

$$x_{fd3} = +S_0/2, y_{fd3} = -(B/2 + b/2), z_{fd3} = 0. \quad (5.1e)$$

The rectangular posture of four foot-tips is converted to parallelogram at time  $T_I$  shown in Figure 5.1(b). The figure clearly shows that foot-tip 2 and 3 advanced to positions 2' and 3' - each ahead of foot-tip 4 and 1 respectively by an amount of  $s_f/2$ . For the present study, during the realization of motion plan in real time, the initialization process has been done with the entire setup suspended in air. The necessary demand during the initiation of static walk as obtained from inverse kinematic model is fed to the control system of all the twelve actuators in order to form the parallelogram by four foot-tips. However, the detail method

of the initialization process and the corresponding equations that are involved during this phase is explained in subsection 5.4.1.

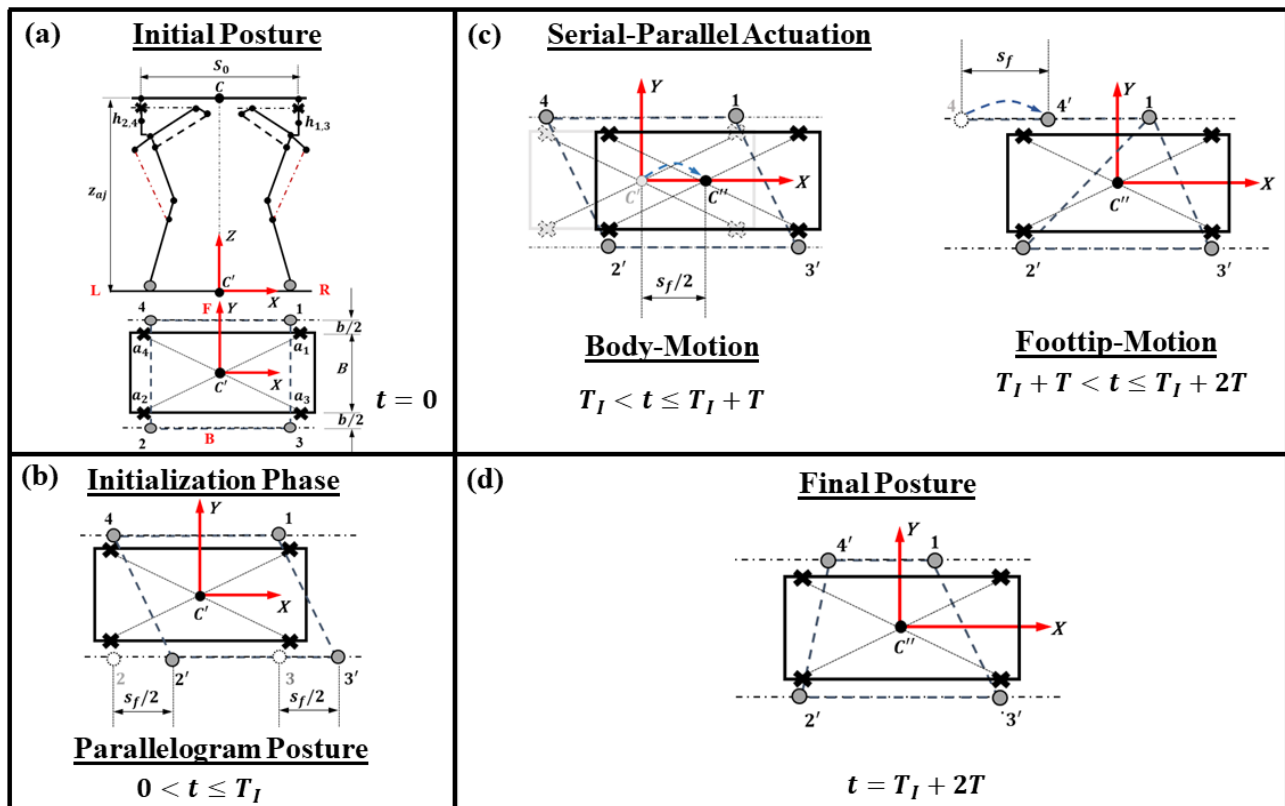


**Figure 5.1: Representative version of static walk motion plan for the realization of combined serial-parallel actuation**

After the initialization process, with parallelogram orientation of foot-tips the setup is lowered to the ground for the initiation of the motion plan. Figure 5.1(c) clearly exhibits the two phases of the motion plan. During the first phase the COM ( $C$ ) is moved by a distance of  $s_f/2$  in the forward direction, where all foot-tips are maintained same parallelogram orientation at the ground as obtained during initialization phase. As already stated, the motion of COM ( $C$ ) in the forward direction of  $X$ , varies sinusoidally with respect to time  $t$ , the corresponding equation of motion during the phase at period of  $T$  can be written as,

$$x_{COMd} = s_f/4 \{1 - \cos(\pi\{t - T_I\}/T)\}, \text{ for } T_I \leq t \leq T_I + T, \quad (5.2a)$$

$$\text{with, } y_{COMd} = 0, \text{ and } z_{COMd} = z_a. \quad (5.2b)$$

For no lateral sway along  $Y$  axis and also to maintain constant body height ( $z_a$ ) throughout the motion plan for COM ( $C$ ).

The corresponding coordinates of four foot-tips after the end of the motion can be written as,

$$x_{fd4} = -S_0/2, y_{fd4} = (B/2 + b/2), z_{fd4} = 0. \quad (5.2c)$$

$$x_{fd1} = +S_0/2, y_{fd1} = (B/2 + b/2), z_{fd1} = 0. \quad (5.2d)$$

$$x_{fd2} = -S_0/2 + s_f/2, y_{fd2} = -(B/2 + b/2), z_{fd2} = 0. \quad (5.2e)$$

$$x_{fd3} = S_0/2 + s_f/2, y_{fd3} = -(B/2 + b/2), z_{fd3} = 0. \quad (5.2f)$$

From the corresponding coordinates of the foot-tips it is clear that the formation of parallelogram obtained by the four foot-tips during initialization process is maintained also after the first phase of the static walk motion plan.

The second phase of motion plan corresponds to the motion of the leg 4, where the foot-tip of the leg 4, is in swing phase by making horizontal and vertical stride of  $s_f$  and  $s_v$  respectively, with a combination of sinusoid and linear motion along positive  $X$  direction and a pure sinusoidal motion along positive  $Z$  direction for a period of time  $T$  keeping all the other legs grounded.

During second phase, for no COM ( $C$ ) motion, the coordinates of COM ( $C$ ) remain same even after the end of the second phase motion and can be written as,

$$x_{COMd} = s_f/2, y_{COMd} = 0, z_{COMd} = z_a. \quad (5.3a)$$

However, the swing phase equation of motion with respect to time ( $t$ ) for the foot-tip 4 along positive  $X$   $Y$  and  $Z$  direction can be written as,

$$x_{fd4} = -S_0/2 + a_f s_f/2 \{1 - \cos(\pi\{t - T_l - T\}/T_s)\},$$

$$\text{for } T_l + T \leq t \leq T_l + T + T_s/2, \quad (5.3b)$$

$$x_{fd4} = -S_0/2 + a_f s_f/2 \{1 + (\pi/T_s)(t - T_l - T - T_s/2)\},$$

$$\text{for } T_l + T + T_s/2 < t \leq T_l + T + T_s/2 + T_c, \quad (5.3c)$$

$$x_{fd4} = -S_0/2 + a_f s_f/2 \{1 + (\pi T_c/T_s) - \cos[\pi(t - T_l - T - T_c)/T_s]\},$$

$$\text{for } T_l + T + T_s/2 + T_c < t \leq 2T. \quad (5.3d)$$

$$y_{fd4} = (B/2 + b/2), \quad (5.3e)$$

$$z_{fd4} = 0.5s_v\{1 - \cos(2\pi t/T)\} \text{ for } T_l + T \leq t \leq 2T. \quad (5.3f)$$

Where,  $T_s$  and  $T_c$  corresponds to the sinusoidal and uniform motion phase of foottip, the detail of which has been given in design of foottip and COM motion for serial -parallel manipulator in sub-section 2.7.1. As the other foot-tips 1,2 and 3 remain grounded during this period, the coordinates remain same as obtained during the first phase of motion plan and can be written as,

$$x_{fd1} = +S_0/2, y_{fd1} = (B/2 + b/2), z_{fd1} = 0. \quad (5.3g)$$

$$x_{fd2} = -S_0/2 + s_f/2, y_{fd2} = -(B/2 + b/2), z_{fd2} = 0. \quad (5.3h)$$

$$x_{fd3} = S_0/2 + s_f/2, y_{fd3} = -(B/2 + b/2), z_{fd3} = 0. \quad (5.3i)$$

However, after the end of the motion at time  $t = 2T$  the final orientation of the four foot-tips forms a trapezium, and the coordinates of COM ( $C$ ) and foot-tip ( $f_j$ ) can be written as,

$$x_{COMd} = s_f/2, y_{COMd} = 0, z_{COMd} = z_a. \quad (5.4a)$$

$$x_{fd4} = -S_0/2 + s_f, y_{fd4} = (B/2 + b/2), z_{fd4} = 0. \quad (5.4b)$$

$$x_{fd1} = +S_0/2, y_{fd1} = (B/2 + b/2), z_{fd1} = 0. \quad (5.4c)$$

$$x_{fd2} = -S_0/2 + s_f/2, y_{fd2} = -(B/2 + b/2), z_{fd2} = 0. \quad (5.4d)$$

$$x_{fd3} = +S_0/2 + s_f/2, y_{fd3} = -(B/2 + b/2), z_{fd3} = 0. \quad (5.4e)$$

From the instantaneous position of the COM ( $C$ ) the coordinates of the 4 anchors ( $a_j$ ) can also be obtained at every instant from the geometry of the body. The coordinates of the 4 anchors ( $x_{adj}, y_{adj}, z_{adj}$ ) in the order of 4-1-2-3 can be written below as

$$x_{ad4} = x_{COMd} - S_0/2 \quad (5.5a)$$

$$y_{ad4} = y_{COMd} + B/2 \quad (5.5b)$$

$$z_{ad4} = z_{aj} \quad (5.5c)$$

$$x_{ad1} = x_{COMd} + S_0/2 \quad (5.5d)$$

$$y_{ad1} = y_{COMd} + B/2 \quad (5.5e)$$

$$z_{ad1} = z_{aj} \quad (5.5f)$$

$$x_{ad2} = x_{COMd} - S_0/2 \quad (5.5g)$$

$$y_{ad2} = y_{COMd} + B/2 \quad (5.5h)$$

$$z_{ad2} = z_{aj} \quad (5.5i)$$

$$x_{ad3} = x_{COMd} + S_0/2 \quad (5.5j)$$

$$y_{ad3} = y_{COMd} + B/2 \quad (5.5k)$$

$$z_{ad3} = z_{aj} \quad (5.5l)$$

The second motion plan considered here represents a vertical reciprocation of the platform with all the foot tips grounded, also termed as body heave motion, that can be achieved by manipulating all the twelve valves over length  $l_{COM}$  in serial-parallel mode. The mathematical expression of this motion plan is given below by the expressions

$$\dot{x}_{COMd} = 0, z_{COMd}(t) = -(l_{COM}/2) \{\sin(2\pi t/T - \pi/2) + 1\}, \quad (5.6)$$

With  $T$  represent the time period of the reciprocation. Normally in agricultural harvesting the heave tracking that forms the parallel mode of motion plan operations are very useful to take care of the seasonal and locational variations of height of the tree table. Such type of motion is also a pre-requisite criteria for adjusting the body height consistent to the desired striding length during the walking of a quadruped.

The relative demanded displacement along  $(X, Y, Z)$  axes at every instant between the foot-tips denoted by  $(x_{fdj}, y_{fdj}, z_{fdj})$  of a particular leg with respect to their corresponding anchor points  $(x_{adj}, y_{adj}, z_{adj})$  provides the input to the inverse kinematic model of each leg of the system that has been designed in Inverse Kinematic and Dynamic Modeling sections of chapter 4.

## 5.3 Feedforward Controller Formulation for Serial-Parallel Manipulator

The OSFF controller formulation for the serial manipulator explained in section **Design of Order-Separated Feedforward Controller** of chapter 4 has been used here to find the expressions of feedforward control signal in its order separated form. For each leg of the present system, the feedforward controller considered to be consisted of two components viz. higher order basic voltage denoted by  $V_{f0i}$  to sustain the desired piston motions and a lower order leak compensation voltage  $v_{li}$  for sustaining respectively the flow leakages.

Based on numerical results and discussions given in section 4.5 accompanied with the manipulator design in section 4.7 a clear picture about the order of magnitude of the dominant forces and about the actuation forces acting on serial manipulator system can be obtained. Moreover, the subsection 4.7.4 also provides insight about the order of magnitude of individual components of feedforward voltages. Hence, in order to simplify the controller formulation of the serial-parallel manipulator several aspects like manipulator weight, the friction between piston and cylinder surface, weight of the pistons and cylinders, the weight of lower and upper limbs, along with inertial component of force due to the moving masses have also been neglected. Moreover, during the motion of the platform, the forces on the actuated members due to ground reactions are also neglected. All these factors have been neglected in the feedforward controller formulation with the understanding that the feedback counterpart in form of PID will take care of this modeling inaccuracy.

The mathematical expressions of inverse kinematic modeling given by equations (4.1a) - (4.1j) followed by the equations of feedforward controller (4.3a) -(4.3c), (4.4), (4.5a) – (4.5d) with (4.6a) -(4.6c) and (4.7a)-(4.7g) by neglecting the dynamic model and the friction between the piston cylinder arrangement have been considered here. By writing  $f_i = 0$  in expression (4.5a). (4.5b) and (4.5d) with  $f_{icp} = 1$ ,  $F_{id} = 0$  in expressions (4.7a), (4.7f) and (4.7g) the higher order motion inducing voltage  $V_{f0i}$  can be formulated as

$$V_{f0ij} = -\dot{y}_{dij}[(A_c^3/c_{vA}^2 + A_r^3/c_{vB}^2)/\{P_p \max\langle \text{sgn}(\dot{y}_{dij}), 0 \rangle A_c\} + P_p \max\langle \text{sgn}(-\dot{y}_{dij}), 0 \rangle A_r\}]. \quad (5.7a)$$

Further by using equations (4.7h) - (4.7k) the expression for the lower order leakage compensating voltage  $v_{lij}$  of feedforward controller can be formulated for each leg as

$$v_{li|\dot{y}_{dij} \geq 0} = c_{lB}\{(P_{rij}|\dot{y}_{dij} \geq 0)^{1/2} - (P_p - P_{rij}|\dot{y}_{dij} \geq 0)^{1/2}\} - c_{lA}\{(P_p - P_{cij}|\dot{y}_{dij} \geq 0)^{1/2} - (P_{cij}|\dot{y}_{dij} \geq 0)^{1/2}\} \times [\{c_{vA}(P_p - P_{cij}|\dot{y}_{dij} \geq 0)^{1/2} - c_{vB}(P_{rij}|\dot{y}_{dij} \geq 0)^{1/2}\}]^{-1}, \quad (5.7b)$$

$$v_{li|\dot{y}_{dij} < 0} = c_{lA}\{(P_p - P_{cij}|\dot{y}_{dij} < 0)^{1/2} - (P_{cij}|\dot{y}_{dij} < 0)^{1/2}\} + c_{lB}\{(P_p - P_{rij}|\dot{y}_{dij} < 0)^{1/2} - (P_{rij}|\dot{y}_{dij} < 0)^{1/2}\} \times [\{c_{vA}(P_{cij}|\dot{y}_{dij} < 0)^{1/2} - c_{vB}(P_p - P_{rij}|\dot{y}_{dij} < 0)^{1/2}\}]^{-1}. \quad (5.7c)$$

Finally, by using the expressions (4.8a) - (4.8f) for forward kinematic model, the tracking performance of the feedforward controller can be extracted by finding the relative position of the foot-tip with respect to the moving anchor fitted over the platform in the two-

dimensional space. However, during the experiment the known parameters, like valve and leakage coefficients with rated pressure, flow, and excitation voltage conditions remain same as that of the previous setup.

## 5.4 Experimental Results and Discussion

For the first motion plan, which represents forward motion of the COM along  $\mathbf{X}$  direction, followed by the motion of one leg in the  $\mathbf{XZ}$  plane, during the experiment, the magnitude of horizontal and vertical strides  $s_f$  and  $s_v$  are considered to be 160mm and 70mm, respectively. The horizontal velocity of the body  $v_{COM}$  during the forward motion is taken as 16mm/s. For the foot-tips, the horizontal velocity  $v_{fx}$  is considered as 32mm/s while the vertical velocity  $v_{fz}$  is taken as 14mm/s.

For the heave tracking motion plan, the reciprocating length  $l_{COM}$  during the experiment is taken as 40mm. The experiments have been conducted for different time periods  $T$  equal to 10s, 5s or frequencies of 0.1, 0.2Hz, respectively.

The tracking performance of the **OSFFPID** controller proposed here have been compared against a conventional **PID** controller. For the **PID** controller in Figures. 5.3 to 5.9, the proportional, integral, and derivative gains have been adjusted respectively as 25V/m, 15V/(m-s) and 0.2V-s/m for each valve actuator pair. Any value of the gains, lower than these results in larger errors. However, for executing the proposed order-separated **FFPID** controller, these gains have been set as 10V/m, 5V/(m-s) and 0.1V-s/m, respectively. The relief valve pressure setting for both the experiments are kept at 9MPa.

### 5.4.1 Comparison of FFPID and PID Controllers for Serial-Parallel Actuation

The first real-time experiment is based on both serial and parallel manipulator actuation of the present system and involves the forward motion of the COM followed by the lifting and subsequent lowering of only one foot-tip over a distance  $s_f$  along horizontal direction – keeping the other 3 foot-tips grounded. It has been already stated that during starting of the motion plan, the four foot-tips are required to form a parallelogram by moving foot-tips 3 and 2 ahead of 4 and 1 by a distance of  $(s_f/2)$  along positive  $\mathbf{X}$  direction from its initial rectangular orientation. The necessary actuations of the four serial manipulators for acquiring the parallelogram configuration have been carried out with the entire setup

suspended in air. As the pump is switched on, all the twelve actuators present in the system will take some arbitrary positions due to leakage flow through the valve and consequently the four foot-tips will take some arbitrary positions. To reorient the foot-tips to the desired condition that they form a parallelogram, necessary demands for all the twelve actuators must be computed using the inverse kinematics model. The final computed values of the 12 pistons are provided to the valve-actuator control systems as ramp signals instead of as step signals. This is done to ensure smooth slewing of the pistons to their desired positions without any sudden jerk.

Let  $y_{ij}$  and  $y_{dij}$  be respectively be the initial arbitrary stroke, acquired after switching on the pump and recorded by the  $i^{\text{th}}$  LVDT of  $j^{\text{th}}$  leg, and the final demanded position, as obtained from the inverse kinematics, of the  $i^{\text{th}}$  actuators, for  $i = l, u$  or  $t$  of any leg and  $\tau_R$  be the time taken in ramp by the actuators to move from the initial position to that final desired position. The setting value of  $\tau_R$  is user defined and is based on the speed of each actuator during ramp motion. It should be kept in mind that the speeds of all the actuators decide the maximum flow that has to be provided by the pump. If slope of the ramp signal is denoted by ‘ $m$ ,’ then it can be written as-

$$m = [(y_{dij} - y_{ij})/\tau_R] \quad (5.8a)$$

The ramp signal demand  $(y_{ij})_D$  for the actuator  $i$  of any leg  $j$  thus can be written as,

$$(y_{ij})_D = y_{dij} + m(t - \tau_R), \quad (5.8b)$$

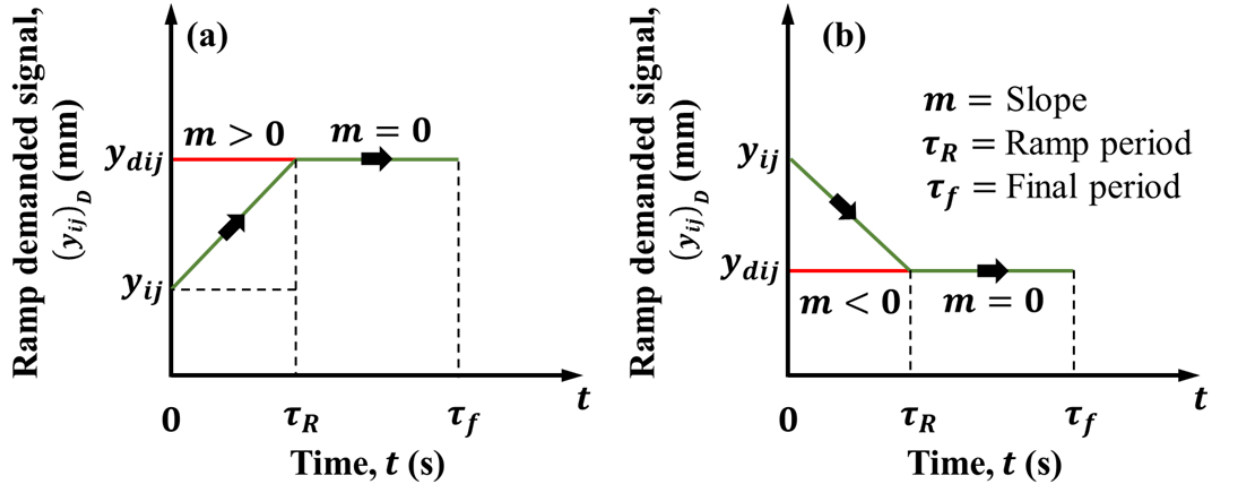
Higher the value of  $\tau_R$  corresponds to slower velocity of the actuators, and  $\tau_R$  tends to zero corresponds to a step demand of the actuator which further makes the motion jerky. However, the slope  $m = 0$  corresponds to holding the desired demanded position of all the actuators up to a certain period denoted by  $\tau_f$ .

Figure 5.2 shows the graphical representation of the ramp signal designed to move the actuator piston to a demanded position and holding it at that position at a given time before initiating the motion plan. From the below figure the desired position of each actuator  $y_{dij}$  from any arbitrary position  $y_{ij}$  can be achieved at time  $\tau_R$  while the actuator remains at this position up to time  $\tau_f$ , when the slope becomes zero. This change in actuator positions ensures the formation of parallelogram orientation of the four foot-tips and holding at that



position up to time denoted by  $\tau_f$  before the initiation of the motion plan. After final time  $\tau_f$  each actuator is given demand signal sequentially to initiate the motion plan. After the end of initialization phase the entire hitherto suspended system is lowered to ground without changing the parallelogram orientation of foot-tips before the initiation of the motion plan in real-time. The holding time  $\tau_f$  is provided for this purpose. It may be noted that the period  $\tau_f$  is selected to ensure sufficient time margin for this operation.

The designed motion plan is then executed in real-time by moving the **COM** along forward **X** direction by an amount of  $S_f/2$  in  $T$  seconds as per eq. (5.2a) shown in Figure 5.1(c) during the time period  $T_l \leq t \leq T_l + T$ , followed by the motion of the foot-tip 4 as per eq. (5.3b)-(5.3f) and depicted in the Figure 5.1(c) by an amount of  $S_f$  in same time duration  $T$  within the time segment of  $T_l + T \leq t \leq 2T$ . During the real time experiment the time  $T$  has been taken as 5 seconds. A one second dwell period has been considered between the motion of **COM** and foot-tip. Considering the time taken for the execution of initialization phase as 10 seconds, with an additional holding time  $\tau_f$  equals to 5 seconds, the total time of execution of entire motion plan becomes 26 seconds.



**Figure 5.2: Ramp demand during initialization phase before execution of forward motion under OSFFPID and PID controllers**

Figure 5.3 exhibits the real time response of all the  $i^{\text{th}}$  actuators, for  $i = l$  or  $u$  of  $j^{\text{th}}$  leg for  $j = 4, 1, 2$  and  $3$  based on demand obtained from inverse kinematic model provided to the valve-actuator control systems as ramp signals based on equation 5.10(a) and (b), for the formation of parallelogram orientation of the four foot-tips during initialization phase. The initialization phase of the motion plan during the experiment has been executed by employing a **PID** controller in closed loop to each of the eight actuators fitted with their

corresponding legs. However, during initiation of motion plan the feedforward control is employed further and coupled with **PID** in loop for the execution of the entire motion plan. The gain values of the **PID** remain same as that has been considered while driving the system with **OSFFPID**. The below Figure 5.3 clearly shows that the response of lower, upper actuators fitted with  $j^{th}$  leg, represented by  $y_{ij}$  approaches towards the corresponding demand of  $y_{dij}$  within the initialization period  $T_l$ , equals to 10 seconds as considered during the experiment. The holding period of  $\tau_f$  equals to 5 seconds is also clearly seen in the given figure. The figure also shows that the demand of all the lower actuators for each leg remain same, while for upper actuators the demand as obtained from inverse kinematics are same in pair for  $j = 4$  and  $3$  and  $j = 1$  and  $2$ . The transverse actuators, always remain in active **PID** control in order to maintain desired foot-tip position with respect to anchor before grounding during initialization phase and to reduce any negligible cross motion of the body COM under the force disturbances arising from the hanging hoses connecting the quadruped body with the external hydraulic power pack.

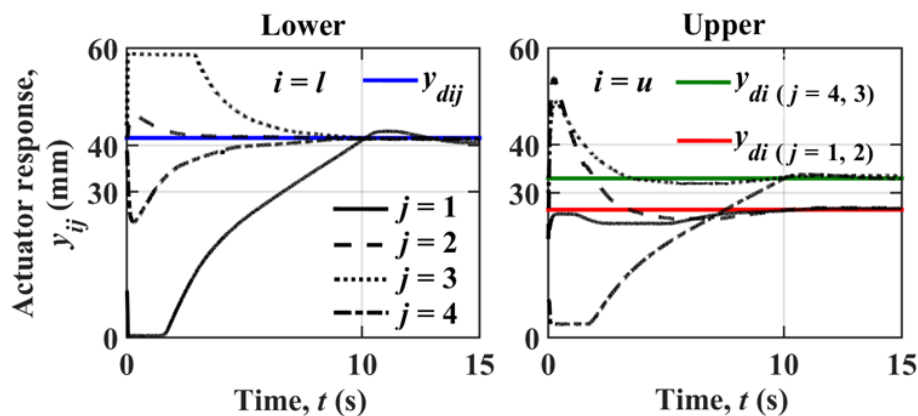


**Figure 5.3: Real time actuator response during initialization phase for the formation of parallelogram orientation of four foot-tips**

Figure 5.4 shown below shows the **COM** and foot-tip demands associated with their tracking response for both **OSFFPID** and classical **PID** alone controller. It clearly exhibits that the tracking performance of **OSFFPID** controller in terms of both tracking of the **COM** and the foot-tip is superior to that of **PID** controller. However, tracking performance of **COM** for **OSFFPID** controller along both the axis **X** and **Z** is slightly better than the tracking of the foot-tip, which can also be seen from Figure 5.5, where the corresponding tracking errors of the responses in time domain along **X** and **Z** axes are shown for both the controllers. The figure expresses the strength of the **OSFFPID** controller compared to simple **PID** controller. The proposed motion plan sequence of the quadruped states that the

velocity of the foot-tip during its motion is twice the velocity of the **COM**. This increased magnitude of velocity further increases the magnitude of inertia forces. The implementation of the feedforward controller while driving the system exhibits almost comparable errors for both foot-tip and **COM** during their motions despite the foot-tip having higher velocity than the **COM**. Both from the response plots as shown in Figure 5.4 and the corresponding error plots in Figure 5.5, it is clear that the magnitude of both the **COM** and foot-tip tracking errors is larger for **PID** as compared to **OSFFPID** controller. This improvement in performance for the designed controller is due to the consideration of higher order feedforward voltage  $V_{f0i}$  to sustain the desired piston motion.

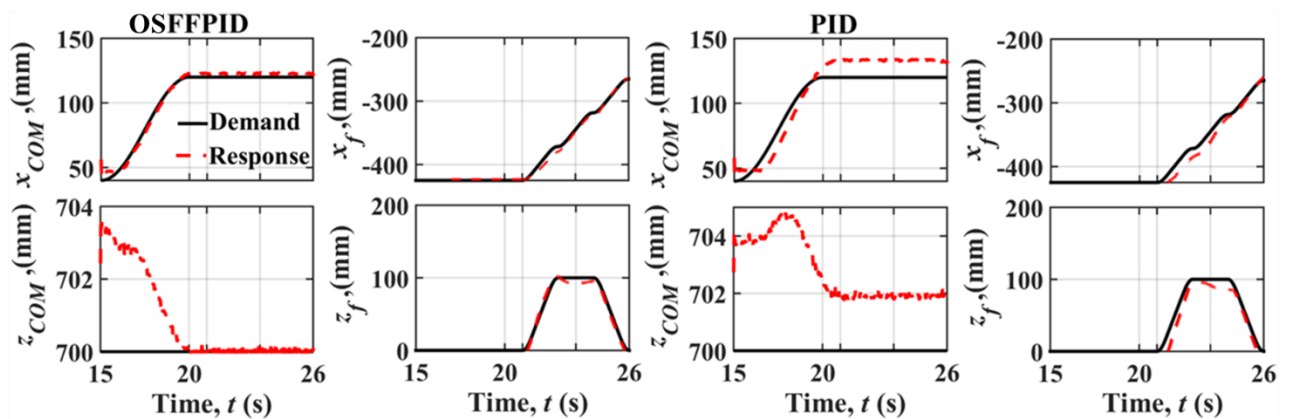


**Figure 5.4: Tracking of COM and foot-tip along (XZ) plane during execution of forward motion under OSFFPID and PID controllers**

Both Figs 5.4 and 5.5 also show that **OSFFPID** controller is capable to handle any cross-coupled error that might occur during the motion of body or foot-tip. During the forward motion of **COM**, the deviation of its height from the desired fixed height can be termed as cross coupled error. The Figure 5.4 and 5.5 shows that apart from some initial cross-coupled error, for **OSFFPID** controller the error almost vanishes, for **PID** controller some fixed residual cross-coupled error remains.

The error in the actuation space for both upper and lower system of each leg has been shown in the Figure 5.6. The figure shows continuous variation of error with time for upper and lower actuation system of leg-4 for its swing phase motion. For other legs, the lower and upper actuators remain active only during the motion of the **COM**. Hence, the actuation error for these legs becomes almost constant near zero line during the motion of the foot-tip 4. However, Figure 5.4 and 5.5 also reveal that during the motion of foot-tip 4 the **COM** also slightly moves both along **X** and **Z** axis. The minute non-zero tracking error in the actuation space for the other three legs is reflective of this situation.

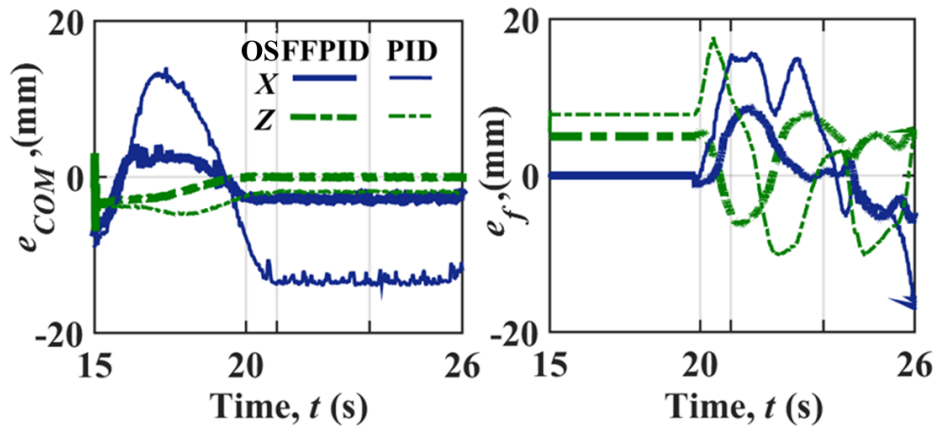


**Figure 5.5: COM and foottip error along (XZ) plane under OSFFPID and PID controllers**

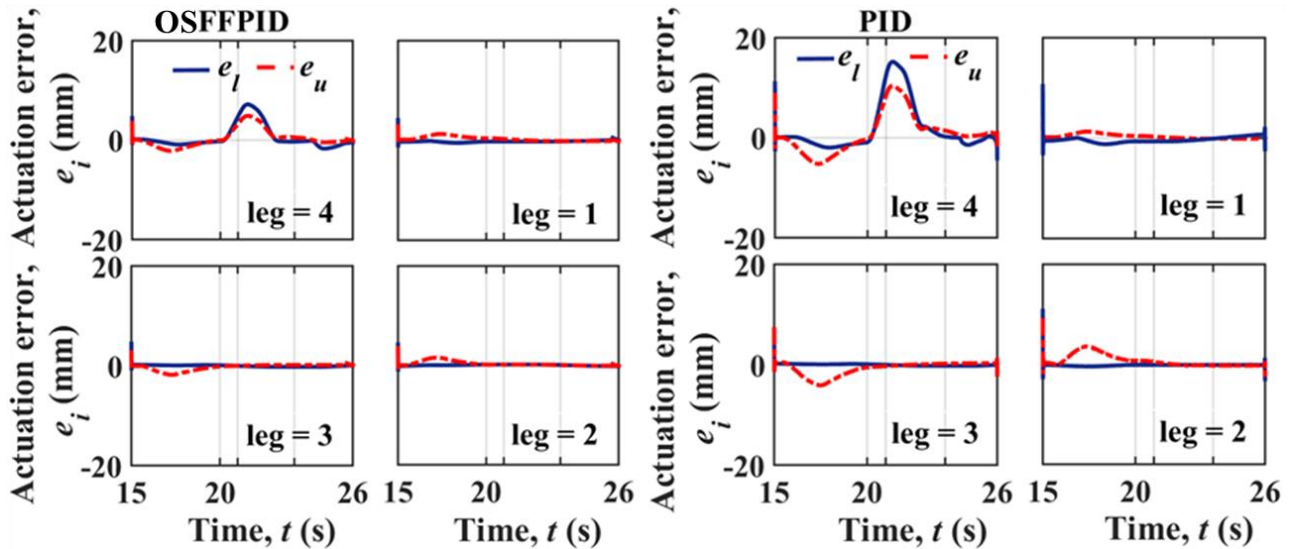


**Figure 5.6: Variations of actuation errors in lower and upper pistons of each leg under OSFFPID and PID controllers**

In Figure 5.7 the individual components of voltages for the **OSFFPID** controller and the feedback voltage for the classical **PID** controller are presented. During motion of the entire system, the major feedforward component support the motion of the piston, whereas a lower order part of control compensates the flow leakages in the valve ports and cylinders. As stated in the previous chapter these are termed as the basic voltage  $V_{f0}$  and the leakage compensation voltage  $v_l$  as shown in Figure 5.6. The **PID** feedback voltage  $v_b$  on the other hand compensates the effect of friction between piston and cylinder arrangement, the actuation force due to weight of the overall system, inertial effects of the moving mass etc.

The figure shows a near constant feedback voltage for both **OSFFPID** and **PID** controller. This constant variation might be attributed due to the lower inertial effect of the moving mass at low frequency. The motion of the system at higher frequency may increase the inertial load further, and the amplitude variation of the feedback voltage can be seen distinctly.

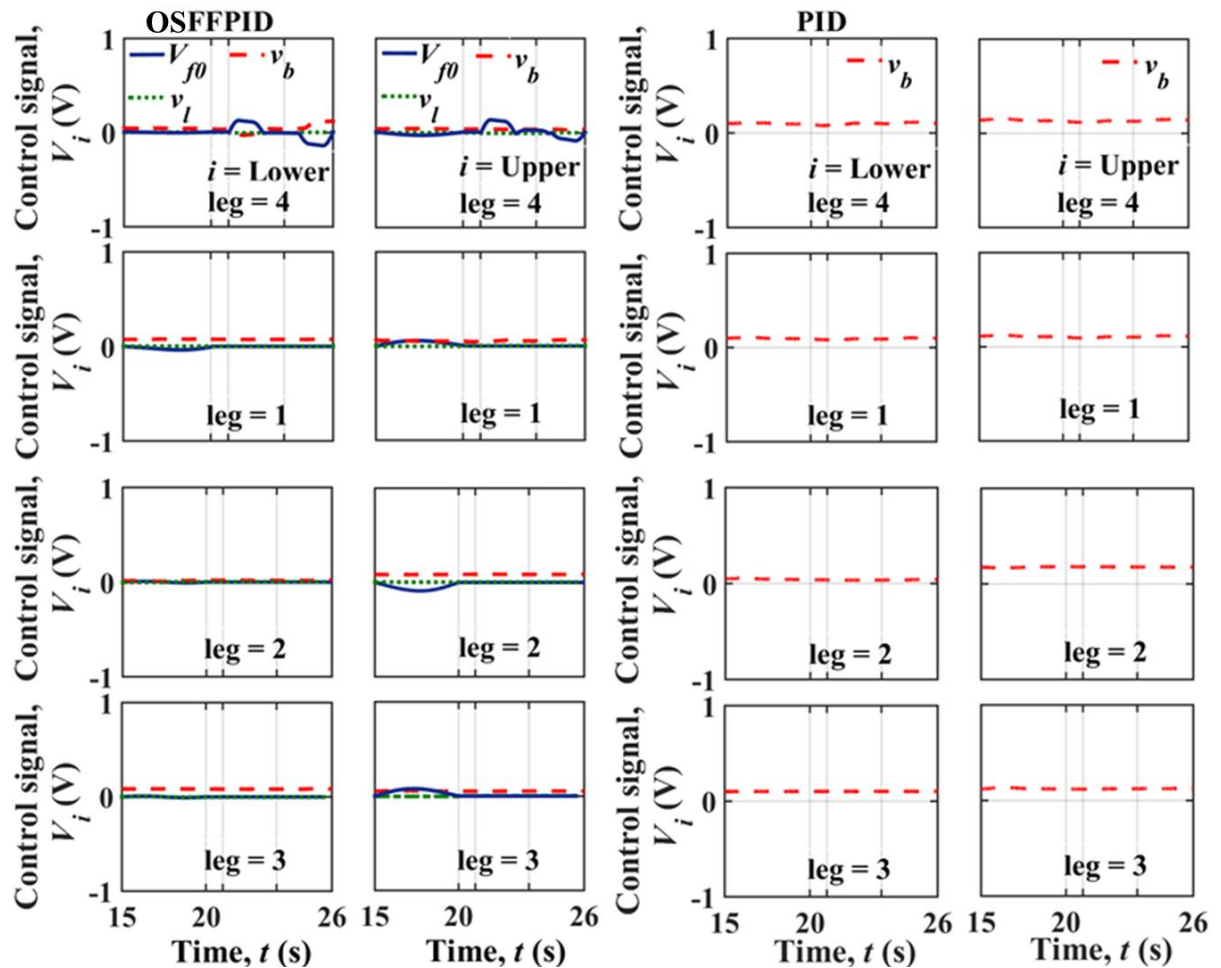


**Figure 5.7: Variations of voltage contribution in lower and upper pistons of each leg under OSFFPID and PID controllers during execution of model static walk**

#### 5.4.2 Comparison of OSFFPID and PID Controllers for Parallel Actuation

The second experiment represents the vertical reciprocation of the platform keeping all the foot-tips grounded, also termed as heave motion. This leads to the operation of the configuration as an electrohydraulic parallel manipulator. The equation of heave motion has been already expressed in (5.6). The amplitude of vertical reciprocation was 40mm during the experiment.

Figure 5.8 shows the reciprocating motion demand of the **COM** and its corresponding response, associated with errors along the respective axes for both **OSFFPID** and **PID**

controller. Better sinusoidal heave tracking performance of the platform in serial-parallel mode under **OSFFPID** control over **PID** control is clearly evident in the above stated figure. With the increase in frequency, the corresponding errors also increases for both the controllers. The amplitudes of both the errors that have been emerged with respect to the demand and in the transverse direction, are essentially due to the tension disturbances induced by the connecting oil hoses appear to be close to each other in the respective cases.

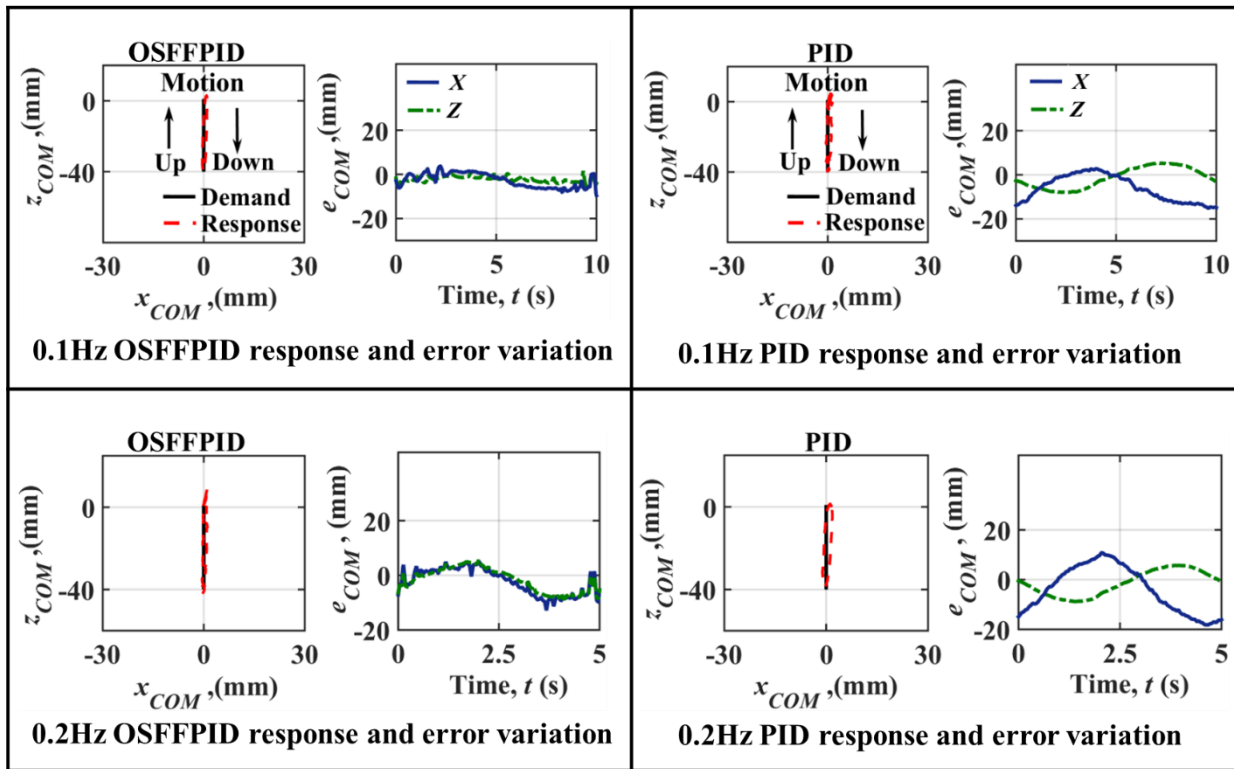


**Figure 5.8: COM motion and error along (XZ) plane under OSFFPID and PID controllers at frequencies of 0.1 and 0.2Hz reciprocation demand**

However, the figure clearly depicts that **OSFFPID** controller exhibits in-phase errors of much lower amplitude compared to **PID** controller which contrast the out of phase error. Despite the increase of the error amplitude with increase in the demanded frequency, the **OSFFPID** controller shows quite good tracking performance and disturbance rejection capability up to 0.2Hz. The magnitude of error shown in the Figure 5.8 of the **COM** during the vertical reciprocation at any instant depends on the position errors in actuation space for both the upper and lower systems of each leg. Figure 5.9 exhibits these errors of lower and upper actuation system of each leg in actuation space. Consistent with the error variation of the **COM** as depicted from Figure 5.8, better tracking performance in actuation space is also evident from Figure 5.9. However, with the increase in frequency the actuation



error also increases for both the controllers. The Figure 5.9 also depicts that each error could have same or opposite signs at the same instant.

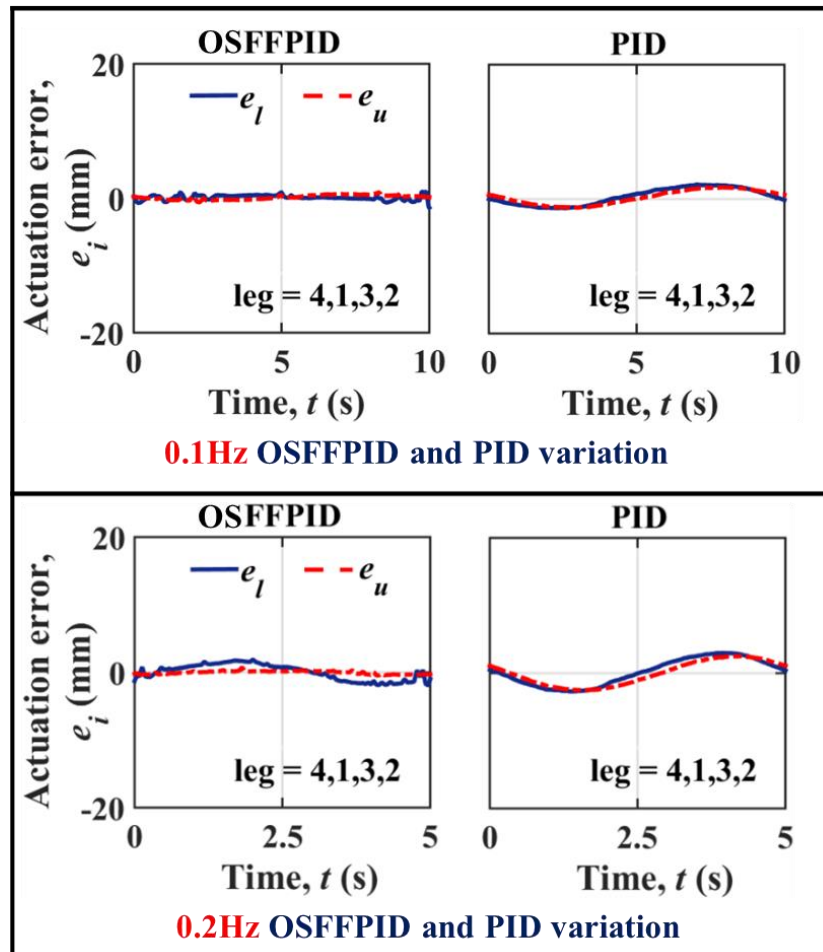


**Figure 5.9: Variations of actuation errors in lower and upper pistons of each leg under OSFFPID and PID controllers at frequencies of 0.1, 0.2Hz reciprocation demand**

The positive and negative signs of error at any instant for upper and lower actuation system can be seen mainly for **OSFFPID** controller and can be concluded due to excess or inadequate excitation signal fed to the valves. However, for the **PID** controller the upper and lower actuator shows almost same kind of error variations. As far as the magnitude of actuation error is concern, the **OSFFPID** controller shows better performance than classical **PID**.

The individual components of **OSFFPID** control voltage, as well as the **PID** control voltage are shown below in Figure 5.10 The figure clearly shows a negligible variation of leakage compensation voltage compared to other two components as stated in the previous chapter is clearly due to the commissioning of present setup with new set of valves.

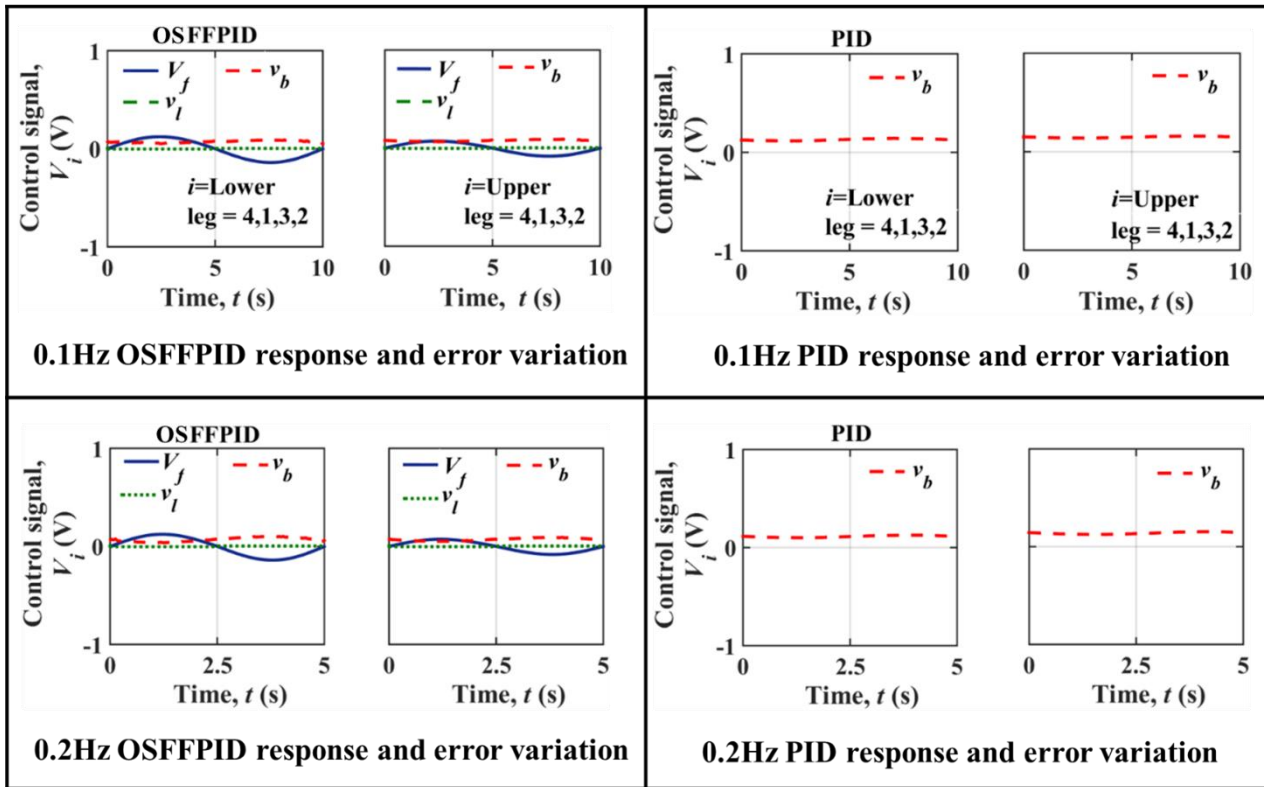


**Figure 5.10: Variations of voltage contribution in lower and upper pistons of each leg under OSFFPID and PID controllers at frequencies of 0.1, 0.2Hz reciprocation demand**

Like Figure 5.7, Figure 5.10 also exhibits a constant variation of feedback voltage for the lowest frequency case of 0.1Hz. both for upper and lower actuators of each leg system. The additional feedforward voltage variations in all the frequency cases executed under the **OSFFPID** controller have shown a significant reduction of the cross-coupled error and the position error along the motion of the **COM** towards negative **Z** axis, as evident in Figure 5.7 above, with respect to the classical **PID** controller. For both **OSFFPID** and **PID** controller one of the most interesting features of positive feedback voltage  $v_{bi}$  in both the upper and lower valves of each leg at low frequencies over the entire cycle is evident in the Figure 5.10. This can be considered to be the **carry-over effect** of the I-gain that dominates over the P-gain throughout the cycle. The detail explanation of this feature has been already explained in section 4.6.2 of the previous chapter.

## 5.5 Summary

The design and real-time implementation of order-separated feedforward position controller has been explained in chapter 3. This design is further extended to drive a serial



manipulator in form of a single leg of quadruped of the present work. The performance of the said feedforward controller to drive the serial manipulator is already explained meticulously in chapter 4. After the successful implementation of the said controller on the serial one, a further effort has been taken to implement this controller in real-time for the entire configuration 3 to realize both serial-parallel combined actuation. The present chapter deals with the implementation of this same controller with some definite considerations to all the upper and lower actuators of each leg to drive the entire setup for the real-time realization of serial-parallel manipulator actuation. The setup used in form of four legs and a body constitutes a four-legged walking robot also termed as quadruped. For the realization of both serial-parallel actuation, demand has been given to move both body and one foot-tip in the forward direction. Also, to realize the parallel actuation only, the body has given a vertical reciprocating motion also termed as heave motion at a frequency of 0.1 and 0.2Hz, respectively.

To drive the entire system twelve servoproportional valves each paired with a low-friction cylinder have been used in the entire setup of the quadruped. During the experimental study, no lateral motion of the body and foot-tip has been considered, so the transverse actuators remain stationary at a definite position. Hence, only the upper and lower valve actuator pair of each leg is driven with the help of **OSFFPID** controller, whereas the transverse actuators fitted with main body is under active **PID** control. As discussed in the previous chapter here also the same fixed-displacement gear pump has been used during several the manipulator experiments. The component of feedforward control involves higher order voltage to sustain piston motion, and a lower order compensation for flow leakage. In view of the newness of the setup the compensation of another low order voltage due to friction between piston and cylinders surface developed in the previous chapter has been neglected. Several other considerations viz. weight of the system, force due to moving mass inertia and other higher order terms has been taken care by the feedback counterpart. The real-time results explained in detail above clearly depicts the superior performance of the simple yet effective feedforward design than a conventional simple **PID** controller.



# CHAPTER 6

## Conclusions and Future Scope

The objective of the present work is to design a novel order separated feedforward control algorithm and its real-time validation for three different actuation systems namely, a one degree-of-freedom single cylinder system, a serial manipulator and finally a serial-parallel manipulator. This chapter provides the principal contributions of the work by drawing conclusions from the investigations that were discussed in the earlier chapters. Furthermore, a variety of potential areas for future research have been identified as a direct consequence of this work.

### 6.1 Conclusions of the Present Work

The major contribution of this work is formulating a generalized order separated feedforward controller (**OSFF**) by exploiting the naturally emerging higher-order motion induced flow in comparison to leakage and compressible flows and its successful implementation in real time for several electrohydraulic motion control systems starting from double-acting single rod cylinder (**DASRC**) to more advance manipulators of serial and serial-parallel type that involves complex kinematics and dynamic structures with two and twelve actuation systems respectively.

The consideration of the variable pressure at the pump supply achieved by a hydro-mechanical compensator is the most noteworthy feature of the formulation. This feature, together with the integration of cylinder friction and deadband in a proportional valve within the same framework, is the most prominent aspect of the formulation. In order to check the acceptability of the proposed formulation an existing conventional feedforward controller design methodology (**CFF**) has also been developed. The existing feedforward models are either constrained for use with double-rod cylinders or with a particular type of single-rod cylinder in which the ratio of the flow areas across its piston is matched with the ratio of the peripheral lengths of the corresponding metering ports in the valve sleeve. The

proposed **OSFF** model is more versatile than either of these models because of absence these constraints. The designed controller is also capable to handle the effects of fluid compressibility and leakage. Offline identification of multiple subsystem parameters with minimal use of sensors is another potential strength of the proposed controller. With long duration usage, the parameters tend to deviate from its initial identified values. For example, it is to be anticipated that a greater quantity of energy will be lost together with the flow of leakage in an ageing valve. Hence time to identification, which can be done offline can point towards potential condition degradation of the system components. This condition monitoring is a significant capability of the proposed methodology. When all of these factors are considered, it becomes clear that the model that was built is quite versatile. The designed controller can be used for tracking motion and force using double-acting cylinders of both the single-rod and double-rod types, for new control valves, and for pump operation in both the fixed-displacement and variable-displacement modes.

In order to establish the validity of the feedforward model as opposed to conventional feedforward one, real-time experiments have been carried out on single cylinder test bench with **PI** feedback to take care of modelling simplifications and approximations in the proposed and its closest existing feedforward models. A prior stability analysis of the linearized error equation using a proposed extension of the Routh criterion for a time variant system was used to estimate the **P** and **I** gains. Another real-time comparison has been carried out in the same setup with an already established nonlinear **ASMIC** and a nonlinear **ARHNNSMC-AB**, executed with constant pump pressure. In connection with this topic, it has also been possible to quantify the typical amount of power that may be saved by using **OSFFPI** controllers that have variable pump pressure. The results of all of the comparisons unambiguously establish the novelty in the design of the controller and further considers to be acceptable and superior.

After successful validation and real time implementation of the designed controller in simple electrohydraulic setup, further effort has been made to implement the same control algorithm in suitable form to manipulators of serial and serial-parallel types with two and twelve actuation systems respectively involving complex kinematics.

Initially the **OSFF** position controller has been devised and implemented in a single leg of an electrohydraulic manipulator system consists of four legs and a body for the realization of serial actuation with the intent that it would eventually function as a quadruped. The hydraulic power pack would be housed on the platform of the quadruped, which at the

moment has a mounting that is earth-fixed and includes flexible oil hoses to connect twelve different pairs of **SPV-DASRC** on the mini-manipulator. The management of various nonlinear features and the resolution of the non-compliance to a cylinder of **DASRC** type are two of the innovative aspects of the formulation that have been provided to the different pairs of **SPV-DASRC** on the manipulator system. In addition to the dominant **FF** voltage that is responsible for maintaining the metered flow through a valve, compensations for leakage in an **SPV** and friction in the cylinder have also been taken into consideration. In order to compensate for the effect of the order separation and to overlook the effects of inertia of the moving mass and the external force on each piston-cylinder pair, the overall **OSFFPID** controller has been designed with a **PID** feedback. This allows for the effect of the order separation to be compensated for. In order to validate the premise that the omitted effects did not have substantial effect, a numerical exercise was carried out. Another consideration in the present methodology involves constructing the translational dynamics of the lower piston relative to that of the corresponding cylinder.

The feedforward and feedback parameters this time have been determined by making use of the catalogue that was provided by the valve manufacturer and also by carrying out an identification exercise that involved performing a straightforward experiment in real-time in conjunction with numerical simulations and optimizations. The studies of two serial-mode manipulations up to 1Hz demand of the single leg with other three grounded correlate to low-load agricultural plucking with response time that is faster than the existing large systems that are only capable of working at 0.05Hz.

The real-time experiments make it apparent that the proposed **OSFFPID** controller has an advantage over a classical **PID** controller in terms of superior tracking and energy efficiency along with a good rejection capability of external disturbance emerging from the flexible oil hoses. The condition monitoring potential of the formulation has been explained, which would be revealed by a large increase in the feedback voltage with ageing of the valves and the cylinders as well as clogging of the tiny radial clearances between the sliding pairs in the electrohydraulic system. The minimization of the instability-related transient oscillations of the response and the excitations by the accompanying low **PID** feedback excitation is a powerful characteristic of the feedforward guidance. Significant oscillations have been seen for a gain that is significantly larger than the value that has been tuned for in the case of the conventional **PID** controller. One of the major achievement of this study is to ensure acceptable tracking of serial manipulators for demands as high as

1Hz compared to below 0.1Hz in the existing studies. A numerical study has also been performed by incorporating the feedforward kinematic and dynamic models of the manipulators to reveal the relative order of different effects. Some results have been given analyzing the sensitivity of altering certain lengths of the manipulator members on a number of variables such as actuation stroke, velocity, force and on other hydraulic parameters like actuation discharge power etc. The purpose of the study is to determine the impact of varying lengths on these above stated variables. A review of these results has shown that its potential application during the pre-fabrication stage can be enhanced by incorporating a strength analysis in order to realise an improved design.

Another attempt has been made to implement the **OSFF** control algorithm in real time for the entire manipulator configuration so as to achieve both serial-parallel and parallel actuation by employing the same control algorithm to all four manipulator legs. The experimental realization of serial-parallel actuation was achieved by a representative walking motion plan, followed by the platform heaving on four grounded legs studied for parallel actuation, by the process of adjusting the height of the platform to match with the approaching gait of a quadruped, pertains to the background of performing static walk gait. The real-time results, that was detailed in previous chapter above, make it abundantly evident that the straightforward yet efficient feedforward architecture delivers far better performance than a traditional and straightforward **PID** controller.

## **6.2 Scope for Future Works**

From the above discussions, it is evident that the use of robotic manipulators is already widespread in many industries and will continue to spread in the near future. However, the use of electrohydraulic systems for the actuation of robotic manipulators and their respective control is still a very challenging task. This has been discussed in detail in earlier chapters. The study of this subject has grown in prominence not only among academics, due to its inherent research challenges, but also among industries because of its immense benefits. It is amply clear from the relevant literature survey that certain aspects regarding the control of electrohydraulic system to drive several manipulators are yet to be explored. For applications requiring large loads, research and development in this field will acquire a great deal of importance in the coming years. This will hold true for both the manipulators themselves and their control. In the current thesis, a sincere attempt was made to address

these issues. However, based on the scope of the current thesis, a list of potential future research directions as an extension of the current work is provided below.

1. **Upgradation of OSFF algorithm for force tracking of EHAS:** Existing controller designs for **EHAS**, according to a review of the relevant literature, are primarily suited to motion analysis, while force tracking has received little attention. The feedforward control algorithm devised in the present work is applicable for both motion and force tracking by single- and double-rod double-acting cylinders. In the near future, a future study investigating the force tracking efficacy of **EHAS** should be regarded as one of the most significant contributions to **EHAS** research.
2. **Effects of several nonlinearities on EHAS and Condition Monitoring Potential of the designed Controller:** The designed control algorithm is able to account for all nonlinearities within a single framework. Consequently, the effects of several nonlinearities on the performance of the **EHAS** can be accurately identified by adding or removing them in the feedforward model; this is regarded as an additional intriguing area of future research in the field of precision control.  
Further, the condition monitoring potential of the **OSFF** formulation described previously, which would be revealed by a significant increase in the feedback voltage with the ageing of the valves and cylinders in the **EHAS**, can be properly revealed by conducting extensive experiments on the electrohydraulic system using both old and newly installed valve-cylinder pairs.
3. **Implementation of different optimization techniques for System Identification:** Multiple feedforward parameters and optimal feedback gain values have been determined using **RCGA**-based system identification in the current work. However, the use of several other optimization techniques, such as **Artificial Bee Colony (ABC)**, **Particle Swarm (PS)**, and **Bacterial foraging (BF)** optimizer etc. which are also very popular optimization techniques, can be implemented in offline mode for determining the converged parametric values of the controller and subsequently compared in real time to determine whether they provide better tracking performance.
4. **Implementation of more advanced controller in feedback path with OSFF:** In the present work, an **OSFF** controller with a conventional **PID** feedback path has

been coupled. It must be determined if the use of any advanced controller coupled with feedforward, such as **SMIC** or its variants, as opposed to **PID**-only control enhances the overall control performance and is capable of rejecting unmodeled disturbances.

5. **Design and Performance analysis of Model free control as opposed to Model based control for EHAS driven manipulator system:** Real-time implementation of an **Artificial Neural Network (ANN)**-based model-free controller based on comprehensive experimental results obtained from **EHAS**-driven manipulators is possible in order to meet the requirements of modern robotic industries. However, in order to train the model, exhaustive experiments must be conducted by providing multiple motion plans ranging from basic to complex. The resulting model can be evaluated in real time to compare its performance to that of a model-based nonlinear feedforward control algorithm coupled with conventional or more sophisticated nonlinear controllers. In addition, the implementation of an **ANN**-based controller requires sophisticated sensors and a computer with a potent processor.
6. **Real time Implementation and Realization of energy saving hydraulic circuit for different manipulator system:** The present work focuses primarily on the real-time implementation of the designed **OSFF** controller for manipulators with sophisticated serial and serial-parallel kinematics. However, the energy-saving potential of the controller has not been implemented in this study, and the controller design is limited to a fixed displacement mode of pump operation. This opens up interesting research avenues for the development of multiple energy-saving hydraulic circuits and their real-time implementation in various manipulator systems.
7. **Realization of serial parallel manipulator as a Quadruped:** A representative version of a static walk motion plan is used to demonstrate the successful implementation of a feedforward control algorithm coupled with conventional **PID** for a serial-parallel manipulator system. However, the realization of entire static walk with a single controller or by implementing other advance controller in feedback loop is an intriguing area for future research. In addition to this, design and real-time implementation of several other gaits like high-speed **dynamic**



walking, **trotting**, **turning**, **gait transition** etc. for a quadruped can be best viewed as a challenging and innovative task to be done in the near future.

8. **Realization of Autonomous Robot:** Several Knowledge bases obtained from simulation and real-time study obtained from softwares like **MATLAB-Simulink**, **SOLIDWORKS**, **Automation Studio** and **LabVIEW** respectively, that further involves design and real-time implementation of more sophisticated controllers, realization of several motion plans in controlled environment, followed by its modification in uneven terrain, modifications in manipulator hardware design, and the successful design and implementation of an energy-saving offboard hydraulic circuit that can be converted into an onboard power pack driven by **IC** engines, thus forms the basis of upgraded hardware of an electrohydraulically driven quadruped torso that can be realized in the future for autonomous navigation in varying environmental conditions.





# References

- Abdellatif, H. and Heimann, B. (2009). Experimental identification of the dynamics model for 6-DOF parallel manipulators. *Robotica*, 28(3), pp.359–368. doi:<https://doi.org/10.1017/s0263574709005682>.
- Altıntaş, Y. and Lane, A.J. (1997). Design of an electro-hydraulic CNC press brake. *International Journal of Machine Tools and Manufacture*, 37(1), pp.45–59. doi:[https://doi.org/10.1016/0890-6955\(95\)00112-3](https://doi.org/10.1016/0890-6955(95)00112-3).
- Ananthanarayanan, H. and Ordóñez, R. (2015). Real-time Inverse Kinematics of  $(2n+1)$  DOF hyper-redundant manipulator arm via a combined numerical and analytical approach. *Mechanism and Machine Theory*, 91, pp.209–226. doi:<https://doi.org/10.1016/j.mechmachtheory.2015.04.011>.
- Anderson, E.H., Bales, G.L. and White, E.V. (2003). Application of smart material-hydraulic actuators. *SPIE Proceedings*. doi:<https://doi.org/10.1117/12.483896>.
- Armstrong-Hélouvry, B., Dupont, P. and De Wit, C.C. (1994). A survey of models, analysis tools and compensation methods for the control of machines with friction. *Automatica*, 30(7), pp.1083–1138. doi:[https://doi.org/10.1016/0005-1098\(94\)90209-7](https://doi.org/10.1016/0005-1098(94)90209-7).
- Astrom KJ & Haggglund K 2006, *Advanced PID Control*, ISA -The Instrumentation, Systems, and Automation Society, NC.
- Baghestan, K., Rezaei, S.M., Talebi, H.A. and Zareinejad, M. (2015). An energy-saving nonlinear position control strategy for electro-hydraulic servo systems. *ISA Transactions*, 59, pp.268–279. doi:<https://doi.org/10.1016/j.isatra.2015.10.012>.
- Bandala, M., West, C., Monk, S., Montazeri, A. and Taylor, C.J. (2019). Vision-Based Assisted Tele-Operation of a Dual-Arm Hydraulically Actuated Robot for Pipe Cutting and Grasping in Nuclear Environments. *Robotics*, 8(2), p.42. doi:<https://doi.org/10.3390/robotics8020042>.
- Bao, Y., Du, W., Tang, D., Yang, X. and Yu, J. (2006). Adaptive Fuzzy Sliding-Mode Control for Non-minimum Phase Overload System of Missile. *Intelligent Control and Automation*, 344, pp.219–228. doi:[https://doi.org/10.1007/978-3-540-37256-1\\_30](https://doi.org/10.1007/978-3-540-37256-1_30).
- Bartolini, G., Pisano, A., Punta, E. and Usai, E. (2003). A survey of applications of second-

order sliding mode control to mechanical systems. *International Journal of Control*, 76(9-10), pp.875–892. doi:<https://doi.org/10.1080/0020717031000099010>.

Bhattacharya, S., Hatwal, H. and Ghosh, A. (1997). An on-line parameter estimation scheme for generalized stewart platform type parallel manipulators. *Mechanism and Machine Theory*, 32(1), pp.79–89. doi:[https://doi.org/10.1016/0094-114x\(96\)00018-3](https://doi.org/10.1016/0094-114x(96)00018-3).

Biswal, P. and Mohanty, P.K. (2020). Development of quadruped walking robots: A review. *Ain Shams Engineering Journal*. doi:<https://doi.org/10.1016/j.asej.2020.11.005>.

Bliman, P.-A. (1991). Friction modelling by hysteresis operators : application to Dahl, sticktion and Stribeck effects. *Proc. Conf. on Models of Hysteresis, Trento, 1991*. [online] Available at: <https://cir.nii.ac.jp/crid/1574231875434876672> [Accessed 10 Mar. 2023].

Bosch Rexroth AG Hydraulics (2012) 4/2 and 4/3 proportional directional valves, direct operated, with electrical position feedback, without/with integrated electronics (OBE) - Type 4WRE and 4WREE.

Bosch Rexroth AG Hydraulics (2017) Hydraulic cylinder Mill type- Series CDH1/CGH1/CSH1.

Březina, L., Holub, M., Cintula, L. and Kovar, J. (2013). Delta Robot Design. *Solid State Phenomena*, 198, pp.9–14. doi:<https://doi.org/10.4028/www.scientific.net/ssp.198.9>.

Briot, S., Krut, S. and Gautier, M. (2015). Dynamic Parameter Identification of Over actuated Parallel Robots. *Journal of Dynamic Systems, Measurement, and Control*, 137(11). doi:<https://doi.org/10.1115/1.4030867>.

Byl, K. and Tedrake, R. (2009). Metastable Walking Machines. *The International Journal of Robotics Research*, 28(8), pp.1040–1064. doi:<https://doi.org/10.1177/0278364909340446>.

Cai, Y., Zheng, S., Liu, W., Qu, Z., Zhu, J. and Han, J. (2021). Adaptive robust dual-loop control scheme of ship-mounted Stewart platforms for wave compensation. *Mechanism and Machine Theory*, 164, p.104406. doi:<https://doi.org/10.1016/j.mechmachtheory.2021.104406>.

Caldwell, D.G., Medrano-Cerda, G.A. and Goodwin, M. (1995). Control of pneumatic muscle actuators. *IEEE Control Systems*, 15(1), pp.40–48. doi:<https://doi.org/10.1109/37.341863>.

- Canudas de Wit, C., Olsson, H., Astrom, K.J. and Lischinsky, P. (1995). A new model for control of systems with friction. *IEEE Transactions on Automatic Control*, 40(3), pp.419–425. doi:<https://doi.org/10.1109/9.376053>.
- Cardozo, W.S. and Weber, H.I. (2017). Dynamic modeling of a 2-dof parallel electrohydraulic-actuated homokinetic platform. *Mechanism and Machine Theory*, 118, pp.1–13. doi:<https://doi.org/10.1016/j.mechmachtheory.2017.07.018>.
- Cerman, O. and Hušek, P. (2012). Adaptive fuzzy sliding mode control for electrohydraulic servo mechanism. *Expert Systems with Applications*, 39(11), pp.10269–10277. doi:<https://doi.org/10.1016/j.eswa.2012.02.172>.
- Cetinkunt, S., Pinoson, U., Chen, C., Egelja, A. and Anwar, S. (2004). Positive flow control of closed-center electrohydraulic implement-by-wire systems for mobile equipment applications. *Mechatronics*, 14(4), pp.403–420. doi:[https://doi.org/10.1016/s0957-4158\(03\)00067-9](https://doi.org/10.1016/s0957-4158(03)00067-9).
- Chan, P.T., Rad, A.B. and Wang, J. (2001). Indirect adaptive fuzzy sliding mode control: Part II: parameter projection and supervisory control. *Fuzzy Sets and Systems*, 122(1), pp.31–43. doi:[https://doi.org/10.1016/s0165-0114\(99\)00180-3](https://doi.org/10.1016/s0165-0114(99)00180-3).
- Chaudhuri, S., Saha, R., Chatterjee, A., Mookherjee, S. and Sanyal, D. (2020a). Adaptive neural-bias-sliding mode control of rugged electrohydraulic system motion by recurrent Hermite neural network. *Control Engineering Practice*, 103, p.104588. doi:<https://doi.org/10.1016/j.conengprac.2020.104588>.
- Chaudhuri, S., Saha, R., Chatterjee, A., Mookherjee, S. and Sanyal, D. (2020b). Development of a Motion Sensing System Based on Visual Servoing of an Eye-in-Hand Electrohydraulic Parallel Manipulator. *IEEE Sensors Journal*, 20(14), pp.8108–8116. doi:<https://doi.org/10.1109/jsen.2020.2979490>.
- Chen, C.-Y., Li, T.-H.S. and Yeh, Y.-C. (2009). EP-based kinematic control and adaptive fuzzy sliding-mode dynamic control for wheeled mobile robots. *Information Sciences*, 179(1-2), pp.180–195. doi:<https://doi.org/10.1016/j.ins.2008.09.012>.
- Chen, J., Yu, C., Xia, X., Zhao, X., Cai, S. and Wang, J. (2019). Design and experimental study of a power matching control system for a working device of a tree transplanting machine. *Proceedings of the Institution of Mechanical Engineers, Part I: Journal of Systems and Control Engineering*, 233(6), pp.689–701.

doi:<https://doi.org/10.1177/0959651818810090>.

Cheng, L., Zhu, Z.-C., Shen, G., Wang, S., Li, X. and Tang, Y. (2020). Real-Time Force Tracking Control of an Electro-Hydraulic System Using a Novel Robust Adaptive Sliding Mode Controller. *IEEE Access*, 8, pp.13315–13328. doi:<https://doi.org/10.1109/access.2019.2895595>.

Chi, W., Cao, D., Wang, D., Tang, J., Nie, Y. and Huang, W. (2015). Design and Experimental Study of a VCM-Based Stewart Parallel Mechanism Used for Active Vibration Isolation. *Energies*, 8(8), pp.8001–8019. doi:<https://doi.org/10.3390/en8088001>.

Chiang, C.-J. and Chen, Y.-C. (2017). Neural network fuzzy sliding mode control of pneumatic muscle actuators. *Engineering Applications of Artificial Intelligence*, 65, pp.68–86. doi:<https://doi.org/10.1016/j.engappai.2017.06.021>.

Clegg, A.C., Dunnigan, M.W. and Lane, D.M. (2003). Self-tuning position and force control of an underwater hydraulic manipulator. *Proceedings 2001 ICRA. IEEE International Conference on Robotics and Automation (Cat. No.01CH37164)*, 4, pp.3226–3231. doi:<https://doi.org/10.1109/robot.2001.933115>.

Czymmek, V., Harders, L.O., Knoll, F.J. and Hussmann, S. (2019). Vision-Based Deep Learning Approach for Real-Time Detection of Weeds in Organic Farming. *2019 IEEE International Instrumentation and Measurement Technology Conference (I2MTC)*. doi:<https://doi.org/10.1109/i2mtc.2019.8826921>.

Daher, N. and Ivantysynova, M. (2014). Energy analysis of an original steering technology that saves fuel and boosts efficiency. *Energy Conversion and Management*, 86, pp.1059–1068. doi:<https://doi.org/10.1016/j.enconman.2014.06.073>.

Dahl, P.R. (1976). Solid Friction Damping of Mechanical Vibrations. *AIAA Journal*, 14(12), pp.1675–1682. doi:<https://doi.org/10.2514/3.61511>.

Dao, H.V., Tran, D.T. and Ahn, K.K. (2021). Active Fault Tolerant Control System Design for Hydraulic Manipulator With Internal Leakage Faults Based on Disturbance Observer and Online Adaptive Identification. *IEEE Access*, 9, pp.23850–23862. doi:<https://doi.org/10.1109/access.2021.3053596>.

Das, J., Mishra, S.K., Ramashankar Paswan, Kumar, A., Sujit Baran Kumar, Saha, R. and S Mookherjee (2016). Characterization and tracking control of a nonlinear electrohydraulic valve-cylinder system. *Proceedings of the Institution of Mechanical Engineers, Part E:*

*Journal of Process Mechanical Engineering*, 230(5).  
doi:<https://doi.org/10.1177/0954408914554021>.

Dasgupta, B. and Mruthyunjaya, T.S. (2000). The Stewart platform manipulator: a review. *Mechanism and Machine Theory*, 35(1), pp.15–40. doi:[https://doi.org/10.1016/s0094-114x\(99\)00006-3](https://doi.org/10.1016/s0094-114x(99)00006-3).

Dasgupta, K. and Watton, J. (2005). Dynamic analysis of proportional solenoid controlled piloted relief valve by bond graph. *Simulation Modelling Practice and Theory*, 13(1), pp.21–38. doi:<https://doi.org/10.1016/j.simpat.2004.08.002>.

Dasmahapatra, S., Saha, R., Mookherjee, S. and Sanyal, D. (2018). Designing an Input-Linearized Adaptive Sliding Mode Coupled Nonlinear Integral Controller. *IEEE/ASME Transactions on Mechatronics*, 23(6), pp.2888–2895. doi:<https://doi.org/10.1109/tmech.2018.2870911>.

Dasmahapatra, S., Sarkar, B.K., Saha, R., Chatterjee, A., Mookherjee, S. and Sanyal, D. (2015). Design of an Adaptive Fuzzy-Bias SMC and Validation for a Rugged Electrohydraulic System. *IEEE/ASME Transactions on Mechatronics*, 20(6), pp.2708–2715. doi:<https://doi.org/10.1109/tmech.2015.2393437>.

Degrave, J., Burm, M., Kindermans, P.-J., Dambre, J. and wyffels, F. (2015). Transfer learning of gaits on a quadrupedal robot. *Adaptive Behavior*, 23(2), pp.69–82. doi:<https://doi.org/10.1177/1059712314563620>.

Destro, M.C. and De Negri, V.J. (2018). Method for combining valves with symmetric and asymmetric cylinders for hydraulic systems. *International Journal of Fluid Power*, 19(3), pp.126–139. doi:<https://doi.org/10.1080/14399776.2018.1483164>.

Djordjevic, V., Stojanovic, V., Tao, H., Song, X., He, S. and Gao, W. (2022). Data-driven control of hydraulic servo actuator based on adaptive dynamic programming. *Discrete and Continuous Dynamical Systems - S*, 15(7), p.1633. doi:<https://doi.org/10.3934/dcdss.2021145>.

Du, C., Plummer, A.R. and Johnston, D.N. (2017). Performance analysis of a new energy-efficient variable supply pressure electro-hydraulic motion control method. *Control Engineering Practice*, 60, pp.87–98. doi:<https://doi.org/10.1016/j.conengprac.2017.01.002>.

Eryilmaz, B. and Wilson, B.H. (1999). Improved Tracking Control of Hydraulic Systems.



*Journal of Dynamic Systems, Measurement, and Control*, 123(3), pp.457–462.  
doi:<https://doi.org/10.1115/1.1386394>.

Faessler, M., Franchi, A. and Scaramuzza, D. (2018). Differential Flatness of Quadrotor Dynamics Subject to Rotor Drag for Accurate Tracking of High-Speed Trajectories. *IEEE Robotics and Automation Letters*, 3(2), pp.620–626.  
doi:<https://doi.org/10.1109/lra.2017.2776353>.

Fales, R. and Kelkar, A. (2009). Robust control design for a wheel loader using and feedback linearization based methods. *ISA Transactions*, 48(3), pp.312–320.  
doi:<https://doi.org/10.1016/j.isatra.2009.01.007>.

Fankhauser, P., Bjelonic, M., Dario Bellicoso, C., Miki, T. and Hutter, M. (2018). Robust Rough-Terrain Locomotion with a Quadrupedal Robot. *2018 IEEE International Conference on Robotics and Automation (ICRA)*.  
doi:<https://doi.org/10.1109/icra.2018.8460731>.

Feng, H., Qiao, W., Yin, C., Yu, H. and Cao, D. (2019). Identification and compensation of non-linear friction for a electro-hydraulic system. *Mechanism and Machine Theory*, 141, pp.1–13. doi:<https://doi.org/10.1016/j.mechmachtheory.2019.07.004>.

Feng, Y., Yu, X. and Han, F. (2013). High-Order Terminal Sliding-Mode Observer for Parameter Estimation of a Permanent-Magnet Synchronous Motor. *IEEE Transactions on Industrial Electronics*, 60(10), pp.4272–4280.  
doi:<https://doi.org/10.1109/tie.2012.2213561>.

FLIESS, M., LÉVINE, J., MARTIN, P. and ROUCHON, P. (1995). Flatness and defect of non-linear systems: introductory theory and examples. *International Journal of Control*, 61(6), pp.1327–1361. doi:<https://doi.org/10.1080/00207179508921959>.

Freidovich, L., Robertsson, A., Shiriaev, A. and Johansson, R. (2010). LuGre-Model-Based Friction Compensation. *IEEE Transactions on Control Systems Technology*, 18(1), pp.194–200. doi:<https://doi.org/10.1109/tcst.2008.2010501>.

Gang, S., Zhen-Cai, Z., Lei, Z., Yu, T., Chi-fu, Y., Jin-song, Z., Guang-da, L. and Jun-Wei, H. (2013). Adaptive feed-forward compensation for hybrid control with acceleration time waveform replication on electro-hydraulic shaking table. *Control Engineering Practice*, 21(8), pp.1128–1142. doi:<https://doi.org/10.1016/j.conengprac.2013.03.007>.

Gao, B., Shen, W., Zheng, L., Zhang, W. and Zhao, H. (2022). A Review of Key

Technologies for Friction Nonlinearity in an Electro-Hydraulic Servo System. *Machines*, 10(7), p.568. doi:<https://doi.org/10.3390/machines10070568>.

Garimella, P. and Yao, B. (2005). *Model based fault detection of an electro-hydraulic cylinder*. [online] IEEE Xplore. doi:<https://doi.org/10.1109/ACC.2005.1469982>.

Garriz, C. and Domingo, R. (2019). Development of Trajectories Through the Kalman Algorithm and Application to an Industrial Robot in the Automotive Industry. *IEEE Access*, 7, pp.23570–23578. doi:<https://doi.org/10.1109/access.2019.2899370>.

Girone, M., Burdea, G., Bouzit, M., Popescu, V. and Deutsch, J.E. (2001). A Stewart Platform-Based System for Ankle Telerehabilitation. *Autonomous Robots*, 10(2), pp.203–212. doi:<https://doi.org/10.1023/a:1008938121020>.

Gosselin, C. and Angeles, J. (1990). Singularity analysis of closed-loop kinematic chains. *IEEE Transactions on Robotics and Automation*, 6(3), pp.281–290. doi:<https://doi.org/10.1109/70.56660>.

Guo, Q. and Chen, Z. (2021). Neural adaptive control of single-rod electrohydraulic system with lumped uncertainty. *Mechanical Systems and Signal Processing*, 146, p.106869. doi:<https://doi.org/10.1016/j.ymssp.2020.106869>.

Guo, Q., Zuo, Z. and Ding, Z. (2019). Parametric Adaptive Control of Single-rod Electrohydraulic System with Block-Strict-Feedback Model. *Automatica*, 113, [108807]. doi:<https://doi.org/10.1016/j.cub.2019.08.012>.

H. Qiu, Q. Zhang and J.F. Reid (2001). FUZZY CONTROL OF ELECTROHYDRAULIC STEERING SYSTEMS FOR AGRICULTURAL VEHICLES. *Transactions of the ASAE*, 44(6). doi:<https://doi.org/10.13031/2013.7005>.

Haessig, D.A. and Friedland, B. (1991). On the Modeling and Simulation of Friction. *Journal of Dynamic Systems, Measurement, and Control*, 113(3), pp.354–362. doi:<https://doi.org/10.1115/1.2896418>.

Herr, H. (2009). Exoskeletons and orthoses: classification, design challenges and future directions. *Journal of NeuroEngineering and Rehabilitation*, [online] 6(1). doi:<https://doi.org/10.1186/1743-0003-6-21>.

Hess, D.P. and Soom, A. (1990). Friction at a Lubricated Line Contact Operating at Oscillating Sliding Velocities. *Journal of Tribology*, 112(1), pp.147–152. doi:<https://doi.org/10.1115/1.2920220>.

- Hirose, S. and Yoneda, K. (1993). Toward Development of Practical Quadruped Walking Vehicles. *Journal of Robotics and Mechatronics*, 5(6), pp.498–504. doi:<https://doi.org/10.20965/jrm.1993.p0498>.
- Hou, X., Gao, X., Bin, L., Peng, Y. and Mao, Y. (2021). Non-destructive Testing Assisted by Six-Axis Manipulator Based on POE Formula. *Journal of Physics: Conference Series*, 1820(1), p.012085. doi:<https://doi.org/10.1088/1742-6596/1820/1/012085>.
- Hu, C., Yao, B. and Wang, Q. (2011). Adaptive Robust Precision Motion Control of Systems With Unknown Input Dead-Zones: A Case Study With Comparative Experiments. *IEEE Transactions on Industrial Electronics*, 58(6), pp.2454–2464. doi:<https://doi.org/10.1109/tie.2010.2066535>.
- Huang, H., Jin, R., Li, L. and Liu, Z. (2018). Improving the Energy Efficiency of a Hydraulic Press Via Variable-Speed Variable-Displacement Pump Unit. *Journal of Dynamic Systems, Measurement, and Control*, [online] 140(11). doi:<https://doi.org/10.1115/1.4040325>.
- Huang, S., Liang, W. and Tan, K.K. (2019). Intelligent Friction Compensation: A Review. *IEEE/ASME Transactions on Mechatronics*, 24(4), pp.1763–1774. doi:<https://doi.org/10.1109/tmech.2019.2916665>.
- Huang, S.-J. and Chen, H.-Y. (2006). Adaptive sliding controller with self-tuning fuzzy compensation for vehicle suspension control. *Mechatronics*, 16(10), pp.607–622. doi:<https://doi.org/10.1016/j.mechatronics.2006.06.002>.
- Huang, Y., Pool, D.M., Stroosma, O. and Chu, Q.P. (2017). Incremental Nonlinear Dynamic Inversion Control for Hydraulic Hexapod Flight Simulator Motion Systems \*  
\*The first author is sponsored by Chinese Scholarship Council. *IFAC-PapersOnLine*, 50(1), pp.4294–4299. doi:<https://doi.org/10.1016/j.ifacol.2017.08.837>.
- Huayong, Y., Hu, S., Guofang, G. and Guoliang, H. (2009). Electro-hydraulic proportional control of thrust system for shield tunneling machine. *Automation in Construction*, 18(7), pp.950–956. doi:<https://doi.org/10.1016/j.autcon.2009.04.005>.
- Humphreys, H., Book, W.J. and Deetjen, G. (2018). Advanced patient transfer assist device. *2018 International Symposium on Medical Robotics (ISMR)*. doi:<https://doi.org/10.1109/ismr.2018.8333290>.
- HUNG, L. and CHUNG, H. (2007). Decoupled control using neural network-based sliding-

mode controller for nonlinear systems. *Expert Systems with Applications*, 32(4), pp.1168–1182. doi:<https://doi.org/10.1016/j.eswa.2006.02.024>.

Hunter, I.W., Hollerbach, J.M. and Ballantyne, J., 1991. A comparative analysis of actuator technologies for robotics. *Robotics Review*, 2, pp.299-342.

Hutter, M., Gehring, C., Hopflinger, M.A., Blosch, M. and Siegwart, R. (2014). Toward Combining Speed, Efficiency, Versatility, and Robustness in an Autonomous Quadruped. *IEEE Transactions on Robotics*, 30(6), pp.1427–1440. doi:<https://doi.org/10.1109/tro.2014.2360493>.

Jang, T.K., Lim, B.S. and Kim, M.K. (2018). The canonical stewart platform as a six DOF pose sensor for automotive applications. *Journal of Mechanical Science and Technology*, 32(12), pp.5553–5561. doi:<https://doi.org/10.1007/s12206-018-1101-0>.

Jiang, Y., Gao, W., Na, J., Zhang, D., Hämmäläinen, T.T., Stojanovic, V. and Lewis, F.L. (2022). Value iteration and adaptive optimal output regulation with assured convergence rate. *Control Engineering Practice*, 121, p.105042. doi:<https://doi.org/10.1016/j.conengprac.2021.105042>.

Kaminaga, H., Amari, T., Niwa, Y. and Nakamura, Y. (2010). *Development of knee power assist using backdrivable electro-hydrostatic actuator*. [online] IEEE Xplore. doi:<https://doi.org/10.1109/IROS.2010.5650671>.

Kang, R., Chanal, H., Bonnemains, T., Pateloup, S., Branson, D.T. and Ray, P. (2011). Learning the forward kinematics behavior of a hybrid robot employing artificial neural networks. *Robotica*, 30(5), pp.847–855. doi:<https://doi.org/10.1017/s026357471100107x>.

Kemmetmuller, W., Muller, S. and Kugi, A. (2007). Mathematical Modeling and Nonlinear Controller Design for a Novel Electrohydraulic Power-Steering System. *IEEE/ASME Transactions on Mechatronics*, 12(1), pp.85–97. doi:<https://doi.org/10.1109/tmech.2006.886257>.

Kim, W., Won, D. and Tomizuka, M. (2015). Flatness-Based Nonlinear Control for Position Tracking of Electrohydraulic Systems. *IEEE/ASME Transactions on Mechatronics*, 20(1), pp.197–206. doi:<https://doi.org/10.1109/tmech.2014.2310498>.

Kock, F. and Ferrari, C. (2011). Flatness-Based High Frequency Control of a Hydraulic Actuator. *Journal of Dynamic Systems, Measurement, and Control*, 134(2). doi:<https://doi.org/10.1115/1.4005047>.

- Koivumäki, J., Zhu, W.-H. and Mattila, J. (2019). Energy-efficient and high-precision control of hydraulic robots. *Control Engineering Practice*, 85, pp.176–193. doi:<https://doi.org/10.1016/j.conengprac.2018.12.013>.
- Komsta, J., van Oijen, N. and Antoszkiewicz, P. (2013). Integral sliding mode compensator for load pressure control of die-cushion cylinder drive. *Control Engineering Practice*, 21(5), pp.708–718. doi:<https://doi.org/10.1016/j.conengprac.2011.12.006>.
- Kurazume, R., Yoneda, K. and Hirose, S. (2002). Feedforward and Feedback Dynamic Trot Gait Control for Quadruped Walking Vehicle. *Autonomous Robots*, 12(2), pp.157–172. doi:<https://doi.org/10.1023/a:1014045326702>.
- Lai, Z.C. and Yang, D.C.H. (1986). A New Method for the Singularity Analysis of Simple Six-link Manipulators. *The International Journal of Robotics Research*, 5(2), pp.66–74. doi:<https://doi.org/10.1177/027836498600500207>.
- Li, K., Zhang, C. and Sun, Z. (2015). Precise piston trajectory control for a free piston engine. *Control Engineering Practice*, 34, pp.30–38. doi:<https://doi.org/10.1016/j.conengprac.2014.09.016>.
- Li, M., Shi, W., Wei, J., Fang, J., Guo, K. and Zhang, Q. (2019). Parallel Velocity Control of an Electro-Hydraulic Actuator With Dual Disturbance Observers. *IEEE Access*, 7, pp.56631–56641. doi:<https://doi.org/10.1109/access.2019.2911658>.
- Li, Y., Yang, X., Wu, H. and Chen, B. (2018). Optimal design of a six-axis vibration isolator via Stewart platform by using homogeneous Jacobian matrix formulation based on dual quaternions. *Journal of Mechanical Science and Technology*, 32(1), pp.11–19. doi:<https://doi.org/10.1007/s12206-017-1202-1>.
- Lian, R.-J. (2012). Design of an enhanced adaptive self-organizing fuzzy sliding-mode controller for robotic systems. *Expert Systems with Applications*, 39(1), pp.1545–1554. doi:<https://doi.org/10.1016/j.eswa.2011.08.052>.
- Liu, S., Hao, R., Zhao, D. and Tian, Z. (2020). Adaptive Dynamic Surface Control for Active Suspension With Electro-Hydraulic Actuator Parameter Uncertainty and External Disturbance. *IEEE Access*, 8, pp.156645–156653. doi:<https://doi.org/10.1109/access.2020.3018442>.
- Liu, T., Gong, G., Yang, H., Cheng, Y., Chen, Y. and Zhou, X. (2019). A novel cutterhead off-stuck strategy for tunnel boring machine based on electro-hydraulic hybrid driving.

*Advances in Mechanical Engineering*, 11(1), p.168781401882417.  
doi:<https://doi.org/10.1177/1687814018824174>.

Liu, Z., Wu, J., Wang, L. and Zhang, B. (2021). Control Parameters Design Based on Dynamic Characteristics of a Hybrid Robot With Parallelogram Structures. *IEEE/ASME Transactions on Mechatronics*, 26(2), pp.1140–1150.  
doi:<https://doi.org/10.1109/tmech.2020.3019424>.

Liyanage, M.H., Krouglicof, N. and Gosine, R. (2011). Development and testing of a novel high speed SCARA type manipulator for robotic applications. *2011 IEEE International Conference on Robotics and Automation*. doi:<https://doi.org/10.1109/icra.2011.5980452>.

Lu, Y., Dai, Z., Ye, N. and Wang, P. (2015a). Kinematics/statics analysis of a novel serial-parallel robotic arm with hand. *Journal of Mechanical Science and Technology*, 29(10), pp.4407–4416. doi:<https://doi.org/10.1007/s12206-015-0939-7>.

Lu, Y., Hu, B. and Yu, J. (2009). Analysis of kinematics/statics and workspace of a 2(SP+SPR+SPU) serial–parallel manipulator. *Multibody System Dynamics*, 21(4), pp.361–374. doi:<https://doi.org/10.1007/s11044-009-9145-7>.

Lu, Z., Xu, C., Pan, Q., Zhao, X. and Li, X. (2015b). Inverse Kinematic Analysis and Evaluation of a Robot for Nondestructive Testing Application. *Journal of Robotics*, 2015, pp.1–7. doi:<https://doi.org/10.1155/2015/596327>.

Mandal, P., Sarkar, B.K., Saha, R., Mookherjee, S. and Sanyal, D. (2016). Designing an optimized model-free controller for improved motion tracking by rugged electrohydraulic system. *Proceedings of the Institution of Mechanical Engineers, Part I: Journal of Systems and Control Engineering*, 230(5), pp.385–396.  
doi:<https://doi.org/10.1177/0959651815622847>.

Mattila, J., Koivumaki, J., Caldwell, D.G. and Semini, C. (2017). A Survey on Control of Hydraulic Robotic Manipulators With Projection to Future Trends. *IEEE/ASME Transactions on Mechatronics*, 22(2), pp.669–680.  
doi:<https://doi.org/10.1109/tmech.2017.2668604>.

Meinsma, G. (1995). Elementary proof of the Routh-Hurwitz test. *Systems & Control Letters*, 25(4), pp.237–242. doi:[https://doi.org/10.1016/0167-6911\(94\)00089-e](https://doi.org/10.1016/0167-6911(94)00089-e).

Merritt, H.E. (1967). *Hydraulic control systems*. Wiley New York.

Mohanty, A. and Yao, B. (2011a). Indirect Adaptive Robust Control of Hydraulic

Manipulators With Accurate Parameter Estimates. *IEEE Transactions on Control Systems Technology*, 19(3), pp.567–575. doi:<https://doi.org/10.1109/tcst.2010.2048569>.

Mohanty, A. and Yao, B. (2011b). Integrated Direct/Indirect Adaptive Robust Control of Hydraulic Manipulators With Valve Deadband. *IEEE/ASME Transactions on Mechatronics*, 16(4), pp.707–715. doi:<https://doi.org/10.1109/tmech.2010.2051037>.

Mondal, N., Saha, R., Mookherjee, S. and Sanyal, D. (2018). A novel method to design pressure compensator for variable displacement axial piston pump. *Proceedings of the Institution of Mechanical Engineers, Part E: Journal of Process Mechanical Engineering*, 233(2), pp.314–334. doi:<https://doi.org/10.1177/0954408918783409>.

Motokura, K., Takahashi, M., Ewerton, M. and Peters, J. (2020). Plucking Motions for Tea Harvesting Robots Using Probabilistic Movement Primitives. *IEEE Robotics and Automation Letters*, 5(2), pp.3275–3282. doi:<https://doi.org/10.1109/lra.2020.2976314>.

Na, B., Choi, H. and Kong, K. (2015). Design of a Direct-Driven Linear Actuator for a High-Speed Quadruped Robot, Cheetaroid-I. *IEEE/ASME Transactions on Mechatronics*, 20(2), pp.924–933. doi:<https://doi.org/10.1109/tmech.2014.2326696>.

Na, J., Ren, X., Herrmann, G. and Qiao, Z. (2011). Adaptive neural dynamic surface control for servo systems with unknown dead-zone. *Control Engineering Practice*, 19(11), pp.1328–1343. doi:<https://doi.org/10.1016/j.conengprac.2011.07.005>.

Nguyen, Q.H., Ha, Q.P., Rye, D.C. and Durrant-Whyte, H.F., 1999, March. Feedback linearisation control for electrohydraulic systems of a robotic excavator. In *Proceedings of the Australian Conference for Robotics and Automation* (Vol. 1, pp. 190-195).

Niranjan, P., Karinka, S., Sairam, K.V.S.S.S.S., Upadhyaya, A. and Shetty, S. (2017). Friction modeling in servo machines: a review. *International Journal of Dynamics and Control*, 6(3), pp.893–906. doi:<https://doi.org/10.1007/s40435-017-0353-3>.

Olsson, H., Åström, K.J., Canudas de Wit, C., Gäfvert, M. and Lischinsky, P. (1998). Friction Models and Friction Compensation. *European Journal of Control*, [online] 4(3), pp.176–195. doi:[https://doi.org/10.1016/s0947-3580\(98\)70113-x](https://doi.org/10.1016/s0947-3580(98)70113-x).

Onder, M., Bayrak, A. and Aksoy, S. (2021). RISE-based backstepping control design for an electro-hydraulic arm system with parametric uncertainties. *International Journal of Control*, 95(10), pp.1–13. doi:<https://doi.org/10.1080/00207179.2021.1939164>.

Owen, W.S. and Croft, E.A. (2003). The reduction of stick-slip friction in hydraulic

actuators. *IEEE/ASME Transactions on Mechatronics*, 8(3), pp.362–371. doi:<https://doi.org/10.1109/tmech.2003.816804>.

Papadopoulos, E., Bin Mu and Frenette, R. (2003). On modeling, identification, and control of a heavy-duty electrohydraulic harvester manipulator. *IEEE/ASME Transactions on Mechatronics*, 8(2), pp.178–187. doi:<https://doi.org/10.1109/tmech.2003.812820>.

Pashkevich, A., Chablat, D. and Wenger, P. (2008). Stiffness Analysis Of Multi-Chain Parallel Robotic Systems. *IFAC Proceedings Volumes*, 41(3), pp.127–132. doi:<https://doi.org/10.3182/20081205-2-cl-4009.00024>.

Pashkevich, A., Klimchik, A. and Chablat, D. (2011). Enhanced stiffness modeling of manipulators with passive joints. *Mechanism and Machine Theory*, 46(5), pp.662–679. doi:<https://doi.org/10.1016/j.mechmachtheory.2010.12.008>.

Patel, Y.D. and George, P.M. (2012). Parallel Manipulators Applications—A Survey. *Modern Mechanical Engineering*, 02(03), pp.57–64. doi:<https://doi.org/10.4236/mme.2012.23008>.

Pi, Y. and Wang, X. (2011). Trajectory tracking control of a 6-DOF hydraulic parallel robot manipulator with uncertain load disturbances. *Control Engineering Practice*, 19(2), pp.185–193. doi:<https://doi.org/10.1016/j.conengprac.2010.11.006>.

Pisla, D., Szilaghyi, A., Vaida, C. and Plitea, N. (2013). Kinematics and workspace modeling of a new hybrid robot used in minimally invasive surgery. *Robotics and Computer-Integrated Manufacturing*, 29(2), pp.463–474. doi:<https://doi.org/10.1016/j.rcim.2012.09.016>.

Plummer, A.R. (2007). Robust electrohydraulic force control. *Proceedings of the Institution of Mechanical Engineers, Part I: Journal of Systems and Control Engineering*, 221(4), pp.717–731. doi:<https://doi.org/10.1243/09596518jsce370>.

Pourghodrat, A., Nelson, C.A. and Oleynikov, D. (2014). Electrohydraulic Robotic Manipulator With Multiple Instruments for Minimally Invasive Surgery<sup>1</sup>. *Journal of Medical Devices*, 8(3). doi:<https://doi.org/10.1115/1.4027040>.

Pradipta, J., Klunder, M., Weickgenannt, M. and Sawodny, O. (2013). Development of a pneumatically driven flight simulator Stewart platform using motion and force control. *2013 IEEE/ASME International Conference on Advanced Intelligent Mechatronics*. doi:<https://doi.org/10.1109/aim.2013.6584085>.



- Quan, Z., Quan, L. and Zhang, J. (2014). Review of energy efficient direct pump controlled cylinder electro-hydraulic technology. *Renewable and Sustainable Energy Reviews*, 35, pp.336–346. doi:<https://doi.org/10.1016/j.rser.2014.04.036>.
- Rahmat, M.F., Zulfatman, Husain, A.R., Sam, Y., Ghazali, R. and Rozali, S. (2011). Modeling and controller design of an industrial hydraulic actuator system in the presence of friction and internal leakage. *INTERNATIONAL JOURNAL OF PHYSICAL SCIENCES*, 6(14), pp.3502–3517. doi:<https://doi.org/10.5897/IJPS>.
- Raibert, M., Blankespoor, K., Nelson, G. and Playter, R. (2008). BigDog, the Rough-Terrain Quadruped Robot. *IFAC Proceedings Volumes*, 41(2), pp.10822–10825. doi:<https://doi.org/10.3182/20080706-5-kr-1001.01833>.
- Ramirez, D., Kotlarski, J. and Ortmaier, T. (2016). Combined Structural and Dimensional Synthesis of Serial Robot Manipulators. *ROMANSY 21 - Robot Design, Dynamics and Control*, pp.207–216. doi:[https://doi.org/10.1007/978-3-319-33714-2\\_23](https://doi.org/10.1007/978-3-319-33714-2_23).
- Ranjan, P., Wrat, G., Bhola, M., Mishra, S.Kr. and Das, J. (2020). A novel approach for the energy recovery and position control of a hybrid hydraulic excavator. *ISA Transactions*, 99, pp.387–402. doi:<https://doi.org/10.1016/j.isatra.2019.08.066>.
- Rice, J.J. and Schimmels, J.M. (2018). Passive Compliance Control of Redundant Serial Manipulators. *Journal of Mechanisms and Robotics*, 10(4). doi:<https://doi.org/10.1115/1.4039591>.
- Rodriguez, E. and Alvares, A. (2019). A STEP-NC implementation approach for additive manufacturing. *Procedia Manufacturing*, 38, pp.9–16. doi:<https://doi.org/10.1016/j.promfg.2020.01.002>.
- Sahoo, S.R., Chiddarwar, S.S. and Alakshendra, V. (2017). Intuitive dynamic modeling and flatness-based nonlinear control of a mobile robot. *SIMULATION*, 94(9), pp.797–820. doi:<https://doi.org/10.1177/0037549717741192>.
- Sarkar, B.K. (2018). Modeling and validation of a 2-DOF parallel manipulator for pose control application. *Robotics and Computer-Integrated Manufacturing*, 50, pp.234–241. doi:<https://doi.org/10.1016/j.rcim.2017.09.017>.
- Sarkar, B.K., Das, J., Saha, R., Mookherjee, S. and Sanyal, D. (2013a). Approaching Servoclass Tracking Performance by a Proportional Valve-Controlled System. *IEEE/ASME Transactions on Mechatronics*, 18(4), pp.1425–1430.

doi:<https://doi.org/10.1109/tmech.2013.2253116>.

Sarkar, B.K., Mandal, P., Saha, R., Mookherjee, S. and Sanyal, D. (2013b). GA-optimized feedforward-PID tracking control for a rugged electrohydraulic system design. *ISA Transactions*, 52(6), pp.853–861. doi:<https://doi.org/10.1016/j.isatra.2013.07.008>.

Semini, C., Barasuol, V., Boaventura, T., Frigerio, M., Focchi, M., Caldwell, D.G. and Buchli, J. (2015). Towards versatile legged robots through active impedance control. *The International Journal of Robotics Research*, 34(7), pp.1003–1020. doi:<https://doi.org/10.1177/0278364915578839>.

Semini, C., Tsagarakis, N.G., Guglielmino, E., Focchi, M., Cannella, F. and Caldwell, D.G. (2011). Design of HyQ – a hydraulically and electrically actuated quadruped robot. *Proceedings of the Institution of Mechanical Engineers, Part I: Journal of Systems and Control Engineering*, 225(6), pp.831–849. doi:<https://doi.org/10.1177/0959651811402275>.

Şener Kaya, A. and Zeki Bilgin, M. (2018). Output Feedback Control Surface Positioning With a High-Order Sliding Mode Controller/Estimator: An Experimental Study on a Hydraulic Flight Actuation System. *Journal of Dynamic Systems, Measurement, and Control*, 141(1). doi:<https://doi.org/10.1115/1.4040436>.

Shi, C., Wang, X., Wang, S., Wang, J. and Tomovic, M.M. (2015). Adaptive decoupling synchronous control of dissimilar redundant actuation system for large civil aircraft. *Aerospace Science and Technology*, 47, pp.114–124. doi:<https://doi.org/10.1016/j.ast.2015.09.012>.

Siciliano, B. and Khatib, O. (2016). *Springer handbook of robotics*. 2nd ed. Verlag Berlin Heidelberg: Springer .

Sira-Ramírez, H., Luviano-Juárez, A., Ramírez-Neria, M. and Zurita-Bustamante, E.W. (2017). *Active Disturbance Rejection Control of Dynamic Systems*. Elsevier. doi:<https://doi.org/10.1016/c2016-0-01983-6>.

Sirouspour, M.R. and Salcudean, S.E. (2001). Nonlinear control of hydraulic robots. *IEEE Transactions on Robotics and Automation*, 17(2), pp.173–182. doi:<https://doi.org/10.1109/70.928562>.

Sneed, R., Smith, R., Cash, M. and Anderson, E. (2007). Smart-Material Based Hydraulic Pump System for Actuation of a Morphing Wing. *48th AIAA/ASME/ASCE/AHS/ASC*

*Structures, Structural Dynamics, and Materials Conference.*  
doi:<https://doi.org/10.2514/6.2007-1702>.

Song, B., Lee, D., Park, S.Y. and Baek, Y.S. (2020). A Novel Method for Designing Motion Profiles Based on a Fuzzy Logic Algorithm Using the Hip Joint Angles of a Lower-Limb Exoskeleton Robot. *Applied Sciences*, 10(19), p.6852.  
doi:<https://doi.org/10.3390/app10196852>.

Sorine, M. and Szymanski, J. (2000). A New Dynamic Multi-D.O.F. Tire-Model. *IFAC Proceedings Volumes*, 33(9), pp.549–554. doi:[https://doi.org/10.1016/s1474-6670\(17\)38201-0](https://doi.org/10.1016/s1474-6670(17)38201-0).

Suling, L., Junying, L. and Lei, Z. (2010). Design and Implementation of Electro-Hydraulic Control System of Multi-station Press. *2010 International Conference on Intelligent Computation Technology and Automation*, [1], pp.{1143-1146}.  
doi:<https://doi.org/10.1109/icicta.2010.572>.

Sun, L., Li, D., Gao, Z., Yang, Z. and Zhao, S. (2016). Combined feedforward and model-assisted active disturbance rejection control for non-minimum phase system. *ISA Transactions*, 64, pp.24–33. doi:<https://doi.org/10.1016/j.isatra.2016.04.020>.

Sun, L. and You, F. (2021). Machine learning and data-driven techniques for the control of smart power generation systems: An uncertainty handling perspective. *Engineering*.  
doi:<https://doi.org/10.1016/j.eng.2021.04.020>.

Tanev, T.K. (2000). Kinematics of a hybrid (parallel–serial) robot manipulator. *Mechanism and Machine Theory*, 35(9), pp.1183–1196. doi:[https://doi.org/10.1016/s0094-114x\(99\)00073-7](https://doi.org/10.1016/s0094-114x(99)00073-7).

Tendick, F., Sastry, S.S., Fearing, R.S. and Cohn, M. (1998). Applications of micromechatronics in minimally invasive surgery. *IEEE/ASME Transactions on Mechatronics*, [online] 3(1), pp.34–42. doi:<https://doi.org/10.1109/3516.662866>.

Totten, G.E. and De, V.J. (2017). *Handbook of Hydraulic Fluid Technology, Second Edition*. CRC Press.

Tripathi, A. and Sun, Z. (2016). Nonlinear Feedforward Control for Electrohydraulic Actuators With Asymmetric Piston Areas. In: *Volume 2: Mechatronics; Mechatronics and Controls in Advanced Manufacturing; Modeling and Control of Automotive Systems and Combustion Engines; Modeling and Validation; Motion and Vibration Control*

*Applications; Multi-Agent and Networked Systems; Path Planning and Motion Control; Robot Manipulators; Sensors and Actuators; Tracking Control Systems; Uncertain Systems and Robustness; Unmanned, Ground and Surface Robotics; Vehicle Dynamic Controls; Vehicle Dynamics and Traffic Control.* doi:<https://doi.org/10.1115/dscc2016-9721>.

Truong, H., Maxon, V. and Goh, A.C. (2021). Robotic Female Radical Cystectomy. *Journal of Endourology*, 35(S2), p.S-106-S-115. doi:<https://doi.org/10.1089/end.2020.1190>.

Truong, H.V.A., Trinh, H.A. and Ahn, K.K. (2020). Safety Operation of n-DOF Serial Hydraulic Manipulator in Constrained Motion with Consideration of Contact-Loss Fault. *Applied Sciences*, 10(22), p.8107. doi:<https://doi.org/10.3390/app10228107>.

Utkin, V.I. (1992). *Sliding Modes in Control and Optimization*. Springer Science & Business Media.

Vegete, van de J. (1994). *Feedback control systems*, 3rd Edition, Prentice Hall, Englewood Cliff, New Jersey.

Vickers (Eaton), 1993, SM4-10/12/15 Servovalves, flows to 57 l/min (15 USgpm) – pressures to 210 bar (3000 psi) datasheet.

Waldron, K.J., Raghavan, M. and Roth, B. (1989). Kinematics of a Hybrid Series-Parallel Manipulation System. *Journal of Dynamic Systems, Measurement, and Control*, 111(2), pp.211–221. doi:<https://doi.org/10.1115/1.3153039>.

Walters, R.B. (2012). *Hydraulic and Electro-Hydraulic Control Systems*. Springer Science & Business Media.

Wapler, M., Urban, V., Weisener, T., Stallkamp, J., Dürr, M. and Hiller, A. (2003). A Stewart platform for precision surgery. *Transactions of the Institute of Measurement and Control*, 25(4), pp.329–334. doi:<https://doi.org/10.1191/0142331203tm092oa>.

Wu, H., Andersen, T.T., Andersen, N.A. and Ravn, O. (2017). Application of visual servoing for grasping and placing operation in slaughterhouse. *2017 3rd International Conference on Control, Automation and Robotics (ICCAR)*. doi:<https://doi.org/10.1109/iccar.2017.7942738>.

Xu, P., Cheung, C.F., Wang, C. and Zhao, C. (2020). Novel hybrid robot and its processes for precision polishing of freeform surfaces. *Precision Engineering*, 64, pp.53–62.

doi:<https://doi.org/10.1016/j.precisioneng.2020.03.013>.

Yanagawa, F., Perez, M., Bell, T., Grim, R., Martin, J. and Ahuja, V. (2015). Critical Outcomes in Nonrobotic vs Robotic-Assisted Cardiac Surgery. *JAMA Surgery*, 150(8), p.771. doi:<https://doi.org/10.1001/jamasurg.2015.1098>.

Yang, G. and Yao, J. (2020). High-precision motion servo control of double-rod electro-hydraulic actuators with exact tracking performance. *ISA Transactions*, 103, pp.266–279. doi:<https://doi.org/10.1016/j.isatra.2020.03.029>.

Yao, B., Al-Majed, M. and Tomizuka, M. (1997). High performance robust motion control of machine tools: an adaptive robust control approach and comparative experiments. *Proceedings of the 1997 American Control Conference (Cat. No.97CH36041)*, 5, pp.2754–2758. doi:<https://doi.org/10.1109/acc.1997.611956>.

Yao, B., Bu, F. and Chiu, G.T.C. (2001). Non-linear adaptive robust control of electro-hydraulic systems driven by double-rod actuators. *International Journal of Control*, 74(8), pp.761–775. doi:<https://doi.org/10.1080/002071700110037515>.

Yao, J., Deng, W. and Sun, W. (2017). Precision Motion Control for Electro-Hydraulic Servo Systems With Noise Alleviation: A Desired Compensation Adaptive Approach. *IEEE/ASME Transactions on Mechatronics*, 22(4), pp.1859–1868. doi:<https://doi.org/10.1109/tmech.2017.2688353>.

Ye, N., Song, J. and Ren, G. (2020). Model-Based Adaptive Command Filtering Control of an Electrohydraulic Actuator With Input Saturation and Friction. *IEEE Access*, 8, pp.48252–48263. doi:<https://doi.org/10.1109/access.2020.2979162>.

Yeshmukhametov, A., Kalimoldayev, M., Mamyrbayev, O. and Amirgaliev, Y. (2017). Design and kinematics of serial/parallel hybrid robot. *2017 3rd International Conference on Control, Automation and Robotics (ICCAR)*. doi:<https://doi.org/10.1109/iccar.2017.7942679>.

Yin, L., Deng, W., Yang, X. and Yao, J. (2021). Finite-Time Output Feedback Control for Electro-Hydraulic Servo Systems with Parameter Adaptation. *Machines*, 9(10), p.214. doi:<https://doi.org/10.3390/machines9100214>.

Yu, H., Feng, Z. and Wang, X. (2004). Nonlinear control for a class of hydraulic servo system. *Journal of Zhejiang University-SCIENCE A*, 5(11), pp.1413–1417. doi:<https://doi.org/10.1631/jzus.2004.1413>.

- Yung, I., Vázquez, C. and Freidovich, L.B. (2017). Robust position control design for a cylinder in mobile hydraulics applications. *Control Engineering Practice*, 69, pp.36–49. doi:<https://doi.org/10.1016/j.conengprac.2017.09.004>.
- Zhang, X., Qiao, S., Quan, L. and Ge, L. (2019). Velocity and Position Hybrid Control for Excavator Boom Based on Independent Metering System. *IEEE Access*, 7, pp.71999–72011. doi:<https://doi.org/10.1109/access.2019.2919953>.
- Zhao, C., Guo, H., Liu, R., Deng, Z., Li, B. and Tian, J. (2019a). Actuation distribution and workspace analysis of a novel 3(3RRIS) metamorphic serial-parallel manipulator for grasping space non-cooperative targets. *Mechanism and Machine Theory*, 139, pp.424–442. doi:<https://doi.org/10.1016/j.mechmachtheory.2019.04.019>.
- Zhao, J.-X., Li, C., Ren, H., Hao, M., Zhang, L.-C. and Tang, P.-F. (2019b). Evolution and Current Applications of Robot-Assisted Fracture Reduction: A Comprehensive Review. *Annals of Biomedical Engineering*, 48(1), pp.203–224. doi:<https://doi.org/10.1007/s10439-019-02332-y>.
- Zheng, D. and Alleyne, A. (2003). Modeling and Control of an Electro-hydraulic Injection Molding Machine With Smoothed Fill-to-Pack Transition\*. *Journal of Manufacturing Science and Engineering*, 125(1), pp.154–163. doi:<https://doi.org/10.1115/1.1540126>.









# APPENDIX

In (2.5a), using (2.5b), (2.5d), (2.5f) and (2.5l) for  $\dot{y} \geq 0$  and (2.5c), (2.5e), (2.5g) and (2.5m) for  $\dot{y} < 0$  in the expressions of  $f_1$  to  $f_5$ , the coefficients  $a_2$ ,  $a_1$ ,  $a_0$  and  $a_{-1}$  in (3.14a) are expressed by employing (3.13a) to (3.13f) as

$$a_2 = N_2/D - f_{5\dot{y}}, \quad (\text{A1})$$

$$a_1 = N_1/D - f_{5\dot{y}}, \quad (\text{A2})$$

$$a_0 = N_0/D - f_{5y} + f_{5V}k_P, \quad (\text{A3})$$

$$a_{-1} = k_I f_{5P_P} \{f_{1Q_P} f_{5V} / (1 - f_{1Q_P} f_{5P_P}) + N_{-1}/D\}, \quad (\text{A4})$$

$$\begin{aligned} \text{where } N_2 = & f_{5P_P} f_{1Q_P} [f_{2P_1} \{f_{1Q_P} (f_{3P_P} f_{3P_2} f_{4\dot{y}} - f_{4P_P} f_{2P_2} f_{3y}) + (1 - f_{1Q_P} f_{2P_P}) f_{3y}\} + \\ & f_{2P_2} \{f_{1Q_P} f_{2P_1} (f_{4P_P} f_{3y} - f_{3P_P} f_{4\dot{y}}) + (1 - f_{1Q_P} f_{2P_P}) f_{4\dot{y}}\}] + (1 - \\ & f_{1Q_P} f_{2P_P}) [f_{5P_1} \{f_{1Q_P} f_{2P_2} (f_{3P_P} f_{4\dot{y}} - f_{4P_P} f_{3y}) + f_{3y} (1 - f_{1Q_P} f_{2P_P})\} + \\ & f_{5P_2} \{f_{1Q_P} f_{2P_1} (f_{4P_P} f_{3y} - f_{3P_P} f_{4\dot{y}}) + f_{4\dot{y}} (1 - f_{1Q_P} f_{2P_P})\}], \end{aligned} \quad (\text{A5})$$

$$\begin{aligned} N_1 = & f_{5P_P} f_{1Q_P} [f_{2P_1} \{f_{1Q_P} f_{2P_2} (f_{4P_P} f_{3y} - f_{3P_P} f_{4\dot{y}}) - (1 - f_{1Q_P} f_{2P_P}) f_{3y}\} + \\ & f_{2P_2} \{f_{1Q_P} f_{2P_1} (f_{4P_P} f_{3y} - f_{3P_P} f_{4\dot{y}} - (1 - f_{1Q_P} f_{2P_P}) f_{4\dot{y}}\} + (1 - \\ & f_{1Q_P} f_{2P_P}) [f_{5P_1} \{f_{1Q_P} f_{2P_2} (f_{3P_P} f_{4\dot{y}} - f_{4P_P} f_{3y}) + f_{3y} (1 - f_{1Q_P} f_{2P_P})\} + \\ & f_{5P_2} \{f_{1Q_P} f_{2P_1} (f_{4P_P} f_{3y} - f_{3P_P} f_{4\dot{y}}) + f_{4\dot{y}} (1 - f_{1Q_P} f_{2P_P})\}], \end{aligned} \quad (\text{A6})$$

$$\begin{aligned} N_0 = & f_{5P_P} f_{1Q_P} \{(f_{2P_1} f_{3y} + f_{2P_2} f_{4y})(1 - f_{1Q_P} f_{2P_P}) - k_P f_{1Q_P} f_{2V} (f_{3P_P} f_{2P_1} + f_{4P_P} f_{2P_2})\} + \\ & (1 - f_{1Q_P} f_{2P_P}) [f_{5P_1} \{f_{1Q_P} f_{2P_2} (f_{3P_P} f_{4y} - f_{4P_P} f_{3y}) + (1 - f_{1Q_P} f_{2P_P}) f_{3y} - \\ & k_P f_{1Q_P} f_{3P_P} f_{2V} + f_{5P_2} \{f_{1Q_P} f_{2P_1} (f_{4P_P} f_{4y} - f_{3P_P} f_{3y}) + (1 - f_{1Q_P} f_{2P_P}) f_{3y} - \\ & k_P f_{1Q_P} f_{4P_P} f_{2V}\}] + k_P f_{5P_2} f_{1Q_P} f_{2P_1} f_{3P_P} (1 - f_{1Q_P} f_{4P_P} f_{2V}), \end{aligned} \quad (\text{A7})$$

$$N_{-1} = f_{1Q_P} f_{2V} [f_{1Q_P} f_{2P_2} f_{4P_P} + f_{1Q_P} f_{2P_1} f_{3P_P} - (1 - f_{1Q_P} f_{2P_P}) \{f_{5P_1} f_{3P_P} + f_{5P_2} f_{4P_P}\}], \quad (\text{A8})$$

and

$$\begin{aligned} D = & \{(1 - f_{1Q_P} f_{2P_P}) - f_{1Q_P} f_{2P_2} f_{4P_P}\} \{(1 - f_{1Q_P} f_{2P_P}) - f_{1Q_P} f_{2P_1} f_{3P_P}\} - \\ & f_{1Q_P}^2 f_{3P_P} f_{4P_P} f_{2P_1} f_{2P_2}. \end{aligned} \quad (\text{A9})$$



Signature of Candidate:

Aniruddha Sarkar (198/17/E)

(Aniruddha Sarkar)

Date : 19/6/2023

Certified by Supervisor(s):

(Signature with date, seal)

1 Saikat Mookherjee 19/6/23

(Prof. Saikat Mookherjee)

Department of Mechanical Engineering

Jadavpur University, Kolkata, India

PROFESSOR  
Mechanical Engineering Deptt  
Jadavpur University  
Kolkata - 700 032

2 Dipankar Sanyal 19/6/23

(Prof. Dipankar Sanyal)

Department of Mechanical Engineering

Jadavpur University, Kolkata, India

PROFESSOR  
Mechanical Engineering Deptt  
Jadavpur University  
Kolkata - 700 032